Physicochemical properties of Fe-bearing minerals and metal alloys at deep Earth conditions

DISSERTATION

zur Erlangung des akademischen Grades eines Doktorin der Naturwissenschaften (Dr.rer.nat.) in der Bayreuther Graduiertenschule für Mathematik und Naturwissenschaften (BayNAT) der Universität Bayreuth

vorgelegt von

Serena Dominijanni

aus Rome (Italien)

Bayreuth, 2022

This doctoral thesis was prepared at the department of Bayerisches Geoinstitut at the University of Bayreuth from *May 2018* until *April 2022* and was supervised by PD Dr. Catherine A. McCammon.

This is a full reprint of the thesis submitted to obtain the academic degree of Doctor of Natural Sciences (Dr. rer. nat.) and approved by the Bayreuth Graduate School of Mathematical and Natural Sciences (BayNAT) of the University of Bayreuth.

Date of submission: 08/04/2022

Date of defence: 09/05/2022

Acting director: Prof. Dr. Hans Keppler

Doctoral committee:

PD Dr. Catherine A. McCammon	(reviewer)
Prof. Dr. Daniel J. Frost	(reviewer)
Prof. Dr. Leonid S. Dubrovinsky	(chairman)
PD Dr. Gerd Steinle-Neumann	

SUMMARY

Understanding the physicochemical properties such as oxidation state, composition, and elastic behavior of candidate materials at the conditions of the Earth's interior is essential for comprehending the evolution and dynamics of our planet. Knowledge of Earth's structure and composition mainly relies on geophysical and cosmochemical evidence, theoretical predictions and laboratory studies. Specifically, experimental works simulate extreme pressure and temperature conditions of the deep Earth using large-volume presses and diamond anvil cells combined with the laser heating system. However, although numerous advancements have been made in experimental techniques during the past decades, we still have an incomplete picture of many processes occurring in the Earth's interior. For example, the oxygen fugacity (f_{O_2}) of Earth's mantle is a fundamental issue in geoscience since it influences numerous processes such as the mobility of volatile species, the depth of partial melting, and the speciation of magmatic gasses. Nevertheless, this parameter has only been poorly controlled or measured during diamond anvil cell (DAC) experiments, which represent the experimental gateway to the deepest region of Earth's mantle. To address this issue, we developed a novel approach to monitor the oxygen fugacity in diamond anvil cell based on the redox sensor method. Ferropericlase and iridium metal were mixed as starting powder and reacted in a DAC after laser heating to obtain a Fe-Ir alloy and use the activity-composition relation to calculate the f_{O_2}. We monitored the variation of redox reactions through Synchrotron Mössbauer Source, X-ray absorption near-edge structure, and electron energy loss spectroscopy measurements and chemical analyses down to the nanometer scale and compared the results with complementary multi anvil experiments. Moreover, we updated the existing thermodynamic model for the Fe-Ir redox sensor, currently available at room pressure, up to 100 GPa including the volume dependence on the activity composition-relations.

The newly calibrated model for the Fe-Ir system was tested in experimental systems designed to simulate the interaction between a carbonated subducting slab and a Fe-saturated lower mantle to vary the local f_{O_2} from the iron-wüstite buffer up to conditions where carbonate and diamond coexist, i.e. the lowest f_{O_2} at which carbonate can survive and the highest f_{O_2} at which diamonds are stable in the lower mantle. We investigated the local oxygen fugacity

variation induced by the influx of carbonates as recorded by the $Fe^{3+}/\Sigma Fe$ ratio in ferropericlase using in-house point source Mössbauer spectroscopy. Furthermore, we confirmed the feasibility of using ferropericlase as an oxybarometer for the lower mantle, observing a positive correlation between oxidation state and oxygen fugacity. Our experimental results are then integrated with measurements of $Fe^{3+}/\Sigma Fe$ on ferropericlase inclusions in sub-lithospheric diamonds from Rio Soriso (Brazil) conducted with the Synchrotron Mössbauer Source to address the role of pressure, temperature and oxygen fugacity. We argue about the compositional and redox heterogeneity recorded by both sets of samples with implications for diamond formation via redox freezing of subducted carbonates at lower mantle conditions. Our results provide unique information on the maximum ferric iron content that ferropericlase can incorporate at the redox conditions where carbonate and diamond coexist to explain processes such as redox-driven diamond formation and redox melting.

Another aspect that is still under debate is the Earth's inner core composition. It is widely accepted that some light elements, such as Si, are predicted to be in the inner core by compositional models to explain the density deficit between pure Fe and seismological observation of the inner core. However, the effect of Si and Ni on the elastic properties, i.e., density and sound wave velocities, of pure Fe is still poorly constrained. Based on the Fe-Si system's phase relations, the inner core might be composed of a Si-enriched B2 and Si-depleted *hcp* phase mixture. In this study, we tested this hypothesis by performing high-pressure measurements of the sound velocities and density of polycrystalline B2-Fe-(7 wt. %)Ni-(15 wt. %)Si using inelastic X-ray scattering and powder X-ray diffraction up to 100 GPa. We compared our results with previous experimental and *ab initio* studies conducted on Fe-Si, Fe-Ni-Si, and Fe-Ni alloys to explore the combined effect of Si and Ni on the bulk sound velocities and density. Moreover, using a thermodynamic model we extrapolated our results to the inner core boundary conditions and matches geophysical observations of density, compressional and shear wave velocities of the inner core. Our main findings provide new constraints on the role of Si as a light element in the inner core and propose a compositional model that accounts for seismological observations of Earth's inner core.

ZUSAMMENFASSUNG

Das Verständnis der physikalisch-chemischen Eigenschaften wie Oxidationszustand, Zusammensetzung und elastisches Verhalten der in Frage kommenden Materialien unter den Bedingungen des Erdinneren ist für das Verständnis der Entwicklung und Dynamik unseres Planeten von wesentlicher Bedeutung. Das Wissen über die Struktur und Zusammensetzung der Erde stützt sich hauptsächlich auf geophysikalische und kosmochemische Erkenntnisse, theoretische Vorhersagen und Laborstudien. Insbesondere experimentelle Arbeiten simulieren die extremen Druck- und Temperaturbedingungen in der Tiefe der Erde mit Hilfe von großvolumigen Pressen und Diamant-Stempelzellen in Kombination mit einem Laserheizsystem. Obwohl in den letzten Jahrzehnten zahlreiche Fortschritte bei den experimentellen Techniken erzielt wurden, haben wir immer noch ein unvollständiges Bild von vielen Prozessen, die im Erdinneren ablaufen. So ist beispielsweise die Sauerstoffugazität (f_{O_2}) des Erdmantels von grundlegender Bedeutung für die Geowissenschaften, da sie zahlreiche Prozesse wie die Mobilität flüchtiger Stoffe, die Tiefe des partiellen Aufschmelzens und die Speziation magmatischer Gase beeinflusst. Dennoch wurde dieser Parameter bei Experimenten mit Diamant-Stempelzellen (DAC), die den experimentellen Zugang zur tiefsten Region des Erdmantels darstellen, bisher nur unzureichend kontrolliert oder gemessen. Um dieses Problem zu lösen, haben wir einen neuen Ansatz zur Überwachung der Sauerstoffugazität in der Diamant-Stempelzelle entwickelt, der auf der Redox-Sensor-Methode basiert. Ferroperiklas und metallisches Iridium wurden als Ausgangspulver gemischt und in einer DAC mithilfe der Laserheizung in eine Fe-Ir-Legierung umgewandelt und dann über die Aktivitäts-Zusammensetzungs-Beziehung zur Berechnung von f_{O_2} verwendet. Wir überwachten die Änderungen in den Redoxreaktionen durch Messungen mit der Synchrotron-Mössbauerspektroskopie, der Röntgen-Nahkanten-Absorptionsspektroskopie und der Elektronenenergieverlustspektroskopie sowie durch chemische Analysen bis in den Nanometerbereich und verglichen die Ergebnisse mit ergänzenden Experimenten in der Vielstempel-Presse. Darüber hinaus haben wir das bestehende thermodynamische Modell für den Fe-Ir-Redoxsensor, das derzeit bei Raumdruck verfügbar ist, auf bis 100 GPa erweitert, einschließlich der Volumenabhängigkeit der Aktivitäts-Zusammensetzungs-Beziehungen.

Das neu kalibrierte Modell für das Fe-Ir-System wurde in experimentellen Systemen getestet, die entwickelt wurden, um die Wechselwirkung zwischen einer karbonisierten subduzierten Platte und einem Fe-gesättigten unteren Mantel zu simulieren, um die lokale f_{O_2} des Eisen-Wüstit-Puffers bis zu Bedingungen zu variieren, bei denen Karbonat und Diamant koexistieren, d.h. die niedrigste f_{O_2}, bei der Karbonat existieren kann, und die höchste f_{O_2}, bei der Diamanten im unteren Mantel stabil sind. Wir untersuchten die durch den Karbonatzufluss hervorgerufene Veränderung der lokalen Sauerstofffugazität, die anhand des $Fe^{3+}/\Sigma Fe$-Verhältnisses in Ferroperiklas in-house mit Hilfe einer Mössbauer-Punktquelle bestimmt wurde. Darüber hinaus bestätigten wir die Möglichkeit, Ferroperiklas als Oxidationsbarometer für den unteren Erdmantel zu verwenden, indem wir eine positive Korrelation zwischen Oxidationszustand und Sauerstofffugazität feststellten. Unsere experimentellen Ergebnisse wurden dann mit Messungen von $Fe^{3+}/\Sigma Fe$ an Ferroperiklas-Einschlüssen in sublithosphärischen Diamanten aus Rio Soriso (Brasilien) kombiniert, die mit der Synchrotron-Mössbauer-Quelle ermittelt wurden, um die Rolle von Druck, Temperatur und Sauerstofffugazität zu untersuchen. Wir diskutieren die Heterogenität der Zusammensetzung und der Redoxeigenschaften der beiden Probensätze, die sich auf die Bildung von Diamanten durch Redoxgefrieren von subduzierten Karbonaten unter Bedingungen im unteren Mantel auswirken. Unsere Ergebnisse liefern einzigartige Informationen über den maximalen Eisengehalt, den Ferroperiklas unter Redox-Bedingungen, bei denen Karbonat und Diamant koexistieren, einbauen kann, um Prozesse wie die Redox-getriebene Diamantbildung und das Redox-Schmelzen zu erklären.

Ein weiterer Aspekt, über den noch diskutiert wird, ist die Zusammensetzung des Erdkerns. Es ist weithin anerkannt, dass einige leichte Elemente, wie Si, nach Zusammensetzungsmodellen im inneren Kern vorhanden sein müssen, um das Dichtedefizit zwischen reinem Fe und seismologischen Beobachtungen des inneren Kerns zu erklären. Die Auswirkungen von Si und Ni auf die Dichte und die elastischen Eigenschaften, d. h., die Schallwellengeschwindigkeiten, von reinem Fe sind jedoch nach wie vor nur unzureichend bekannt. Ausgehend von den Phasenbeziehungen des Fe-Si-Systems könnte der innere Kern aus einer mit Si angereicherten B2- und einer an Si verarmten hcp-Phasenmischung bestehen. In dieser Studie haben wir diese Hypothese durch Hochdruckmessungen der Schallgeschwindigkeiten und der Dichte von polykristallinem B2-Fe-(7 Gew.-%)Ni-(15 Gew.-%)Si mittels inelastischer Röntgenstreuung und Pulverröntgendiffraktometrie bis zu 100 GPa getestet. Wir verglichen unsere Ergebnisse mit

früheren experimentellen und ab initio-Studien, die an Fe-Si-, Fe-Ni-Si- und Fe-Ni-Legierungen durchgeführt wurden, um die kombinierte Wirkung von Si und Ni auf die Gesamtschallgeschwindigkeit und -dichte zu untersuchen. Darüber hinaus haben wir unsere Ergebnisse mithilfe eines thermodynamischen Modells auf die Bedingungen an der Grenze des inneren Kerns extrapoliert und mit geophysikalischen Beobachtungen der Dichte sowie der Kompressions- und Scherwellengeschwindigkeiten des inneren Kerns abgeglichen. Unsere Ergebnisse liefern neue Hinweise auf die Rolle von Si als leichtem Element im inneren Kern und begründen ein Zusammensetzungsmodell, das die seismologischen Beobachtungen des inneren Erdkerns erklärt.

CONTENTS

Summary 1

Zusammenfassung 3

1 Introduction 9

1.1 Structure and composition of deep Earth 9

1.1.1 Physics and chemistry of the lower mantle and core 11

1.1.2 The mineralogy of the lower mantle: phase stability as a function of the redox state 14

1.2 Redox state of Earth's interior 18

1.2.1 Redox state of the present-day mantle 22

1.2.2 Evolution of mantle oxygen fugacity after the core formation event 25

1.2.3 Redox freezing/melting processes in Earth's mantle and the deep carbon cycle 27

1.2.4 Redox mechanism of diamond formation 30

1.3 Redox sensors 32

1.3.1 Thermodynamics of binary systems 33

1.3.2 Phase relations of metal alloys commonly used as sliding redox sensors 36

1.4 Earth's core 39

1.4.1 Earth's inner core structure and compositional models 39

1.4.2 Phase relations and elasticity of Fe-(Ni)-Si alloys 42

1.5 Aim of the study 45

2 Methods 47

2.1 High pressure experiments 47

2.1.1 Pressure Generation 47

2.1.2 Sample synthesis and phase equilibria experiments with the multi anvil press 49

2.1.3 The diamond anvil cell 52

2.2 Analytical techniques 58

2.2.1 Scanning electron microscopy 58

2.2.2 Electron microprobe microanalysis 60

2.2.3 Mössbauer spectroscopy 61

2.2.4 X-ray diffraction 65

2.2.5 Focused Ion Beam: TEM foils preparation 67

2.2.6 Transmission Electron Microscopy 70

2.3 Synchrotron-based spectroscopies 74

2.3.1 Synchrotron Mössbauer Source Spectroscopy 74

2.3.2 Synchrotron X-ray diffraction 77

2.3.3 X-ray absorption near-edge structure 79
2.3.4 Inelastic X-ray scattering 81
2.4 Data analysis 85
2.4.1 Equation of state 85
2.4.2 Determination of fO_2 during high-pressure experiments 86
2.4.3 Determination of the Fe valence state in minerals: a comparison between SMS/MS, XANES and EELS methodologies 87
3 Determination of the oxygen fugacity in diamond anvil cell experiments 89
3.1 Introduction 89
3.2 Experimental procedures 90
3.2.1 Starting materials 90
3.2.2 Diamond anvil cell experiments 91
3.2.3 Multi anvil experiments 92
3.2.4 Synchrotron powder X-ray diffraction 92
3.2.5 Synchrotron Mössbauer Source 93
3.2.6 X-ray absorption near-edge structure spectroscopy 93
3.3 Analytical procedures 95
3.3.1 TEM lamella preparation 95
3.3.2 Transmission Electron Microscope (TEM) analyses 96
3.3.3 Chemical analyses of the multi anvil run product 97
3.4 Results 98
3.4.1 XRD results and equations of state 98
3.4.2 Chemical analyses results 103
3.4.3 Fe oxidation state in ferropericlase determined by EELS, XANES and SMS spectroscopies 106
3.4.4 Mass balance calculation 111
3.4.5 Oxygen fugacity 112
3.5 Discussion 116
3.5.1 Calibration of the Fe-Ir oxybarometer at high pressure 116
3.6 Conclusion remarks 122
4 Ferric iron content of natural diamond inclusions from Rio Soriso (Juina, Brazil) and synthetic ferropericlase: implications for redox mechanisms of diamond formation 123
4.1 Introduction 123
4.2 Materials and analytical techniques 124
4.2.1 Experimental multi anvil runs 124

4.2.2 Natural ferropericlase inclusions 125
4.2.3 Mössbauer Spectroscopy measurements on synthetic and natural ferropericlases 125
4.2.4 Textural observation and chemical analyses of synthetic and natural ferropericlase 127
4.2.5 Analyses of synthetic run products by Focus Ion Beam-assisted Transmission Electron Microscopy 127
4.3 Results 129
4.3.1 Textural and chemical analyses of the experimental run products 129
4.3.2 Determination of Fe oxidation state of natural and synthetic ferropericlase 131
4.3.3 Results from transmission electron microscope analyses 134
4.4 Discussions 137
4.4.1 Oxygen fugacity at which carbonate and diamond coexist in the lower mantle 137
4.4.2 Oxygen fugacity of the lower mantle revealed by natural ferropericlase inclusions 139
4.4.3 Mechanisms of super deep diamond formation: evidence of primordial lower mantle 142
4.5 Conclusions 144
5 Sound velocity measurements of B2-Fe-Ni-Si alloy under high pressure by inelastic X-ray scattering: Implications for the composition of Earth's core 145
5.1 Introduction 145
5.2 Materials and Methods 146
5.2.1 Sample synthesis 146
5.2.2 Diamond anvil cell experiments 147
5.2.3 IXS measurements at SPring-8 148
5.2.4 Synchrotron powder XRD measurements 151
5.3 Results 152
5.3.1 XRD results and equation of state 152
5.3.2 Sound velocity and Birch’s law 154
5.4 Discussion 159
5.5 Conclusions 165
6 Major conclusions and future outlooks 166
7 Acknowledgments 169
8 Appendix 171
9 References 184

Chapter 1

1 INTRODUCTION

1.1 STRUCTURE AND COMPOSITION OF DEEP EARTH

Physicochemical properties of the lower mantle and core determine the compositional, seismological, and thermal structure of the deep Earth as well as the dynamic of the planet as a whole. The current layered structure and dynamic activity (e.g., plate tectonics, volcanism, etc.) of Earth are the results of petrological processes that have been occurring since the planet's formation and through its evolution history. Studying the seismic wave signatures of the lower mantle and core represents the sole direct evidence of these inaccessible regions of the planet since their propagation velocities depend on the density and elasticity of the medium they travel through. Therefore, any reliable mineralogical model design to explain the composition of mantle and core materials has to match the geophysical models, such as the "preliminary reference Earth model" (PREM; Dziewonski, and Anderson, 1981). Figure 1.1 shows the layered structure of the Earth as identified by the PREM which describes the bulk elastic properties (density, compressional, and shear wave velocity) as a function of depth. The PREM model as well as other 1D global seismological profiles (e.g., IASP91-Kennett & Engdahl, 1991; and AK135-Kennett et al., 1995) do not provide compositional information but only pressure, density, and wave velocities of the traversed materials. Nevertheless, through indirect derivation of the latter parameters one can retrieve compositional information.

A comprehensive strategy to explain seismological evidence of Earth's structure is a multidisciplinary approach based on the combination of scientific data from different branches of solid Earth research (such as *ab initio* numerical simulations and high-pressure mineral physics) and geochemistry. However, the interpretation of geophysical observations of Earth's interior has long been under debate, mainly because of technical limitations in experimental procedures designed to reproduce the extreme conditions existing in the lower mantle and core. Recent advancements in laboratory techniques made possible to experimentally simulate the pressure and temperature of the entire Earth (e.g., Tateno et al., 2010) leading to major advances toward the understanding of the composition, structure, and dynamics of Earth's interior.

In spite of these progresses in experimental capabilities, a number of disagreements remain on the stability, phase equilibria, and physical properties of high-pressure phases relevant to the lower mantle and core. For instance, experimental studies showed contradictory results about whether CO_4-based $FeCO_3$ (Cerantola et al., 2017) or $CaCO_3$ (Dorfman et al., 2018) phases persist or undergo breakdown at lower mantle conditions, which may potentially derive from different redox conditions existing during the experiments. In this context, is fundamental to monitor thermodynamic variables, such as the oxygen fugacity, when simulating Earth's mantle conditions in the laboratory. This parameter, however, is still poorly constrained in ultra-high-pressure experiments leaving open questions about the stability of high-pressure phases (mid-lower mantle conditions) as a function of the redox state.

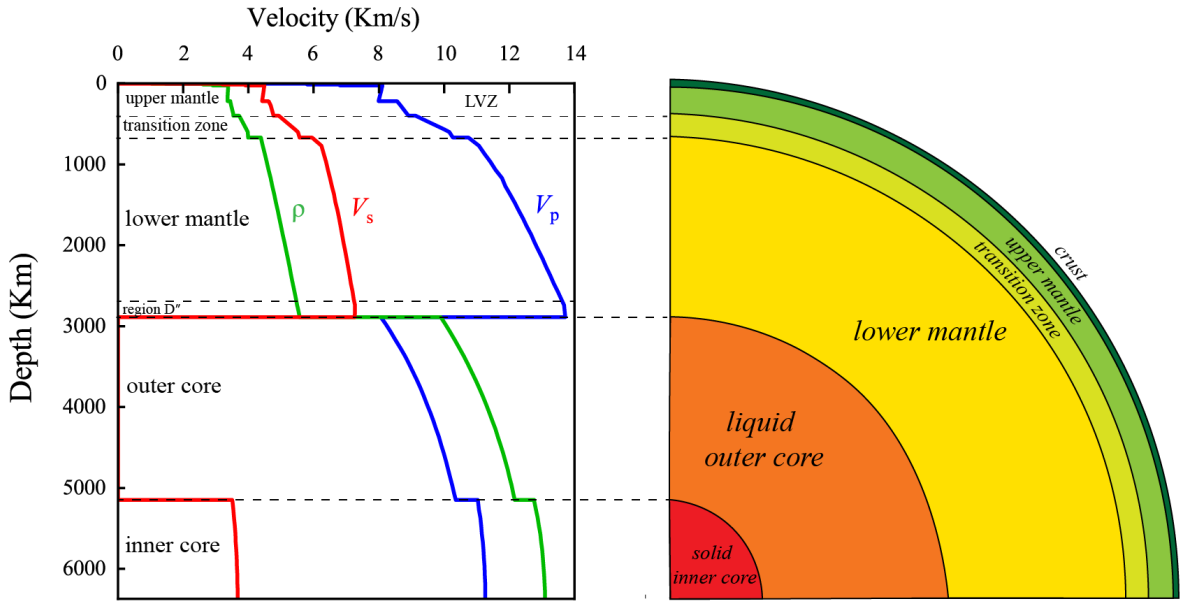

Figure 1.1: Density and velocity profile of Earth (Dziewonski, and Anderson, 1981).

1.1.1 Physics and chemistry of the lower mantle and core

The physics and chemistry of Earth's lower mantle and core are inferred from analysis of 1D global seismic profiles as well as from petrological models based on the bulk chemical composition of the Earth. From geophysics it is known that the planet is divided in three main layers (i.e., crust, mantle, and core) separated with one another by discontinuities corresponding to a drastic change in the seismic wave velocities. Major seismic discontinuities occur at 410 and 660 km depth wherein a sharp velocity gradient characterizes the mantle transition zone (MTZ). Beneath the 660 km the lower mantle extends up to the core-mantle boundary (2900 km) accounting for nearly three quarters of the mass of the bulk silicate Earth. Differently from the shallower portions of the planet, seismic profiles of the lower mantle exhibit a general increase in the velocity as a function of depth up to the D" layer, which is instead venue of anisotropies and anomalous seismic velocities (Birch, 1952).

A longstanding debate is whether the lower mantle is chemically distinct from the upper mantle or a heterogeneous "marble-cake-like" composition exists due to convection. Although some geochemical evidence supports the existence of a chemically isolated reservoir (Van Keken et al., 2002), data from seismic tomography suggest that many subducting slabs penetrate through the 660 km discontinuity (Van Der Hilst & Kárason, 1999) reaching perhaps the depths of the core mantle boundary (CMB). This scenario would imply a compositional heterogeneity in the lower mantle ruling out the hypothesis of an isolated reservoir (Kellogg et al., 1999; Van Der Hilst & Kárason, 1999). The observed minor variations in the seismic velocities are attributed not only to the presence of subducted oceanic crust in the lower mantle (Kawakatsu & Niu, 1994 ; Kaneshima & Helffrich, 1999) but also to local structural changes as well as electronic spin transitions in Fe-bearing minerals (Kawakatsu & Niu, 1994; Badro et al., 2003).

The upper mantle mineralogy is inferred by near-surface rocks sampling (i.e., basalts deriving by partial melting of mantle peridotites erupted at mid-ocean ridges and xenoliths inclusions in igneous rocks) that provide constrains on the chemistry of the upper mantle until approximately the first 200 km of depth. Further insights are reported in Anderson & Bass (1984), Haggerty (1995) and Frost (2008). Conversely, constrains on the chemistry of the MTZ and lower mantle mainly rely on indirect evidence (i.e., seismology, petrology, and geochemistry) besides from direct investigations of mineral inclusions in sub-lithospheric diamonds believed to origin at depth up to the lower mantle (e.g., Stachel et al., 2000; McCammon, 2001a; Kaminsky, 2012). In

this context, the interpretation of minerals trapped in diamonds and their comparison with laboratory results is essential to build a reliable compositional model for the deep mantle. However, discrepancies between natural and experimental data are reported in the literature possibly as a result of local chemical heterogeneities induced by the influx of subducting slabs that contaminate the mantle with crustal sediments (e.g., Dasgupta & Hirschmann, 2010) as well as by the circulation of volatiles elements (such as carbon, hydrogen, nitrogen and halogens) that migrate within the interior affecting a number of geological processes such as partial melting and metasomatism (Jambon, 2018).

The major mineral phases in the lower mantle are orthorhombic Mg-silicate perovskite or bridgmanite $(Mg,Fe,Al)(Si,Al)O_3$ (~80 volume %), cubic magnesiowüstite also known as ferropericlase (Mg, Fe)O (~13 volume %), and cubic calcium-silicate perovskite $CaSiO_3$ (~6 volume %) according to the pyrolite compositional model (Ringwood, 1991; Kesson et al., 1998; Hirose, 2002; Irifune et al., 2010). Majorite garnet $(Mg,Fe,Ca)_3(Mg,Si,Al)_2Si_3O_{12}$ and post-perovskite phases are also known to be present in the shallower and deepest regions of the lower mantle, respectively (Irifune, 1994; Murakami et al., 2004). Another viable compositional model for the bulk lower mantle is the midocean ridge basalt (MORB), which supports geophysical evidence of a subducting slab transporting oceanic crust in the deep mantle (Irifune & Ringwood, 1993; Ono et al., 2001; Hirose et al., 2005; Ricolleau et al., 2010). This model proposes different volume proportions for lower mantle minerals, such as a larger stability region of $CaSiO_3$, free SiO_2, and Al-bearing phases, compared to the pyrolite. Figure 1.2 shows a schematic of pyrolite and MORB compositional models.

Earth's core extends from ~2900 km depth (~136 GPa) to the center (~6371 km corresponding to ~ 360 GPa) constituting more than half of the planet's radius and accounting for approximately a sixth of its volume and a third of its mass. From the analysis of 1D seismic profiles (e.g., PREM, Figure 1.1), we know that the structure of the core is characterized by two physically distinct domains: a molten external shell and a solid inner sphere. Beyond the Gutenberg discontinuity, which marks the transition between mantle and core, seismic profiles record the disappearance of shear sound wave velocities and a strong decrease of the bulk sound wave velocities as a consequence of the molten state of the traversed material. Convection of the liquid outer core occurs under temperatures of ~5000 K (Terasaki et al., 2011) and generates the Earth's magnetic field. At greater depths, at ~5150 km beneath the surface (Lehmann discontinuity), a

rapid increase of body waves velocities marks the transition between liquid-outer and solid-inner core.

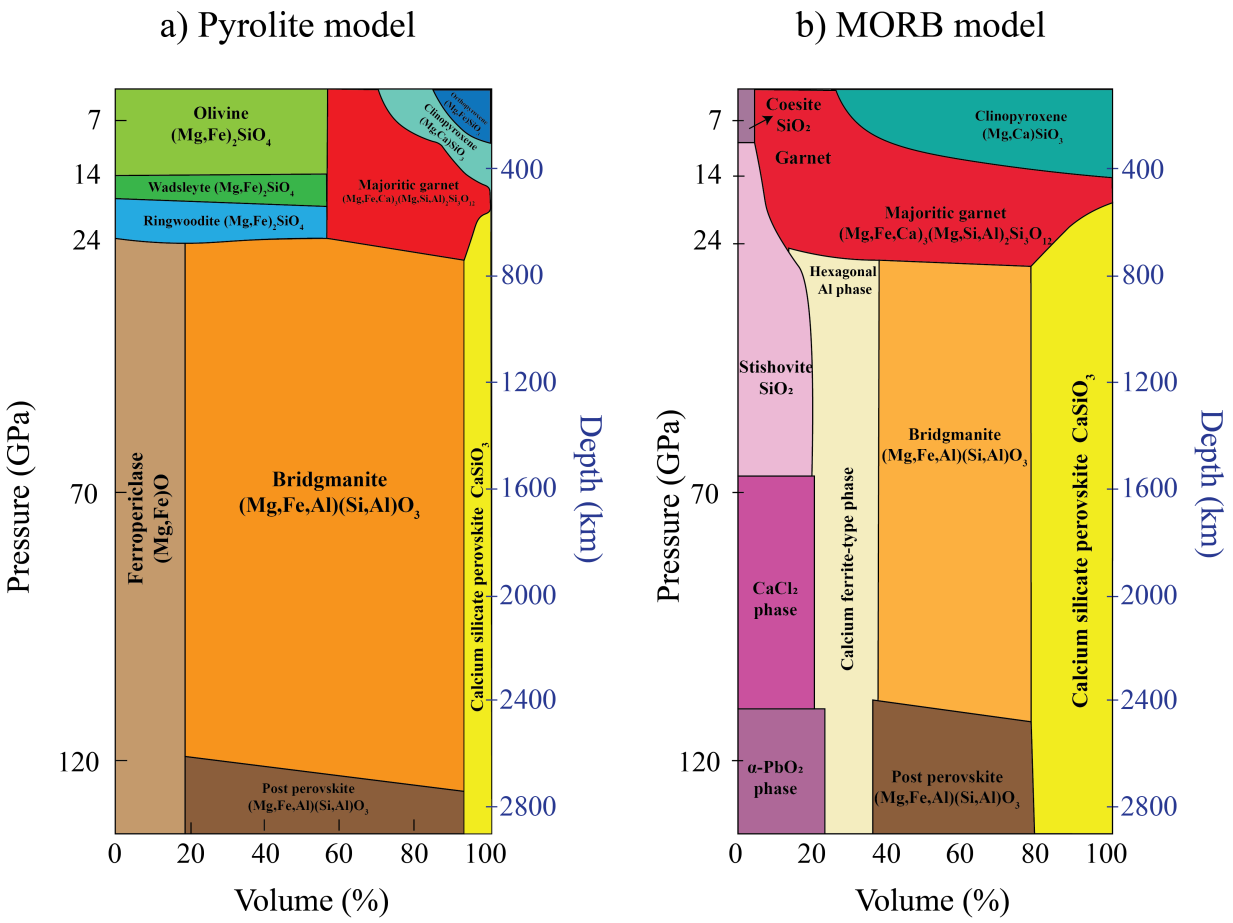

Figure 1.2: Expected volume proportions of lower mantle minerals in **a)** pyrolite and **b)** MORB compositional models (modified after Irifune & Ringwood, 1993; Ringwood, 1991; Ono et al., 2001; Hirose et al., 2005; Frost, 2008).

Compositional models for Earth's core mainly rely on experimental studies, first principles calculations, geochemistry, cosmochemistry, and from the interpretation of geophysical data of density (ρ), compressional (V_P) and shear (V_S) sound velocities. The latter parameters are defined by the Adams–Williamson equations,

$$V_P = \sqrt{\frac{\frac{4}{3}\mu + K}{\rho}} \quad , \quad V_S = \sqrt{\frac{\mu}{\rho}} \tag{1.1}$$

where K and μ are respectively the bulk and shear moduli which describe the incompressibility and the rigidity of the traversed material. Model core compositions suggest that it is mainly composed of Fe-Ni alloys with some trace of lighter elements (5-10 wt. %) to account for the density deficit existing between pure iron and geophysical observations. Yet, the nature of the light alloying elements in the core as well as their effect on elastic properties of pure Fe, such as density and sound velocities, remain enigmatic. Constrains on both nature and amount of light elements in the core would be of significant impact not only to build a solid compositional model but also for understanding their role in the production of the geodynamo of the planet.

1.1.2 The mineralogy of the lower mantle: phase stability as a function of the redox state

The bulk assemblage of Earth's lower mantle is dominated by bridgmanite and ferropericlase based on seismological observations, laboratory experiments, and natural inclusions in sub-lithospheric diamonds (Kaminsky, 2012). The stability of these minerals is closely related to their iron oxidation state which in turn influences the physicochemical properties and the oxygen fugacity (i.e., the oxygen reactivity in mineral assemblages) of the mantle at a larger scale. The degree of oxidation of a single mineral or a bulk assemblage is commonly quantified in terms of relative abundance of Fe^0, Fe^{2+} and Fe^{3+} components by means of $Fe^{3+}/\Sigma Fe$ (e.g., Mccammon, 2005a). The intuitive relation between ferric iron content and oxygen fugacity suggests that high redox conditions corresponds to high concentrations of Fe^{3+}. This positive correlation takes place at upper mantle conditions, for which the $Fe^{3+}/\Sigma Fe$ ratio can be used as a proxy for redox conditions of the system. On the contrary, in the deep mantle, the Fe^{3+} content of Fe-bearing minerals is also related to their crystal chemistry, not only to the oxygen fugacity. Therefore, the $Fe^{3+}/\Sigma Fe$ ratios of these minerals do not necessarily indicate the redox state of the environment. In some cases, in fact, high Fe^{3+} concentrations correspond to reducing conditions. This paradoxical relationship between oxidation state and oxygen fugacity of the mantle (Figure 1.3) is documented in McCammon (2005b).

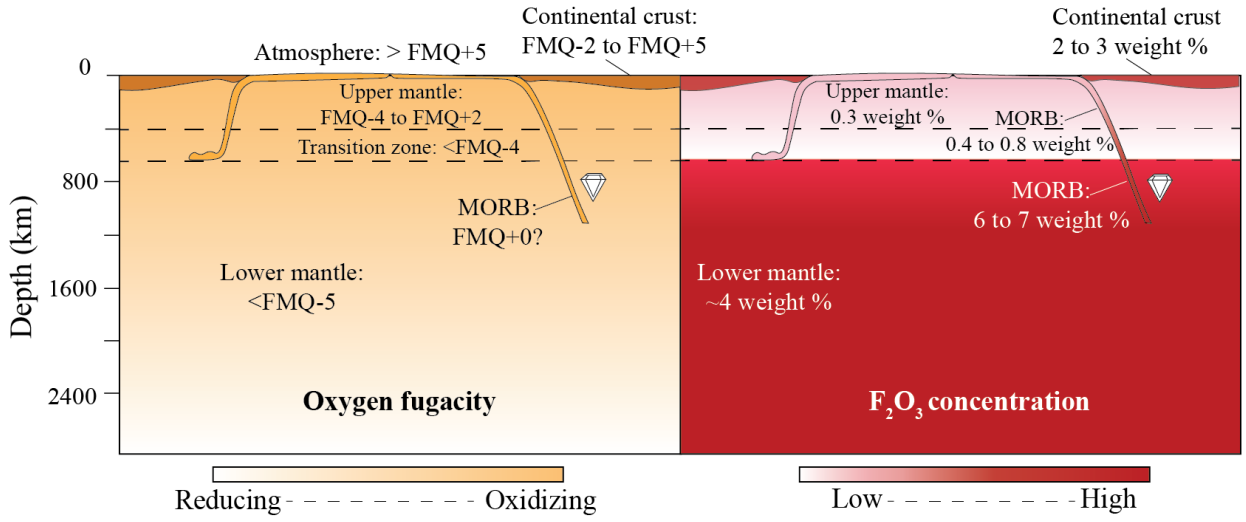

Figure 1.3: The oxygen fugacity (left) and Fe^{3+} concentration (right) in Earth's mantle (modified after McCammon, 2005).

Bridgmanite at lower mantle conditions has a perovskite-type structure (Horiuchi et al., 1987) with orthorhombic symmetry (*Pbnm* space group), consisting of a three-dimensional framework of corner-linked SiO_6 octahedra (B site) forming cavities in the shape of bicapped trigonal prisms (A site) occupied by Mg (Wicks & Duffy, 2016). The general formula is ABO_3, where O is the anion site, occupied by oxygen, and the A and B sites are occupied by large-radius and smaller cations, respectively. Previous studies show that the Fe^{3+} content that bridgmanite can incorporate reaches up to ~82 % $Fe^{3+}/\Sigma Fe$ for Al-rich compositions (~0.08-0.1 a.p.f.u.) (McCammon et al., 1997a; Lauterbach et al., 2000; Frost & Langenhorst, 2002). These high concentrations derive from the favorable energetics of Fe^{3+}-Al^{3+} substitution into the bridgmanite structure (Richmond & Brodholt, 1998; Navrotsky, 1999). This mechanism, known also as Tschermak coupled stoichiometric substitution, involves both A and B sites (Catalli et al., 2010) maintaining charge balance ($Mg^{2+}+Si^{4+}=2Al^{3+}$). Another type of nonstoichiometric mechanism for Al incorporation into bridgmanite can take place via formation of oxygen vacancies, although as mentioned above, the coupled-substitution process is considered more energetically favorable at lower mantle conditions (Liu et al., 2017). A strong positive correlation between $Fe^{3+}/\Sigma Fe$ and Al content in $(Mg,Fe)(Si,Al)O_3$ perovskite exists independently from the oxygen fugacity of the system (Lauterbach et al., 2000; Frost & Langenhorst, 2002); in fact, high values of Fe^{3+} can occur even at significantly reducing redox conditions (McCammon et al., 1997a; 1997b; 2005a; 2005b).

At this low oxygen fugacities, charge balance is maintained by means of the following disproportionation reaction (Lauterbach et al., 2000; Frost et al., 2004),

$$3Fe^{2+} = Fe^{0} + 2Fe^{3+}. \quad (1.2)$$

This scenario proposed in line with experimental results is supported by the $Fe^{3+}/\Sigma Fe$ content and Al concentration found in natural bridgmanite trapped in sub-lithospheric diamond (McCammon et al., 2004a).

The ferropericlase ($(Fe_xMg_{1-x})O$, $x \leq 0.5$) – magnesiowüstite solid solution is the second most abundant phase in Earth's lower mantle according to the pyrolite model (Ringwood, 1991; Kesson et al., 1998; Hirose, 2002; Irifune et al., 2010). This phase has the NaCl-type (B1) structure ($Fm\bar{3}m$ space group) consisting of interpenetrating *fcc* (face-centered-cubic) lattices that generate an alternating framework of both Mg^{2+}/Fe^{2+} cations and O^{2-} anions in octahedral coordination (Wicks & Duffy, 2016). Experimental studies performed at high pressures and temperatures on coexisting ferropericlase and bridgmanite suggest that iron partitions preferentially into the ferropericlase structure, which exhibits a Fe# (i.e., Fe/(Fe+Mg)) of ~0.2 (Auzende et al., 2008; Sakai et al., 2009; Tange et al., 2009) and a predominantly ferrous Fe valence state (McCammon et al., 1998). The ferric iron that ferropericlase can incorporate at lower mantle conditions varies from 0 to 10 % $Fe^{3+}/\Sigma Fe$ depending on pressure, Mg# (i.e., Mg/(Mg+Fe)), and oxygen fugacity of the system (e.g., McCammon et al., 1998), and can occupy both the octahedrally coordinated cation sites and the tetrahedrally coordinated interstitial sites. This estimated $Fe^{3+}/\Sigma Fe$ range is significantly lower than the one at atmospheric pressures at the phase boundary with spinel phases (e.g., Andrault & Bolfan-Casanova, 2001; Uenver-Thiele et al., 2017), where the redox conditions are more oxidizing than those existing in the lower mantle (Frost & McCammon, 2008). Literature studies reported the occurrence of tetrahedral Fe^{3+} in ferropericlase at the high-pressure and low oxygen fugacity conditions of the lower mantle as a consequence of the configurational entropy of the system (Otsuka et al., 2010).

Despite that ferropericlase constitutes only about 20 % of the lower mantle by volume, it is one of the most commonly found inclusions in sub-lithospheric diamonds (McCammon et al., 1997b; Stachel et al., 2000), which are an extremely rare category of diamonds believed to form at depths comprised between ~300 km and perhaps greater than ~1000 km (e.g., Walter et al., 2011;

Kaminsky, 2012; Pearson et al., 2014; Smith et al., 2016; Nestola et al., 2018). Previous studies showed that ferropericlase grains encompass up to ~50-56 % of all mineral inclusions assigned to the lower mantle retrieved worldwide (Kaminsky, 2012 and references therein). This evidence appears contradictory with the expected lower mantle phases' volume proportions inferred by experimental and computational studies, where ferropericlase should only make up ~16-20 % of the lower mantle assemblage (e.g., Irifune, 1994). A possible reason for the high frequency of the mineral as a natural inclusion relates to its potential involvement in redox reactions that lead to diamond formation at deep mantle conditions (Liu, 2002; Nimis et al., 2019; Zhu et al., 2019). Others explanations such as the higher stability of ferropericlase in Earth's mantle compared to bridgmanite, or possible differences between the actual mantle composition and the pyrolite model, have also been reported (Kaminsky, 2012 and references therein). Moreover, investigations to date of (Mg,Fe)O inclusions trapped in sub-lithospheric diamonds show evidence of magnesioferrite phases exsolved from the ferropericlase matrix (Wirth et al., 2014; Nimis et al., 2019; Kaminsky et al., 2015a,c; Palot et al., 2016; Nestola et al., 2016), likely as a consequence of Fe^{3+} saturation within ferropericlase. There is speculation whether these exsolutions can be related to the effect of cooling due to diamond exhumation or rather the product of an increase of the oxygen fugacity of the system (Longo et al., 2011). The latter hypothesis is supported by evidence of magnesioferrite along with a carbonated mineral assemblage, which highlights the important role of oxidizing redox conditions on the initial bulk $Fe^{3+}/\Sigma Fe$ (Kaminsky et al., 2015c).

Additional minor phases in terms of volume abundance, such as Ca-perovskite ($CaSiO_3$), $MgSiO_3$ post-perovskite, SiO_2 polymorphs, aluminous and hydrous phases, also occur at lower mantle conditions. Insights on the stability of these phases are documented elsewhere (e.g., Wicks & Duffy, 2016).

1.2 REDOX STATE OF EARTH'S INTERIOR

The redox state of Earth's interior is controlled by the oxygen fugacity (f_{O_2}). The concept of oxygen fugacity was introduced for the first time in petrology by Eugster (1957), who described the f_{O_2} as the partial pressure $p(O_2)$ or the chemical potential of oxygen in reactions where reagents and products contain the same elements with different oxidation states. In the following, we present the oxygen fugacity definition starting from the notion of equilibrium as reported for example in Cemič (2005).

A system is in thermodynamic equilibrium when the change in the Gibbs free energy is equal to zero, such as,

$$d\mathrm{G} = d\mathrm{H} - TdS = 0 \tag{1.3}$$

where H and S are respectively the enthalpy and entropy of the system.
Since,

$$dH = TdS + VdP \tag{1.4}$$

in which V is the volume as a function of pressure, substituting Equation 1.4 in Equation 1.3 the Gibbs free energy change as a function of temperature and pressure reads,

$$dG = -SdT + VdP. \tag{1.5}$$

If the Gibbs free energy of a pure substance is divided by its number of moles the chemical potential μ function of state is obtained,

$$\frac{G}{n} = \mu. \tag{1.6}$$

Thus, Equation 1.6 expresses the molar Gibbs free energy that can be also written as,

$$d\mu = -SdT + VdP. \tag{1.7}$$

in which S and V indicate the molar entropy and molar volume of the pure phases, respectively. For a system at constant temperature, variation of the chemical potential corresponds only to

changes in volume/pressure. Equation 1.7 can therefore be rewritten as the volume dependence on the chemical potential, i.e.,

$$d\mu = VdP. \tag{1.8}$$

In the case of an ideal gas, V can be replaced by RT/P according to the ideal gas law (i.e., $PV = nRT$),

$$d\mu = \frac{RT}{P}dP \; = \; RTdlnP. \tag{1.9}$$

Integration of Equation 1.9 between the initial (P_0) and final pressure (P) yields,

$$\int_{\mu(P_0)}^{\mu(P)} \mu = RT \int_{P_0}^{P} dlnP = \mu(P) - \mu(P_0) = RTln\frac{P}{P_0} \tag{1.10}$$

that is,

$$\mu^{ideal} = \mu^{o} + RTln\frac{P}{P_0} \tag{1.11}$$

where μ^{o} is the standard chemical potential (also referred to as $\mu(P_0, T)$) at ambient pressure and at the temperature of the experiment.

On the other hand, for non-ideal gases the pressure P has to be replaced with the fugacity f, because free oxygen in petrologic environments is never present in great quantities, and therefore the chemical potential is given as,

$$d\mu = RTdlnf. \tag{1.12}$$

The relation between P and f is,

$$f = \varphi P \tag{1.13}$$

in which φ is the fugacity coefficient. At very low pressure the fugacity of a gas equals its pressure, meaning that at sufficiently low P the gas behaves ideally. Integrating Equation 1.12 between f_0 and f limits yields,

$$\mu^{real} = \mu^{o} + RTln\frac{f}{f_0} \tag{1.14}$$

where μ^{o} the standard chemical potential relates to the standard fugacity f_0, whose value corresponds to ambient pressure for all temperatures.

In geological systems, the f_{O_2} is defined as a measure of the free energy change between the oxidized and the reduced portions of a mineral assemblage in a rock or in a buffered capsule (Frost, 1991). The "redox" reactions governing these changes can be described by univariant f_{O_2}-temperature curves where above and below each curve the oxidized and the reduced phase of an assemblage will be stable, respectively. Figure 1.4 illustrates the most commonly employed solid-state buffer equilibria that describe the redox conditions at which silicates and oxides coexist in Earth's mantle, i.e.,

$$\underset{\text{wüstite}}{2FeO} = \underset{\text{iron}}{2Fe} + O_2 \qquad IW-(1.15)$$

$$\underset{\text{magnetite}}{2Fe_3O_4} + \underset{\text{quarz}}{3SiO_2} = \underset{\text{fayalite}}{3Fe_2SiO_4} + O_2 \qquad FMQ-(1.16)$$

$$2NiO = 2\,Ni + O_2 \qquad Ni-NiO-(1.17)$$

$$\underset{\text{hematite}}{6Fe_2O_3} = \underset{\text{magnetite}}{4Fe_3O_4} + O_2 \qquad MH-(1.18)$$

In these assemblages f_{O_2} is imposed by the reaction that involves two or more solid phases (e.g., fayalite-magnetite-quartz, Ni-NiO, Fe-FeO, etc.)

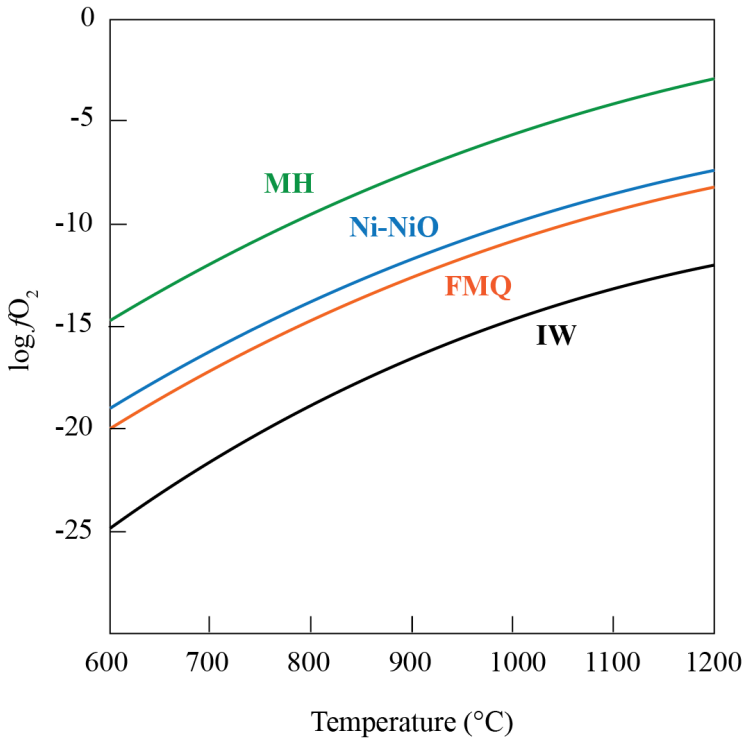

Figure 1.4: Logarithm of the oxygen fugacity as a function of temperature at constant pressure (1 bar) for common buffer equilibria (modified after Frost, 1991). MH = magnetite–hematite buffer, Ni-NiO = nickel–nickel oxide buffer, FMQ = fayalite–magnetite–quartz buffer, IW= iron–wüstite buffer.

To calculate the oxygen fugacity starting from a redox buffer (e.g., FMQ in Equation 1.16) one can calculate first the equilibrium constant as,

$$K_{FMQ} = \frac{a_{fay}^3}{a_{SiO_2}^3 * a_{magn}^2} * a_{O_2} \tag{1.19}$$

where a_i marks the activity of the component i. For pure phases $a_i = 1$. Therefore, for a system with pure substances such as magnetite, fayalite, and quartz, Equation 1.19 can be rewritten as:

$$K_{FMQ} = a_{O_2} = \frac{f_{O_2}}{f_{O_2}^{\circ}} = f_{O_2} \tag{1.20}$$

in which $f_{O_2}^{\circ}$ is the oxygen fugacity at the standard state (at 1 bar and temperature of interest) that equals unity, and f_{O_2} is the oxygen fugacity at a given P and T.

Considering that,

$$\log K_{FMQ} = -\frac{\Delta G^{\circ}_{FMQ}}{2.303 * R * T} \quad (1.21)$$

then,

$$\log f_{O_2} = -\frac{\Delta G^{\circ}_{FMQ}}{2.303 * R * T} \quad (1.22)$$

in which ΔG°_{FMQ} is the standard Gibbs free energy for reaction 1.16 and R is the gas constant.

1.2.1 Redox state of the present-day mantle

The redox state of Earth's interior is mainly influenced by volatile elements (i.e., carbon, hydrogen, sulfur, nitrogen, and oxygen) that migrate from the deep portion of the planet up to the atmosphere as well as from the physicochemical properties such as oxidation state of mantle minerals at depth. In this context, the oxygen fugacity (f_{O_2}) is a key thermodynamic variable that controls the occurrence of multiple valence states of a certain element in minerals, liquids, and gases (e.g., Frost & McCammon, 2008; Stagno & Fei, 2020).

In the upper mantle, the oxygen fugacity can be directly measured by determining the Fe^{3+} content in MORB (mid-ocean ridge basalt) or in xenoliths brought to the surface via volcanic eruptions or exposed in peridotites massifs, even though this region is complicated by the occurrence of rock alteration via metasomatism and partial melting. $Fe^{3+}/\Sigma Fe$ ratio recorded by rapidly quenched glassy rims of pillow basalts (MORB) ranges between 8 and 15 % (Christie et al., 1986; Bézos & Humler, 2005) and does not vary significantly among different localities. The f_{O_2} obtained through an empirical relationship between Fe valence state and oxide molar fractions from MORB glasses suggests a global average of -0.41 ± 0.43 log units normalized to the FMQ oxygen buffer (Frost & McCammon, 2008 and references therein). Specifically, assuming a closed system, estimations report a f_{O_2} of ~FMQ for MORB at the conditions of partial melting and between ΔFMQ -2.5 and FMQ for abyssal peridotites, which are considered to be the mantle residue of the partial melting. At greater depths, between 30 and 60 km, evaluation of the redox

state of this portion of the mantle relies on analyses of spinel peridotites, that have a $Fe^{3+}/\Sigma Fe$ of ~1-3 % (Canil & O'Neill, 1996; Woodland et al., 2006). Spinels, which make up only ~3 % of the whole rock, exhibit a $Fe^{3+}/\Sigma Fe$ of 15-34 % that can decrease to 5-15 % in peridotites that have been subjected to extensive melt extraction. Calculated oxygen fugacities in spinel peridotite facies fall between ΔFMQ -2 and +2 log units and show significant variation as a function of the setting, indicating mantle heterogeneity even at a small scale. The redox conditions recorded by xenoliths from the subcontinental lithospheric mantle are slightly higher than those of abyssal peridotites potentially as a result of metasomatism associated with subduction zones. Further details can be found in Frost & McCammon (2008). Xenoliths retrieved from kimberlitic eruptions host garnet peridotite rocks that posses a $Fe^{3+}/\Sigma Fe$ in the range of 2-14 % (Canil & O'Neill, 1996), similar to peridotite xenoliths. For these rocks, f_{O_2} can be determined using a redox equilibrium that involves skiagite garnet ($Fe_3Fe_2^{3+}Si_3O_{12}$) (Gudmundsson & Wood, 1995). Results show a general trend of decreasing oxygen fugacity with depth as a consequence of the volume change of the reaction. Assuming a constant $Fe^{3+}/\Sigma Fe$ ratio down to the bottom portions of the upper mantle, f_{O_2} will decrease with depth both as a consequence of the volume change of the employed redox equilibrium (which promotes the stability of Fe_2O_3 with depth) and because of the reduction of the activity of Fe_2O_3 components as they partition into minerals that dominate the mineralogy of the mantle with depth (Frost & McCammon, 2008). In the olivine stability field, the most abundant minerals in the mantle assemblage have negligible Fe_2O_3 content, which is instead concentrated in spinels and clinopyroxenes of relatively low abundance. At these conditions, the obtained oxygen fugacity is relatively high since it is proportional to the activity of Fe_2O_3-bearing phase. In the deeper mantle, olivine transforms to its polymorphs wadsleyite and ringwoodite which are stable together with garnet in the mantle assemblage and can incorporate higher amounts of Fe_2O_3, whose activity will be low and as a consequence the calculated f_{O_2} will also be low. The $Fe^{3+}/\Sigma Fe$ ratio measured in low metasomatized spinel and garnet peridotite xenoliths rocks is ~2 % (Frost & McCammon, 2008).

At ~ 8 GPa corresponding to ~250 km depth, (Fe, Ni)-bearing olivine will break down, causing precipitation of Fe and Ni metals while garnet, a phase which hosts significant amount of Fe^{3+}, will become stable. As a consequence, the disproportionation of FeO contained in olivine (Equation 1.23) explains the coexistence of phases where Fe is in both high and low oxidation state,

$$\underset{\text{olivine}}{3FeO} = \underset{\text{metal}}{Fe} + \underset{\text{garnet}}{Fe_2O_3}. \quad (1.23)$$

When Fe-Ni metal precipitates and the $Fe^{3+}/\Sigma Fe$ ratio of the assemblage increases at the base of the upper mantle (at 14 GPa ~440 km depth) the calculated f_{O_2} is ~0.3 log units below the nickel precipitation NiPC buffer curve (O'Neill & Wall, 1987), which is slightly below iron wüstite IW.

In the transition zone, wadsleyite and ringwoodite can incorporate approximately 2 % of ferric iron in equilibrium with stishovite, Fe metal and majorite garnet (phase that can host up to ~7 % of ferric iron), which translates to a bulk rock $Fe^{3+}/\Sigma Fe$ ratio with a minimum of 3%. This amount falls in the same range to that at the base of the upper mantle as well as the calculated oxygen fugacity (below the IW buffer) and metal content ~0.12 wt. % of Fe-Ni metal (Frost & McCammon, 2008).

The redox state of the lower mantle can be assessed by investigating the minimum $Fe^{3+}/\Sigma Fe$ content of lower mantle minerals that can occur when they coexist with Fe metal. As described in section 1.1.2, Al-bearing and Al-free bridgmanite can incorporate the highest amount of ferric iron with respect to other silicate phases at the same f_{O_2} conditions, either via the coupled substitution mechanism or by the formation of oxygen vacancies (McCammon et al., 1998; Lauterbach et al., 2000; Navrotsky et al., 2003). Experimental studies show that the high Fe_2O_3 concentration in bridgmanite is the result of the disproportionation of FeO into Fe_2O_3 and metallic Fe which also contains ~10 % of Ni and ~1 wt. % of S and has an abundance of ~1 wt. % (Frost et al., 2004). Calculated f_{O_2} for the lower mantle using a redox equilibrium which employs Fe metal and ferropericlase is about -1.4 log units below IW. Results show well buffered conditions in the lower mantle for values comprised within -1.5 log units below the IW curve. At the bottom of the lower mantle, at depths of the D" region, bridgmanite transforms to postperovskite (Murakami et al., 2004) which can host $Fe^{3+}/\Sigma Fe$ from less than 15 % up to 60 % in equilibrium with metallic Fe (Frost et al., 2004).

At the core mantle boundary Fe metal may be molten and could potentially separate to the outer core causing a parallel oxygen increase in the mantle. Several mechanisms have been suggested in contradiction of this hypothesis and are discussed elsewhere (Takafuji & Hirose, 2005; Asahara et al., 2007).

1.2.2 Evolution of mantle oxygen fugacity after the core formation event

The oxygen fugacity of the present-day mantle is orders of magnitude higher than that existing at the time of core formation, when the atmosphere was anoxic and prohibitive for life, characterized by outgassing of H_2O-vapor, CO_2, and CO with almost complete absence of free oxygen (Figure 1.5). The current mantle redox state has been preserved since 3.5 Ga (time that coincides with the appearance of life on Earth and the initiation of plate tectonics) as reported by the concentration of geochemical tracers such as Cr and V in the oldest known rocks (Delano, 2001; Canil, 2002; Li & Lee, 2004).

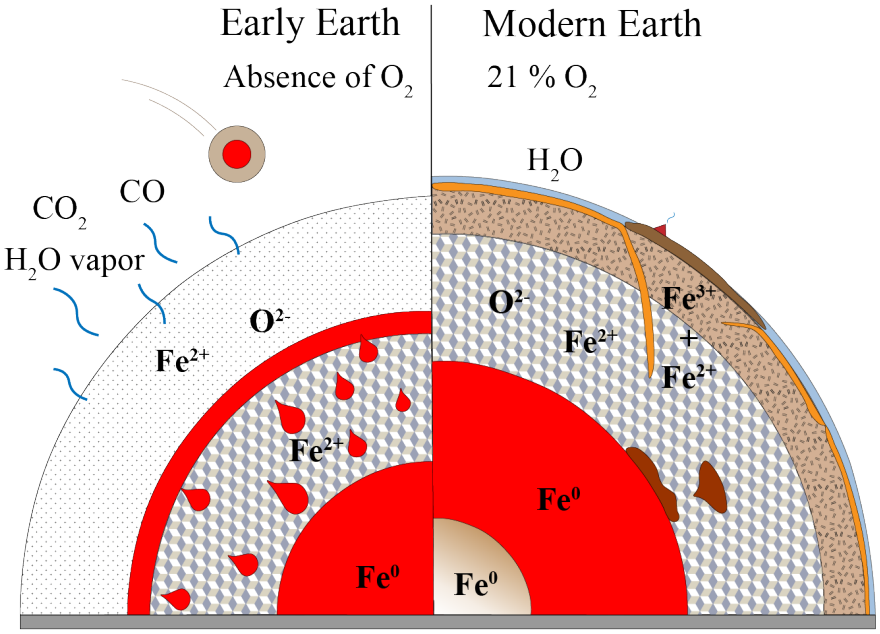

Figure 1.5: Evolution of the redox boundary of Earth's interior (adapted from Stagno & Fei, 2020). **Left**: Early-Earth oxidation state. **Right**: The oxidation state of the modern Earth significantly modified by the influx of subducting slab in the mantle.

Previous studies argue that the differentiation of metal and silicate, which occurred at the stage of the planet accretion, produced the redistribution of oxygen as well as the stratification of the oxidation state of major elements, such as Fe, in Earth's interior. As a consequence of this fractionation process, Fe^0 has descended into the core while it has bonded with O^{2-} in the mantle forming silicates (e.g., Stagno & Fei, 2020). According to this scenario, during the core formation event (~4.5 Ga), the silicate part of the Earth in a solid or liquid state must have been in equilibrium with Fe-Ni metal alloys, with a resulting oxygen fugacity of ~4.5 log units below the FMQ buffer

in the upper mantle. At these conditions, silicates contained negligible Fe_2O_3 whereas the current upper mantle is known to hold ~0.2 wt.% of Fe_2O_3. Different models have been proposed to explain the oxidation process in the mantle, but whether the mantle oxidation state has changed gradually or suddenly over time is still highly debated. Among those, a plausible mechanism that would have triggered a rapid increase of the mantle oxidation state is via the reduction of H_2O and release of H_2 to the atmosphere, during the late stages of accretion. Considering the large depth scale of core formation, it is likely that part of the H_2 was incorporated in the core, perhaps along with other light elements. Therefore, understanding the redox mechanism that led to the current mantle oxidation state would be of great impact, not only to reconstruct the planetary formation process but also to shed light on the redox path taken during accretion with implications for the nature of light elements in Earth's core. Hitherto, controversies persist if H_2O may have been incorporated in the mantle as accretion proceeded or via subduction of hydrated lithosphere. Another hypothesis that may explain the rise of the mantle oxidation state concerns the precipitation of metallic Fe by disproportionation of FeO in the lower mantle. This theory supports the possibility of an early-Earth silicate mantle in equilibrium with Fe metal and depleted in ferric iron, which would increase only once bridgmanite crystallized and incorporated Fe_2O_3 via disproportionation. Moreover, if approximately 10 % of this precipitated metal entered the core, the lower mantle would have had an excess of Fe_2O_3 sufficient to explain the current redox state of the upper mantle (Frost et al., 2004). Several mechanisms have been suggested to support this scenario, such as i) a diapiric intrusion of disproportionated Fe metal from the lower mantle into the core (Li & Agee, 1996; Righter et al., 1997; Rubie et al., 2003; Frost et al., 2008), ii) a diapiric sinking of precipitated Fe metal that occurred at the same time of Fe_2O_3-bearing perovskite crystallization from a deep magma ocean, iii) a large magma ocean (extending up to the lower mantle) as a source for metallic iron entering the core. This latter mechanism of Fe segregation into the core would have increased the mantle Fe_2O_3, that in turn, would have back-reduced to FeO by the concurrent addition of Fe metal by accreting bodies.

Geochemical models argue for an initial reduced phase of core formation to justify the depletion of weakly siderophile elements, such as Cr, V, Nb, etc. However, in this scenario, the disproportionation of FeO coupled with the loss of Fe to the core, would be insufficient to account for the required high f_{O_2}. On the other hand, the presence of Fe metal in Earth's mantle at the time of core formation may potentially explain the high abundance of highly siderophile elements, such

as PGE (platinum group elements) like Ir, Pt, Rh in the mantle. In this context, it is expected that the lower mantle formed from a material that had already undergone core-mantle differentiation so that metallic Fe would have precipitated from material already stripped of siderophile elements, meaning that only core-forming Fe metal would exhibit high concentration of siderophile elements. One possibility to explain the overabundance of highly siderophile elements in the mantle is to consider that some "core-forming" metals may have been trapped in the lower mantle to coexist with disproportionated Fe at the last stage of accretion, but the redox mechanism remains unclear. Further insights can be found in Frost & McCammon (2008) and references therein.

1.2.3 Redox freezing/melting processes in Earth's mantle and the deep carbon cycle

The redox state of Earth's interior strongly affects the speciation of volatile elements, such as carbon, which can be present in the mantle as a oxidized phase (carbonate and CO_2-rich melts) or as elemental carbon (graphite/diamond and carbide) as a function of the oxygen fugacity (e.g., Stagno, 2019) (Figure 1.6a). The f_{O_2} in Earth's mantle is buffered by the local abundance of silicate minerals (see section 1.2.1) and varies with pressure and temperature. The general tendency of the oxygen fugacity in the upper mantle, as recorded by unaltered spinel and garnet peridotite or eclogite rocks, is to decrease with increasing pressure, such that carbonate phases are expected to be stable at depths no greater than ~120 km. However, both experimental studies (e.g., Cerantola et al., 2017; Bayarjargal et al., 2018; Dorfman et al., 2018) and natural carbonate inclusions in sub-lithospheric diamonds (Brenker et al., 2007; Walter et al., 2008; Kaminsky, 2012; Pearson et al., 2014; Kaminsky et al., 2015b) emphasise that carbonates can be stable at greater depths (>250 km), if the local redox environment is perturbed for example by the influx of a subducting slab that generates anomalous oxidizing conditions favourable for the stability of CO_3^{2-}-bearing phases. In this way, the f_{O_2} increases in a small mantle domain, at the "redox front" of the subducting lithosphere, where carbonates become stable at oxygen fugacities buffered by redox equilibria, e.g., enstatite + magnesite = olivine + graphite/diamond redox (EMOG/D) (Stagno & Frost, 2010) (Figure 1.6b). For oxygen fugacity values above EMOG/D carbon is stable as carbonate whereas for f_{O_2} values below EMOG/D carbon is stable as graphite or diamond (Stagno & Frost, 2010; Stagno et al., 2013).

Subduction related carbonates are important carriers of C down to the deep mantle since they are subject to polymorphic transformations (e.g., from rhombohedral dolomite I to triclinic dolomite II at 17 GPa to dolomite III at ~ 35 GPa; Mao et al., 2011a) as well as melting processes at various depths as a function of the bulk rock chemistry, P-T (Hammouda & Keshav, 2015), and redox path (e.g., Rohrbach & Schmidt, 2011). The concept of "redox melting" (Taylor & Green, 1988; Green et al., 1993) refers to a melting reaction triggered by changes in the f_{O_2} of the mantle that arise by the oxidation of carbon (and hydrogen) which acts as a fluxing agent.

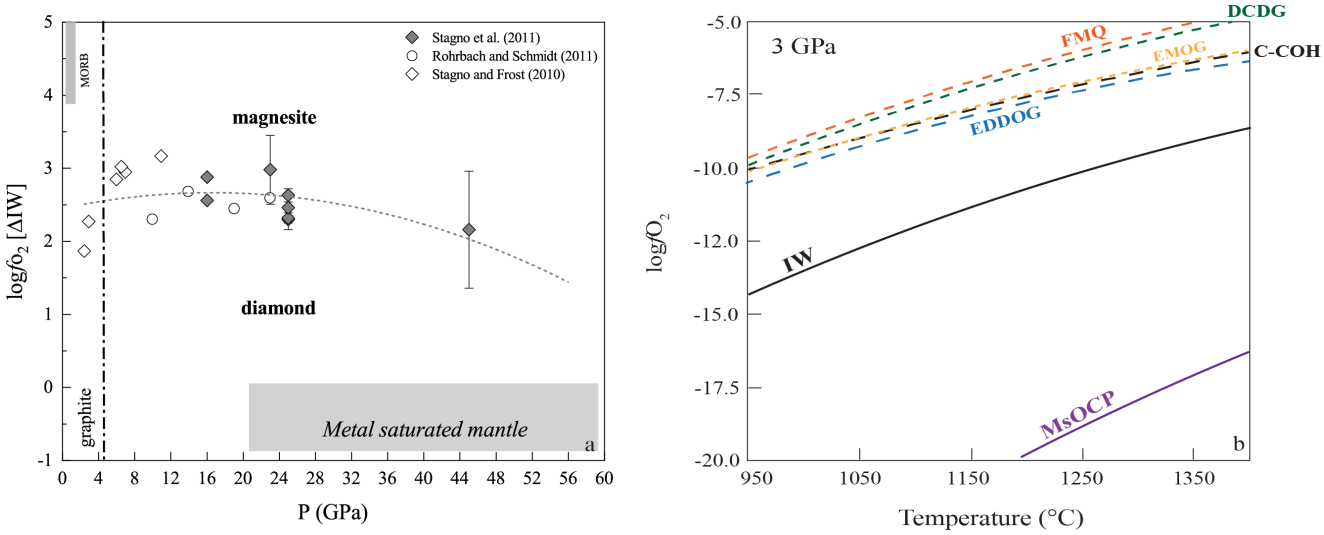

Figure 1.6: **a)** The log f_{O_2} normalized to IW at buffered redox conditions by the coexistence of carbonate (magnesite) and diamond as a function of pressure at 1500-1700 °C (modified after Stagno et al., 2011); **b)** The log f_{O_2} versus temperature of commonly employed oxy-thermobarometers in petrology for C phases (adapted from Stagno, 2019). Buffer curves were calculated at 3 GPa and 950-1400 °C. Abbreviations: FMQ, fayalite-magnetite-quartz (O'Neill, 1987b); DCDG, dolomite-coesite-diopside-graphite (Luth, 1993); EMOG, enstatite-magnesite-olivine-graphite and EDDOG, enstatite-dolomite-diopside-olivine-graphite (Stagno & Frost, 2010); IW, iron-wüstite (O'Neill, 1987b); C-COH, graphite-COH fluid (Ulmer & Luth, 1991); MsOCP, moissanite-olivine-graphite-enstatite (Ulmer & Luth, 1991).

Specifically, the upward migration of C-O-H fluids, from the lower portions of the asthenosphere (low f_{O_2}) towards oxidized regions of the mantle (high f_{O_2}), causes the reaction with $H_2O + CO_2$ local fluids resulting in modifications in the redox state. This redox contrast produces the depression of the carbonated peridotite solidus which induces melting (Taylor & Green, 1988; Green et al., 1993). Another suggested mechanism of redox melting implies the ascent of C-bearing material that undergoes melting when crossing the EMOG/D redox boundary (Stagno & Frost, 2010; Rohrbach & Schmidt, 2011; Stagno et al., 2013). In spite of the importance of carbonatitic

fluids as metasomatic agents of the asthenosphere (Rosenthal et al., 2014), the interaction between these fluids and the metal saturated mantle, taking into account the initial Fe/C ratio, can cause their reduction to diamond or graphite via "redox freezing" (Rohrbach & Schmidt, 2011) e.g.,

$$MgCO_3 + 2(Fe, Ni) = 3(Fe, Ni, Mg)O + C\,. \qquad (1.24)$$

A schematic drawing of the mantle carbon cycle is illustrated in Figure 1.7.

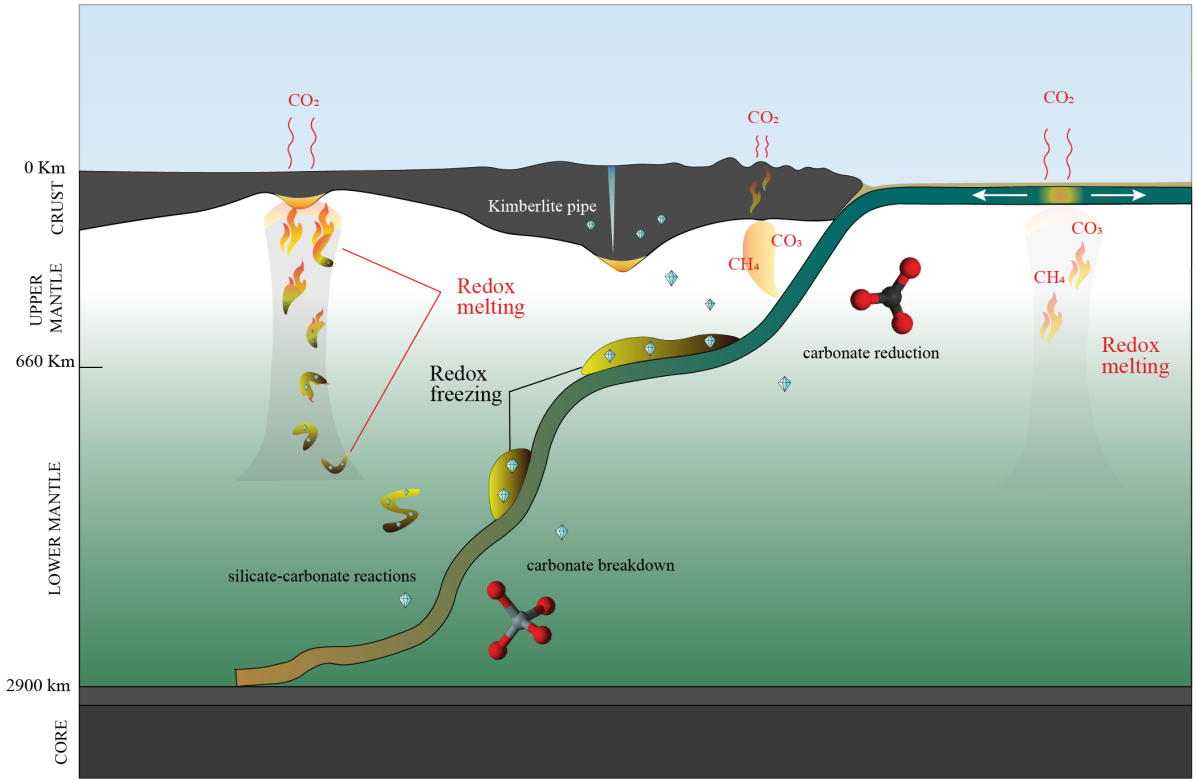

Figure 1.7: Schematic cartoon of the deep carbon cycle (modified after Rohrbach & Schmidt, 2011; Stagno et al., 2019).

Evidence of this process is documented for example in natural inclusions in sub-lithospheric diamonds, where majorite garnet and Ca-silicate are reported to form by the interaction of alkali-rich carbonatitic melts and reduced asthenospheric mantle (Thomson et al., 2016). Moreover, experimental studies simulating an interaction between a reduced mantle (metal saturated) and a subducting slab reported also the formation of Fe_3C as a result of C extraction from carbonate by Fe to form iron carbide. The latter was observed to further react with initial carbonate to produce

a mixture of magnesiowüstite (Mg# = 0.38) + metastable graphite and Ca-rich carbonate at ~ 1000-1100 °C and f_{O_2} of ~ IW (Pal'yanov et al., 2013).

Despite the crucial importance of f_{O_2} on the fate of subducted carbonates and the numerous steps performed over the last decades in the comprehension of their physicochemical behaviour at deep mantle conditions, controversies still remain on the oxygen fugacity variation induced by the influx of subducting carbonates in a metal saturated environment that affects the Fe valence state of redox-sensitive lower mantle minerals, such as ferropericlase.

1.2.4 Redox mechanism of diamond formation

The mechanism of diamond formation can be described as a metasomatic process (Haggerty, 1999; Stachel et al., 2005) guided by fluids or melts that react with the mantle rocks (peridotites or eclogites) which they pass through leading to diamond crystallization via reduction of carbon. Simple examples of redox reactions (Equation 1.25 and 1.26) are given as follows (Shirey et al., 2013),

$$CO_2 = C + O_2 \quad (1.25)$$

$$CH_4 + O_2 = C + 2H_2O\,. \quad (1.26)$$

As described in the previous paragraph, the speciation of carbon and the diamond formation event are closely related to the oxidation state of the local rock-forming minerals, which in turn, is controlled by the iron valence state at upper mantle conditions (see sections 1.2.1 and 1.2.3) (Frost & McCammon 2008; Rohrbach & Schmidt, 2011). One of the suggested mechanisms for diamond synthesis in the mantle involves volatile-bearing fluid migration that perturbs the local f_{O_2} (Frost & McCammon 2008).

Direct diamond growth from C-O and C-O-H fluids was tested experimentally between 5 and 8 GPa with results showing diamond formation for a wide range of fluid composition at or below the diamond-carbon-oxygen buffer (DCO) (Hong et al., 1999; Akaishi et al., 2000; 2001; Kumar et al., 2000; Pal'yanov et al., 2000; Sun et al., 2001; Sokol et al., 2001; 2009; Yamaoka et al., 2002), which is generally 1 log unit above EMOD (Stagno & Frost, 2010) at lithospheric conditions.

Alternatively, diamond formation can occur by reduction of carbonates (redox freezing) either in a solid or a liquid state (Rohrbach & Schmidt, 2011). A wide range of fluid/mineral starting compositions was explored by laboratory studies. For instance, Sato et al. (1999) and Arima et al. (2002) show that at 7.7 GPa diamonds can form from Ca and Mg-carbonate minerals or melts in equilibrium with CH_4-H_2O reduced fluids (Yamaoka et al., 2002). CO_2-rich ferrous carbonate melts (Bataleva et al., 2012) as well as alkali based (e.g., Litvin & Zharikov, 1999) carbonated fluids have been also proposed as possible redox sources for diamond synthesis. It is also worth mentioning the complexity of fluid and melt compositions (namely C-O-H fluids, carbonates, chlorides) from which diamonds nucleate arising by their reaction with local silicate minerals in peridotite and eclogite rocks (Pal'yanov et al., 2002; Pal'yanov et al., 2005). Previous work (e.g., Bulanova et al., 1998) emphasized also the importance of carbon saturated sulfide-rich melts from which diamond may form. Petrological arguments suggest that Fe-S melts may dissolve sufficient oxygen such that carbonates will undergo reduction. Moreover, different studies (such as Bundy et al., 1955; Fedorov et al. 2002; Strong & Hanneman, 1967; Sumiya et al., 2000) argue about the potential importance of Fe-Ni-C metallic melts as a viable medium for diamond growth in the lithosphere at appropriate P-T- f_{O_2} conditions, although it is still under debate why metallic iron inclusions would precipitate from liquids in equilibrium with diamond.

Similar to lithospheric diamonds, sub-lithospheric (or superdeep) diamonds are likely formed via metasomatic processes involving subduction-related C-bearing fluids in a highly reduced mantle (metal saturated) as a result of redox equilibria between the metasomatic melt and the mineral assemblage. Pal'yanov et al. (2013) proposed a mechanism of diamond formation both in front of and behind the mantle-slab redox boundary performing HP-HT experiments on the Fe^0-$(Mg,Ca,Fe)CO_3$ system. In this study, two distinct diamond media have been suggested as a function of the redox gradient between the descending oxidized slab and the reduced surrounding mantle: at high f_{O_2} conditions and low temperature the diamond source is represented by a Ca-rich carbonate melt produced by the carbonate-iron interaction, while at reducing conditions diamond crystallizes from a Fe-C melt produced by the reaction of carbonate with C-free Fe.

1.3 REDOX SENSORS

The redox sensor methodology introduced by Taylor et al. (1992) is based on metal-metal oxide (MMO) buffer equilibria to measure the oxygen fugacity in laboratory experiments designed to simulate conditions of Earth's interior.

A generic formalism for a MMO equilibrium reads,

$$xM + \frac{y}{2}O_2 = M_xO_y \tag{1.27}$$

where *M* is the metallic element, and *x* and *y* are stoichiometric coefficients (Taylor et al., 1992). The equilibrium constant $K_{T,P}$ of reaction 1.27 at a certain *P* and T is given as,

$$\log K_{T,P} = \log(a_{M_xO_y}) - \left[x\log(a_M) + \frac{y}{2}\log(f_{O_2})\right] \tag{1.28}$$

in which a is the activity of the species *i* and f_{O_2} is the oxygen fugacity. For a pure phase the activity equals unity, and hence, the equilibrium constant can be rewritten as,

$$\log K_{T,P} = -\frac{y}{2}\log(f_{O_2}) \ . \tag{1.29}$$

In the case of a binary solid solution in which the metal is diluted into another divalent metal oxide component, $a_{M_xO_y} < 1$. The effect of $a_{M_xO_y} < 1$ on the f_{O_2} can be quantified as,

$$\log(f_{O_2}) = -2\left[\log K_{(T,P)} - \log\left(a_{M_xO_y}\right)\right] \tag{1.30}$$

resulting in a shift of the buffer equilibrium to lower oxygen fugacity at a given *P* and *T*. The dilution of the metal with another metal component, which exhibits an ideal binary solid solution, displaces the end member buffer equilibrium to higher f_{O_2} at a certain *P* and *T,* such as,

$$\log(f_{O_2}) = -2\left[\log K_{(T,P)} + \log\left(a_{M_xO_y}\right)\right]. \tag{1.31}$$

These changes in the oxygen fugacity of the experimental system are related to compositional readjustments with temperature of the sensor material to approach equilibrium (Taylor et al., 1992). For instance, considering the iron-wüstite buffer at a given temperature with the addition of a noble metal in the system (e.g., Ir, Pd, Pt, etc.), whether the metal oxidizes would depend not only on the f_{O_2} of the system but also on the activity of Fe in the alloy, which is ultimately related to the composition. To expand the applicability of the redox sensor over a wider range of f_{O_2}, the oxide phase can also be a solid solution (e.g., FeO-MgO in ferropericlase).

1.3.1 Thermodynamics of binary systems

Noble metals (NM), are commonly employed in geochemistry as sliding redox sensors (Taylor et al., 1992) to measure the oxygen fugacity conditions during HP-HT laboratory experiments. The NM comprise in addition to Au and Ag the so-called platinum group elements (PGE) (i.e., Ir, Pt, Pd, Rh, Ru and Os), which possess high metal/silicate partition coefficients and are therefore, generally referred to as highly siderophile elements (HSE). The solubility of these transition metals in silicates and oxides was widely investigated at 1 atmosphere and at high-temperature (Borisov et al., 1994; Borisov and Palme 1995; 1996; 1997; 2000; Woodland & O'Neill, 1997; Borisov & Nachtweyh, 1998).

The thermodynamic properties of metal-bearing oxide and silicate are commonly given by reducing reactions such as Equation 1.27, that we can also express as the following,

$$\mathrm{NM(alloy)} + (m/4)\mathrm{O_2} = \mathrm{NMO}_{m/2}\ \mathrm{(silicate/oxyde)} \tag{1.32}$$

where m is the valence state of metal iron (Woodland & O'Neill, 1997; Borisov and Palme, 2000). At constant temperature, the logarithm of the noble metal concentration (C_{NM}) in equilibrium with an alloy varies linearly with the logarithm of the oxygen fugacity and the alloy composition, such as,

$$\log C_{\mathrm{NM}} = (m/4)\log f_{O_2} + \mathrm{const} + \log a_{\mathrm{NM}} \tag{1.33}$$

where $\mathrm{const} = \log(A * K/\gamma_{\mathrm{NMO}_{m/2}})$, $\gamma_{\mathrm{NMO}_{m/2}}$ is the activity of the NM-oxide in the oxide/silicate phase, and A is a conversion factor (e.g., mole to weight fraction) of the NM-oxide.

To evaluate how the thermodynamic properties of NM-Fe binary systems affect the solubility of a certain NM in a FeO-bearing mineral or melt as a function of the f_{O_2} one can calculate the activity of Fe in the alloy (Equation 1.35) starting from a buffer equilibrium (Borisov and Palme, 2000), such as IW:

$$\mathrm{Fe(alloy)} + 0.5\mathrm{O_2} = \mathrm{FeO\ (melt)} \tag{1.34}$$

$$\log a_{\mathrm{Fe}}(\mathrm{alloy}) = -0.5\log f_{\mathrm{O_2}} + \log a_{\mathrm{FeO}}(\mathrm{melt}) - \log \mathrm{K}\,. \tag{1.35}$$

For a given mineral/melt composition and constant temperature, changes in activity are analogous to variation in oxygen fugacity such as,

$$\Delta \log f_{\mathrm{O_2}} = -2\Delta \log a_{Fe}\,. \tag{1.36}$$

Therefore, the effect of the FeO content in a mineral/melt on the NM solubility at different redox conditions can be derived by examining the dependence of $\log a_{\mathrm{NM}}$ (alloy) versus $\log a_{Fe}$ (alloy) (Borisov and Palme, 2000). Along the same lines, Borisov and Palme (2000) reported that the relationship between X_{Fe} (alloy) and a_{Fe} (alloy) provides information on the affinity of Fe for different noble metals at different oxygen fugacities. Figure 1.8 illustrates the activity-composition relations for different binary solid alloys at 1200 °C. A decrease in oxygen fugacity at a certain temperature (e.g., 1200 °C) will cause an increase in the activity of Fe as well as a higher mole fraction of Fe dissolved in the alloy (Borisov and Palme, 2000).

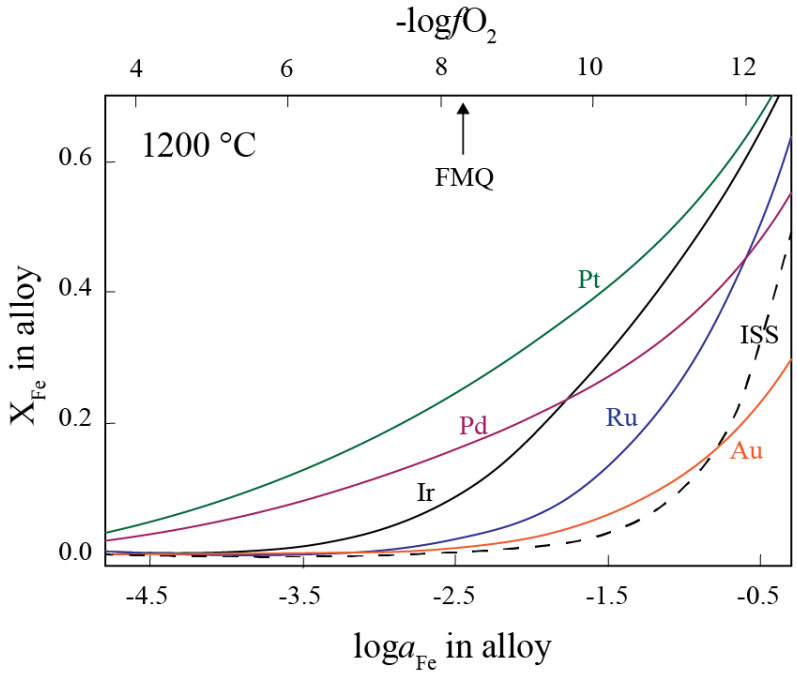

Figure 1.8: Composition of alloys coexisting with FeO-bearing minerals/melts at 1200 °C. ISS indicate the trend for an ideal solid-solution (modified after Borisov and Palme, 2000)

The activity of Fe in a certain noble metal a_{Fe}^{alloy} describes the excess free energy of mixing between Fe and the NM, i.e.,

$$a_{Fe}^{alloy} = X_{Fe}^{alloy} * \gamma_{Fe}^{alloy} \tag{1.37}$$

where γ_{Fe}^{alloy} is the non-ideality component of the solid-solution and is frequently parametrized using the Margules formalism.

For an asymmetric binary solid solution between Fe (*i* component) and a chosen NM (*j* component), γ_{Fe}^{alloy} is given as,

$$RTln\gamma_i^{alloy} = \left(X_j^{alloy}\right)^2\left[W_{ij}^{alloy} + 2X_{ij}\left(W_{ji}^{alloy} - W_{ij}^{alloy}\right)\right] \tag{1.38}$$

where W_{ij}^{alloy} and W_{ji}^{alloy} are the asymmetric Margules interaction parameters. Equation 1.39 describes the pressure and temperature dependence of the interaction parameters:

$$W_{ij}^{alloy} = W_{ij}^{H} - TW_{ij}^{S} + PW_{ij}^{V}. \quad (1.39)$$

The enthalpy W_{ij}^{H} and entropy W_{ij}^{S} dependent Margules parameters can be obtained at 1 bar by imposing the f_{O_2} at known values using a gas mixing furnace, while W_{ij}^{V} describes the volume dependence of the interaction parameters. The W_{ij}^{V} term can be calculated from the excess molar volume of mixing $\Delta_m V^{ex}$ between the *i* and j components, i.e.,

$$\Delta_m V^{ex} = \left(X_j^{alloy}\right)^2\left(1 - X_j^{alloy}\right)W_{ij}^{V} + \left(X_i^{alloy}\right)^2\left(1 - X_i^{alloy}\right)W_{ij}^{V}. \quad (1.40)$$

However, so far, the effect of pressure on the W_{ij}^{V} parameter, and consequently, on the activity composition-relations for a Fe-NM redox sensor (such as Fe-Ir, Fe-Pt or Fe-Pd binary systems) was never investigated.

1.3.2 Phase relations of metal alloys commonly used as sliding redox sensors

Ideally, many noble metals can be used to monitor the oxygen fugacity during laboratory experiments as long as their activity composition-relations are well established (Woodland & O'Neill, 1997). Commonly employed redox sensors are face-centered cubic (*fcc* or γ) Pt-Fe (Hultgren et al., 1973), Pd-Fe (Hultgren et al., 1973; Tomiska, 1989), and Ir-Fe (Schwerdtfeger & Zwell, 1968; Swartzendruber, 1984). The choice of using either of these binary systems can be made according to these criteria: i) a continuous solid-solution series must occur at high-temperature over the range that will be used in the experiment; ii) the activity-composition relations for the system must be well defined over the chosen temperature interval; iii) the oxide component must be insoluble in the metal phase and vice versa. If those conditions are fulfilled, the binary alloy system will respond to the imposed f_{O_2} through sliding compositional readjustment. Therefore, the oxygen fugacity can be monitored at fixed *P* and *T* and calculated at equilibrium conditions from the composition of the redox-sensitive solid solution (Taylor et al., 1992).

The phase relations of Pd-Fe (Hansen & Anderko, 1958) (Figure 1.9a) show a complete solid solution between Fe and Pd in the γ phase between 900 and 1304 °C, temperature that corresponds to the lowest melting point along the solid solution. Below 900 °C a series of magnetic transitions occur and two intermediate phases become stable, i.e., FePd and $FePd_3$. Activity

composition relations for this binary alloy in the *fcc* structure were studied by Hultgren et al. (1973) and Tomiska (1989), and later parametrized by Borisov and Palme (1997).

Similar to the Fe-Pd system, the phase diagram of Fe-Pt (Figure 1.9b) shows a series of structural transitions below 1350 °C where Fe_3Pt, $FePt_3$, and FePt are stable as a function of the Pt concentration in the alloy (Elliot, 1965). Activity-composition relations for γ-Fe-Pt system were derived by Heald (1967), Gudmundsson & Holloway (1993), and Kessel et al. (2001) showing reasonable agreement with one another. However, the employment of either of these binary systems as sliding redox sensors has several limitations especially correlated with the occurrence of structural phase transitions over a large temperature interval.

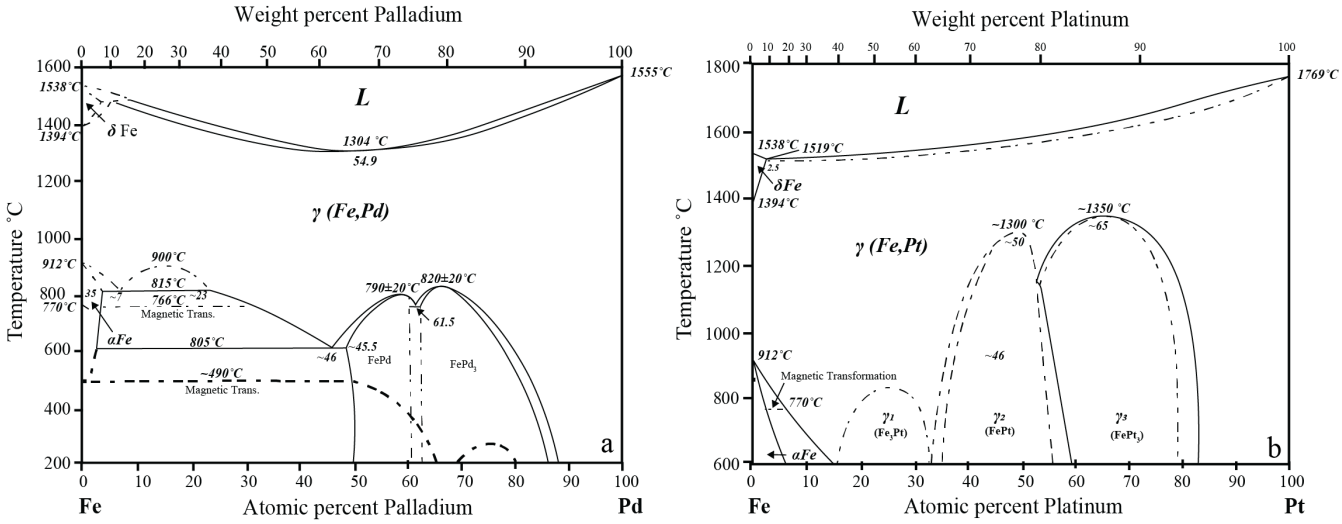

Figure 1.9: a) Binary Fe-Pd (modified after Hansen & Anderko, 1958) and **b)** Fe-Pt (modified after Okamoto, 2000) solid solution phase diagrams at room pressure and high temperature.

Iridium has favourable thermodynamic properties that make it one of the most viable metal to be used as a redox sensor. In the temperature interval between 650 and 1400 °C only one phase γ-Fe-Ir (*fcc*) is stable over a wide compositional range. Figure 1.10 displays the phase relations for the Fe-Ir system at 1 bar as a function of temperature (Swartzendruber, 1984) with peritectic point (liquidus (2.1 at. % Ir) + γ (3.0 at. % Ir) ↔ δ(2.5 at. % Ir)) located at 1546 °C.

The activity-composition relations and volume of mixing were investigated by Schwerdtfeger & Zwell (1968) at 1200 °C and 1 bar using the gas mixing furnace, and then further parametrized by Woodland & O'Neill (1997) and Stagno et al. (2013).

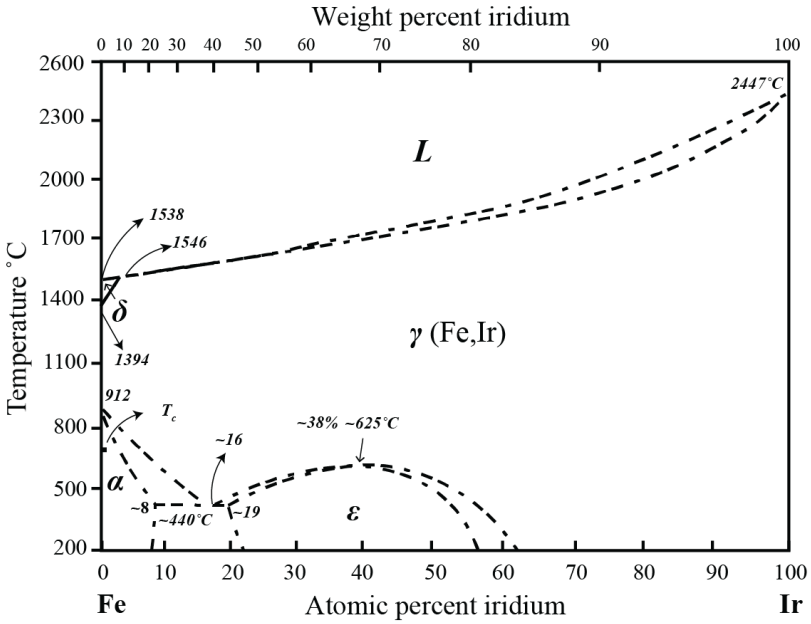

Figure 1.10: Phase diagram of the Fe-Ir system (modified after Swartzendruber, 1984).

1.4 EARTH'S CORE

1.4.1 Earth's inner core structure and compositional models

Our knowledge of the structure and composition of Earth's core is based on sparse direct evidence (e.g., from seismology, geodesy, geo- and paleo-magnetism) and many indirect observations (from cosmochemistry, experimental petrology, and mineral physics) (Allègre et al., 1995; McDonough & Sun, 1995). Cosmochemical studies on iron meteorites and comparison of mineral physics data with seismological observations (measurements of density (ρ) and compressional (V_P) and shear (V_S) wave velocities under extreme conditions) suggest that Earth's inner core is primarily composed of metallic Fe-Ni alloy (5-25 wt. % Ni) (Wasson & Chou, 1974; McDonough & Sun, 1995). However, the inner core density is ~5 % lower than pure Fe (Figure 1.11a) at corresponding pressures and temperatures (Dewaele et al., 2006; Fei et al., 2016), presumably due to the presence of light elements (Birch, 1952) that were incorporated in the core during its formation (Wade & Wood, 2005; Rubie et al., 2011; Siebert et al., 2013). Oxygen, silicon, sulfur, carbon and hydrogen have been proposed as candidates based on geochemical and geophysical evidence (Figure 1.11b) (Birch, 1964; Mao et al., 1990). Si is favored based on its effect on the compressional wave velocities of iron (Badro et al., 2007) and its affinity for the metallic phase during Earth's differentiation (Lin et al., 2003; Antonangeli et al., 2010; Mao et al., 2012; Siebert et al., 2013; Fischer et al., 2015; Tateno et al., 2015).

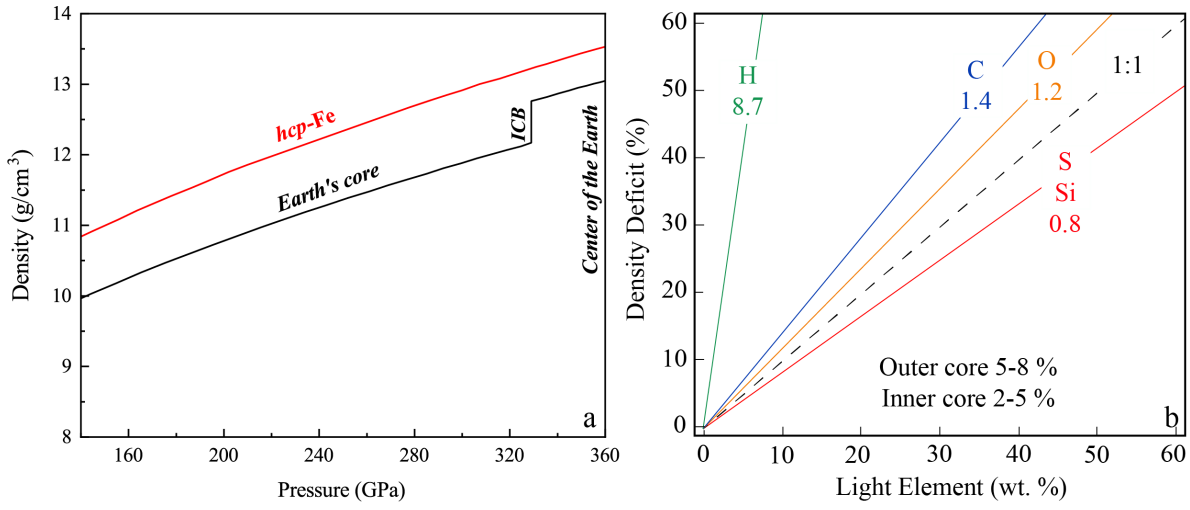

Figure 1.11: **a)** Earth's core density deficit. The red curve represents experimental data of *hcp*-Fe (Fei et al., 2016) in comparison with geophysical observations of the core (black curve-Dziewonski, and Anderson, 1981); **b)** candidate light elements in Earth's core (Li et al., 2019).

Identifying the nature of light elements and their effect on crystal structure and physical properties of Fe alloys motivates the comparison of laboratory results and geophysical observations. Fe has been proposed to be stable in the hexagonal close packed (*hcp*) phase at inner core conditions (Mao et al., 2001; Tateno et al., 2010; Ohtani et al., 2013) based on its broad stability field at high pressure (Takahashi & Bassett, 1964). However, experimental and theoretical evidence suggests that a body centered cubic (*bcc*) phase is stable at high pressures and high temperatures (Belonoshko et al., 2003; Dubrovinsky et al., 2007). Strong arguments that favor the stability of *bcc* Fe under these conditions include: i) transition metals are known to transform from close-packed structures to the *bcc* structure at temperatures close to their melting curves (Vočadlo et al., 2003 and references therein); and ii) the dissolution of Si in *hcp* Fe or Fe-Ni alloy expands the stability field of the *bcc* structure at high pressure (Vočadlo et al., 2003; Lin et al., 2002).

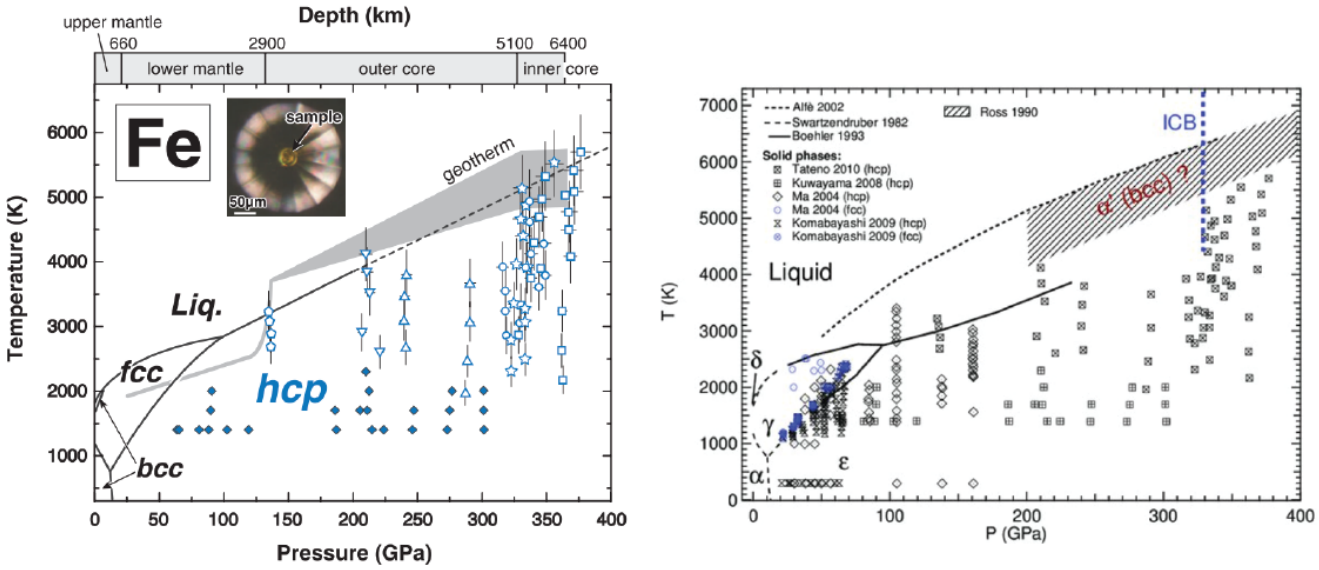

Figure 1.12: Crystal structure of Fe at Earth's core condition modified from **(a)** Tateno et al. (2010) and (**b**) Anzellini et al. (2014).

The presence of Ni can also affect phase relations and thermodynamic properties of Fe alloys, modifying the extent of their stability fields at high pressures and temperatures. At ambient pressure and up to 25 at. % Ni, Fe-Ni alloys have a *bcc* structure, whereas higher Ni content and/or higher temperatures stabilize the face-centered cubic (*fcc*) phase (Lin et al., 2003; Dubrovinsky et al., 2007). Upon compression, the initial *bcc* phase transforms to *hcp* (at ~10 GPa and room temperature), which persists up to 200 GPa and 2900 K for a given alloy containing 9.8 at. % Ni

(Dubrovinsky et al., 2007). At 225 GPa and 3400 K, Dubrovinsky et al. (2007) observed the complete transformation of *hcp* $Fe_{0.9}Ni_{0.1}$ into the *bcc* structure, confirming the existence of an ultra-high-pressure *bcc* phase, previously predicted by Brown & McQueen (1986) and Brown (2001) for pure Fe (Figure 1.13). In general, both theoretical and experimental work (Lin et al., 2002; Vočadlo et al., 2003; Dubrovinsky et al., 2007) emphasize that Fe-Ni alloys with Ni concentrations of ~10-15 wt.% and substantial Si content (possibly coupled with other light elements) (Vočadlo et al., 2003) may be more stable in the *bcc* phase compared to *hcp* at Earth's core conditions (Dubrovinsky et al., 2007).

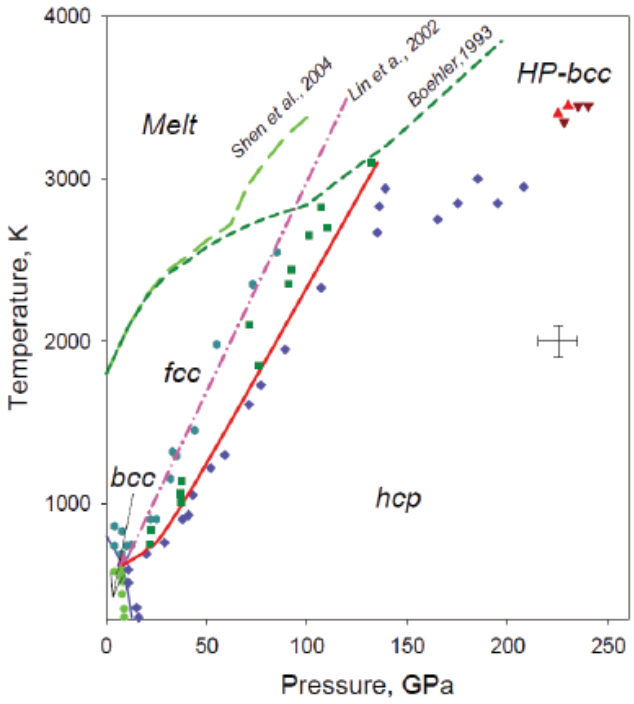

Figure 1.13: Phase relations of $Fe_{0.9}Ni_{0.1}$ alloy at high pressures and temperatures as determined by in situ X-ray diffraction experiments (Dubrovinsky et al., 2007).

1.4.2 Phase relations and elasticity of Fe-(Ni)-Si alloys

Phase relations and *P-V-T* equations of state in the Fe-Si and Fe-Ni-Si systems have been investigated for various compositions (Figure 1.14): Fe-8.9 wt. % Si (Zhang & Guyot, 1999a, 1999b); FeSi (Dobson et al., 2002, 2003); Fe-8.7 wt. % Si (Hirao et al., 2004); Fe-3.4 wt. % Si (Asanuma et al., 2008); Fe-6.4 wt.% Si and Fe-9.9 wt. % Si (Kuwayama et al., 2009); FeSi (Lord et al., 2010); Fe-7.9 wt. % Si (Lin et al., 2009); Fe-4.8 wt. % Ni-4 wt. % Si (Sakai et al., 2011); Fe-16 wt. % Si (Fischer et al., 2012); Fe-10 to 29 wt. % Si (Fischer et al., 2013); Fe-10 wt. % Ni-5 wt. % Si (Morrison et al., 2018); Fe-10 to 29 wt. % Si (Edmund et al., 2019a); Fe-5 wt. % Si (Edmund et al., 2019b); Fe-5 wt. % Ni-5 wt. % Si (Edmund et al., 2020); Fe-7 wt. % Ni, Fe-7 wt. % Ni-5 wt. % Si, Fe-7 wt. % Ni-9 wt. % Si and Fe-7 wt. % Ni-15 wt. % Si (Ikuta et al., 2021). Stoichiometric FeSi is known to be stable in the B20 (FeSi-type) structure at ambient conditions (Fischer et al., 2013). With increasing pressure and temperature, a B20 + B2 (CsCl-type) mixture becomes stable at least up to ~40 GPa (Vočadlo et al., 1999; Dobson et al., 2002, 2003; Caracas & Wentzcovitch, 2004; Lord et al., 2010; Fischer et al., 2013), where it transforms to the B2 structure that persists up to 145 GPa (Fischer et al., 2013).

Variation of the Si content in the Fe-FeSi system promotes the stability of the *hcp* structure at high pressure (Fischer et al., 2013). Specifically, for a Fe-Si alloy with Si content ranging from 9 to 16 wt. %, the coexistence of B2 + *hcp* phases was observed up to 145 GPa and 2400 K (Fischer et al., 2013). Extrapolation of the *hcp* + B2 phase boundaries at 329 GPa and 6650 K indicates that Si-bearing Fe alloys could be stable as a mixture of Si-depleted (Si < 2 wt. %) *hcp* and Si-enriched (Si > 10-15 wt. %) B2 phases at Earth's inner core conditions (Fischer et al., 2012, 2013; Fischer & Campbell, 2015).

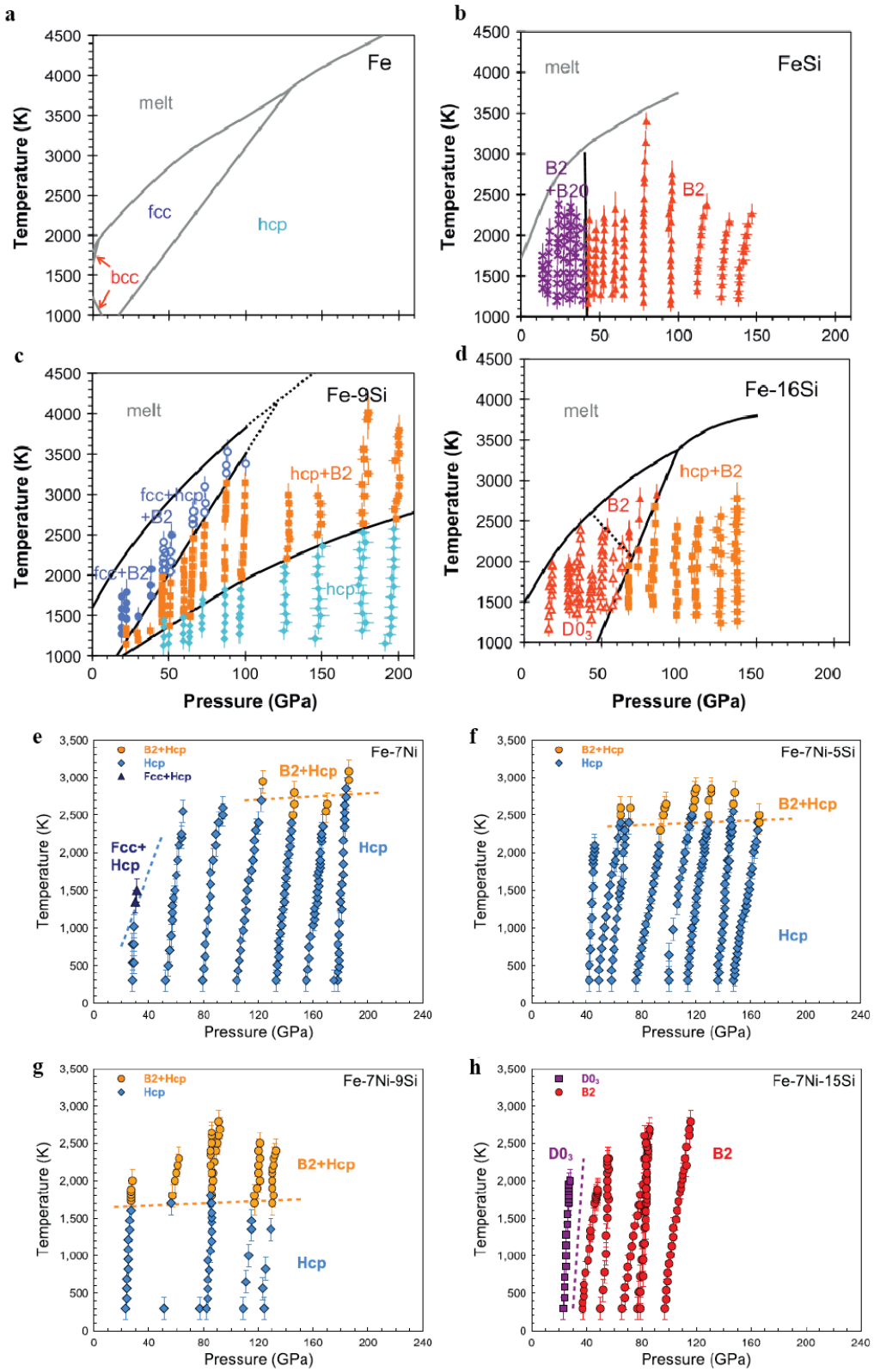

Figure 1.14: Pressure–temperature phase relations in the Fe-Si (**b-d**, Fischer et al., 2013), Fe–Ni and Fe–Ni–Si systems (**e-h**, Ikuta et al., 2021). The phase diagram of pure Fe (**a**) is reported for comparison (Komobayashi & Fei, 2010; Ma et al., 2004).

Although extensive work has been conducted in understanding Earth's core structure and composition, controversies remain about the effect of Si (as well as other light elements) on the elastic properties of Fe-Ni alloys and its abundance in Earth's core. Previous studies have shown that core composition can be inferred by comparing experimentally measured density and sound velocities with the preliminary reference Earth model (PREM, Dziewonski and Anderson, 1981). The sound velocity of Fe and Fe-Si alloys has been investigated under high-pressure conditions using different methods, including inelastic X-ray scattering (IXS): Fe (Mao et al., 2001); Fe-Si (Antonangeli et al., 2010); Fe (Shibazaki et al., 2012); Fe (Ohtani et al., 2013); Fe (Liu et al., 2014); Fe (Sakamaki et al., 2016); Fe-Si (Antonangeli et al., 2018); Fe-Si (Sakairi et al., 2018), nuclear resonance inelastic X-ray scattering (NRIXS): Fe-Si (Lin et al., 2003), ultrasonic: Fe (Shibazaki et al., 2016), shock wave: e.g., Fe-Si (Brown & McQueen, 1986), and Picosecond Acoustics (PA) experiments: Fe-Si (Edmund et al., 2019a, 2019b). However, not all results are consistent with one another, which might be due to differences in starting compositions, structures of synthesized samples and experimental techniques. Using IXS, Badro et al. (2007) and Antonangeli et al. (2010, 2018) concluded that an Fe-Si mixture with about 2 wt. % Si could account for geophysical observations of the inner core. Conversely, Mao et al. (2012) and Sakairi et al. (2018) proposed higher silicon contents, 8 wt. % and 3-6 wt. % Si, respectively, to match seismological observations. The highest estimate indicates a Si content up to ~20 wt. % in Earth's core (Balchan & Cowan, 1966; Ringwood, 1959). Recent measurements performed using the PA technique (Edmund et al., 2019a) report that Fe alloy containing 5 wt. % Si matches PREM inner core density, but does not account for geophysically observed compressional and shear wave velocities.

1.5 AIM OF THE STUDY

This thesis examines physicochemical properties such as elastic behaviour and redox state of Fe-bearing minerals and metal alloys at deep Earth conditions.

A primary goal consists in calibrating an oxybarometer for diamond anvil cell experiments that represent exclusive tools to simulate the extreme conditions within and beyond the Earth's lower mantle. Adapting the redox sensor methodology, well established for HP-HT experiments in large volume presses, to the DAC we monitor oxygen fugacity variations using the Fe-Ir binary system upon laser heating combining Fe oxidation state and chemical analysis results via mass balance. The introduction of an oxybarometer for the DAC may reconcile previous contradictory results (e.g., Cerantola et al., 2017 and Dorfman et al., 2018) possibly due to diverse redox conditions during DAC experiments. Moreover, we intend to calibrate the existing thermodynamic model for the Fe-Ir redox sensor, well constrained as a function of temperature and composition, at high pressure implementing the current activity-composition relations with the volume dependency on the interaction parameter (W_{ij}^{V}) between Fe and Ir.

A secondary goal is to test the applicability of the newly calibrated redox sensor and examine potential differences with the existing thermodynamic model for experimental systems simulating the interaction between a carbonate-bearing subducting slab and a metal saturated lower mantle. We investigate the local oxygen fugacity variation induced by the mantle-slab interaction determining the $Fe^{3+}/\Sigma Fe$ ratio in synthetic ferropericlase equilibrated with magnesite and diamonds and in natural ferropericlase inclusions from Rio Soriso (Brazil) using Mössbauer spectroscopy. We aim to address the maximum ferric iron content that ferropericlase can incorporate during redox-driven diamond formation and compare experimental results with the few data available of natural ferropericlase inclusions in sub-lithospheric diamond. We examine the viability of using ferropericlase as oxybarometer for the lower mantle and argue about the effect of oxygen fugacity on ferropericlase' Fe valence state at the conditions where diamond forms through redox freezing of subducted carbonate.

A third goal is to investigate the elastic properties of Fe-Ni-Si alloys with implications for the Earth's inner core composition. We test the hypothesis that the inner core is composed of a mixture of Si-depleted *hcp* and Si-enriched B2 phases, performing high-pressure measurements of the sound velocities and density of polycrystalline B2-$Fe_{0.67}Ni_{0.06}Si_{0.27}$ using inelastic X-ray

scattering and powder X-ray diffraction to provide new constraints on the role of Si as a light element in the inner core. We examine the combined effect of Ni and Si on elastic properties of pure Fe at high pressure and at room temperature, and extrapolate at inner core conditions using thermodynamic calculations to enable comparison with geophysical observation of Earth's inner core and previous experimental and theoretical studies.

Chapter 2

2 METHODS

This section provides a summary of the experimental, analytical, and spectroscopic techniques employed to probe the samples' properties examined in this thesis. Additional details are reported separately in the following chapters.

2.1 HIGH PRESSURE EXPERIMENTS

2.1.1 Pressure Generation

Studying the physicochemical properties of candidate materials under high-pressure (HP) and high-temperature (HT) conditions is fundamental for the comprehension of the structure, dynamics, and evolution history of Earth and planetary interiors. To simulate in the laboratory the extreme conditions existing in planetary bodies, novel experimental techniques have been developed and perfected over the past decades.

The principle of pressure generation is expressed as $P = \frac{F}{A}$, where *F* is the applied force and *A* is the area on which the force is applied. Based on this relation, high pressures can be attained by either increasing the force *F* or decreasing the surface *A*.

By maximizing the force, large volume press devices, such as piston cylinder (PC) and multi anvil (MA) apparatus, produce uniaxial and/or multi axial static compression on relatively large samples (from millimeter to few centimeter sizes). Piston cylinder and multi anvil presses allow simulating pressures and temperatures from the shallower region of the upper mantle (PC up to ~5 GPa-2200 °C) to the mid-lower mantle (MA press with sintered diamond anvils, up 90 GPa-2500 °C).

By reducing the volume of the investigated object down to a few cubic micrometers, the same load can be generated with a small volume device, the diamond anvil cell (DAC), a unique apparatus capable of generating pressures of several hundreds of GPa, far beyond the conditions existing at the center of Earth. A cross-section of Earth's interior along with the appropriate experimental device for simulating the desired HP-HT conditions is given in Figure 2.1.

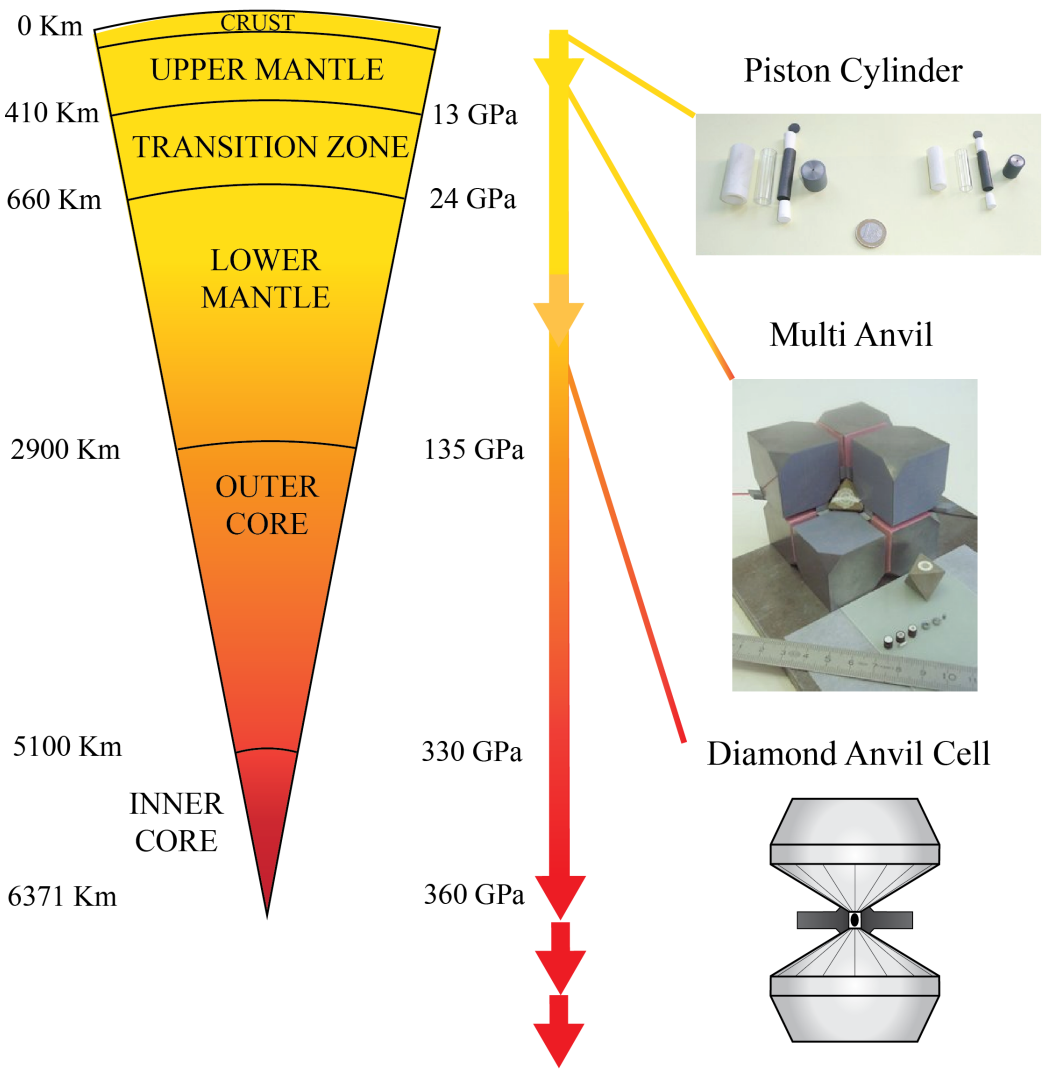

Figure 2.1: Cartoon sketch of Earth's interior along with pressure distribution with depth and the most appropriate experimental tool to simulate the desired conditions.

2.1.2 Sample synthesis and phase equilibria experiments with the multi anvil press

The samples discussed in this thesis were synthesized using a 6-8 Kawai type multi anvil apparatus (Kawai & Endo, 1970) at Bayerisches Geoinstitut. The split-sphere multi anvil system consists of a hydraulic press that can generate a load up to 600-2000 tons in a pressure range of ~3-28 GPa (Rubie, 1999; Keppler & Frost, 2005). Pressure is applied driving together two opposite guide blocks made of three hardened-steel anvils each (first stage or outer anvils) which define a cubic cavity where a set of eight cubes (second stage or inner anvils) is compressed in a uniaxial direction (Figure 2.2, bottom). The cubic packet consists of tungsten carbide cubes of an edge length of 25 or 32 mm with a truncated corner of a triangular shape. Cube truncations are placed facing each other to generate an octahedral gap where the pressure medium is contained (Figure 2.2, top). Second stage anvils are separated by pyrophyllite gaskets located at the edges of each truncation with the purpose of restraining the octahedron pressure medium, supporting the truncations and sealing the high-pressure region. By varying the truncation size (TEL: truncation edge length) of the second stage anvils, the octahedron dimension (OEL: octahedral edge length), and the force exerted by the hydraulic piston, different pressures can be attained. The pressure medium is made of polycrystalline MgO doped with 5 wt. % of Cr_2O_3, provides hydrostatic stress conditions during compression, and contains a hole filled with a zirconia sleeve (thermal insulator) and a resistance heater. The experimental sample is located at the center of the assembly inside a capsule and it is separated from the furnace by a MgO sleeve. MgO spacers fill the space above and below the capsule. An example of schematic cross section for the 7/3 (OEL/TEL notation) pressure cell is illustrated in Figure 2.3. W-Re based thermocouples are usually inserted from the top inside the drilled MgO spacer within an alumina tube or placed horizontally through the wall of the furnace to be directly in contact with the capsule. Copper wire coils are frequently used to protect the thermocouple from breaking as it passes through the gasket.

For the scope of this thesis (see paragraph 1.5), we used 18/11 and 7/3 cell assembly configurations to apply pressures of 8 and 26 GPa, respectively, using the Sumitomo (1200 tons) and Hymag (1000 tons) multi anvil presses installed at the Bayerisches Geoinstitut. Pressure calibration as a function of the oil pressure is based on minerals phase transitions as described in Keppler & Frost (2005). Calibration curves are shown in Figure 2.4.

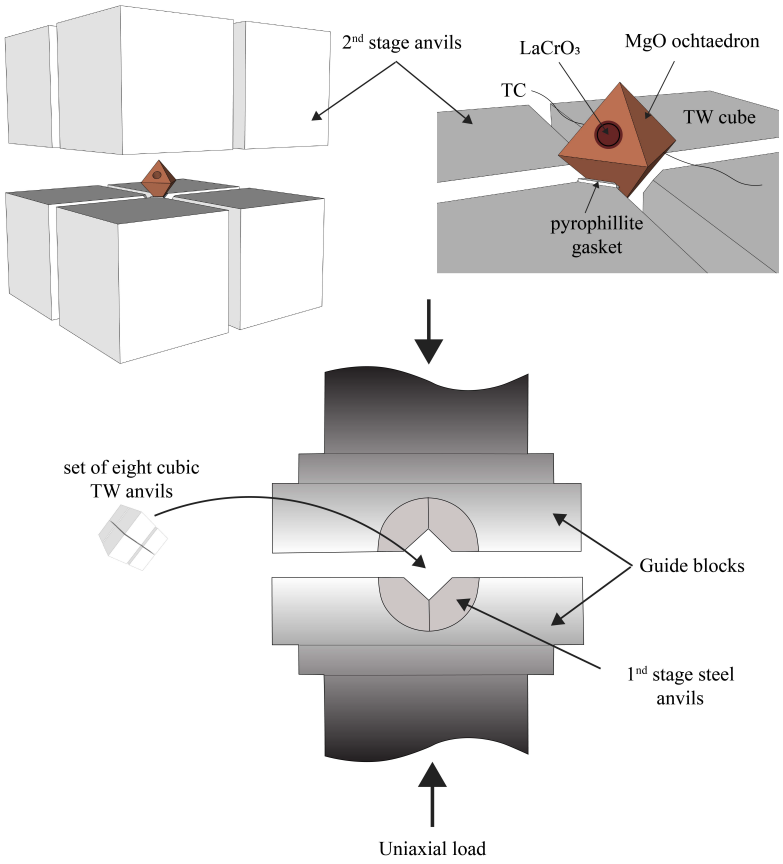

Figure 2.2: Details of a multi anvil apparatus (modified after Rubie, 1999). **Top**: eight WC cubic anvils compress an octahedral MgO pressure assembly. On the right, a magnified sketch of the core of the cubic packet (left) with visible pyrophyllite gasket strips attached to the surface around four of the truncations. **Bottom**: two opposite guide blocks containing a set of six first stage anvils are guided together by the hydraulic piston.

Synthesis experiments of Fe-Ni-Si alloy discussed in Chapter 5 were performed at sub-solidus conditions at 8 GPa and 1200 °C employing single crystal MgO capsules and triple-stepped graphite heaters to reduce the thermal gradient inside the capsule (Rubie, 1999). Sample temperature was monitored using a D-type $W_{97\%}Re_{3\%}$–$W_{75\%}Re_{25\%}$ (0.08 or 0.013-mm thick) thermocouple wire directly in contact with the top of the MgO capsule. After 1 hour, during which temperature was maintained within ± 10-20 °C, experiments were quenched rapidly by switching off the power and then decompressed to ambient pressure over 15 hours. In the case where the thermocouple broke during compression or became unstable while heating, the temperature was estimated from the electrical power to the furnace and compared with other experiments performed on the same pressure cells. Uncertainties are reported as described in Rubie (1999).

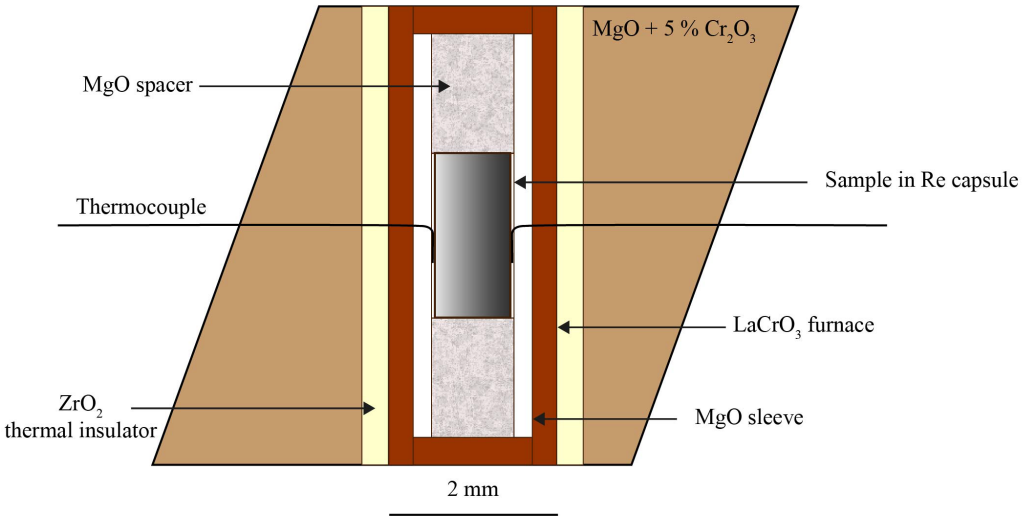

Figure 2.3: Schematic cross section of a 7/3 cell assembly for multi anvil experiments.

A phase equilibria experiment was performed employing the 7/3 cell assembly configuration at the conditions of the upper portion of the Earth's lower mantle (26 GPa and 1700°C) using ferropericlase and pure Ir metal as starting powder enclosed in a Re capsule (Chapter 3). High temperature was reached using a $LaCrO_3$ heater, kept for about 1 hour, and monitored with a conventional D-type thermocouple in contact with the capsule. The experiment was rapidly quenched by shutting off the electric power while the pressure was slowly released over 15 hours.

Experiments discussed in Chapter 4 on ferropericlase equilibrated with magnesite and diamond, were synthesized in a previous study (Stagno et al., 2011) at top-mid lower mantle conditions (25-45 GPa and 1500-1700 °C) using Kawai-type and D-DIA multi anvil presses available at the Bayerisches Geoinstitut and at the Geodynamic Research Center (Ehime, Japan). All run products are described in detail in the referred chapters.

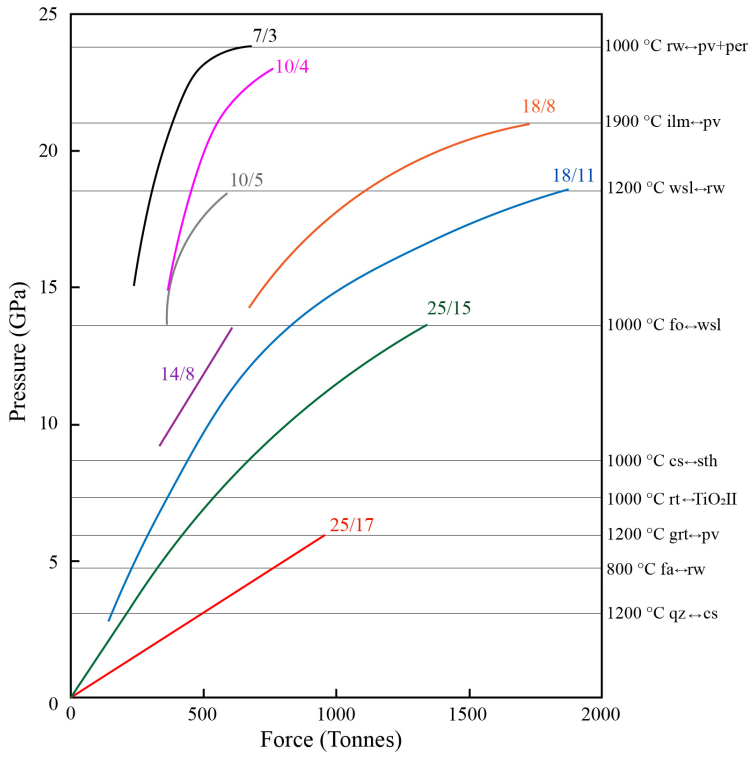

Figure 2.4: Pressure calibrations performed using 1200 tonne split-sphere and 5000 tonne split-cylinder multi- anvil presses (modified after Keppler & Frost, 2005). High temperature mineral phase transformations used are: quartz (qz) ↔ coesite (cs), Fe_2SiO_4 fayalite (fa) ↔ ringwoodite (rw), $CaGeO_3$ garnet (grt) ↔ perovskite (pv), rutile (rt) ↔ TiO_2II, coesite (cs) ↔ stishovite (sth), Mg_2SiO_4 fosterite (fo) ↔ wadsleite (wsl), $MgSiO_3$ ilmenite (ilm) ↔perovskite (pv), Mg_2SiO_4 ringwoodite (rw) ↔ perovskite (pv) + periclase (per).

2.1.3 The diamond anvil cell

The diamond anvil cell (DAC) technique, introduced for the first time by Weir et al. (1959), is perhaps one of the most commonly used methods for ultra-high-pressure studies in geoscience, physics, and related fields (Bassett, 1979; 2009). This instrument is capable of generating the highest pressure of any static compression device up to 1 TPa (Dubrovinskaia et al., 2016), simulating the conditions of Earth's core and larger planetary bodies (Mao et al., 1990).

The operating principle of the DAC consists in compressing a sample between coaxial, perfectly aligned, flattened, and opposite diamond anvils (culets). The culet dimension can vary from 1 mm to a few tens of micrometers. A smaller culet diameter allows reaching higher pressures but, at the same time, limits the sample dimension to be placed between the anvils. To simulate conditions down to the lower portion of Earth's lower mantle we used culet sizes of 250 and 120

μm. Diamond anvils are glued on WC seats that transport the load from the cell body onto the anvils and are separated by a drilled and pre-indented (to a thickness of ~20-30 μm) metallic gasket, commonly made of rhenium metal. The latter prevent the occurrence of several problems during compression, e.g., diamond fracture or escape of the compressed material due to the axial stress. The sample is placed inside the pressure chamber created by the gasket hole, filled by either an inert gas (e.g., Ne, Ar, He etc.), a liquid, or a solid (e.g., KCl, NaCl, MgO as a sandwich-like assembly) material to act as pressure transmitting medium. In this way, the material surrounding the sample ensures quasi-hydrostatic conditions during compression and prevents non-homogeneous strains. In all experiments discussed in this thesis Ne was chosen as pressure transmitting medium and loaded using the gas loading system developed at BGI (Kurnosov et al., 2008).

One of the valuable characteristics of the DAC is the transparency of the diamonds to a wide range of electromagnetic radiation, which allows *in situ* studying of material properties under pressure using different spectroscopic techniques. Depending on employed experimental methods and the purpose of the measurements, different DAC geometries can be used (see Jayaraman, 1983 for further details). Two main design are mostly employed: i) a piston-cylinder type, where diamonds are placed on perfectly matching metallic bodies, favorable for the possibility of increasing the opening angle, and ii) a plate-type or Merrill-Bassett design (Miletich et al., 2000; Bassett, 2009) limits the possibility of increasing the opening angle and upon pressure may not maintain a perfect alignment.

In the present thesis, we used screw driven symmetric piston-cylinder-type BX90 (acronym for Brillouin scattering–X-ray diffraction with a 90° opening angle) and BX90 mini DAC (Kantor et al., 2012), machined at BGI, with Bohler Almax (Boehler & De Hantsetters, 2007) diamond anvils and seats design. A simple sketch of the cell body is given in Figure 2.5.

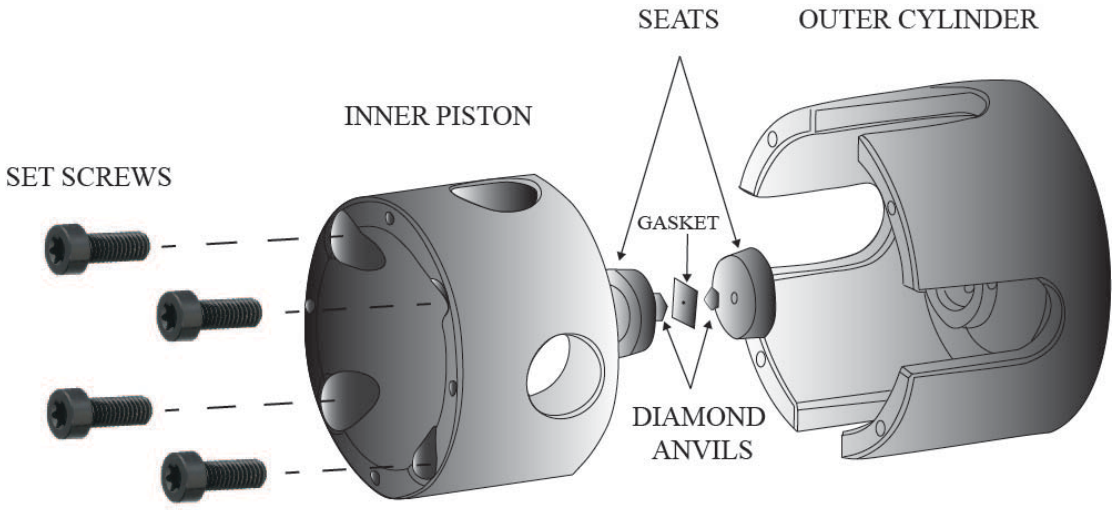

Figure 2.5: BX90 diamond anvil cell design modified after Kantor et al. (2012).

This DAC geometry is suitable both for single crystal and powder X-ray diffraction thanks to the wide conical opening angle which provide a high number of Bragg reflections to be detected for a given wavelength (Kantor et al., 2012). Numerous advantages characterize the BX90 design with respect to other configurations such as an easy alignment, a stable pressurization, mechanical stability, and maintenance of the pressure constant for a long time.

DAC experiments rely on *in situ* determination of pressure inside the pressure chamber. To estimate the pressure, different methodologies can be employed, including the ruby fluorescence (Mao et al., 1986; Chijioke et al., 2005), the diamond Raman (Akahama & Kawamura, 2006), and the use of calibrants with a well-known equation of state (usually phases with cubic structure are preferable to minimize the number of diffraction lines). Alternatively, materials commonly utilized as pressure media, i.e., KBr, KCl, Ne, MgO and NaCl, can be used as a pressure gauge. In the present work, we adopted different approaches, depending on the purpose of the specific measurements. For powder X-ray diffraction (XRD) experiments conducted on ferropericlase equilibrated with Fe-Ir alloy (Chapter 3), the pressure was derived from a Ne equation of state (Fei et al., 2007). Similarly, pressure determination during the acquisition a Fe-Ni-Si alloy equation of state (Chapter 5) was carried out using both Ne diffraction lines and an EOS of gold (Fei et al., 2007), placed in the sample chamber to act as a pressure gauge. During Inelastic X-ray scattering measurements of Fe-Ni-Si alloy discussed in Chapter 5, the experimental pressure was initially

derived by the first order Raman mode of the diamond culet (Figure 2.6), and then more accurately, comparing Fe-Ni-Si lattice parameters with the equation of state determined in this study for the same compound. Pressure determination using the diamond Raman procedure, described for example in Akahama & Kawamura (2006), rely on the correlation between the high-wavenumber of the Raman band with the normal stress of the culet surface. The analytical expression for quasi-hydrostatic pressure determination (Akahama & Kawamura, 2006) is,

$$P(GPa) = K_0 \left(\frac{\Delta v}{v_0}\right)\left[1 + \frac{1}{2}(K_0' - 1)\left(\frac{\Delta v}{v_0}\right)\right] \quad (2.1)$$

where Δv is the measured wavenumber of the high frequency edge, v_0 is the edge frequency at ambient pressure (v_0 =1334 cm^{-1}), K_0 = 547 GPa and K_0' = 3.75 are, respectively, the bulk modulus and the bulk modulus pressure derivative of a hydrostatically compressed elastic material, with comparable properties of the existing relation between Raman frequency and normal stress at the diamond anvil culet.

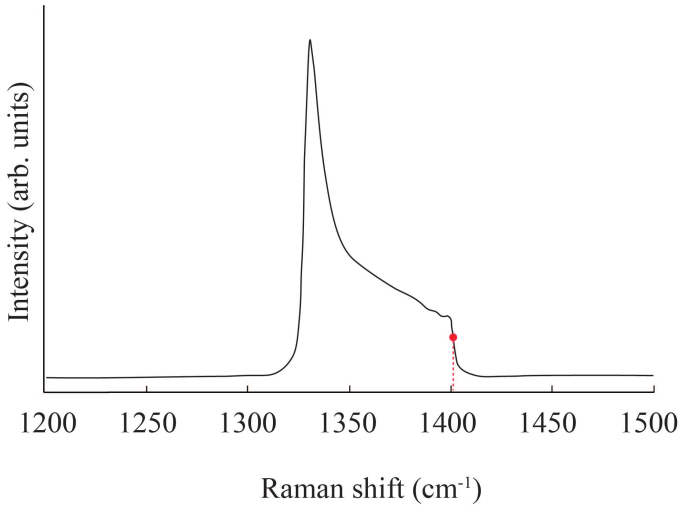

Figure 2.6: Raman shift spectrum of a diamond anvil under stress. The high wavenumber edge position is used as pressure gauge.

High-temperature in DAC can be generated using laser-heating (LH) systems with different type of sources, i.e., SPI fiber, ruby, Nd:YAG, CO_2 and others. In this thesis, we describe high temperature experiments (Chapter 3) performed using the double-sided laser heating system developed at BGI (Kupenko et al., 2015; Aprilis et al., 2017), emitting a near infrared radiation (NIR) wavelength of 1064 nm by means of a Nd-doped yttrium aluminum garnet (Nd:YAG) crystal

source. The optical components of the double-sided laser heating setup allow to precisely focus the laser beam on the sample surface minimizing the temperature gradient and promoting equilibrium between crystallized phases. Temperature is usually determined by spectroradiometry (Campbell, 2008). The employed double side laser heating setup is shown in Figure 2.7 and is extensively described in Aprilis et al. (2017). Figure 2.8 shows a sketch of a BX90 DAC with upstream and downstream laser beams passing through the diamond anvils.

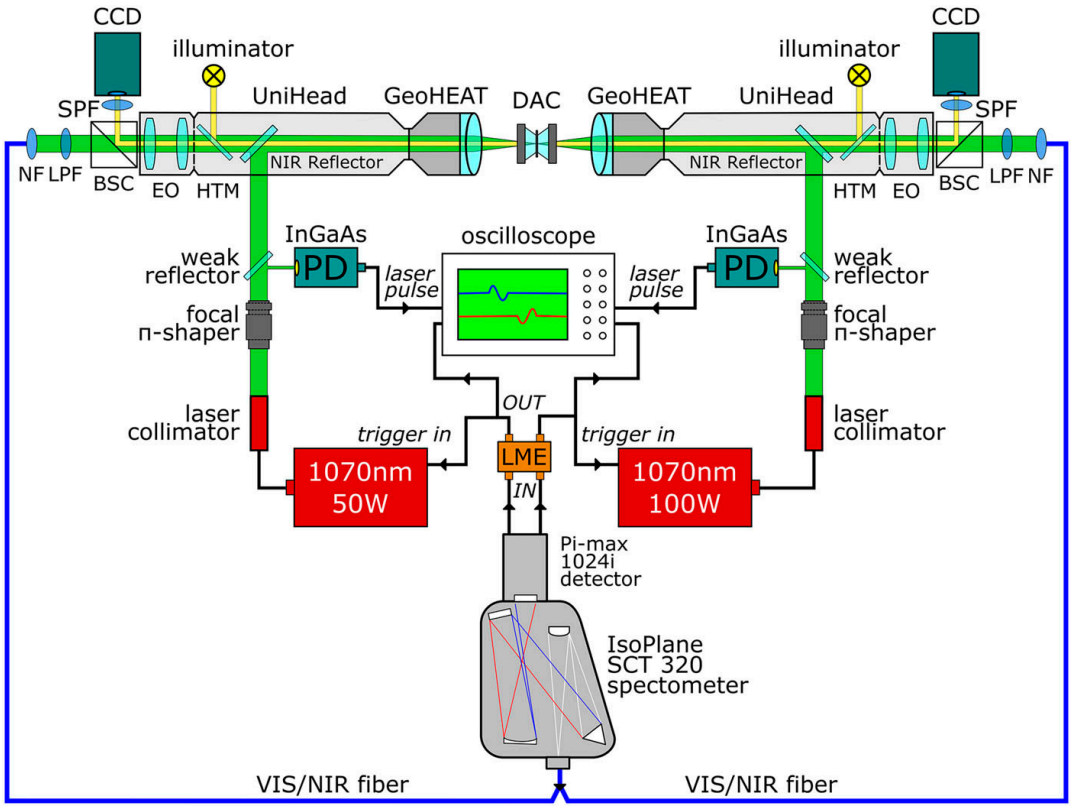

Figure 2.7: Double-sided pulsed laser heating system for diamond anvil cells (Aprilis et al., 2017). SPFs: short-pass filters; CCDs: cameras for sample visual observation; NFs: notch filters used to isolate the laser beam from the detector; LPFs: longpass filters that avoid contamination from the second order diffraction of the grating; BSCs: beam-splitter cubes; Eos: "eyepiece" optics of the UniHead modules that focus the image on the viewing cameras and optical fibers; HTMs: half-transparent mirrors that reflect illumination light; GeoHEATs: achromatic lenses for laser focusing and collection of thermal radiation; PDs: fast InGaAs photo-detectors used to capture laser pulses; LMEs: laser modulation electronics.

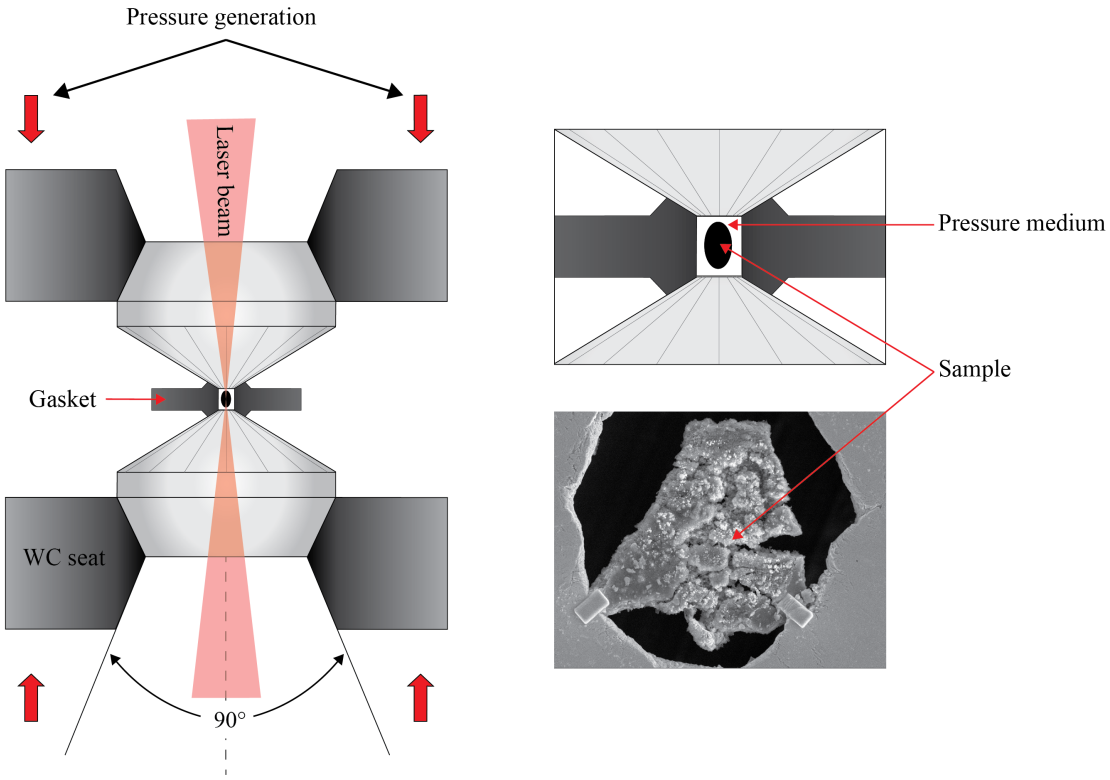

Figure 2.8: **Left**: Cartoon sketch of a BX90 type diamond anvil cell. Red bands simulate the double stream laser beam. **Right**: Magnification of the pressure chamber created by the drilled Re gasket where sample and pressure medium (also thermal insulator) are located.

2.2 ANALYTICAL TECHNIQUES

2.2.1 Scanning electron microscopy

Sample textural and chemical characterization was performed using the scanning electron microscope (SEM) Zeiss Gemini 1530 installed at BGI, which provides a spatial resolution of ~10 nm in topographic mode and up to 100 nm in compositional mode (Reed, 2005). Prior to the analyses, recovered run products from multi anvil experiments were placed in epoxy resin, polished to expose the samples surface and coated with carbon powder (~8-12 nm layer thickness) to prevent electrical charging of the specimen under the electron beam. This instrument was primarily used for highly detailed imaging of coexisting phases and semi-quantitative chemical analyses.

A typical SEM instrumentation geometry consists in a source of electrons or "electron gun" operating at 10-30 kV, a "column" comprising a set of lenses to focus the beam on the specimen, beam deflection coils, and electron detectors (Figure 2.9).

Electrons emitted by the electron gun are focused by a series of electromagnetic lenses onto the specimen located on a mobile stage. Once electrons impact the sample they interact with its atomic structure and penetrate up to a certain depth called "interaction volume". The radiation produced during the interaction comprises i) back-scattered electrons (BSE), ii) secondary electrons (SE), and iii) auger electrons, visible light, and X-rays as additional components. Among these types of emissions, back-scattered and secondary electrons are of major interest for the scope of this thesis. BSE radiation is generated when an incident electron is elastically scattered by the atoms in the sample. The number of back-scattered electrons depends on the charge and it is directly correlated with the atomic number of the material. As a consequence, heavy elements will appear brighter in the resulting image. The BSE signal gives information about the sample topography and local atomic composition. The SE signal occurs when the striking electrons transfer part of their energy to the specimen atoms, inducing re-emission of secondary electrons. Small variations in the sample topography will modify the amount of emitted secondary electrons, directly correlated with sample's topographic features. The interaction between the incident electrons and the target atoms also produced emission of X-ray photons that can be detected by energy dispersive (EDS) or wavelength dispersive (WDS) spectroscopies. Specifically, emission of characteristic X-rays occurs since primary electrons excite the electrons of the target atom

inducing quantum transitions firstly to a higher energy level and then back to a lower energy shell. A detailed explanation of the methodology can be found elsewhere (e.g., Reed, 2005).

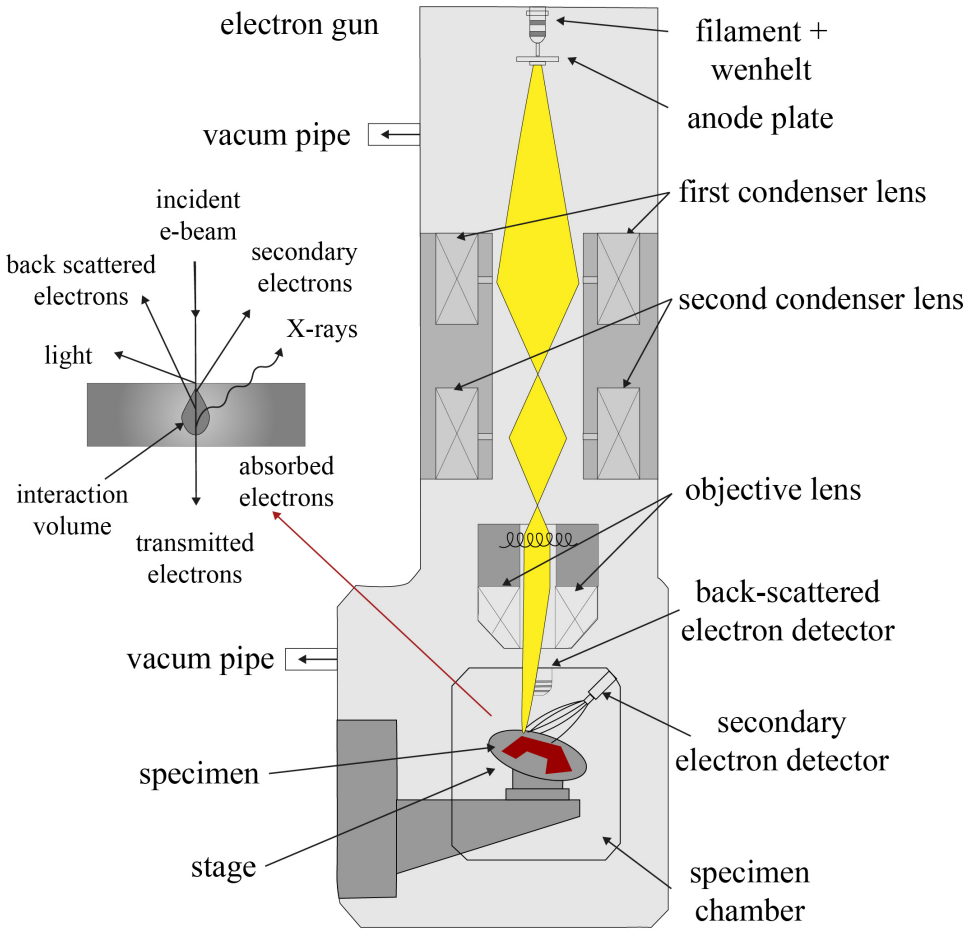

Figure 2.9: Schematic drawing of a typical scanning electron microscope (modified after Sutton et al., 2007).

In this thesis we performed high resolution imaging and EDS quantitative chemical analyses to observed textural evidence of redox reactions (Chapter 4) and determine the chemical composition of coexisting phases. Data evaluation was performed using the Aztec software (Oxford instrument). Details of the individual measurements and imaging can be found in the following chapters.

2.2.2 Electron microprobe microanalysis

Quantitative chemical analyses and images of recovered multi anvil run products were performed by means of the electron microprobe microanalysis (EMPA) using the Jeol JXA 8200 instrument installed at BGI.

Accelerated electrons created by a tungsten filament impinge the specimen after being focused and collimated. This interaction produces different signals, such as BSE, SE, and characteristic X-rays, similarly to the SEM (see section 2.2.1). A typical electron microprobe is commonly equipped with four or five wavelengths dispersive (WD) spectrometers and one energy dispersive (ED) spectrometer used for quantitative and qualitative analyses, respectively. Every single WD spectrometer consists of a crystal with a known interplanar spacing (*d*) that enables detecting photons of a specific wavelength. Hence, the emission of characteristic X-rays with various wavelengths require the use of different crystals, e.g., LiF (lithium fluoride), PET (pentaerythritol) or TAP (thallium acid phthalate) (Reed, 2005). Accurate quantitative analyses (± 1% of accuracy with a detection limit in the order of ppm by weight) are attained comparing the intensities of characteristic X-rays scattered by the sample with those emitted by standards with known composition. A full description of the EMPA rudimental principle and instrumentation is reported in Reed (2005).

In the present thesis, we performed EMPA measurements on a sample synthesized with the multi anvil apparatus (see Chapter 3). Prior to the analysis, the recovered MA assembly was placed in epoxy, polished to expose the capsule material, and carbon coated to a thickness of ~8-12 nm in order to avoid electrical charging of the surface. Employed standard materials were synthetic crystals and metals, i.e., Mg-enstatite, Fe-Fe metal, Ir-Ir metal. After data acquisition, raw intensity values were corrected using ZAF (atomic number-absorption-fluorescence) and phi-rho-Z (similar algorithm of the ZAF) matrix correction routines. A complete description of EMPA measurements is given in Chapter 3.

2.2.3 Mössbauer spectroscopy

Mössbauer spectroscopy (MS) is a versatile technique that provides valuable information in many areas of science allowing to probe structural, bonding, magnetic, and dynamical properties of a solid substance. In the present work, MS was used for determining the Fe valence state in natural inclusions and synthetic ferropericlase samples discussed in Chapters 3 and 4.

The principle of Mössbauer spectroscopy is based on the Mössbauer effect, recognized for the first time by Rudolf Mössbauer in 1958. The discovery awarded the Nobel Prize in 1961, concerns the recoil-free emission and absorption of gamma radiations by nuclei in a solid matrix (Mössbauer, 1958). The foundations of Mössbauer methodology are described in detail in Bancroft (1973) and Gütlich et al. (1978) and reviewed in (McCammon et al., 1991; 2000; Dyar et al., 2006).

A nucleus confined within a solid emits and absorbs gamma rays without energy loss, which would otherwise occur due to the recoil of an isolated nucleus. In a solid, the recoil momentum is transferred to the surrounding crystal lattice resulting in a strong resonance at the same energy level. The absorption/emission energy range is restricted to the full-width half maximum (FWHM) of the nuclear transition, as dictated by the Heisenberg uncertainty principle, and it is related to the lifetime of the nuclear excited state. Since the recoilless event depends on the energy of the nuclear gamma ray, the Mössbauer effect is limited to specific isotopes with a low-lying excited state.

Over one hundred isotopes exhibit Mössbauer nuclear transitions, although inappropriate nuclear properties limit the number of commonly used nuclei (e.g., Gibb, 2013). The ^{57}Fe isotope at the nuclear transition at 14.4 keV is generally favored with respect to other candidates (i.e., ^{119}Sn, ^{61}Ni, ^{195}Pt, ^{197}Au, etc.) due to its advantageous properties for Mössbauer spectroscopy (e.g., the half-life of the parent isotope is 270 days, the natural linewidth is small ~0.097 mm/s, etc.), and its importance for technological applications and geological studies. As a result, the majority of scientific researches involve ^{57}Fe for the investigation of Fe-bearing systems.

The most common configuration for Mössbauer spectroscopy comprises a radioactive source containing an isotope in an excited state (parent isotope) and an absorber (experimental sample) which includes the same Mössbauer isotope in its ground state. In the case of ^{57}Fe, the radioactive source is ^{57}Co which decays primarily to the 136.6 keV energy level with a half-life of 270 days and then undergoes to the electron capture transition (β decay) giving ^{57}Fe* in a metastable state. With a 9 % probability, deexcitation leads to the direct nuclear transition to the

ground state, while 91 % of the cases produces an intermediate decay to the 14.4 keV energy level and then to the ground state with the emission of gamma rays (11% of the total emitted radiation) with a life time of ~141 ns (Figure 2.10). The ^{57}Co radioactive parent is commonly included in a Rh matrix to prevent ^{57}Co magnetic interactions.

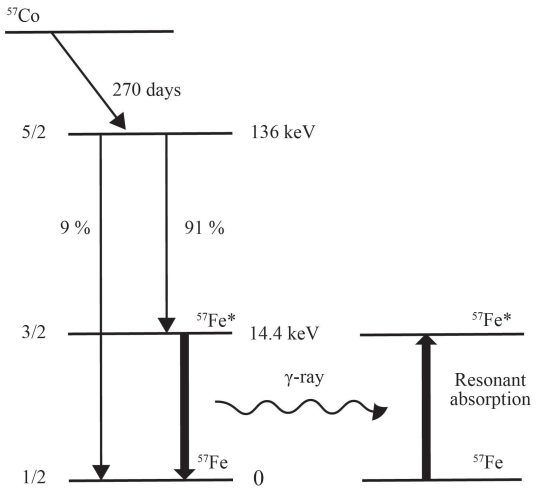

Figure 2.10: Nuclear decay scheme of ^{57}Co → ^{57}Fe showing the transition giving the 14.4 keV gamma ray modified after Gütlich et al. (1978).

A conventional Mössbauer apparatus has a simple geometry made of a source (e.g., conventional source (1 cm diameter), point source (500-µm diameter), or synchrotron light source (~10-µm diameter)), an absorber, and a detector (Figure 2.11). The radioactive source is mounted on an oscillating drive system that moves the source back and forth relative to the absorber (Doppler effect) and permits modulating the photon energies in a narrow interval, similar to the initial emitted energy. A detector behind the absorber receives the transmitted γ-rays.

An important aspect of Mössbauer spectroscopy relates to the interaction between the nuclear energy levels and the surrounding electrons which lead to the so-called hyperfine interactions, relevant for analytical purposes. Three types of hyperfine interactions are typically observed: isomer shift or chemical shift or center shift (IS or δ), quadrupole splitting (QS or ΔE_Q), and hyperfine splitting or magnetic hyperfine field (B_{hf}) (Figure 2.12). The resulting parameters are the products of fixed nuclear and variable electronic properties (Dyar et al., 2006).

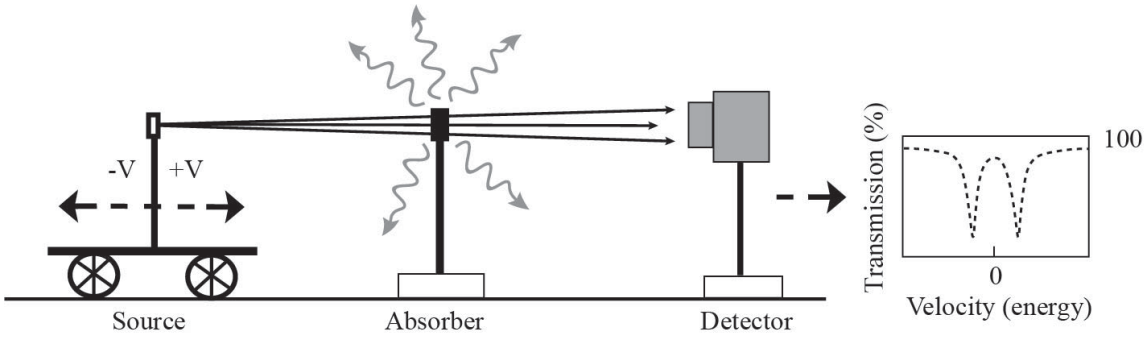

Figure 2.11: Schematic drawn of a Mössbauer spectrometer based on Gütlich et al. (1978) and McCammon & Beran (2004). The source is moved relative to the absorber with different velocities that shift the energy of the emitted gamma rays according to the Doppler effect. Emitted gamma rays pass through the absorber unperturbed and reach the detector or are deviated in different directions from the detector.

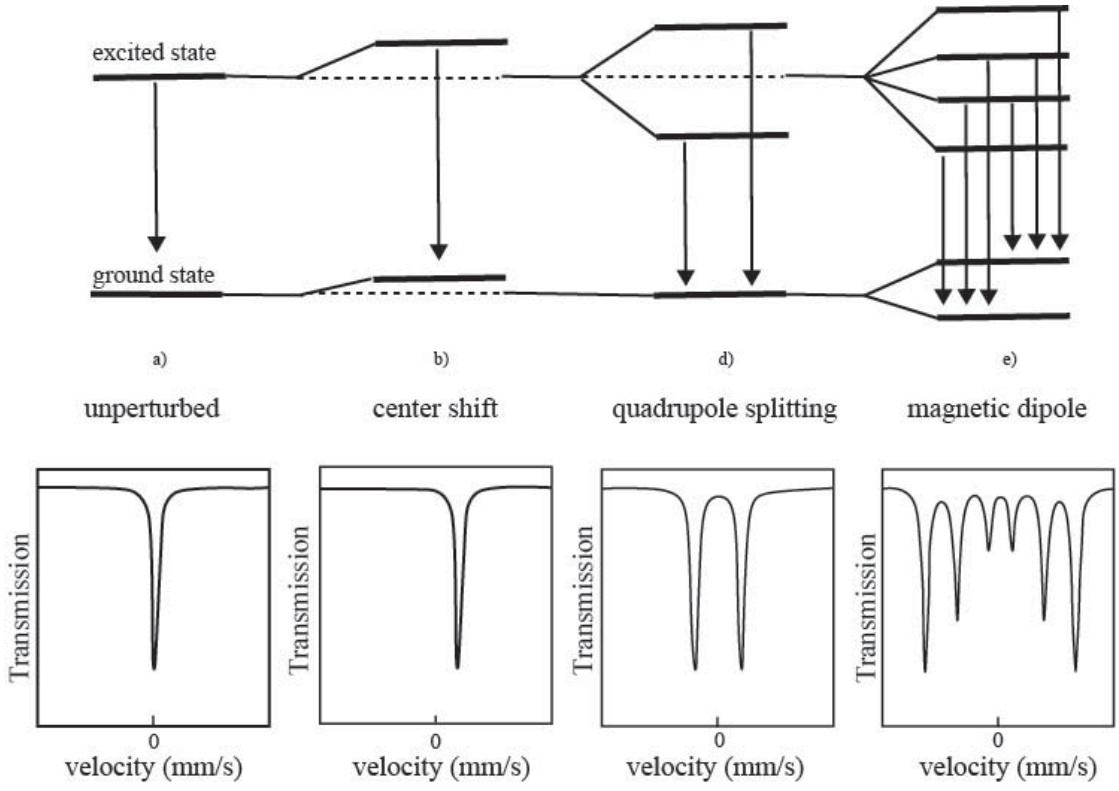

Figure 2.12: Top: Nuclear hyperfine interactions scheme for ^{57}Fe (modified after McCammon, 2000), showing the nuclear energy levels for (**a**) an unperturbed nucleus; (**b**) a change in center shift; (**c**) with quadrupole splitting; and (**d**) with magnetic dipole interaction. **Bottom**: At each hyperfine interaction is associated the resulting Mössbauer spectrum.

The isomer shift defines the relative changes in the resonance energy of a nucleus caused by the transition of its *s*-orbital electron due to a variation in the oxidation state. This results in the transmission spectrum offset from the zero-velocity position. The IS parameter is generally reported relative to α-Fe standard absorber, and reveals important information such as valence, spin and coordination state of the examined atom in the sample.

The quadrupole splitting relates to the splitting of the nucleus spin state into a different state with a different energy level. This phenomenon is similar to the splitting of *3d* electronic orbitals that occurs in transition metals due to the crystal field splitting, and is caused by the asymmetric electronic charge distribution of an atom that produces an electric field gradient around the nucleus. For ^{57}Fe nucleus the excited state is split in two sublevels which appear as two distinct absorption lines (doublet) in a Mössbauer spectrum. In a doublet QS is defined as the difference between the two transition energies or rather the separation between the two component peaks. Hyperfine magnetic splitting refers to the splitting of the nucleus spin state into sublevels as a consequence of a magnetic field. The excited state of ^{57}Fe split into four energy levels for a total of six possible transitions that form six absorption line peaks in the Mössbauer spectrum. This parameter gives information about the magnetic structure of the investigated material.

For the purposes of this study, the collected spectra were fitted using a full transmission integral with a normalized pseudo-Voigt and pseudo-Voigt-squared source line-shape for MS and SMS, respectively, using the MossA software package (Prescher et al., 2012).

2.2.4 X-ray diffraction

X-ray diffraction (XRD) is a non-destructive method that allows investigating the atomic structure of solid matter and identifying coexisting phases in rock assemblages or in organic/inorganic compounds. In high-pressure mineralogy, XRD is a fundamental methodology for determining the unit cell dimensions (molar volume) and the compressibility (bulk modulus) of mineral phases, essential properties for interpreting seismic data of Earth's interior and developing thermodynamic models.

By definition, XRD is described as the coherent elastic scattering of X-ray photons (with a given wavelength λ) by the electrons of an atom arranged in a periodic crystal lattice. When atoms are organized with characteristic periodicities in crystallographic planes, incident monochromatic X-rays will interfere constructively or destructively once scattered from a crystal. Only in some specific directions re-emitted X-rays will be in phase reinforcing one another, i.e., in constructive interference, producing a cooperative scattering effect known as diffraction. Specifically, in the case of an X-ray beam striking a crystal, the resulting diffraction effect derives from an infinite number of parallel and equispaced planes where each individual "reflection" adds constructively with one another. The conditions for constructive interference are described by Bragg's law (Bragg, 1914), i.e.,

$$2d_{hkl}\sin\theta = n\lambda \tag{2.2}$$

where d is the interplanar spacing of successive families of hkl lattice planes, θ is the angle of incident and reflection of the X-ray beam from the given atomic plane, λ is the wavelength, and n is any integer number (1,2,3…, n) or reflection order (Figure 2.13). According to Bragg's law, diffracted radiations can only appear if constructive interference conditions are fulfilled, i.e., when the difference in the travel path between the two scattered waves ($2d_{hkl}\sin\theta$) is equal to an integer multiple n of the wavelength λ.

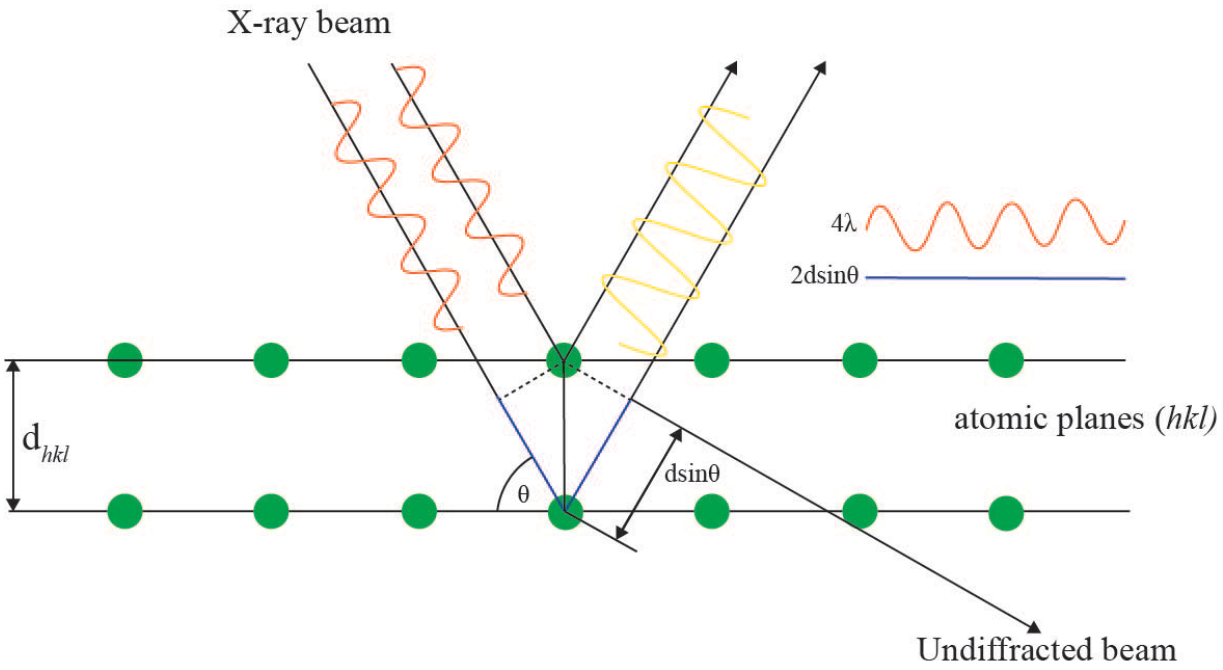

Figure 2.13: Geometry of X-ray diffraction (Bragg's law). Green circles represent the atoms while arrows denote the travel path of the X-rays. Two X-ray beams with same λ and phase bombard a crystalline solid and are reflected by two different atoms within it. The lower beam traverses an extra length (blue) of 2dsinθ. Constructive interference (yellow) is accomplished when this length is equal to an integer multiple of the wavelength of the radiation.

A typical diffractometer generally consists of a radiation source (X-ray tube) of a certain wavelength, a sequence of slits to adjust the beam shape, a sample holder where the specimen is located, and a counter detector that recorded the diffracted waves. Various geometries were developed over the last century for different scopes of the analyses and mainly distinguished for powder and single-crystal X-ray diffraction which lead to different crystallographic information.

Powder XRD is commonly used for unit cell parameter determination and phase identification while single crystal XRD is primarily employed for structure solution and refinement. A clear differentiation is in the respective diffraction patterns: a typical powder pattern is characterized by spherical concentric *hkl* Debye rings deriving from the scattering of countless grains randomly orientated, while a single-crystal pattern is made of discrete spots (Bragg reflections) originated by the scattering of atoms in a specific orientation that replicate the symmetry of the investigated material. Further insights can be found for example in Tilley (2006) and Chatterjee (2008).

In this thesis powder X-ray diffraction measurements in house and at synchrotron facilities were performed to identify coexisting phases in polycrystalline samples and to investigate the

compressibility behaviour of selected compounds. Details of the specific measurements are given in the following chapters.

Phase identification of recovered multi anvil run products was performed using the micro-focus X-ray diffractometer installed at BGI. The Bruker D8 DISCOVER diffractometer is equipped with the VÅNTEC500 two-dimensional solid-state detector and micro-focus Co-K_α source radiation (IμS) operating at 40 kV and 500 μA. During data acquisition, the X-ray beam was focused to a minimum of a 50 μm spot diameter using an IFG polycapillary X-ray mini-lens. The existing 2-dimentional large-area detector allows probing a large reciprocal space and high diffraction angles. XRD patterns were collected for about 2400 - 6000 s in a 2θ range of 25°- 85°. Each diffraction pattern was integrated and indexed using the DIFFRAC.EVA software. Lattice parameters, background and peak shapes were refined using the Le Bail method employing JANA software package (Prescher & Prakapenka, 2015).

2.2.5 Focused Ion Beam: TEM foils preparation

In this thesis, we employed the Focus Ion Beam (FIB) microscope installed at BGI (FEI, Scios DualBeam) to prepare recovered samples from high pressure experiments for nanoscale analyses with the transmission electron microscope (TEM). The instrumentation of the device is strongly comparable to that of a SEM (section 2.2.1) except that the beam directed towards the sample is an ion beam rather than an electron beam. The advanced technology of the dual beam (FIB + SEM) system (Figure 2.14) available at BGI allows ultra-high-resolution imaging, material removal and deposition from nanometers to micrometers length scales. The basic principle behind the FIB milling technique is the sputtering of the target material with Ga^+ ions focused on the specimen through electromagnetic lenses at ~20-30 kV voltage and at ~1.6 nA probe current. A detailed explanation of the physical process is given elsewhere (e.g., Overwijk, 1993; Heaney et al., 2001; Wirth, 2004; Miyajima et al., 2010).

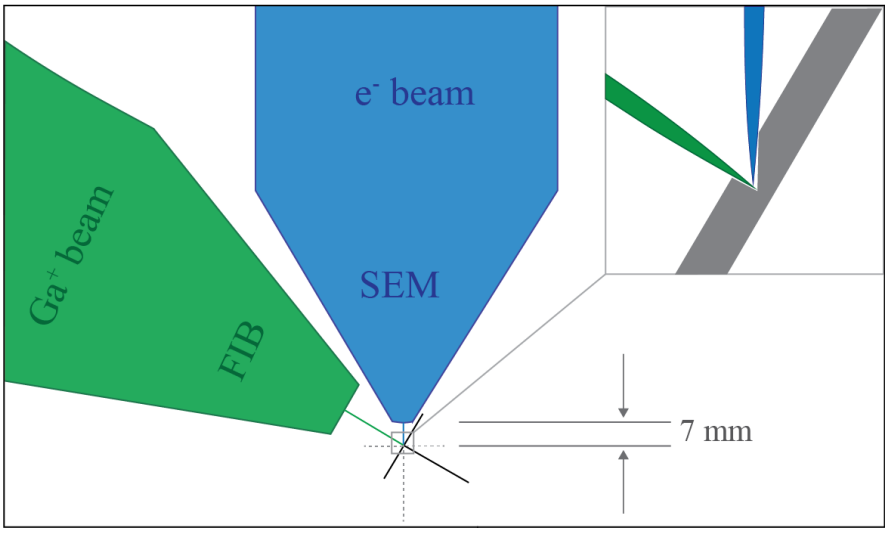

Figure 2.14: Schematic drawing of the dual beam FIB-SEM instrument (inspired by http://emc.missouri.edu/fib-sem/).

In the present thesis, a total of four FIB thin foils with dimensions of 20 µm × 5 µm × 100 nm were extracted from recovered samples synthesized using either the DAC or the multi anvil apparatus (see Chapters 3 and 4). The same extraction sequence was performed to retrieve all FIB lamellae, although extra caution was taken for the DAC sample due to the brittleness of the material. Carbon coating of the samples (to a thickness of ~ 17 nm) was necessary to prevent electrical charging of the specimen surface under the electron beam. Each sample was mounted on apposite sample holders and fixed to the stage using manual knobs. Once vacuum was created, the stage was moved to a working distance of 7 mm. Focus, stigmation, and brightness were manually adjusted. After selection of the interested area, a Pt layer of ~ 20-µm length and 2-µm height was deposited by a gas injection system (GIS), setting an acceleration voltage of ~2 kV and a probe current of 0.8 nA. This Pt layer served as an indicator of the topography of the chosen region and as a protective coating for the foil during the milling procedure. Then, opposite trenches were excavated from both sides of the Pt strip to a depth of ~5 µm using a step-cut geometry (i.e., "regular cross section") with an ion beam current of ~30 nA. The "cleaning-cross section procedure" was also performed for thinning down the sample at ~10 pA ion beam current. Next, the sample was rotated to 7° (plan view) for the undercutting procedure (U-cut) which is attained by ion beam perforation of the specimen along the sides and bottom edges (Figure 2.15a). The lift out process was performed moving back the stage to the horizontal plane directing the needle micromanipulator towards the excavation site and fixing it to the foil by Pt deposition (Figure

2.15b). The removed sample foil was then transferred to a 3 mm membrane of a TEM copper grid using Pt stripes (Figure 2.15c) and polished by Ga^+ beam to a final thickness of 100 nm (Figure 2.15d) at 30 kV and ~0.10 nA. Finally, we set operating conditions at 5 kV and 80 pA to remove the Ga contamination ("ion shower"). At last, the sample was removed from the FIB machine and moved to the Transmission Electron Microscope device for nanoscale analyses (see next paragraph). Additional details of individual sample cutting, imaging, and analyses are given in the following chapters.

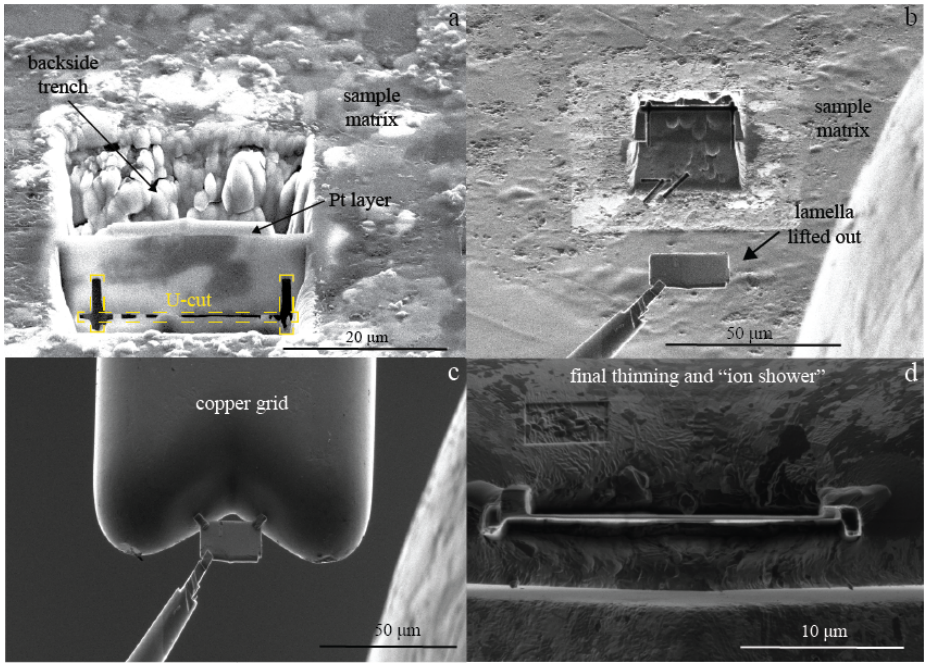

Figure 2.15: SE images displaying a typical FIB lamella cutting procedure performed on H2981 recovered MA sample; **a)** sample stage tilted at 57° with visible backside trench and partial U-cut on the lamella cross-section; **b)** sample foil transfer procedure using a needle micromanipulator; **c)** FIB lamella fixed on the TEM copper grid; **d)** final thinning by Ga^+ beam at 0.10 nA and "ion shower".

2.2.6 Transmission Electron Microscopy

Nanocharacterization of the extracted FIB films was performed using the Transmission Electron Microscope (TEM) FEI Titan G2 80-200 S/TEM Gatan Quantum SE, installed at BGI.

The TEM technology provides morphologic, chemical, crystallographic, and spectroscopic information of nanomaterials with atomic spatial resolution. The basic instrumentation is characterized by an electron gun (source radiation), an illumination stage, objective lens, an electron transparent sample surrounded by its magnetic field, a magnification and projection system equipped with three or more lenses, and detectors (Figure 2.16). In a TEM device, a monochromatic electron beam is accelerated and focused under vacuum on a wafer sample at very high energy ~200-300 kV. The interaction between the incident beam and the specimen can be used for different purposes, such as nanoscale imaging, determination of chemical composition, oxidation state, and crystal structure of the investigated matter.

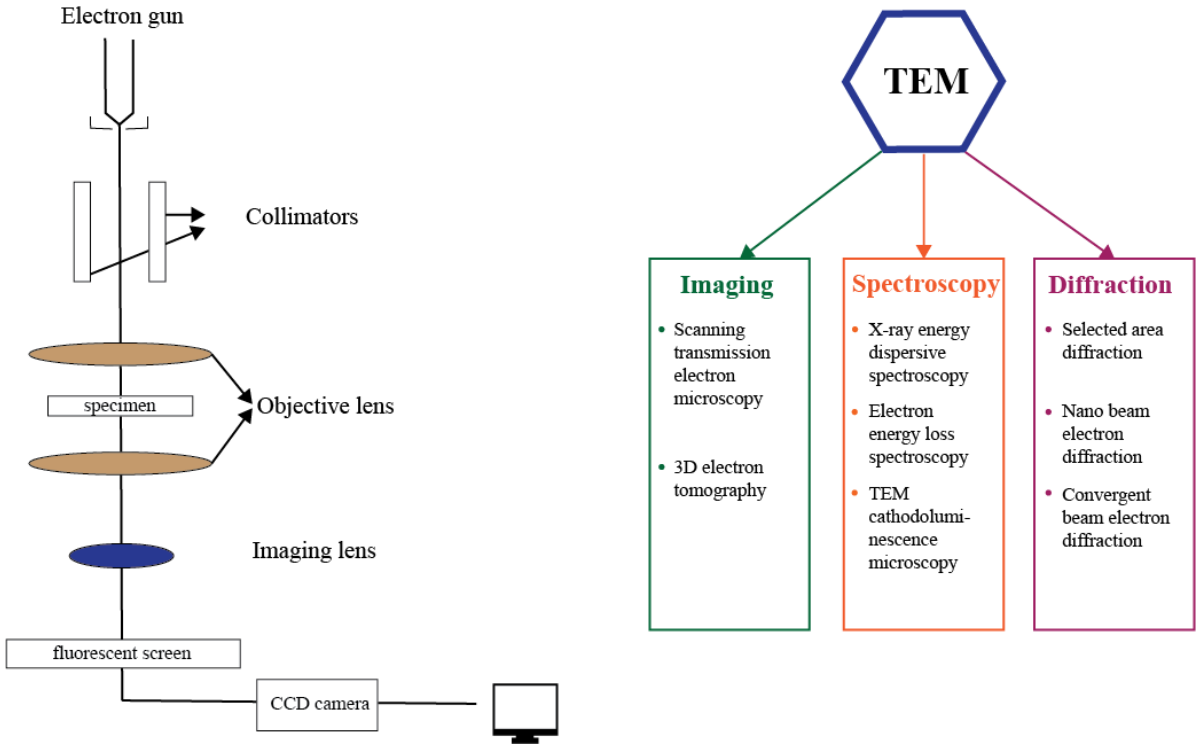

Figure 2.16: Transmission electron microscope working principle (modified after Kumar et al., 2019)

When transmitted electrons are elastically scattered by the specimen according to Bragg's law (see section 2.2.4) selected area electron diffraction (SAED) micrographs can be obtained. The advantage of this method is the possibility to "select" and distinguish among coexisting phases in a polycrystalline sample and obtain single crystal electron diffraction patterns. The electron beam-sample interaction produces also emission of characteristic X-rays which can be analyzed by EDS, yielding information of the sample's chemical composition (see section 2.2.1). A detailed description of the physics process behind the technique and its applications can be found in Williams & Carter (1996). In this thesis, we performed high-resolution TEM (HR-TEM) imaging of synthetic ferropericlase samples (~100 nm thickness) equilibrated with metal alloys (Chapter 3), diamonds and carbonates (Chapter 4), employing Bright Field (BF), Dark field (DF), and High-Angle Annular Dark-Field (HAADF) detectors. Element maps of the selected samples were also acquired to examine element partitioning between phases (an example is given in Figure 2.17). For all measurements, major element standards were calibrated using a natural pyrope-almandine garnet (Pyc-garnet, Prp73Alm17Grs11 in Fujino et al., 1998; Miyajima et al., 1999; 2004) while minor elements were quantified with theoretical *k*-factors (Z-number correction).

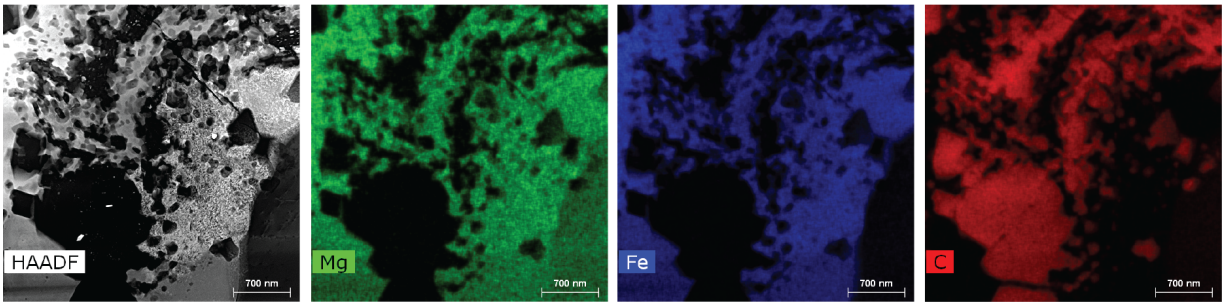

Figure 2.17: Elemental maps of H2981 sample (details are given in Chapter 4). The High-Angle Annular Dark-Field image shows diamonds (black) in ferropericlase matrix (grey).

Experimental samples discussed in Chapter 4 were also studied using SAED to explore the potential presence of impurities exsolution in the ferropericlase matrix. A comprehensive description of these measurements and experimental results are reported in the related chapter.

Interaction between incident electrons and the solid matter part of the re-emitted radiation is inelastically scattered, losing part of its energy. The electron energy-loss spectroscopy (EELS) method detects the change in kinetic energy of inelastically scattered electrons from a solid specimen providing structural and chemical information of the investigated matter, with a spatial

resolution down to the atomic level and an energy resolution between 0.1 and 1 eV (Egerton, 2009). The conventional instrumentation consists of a magnetic prism, placed below the TEM image-view chamber, which generates a magnetic field wherein electrons travel in a circular path and are deflected at ~90°. By rotating the TEM screen in vertical position electrons can access the spectrometer and be recorded by the detector. Other configurations are also possible, and incorporate the spectrometer inside the TEM column, which includes a "omega filter" made of magnetic prisms. Further detail about the instrumentation geometry and the physics process behind EELS techniques are given elsewhere (e.g., Egerton, 2009; Hofer et al., 2016).

A typical "low-loss" EELS spectrum region (< 50 eV) shows a first intense peak at ~0 eV ("zero-loss peak") representing the elastically scattered electrons from the target atomic nuclei as well as the non-scattered (transmitted) electrons. Additional low-loss spectral features arise from inelastic scattering by conduction and valence electrons (Figure 2.18a). The spectrum region (energy > 50 eV) defined as "core-loss spectrum" represents the inelastic scattering of inner shell-electrons of iron atoms. The characteristic spectral features are named "ionization edges" due to their typical shape (rapid rise followed by a gradual fall) and are equivalent to a XAS absorption edge occurring from the same process. Additional ionization edges appear at higher energy-loss, namely *K*-edge and $L_{2,3}$ edges exhibiting a more complex shape (Figure 2.18b). The latter includes the white lines (sharp excitations at the onset of the absorption edge) crucial to retrieve information related to the Fe oxidation state (e.g., Egerton, 2009; Hofer et al., 2016).

In this study, we collect EELS spectra at the Fe $L_{2,3}$ edges to investigate the Fe valence state of ferropericlase grains as a function of the redox state. The sample was recovered from a DAC experiment and prepared using the FIB (see section 3.2.6). Quantification of the ferric to total iron ratio was determined according to the procedure described by Van Aken & Liebscher (2002). This approach requires the integration of the energy windows of the L_2 and L_3 Fe ionization edges whose intensity ratio yields $Fe^{3+}/\Sigma Fe$. A detailed description of EELS spectra acquisition and data processing is given in Chapter 3.

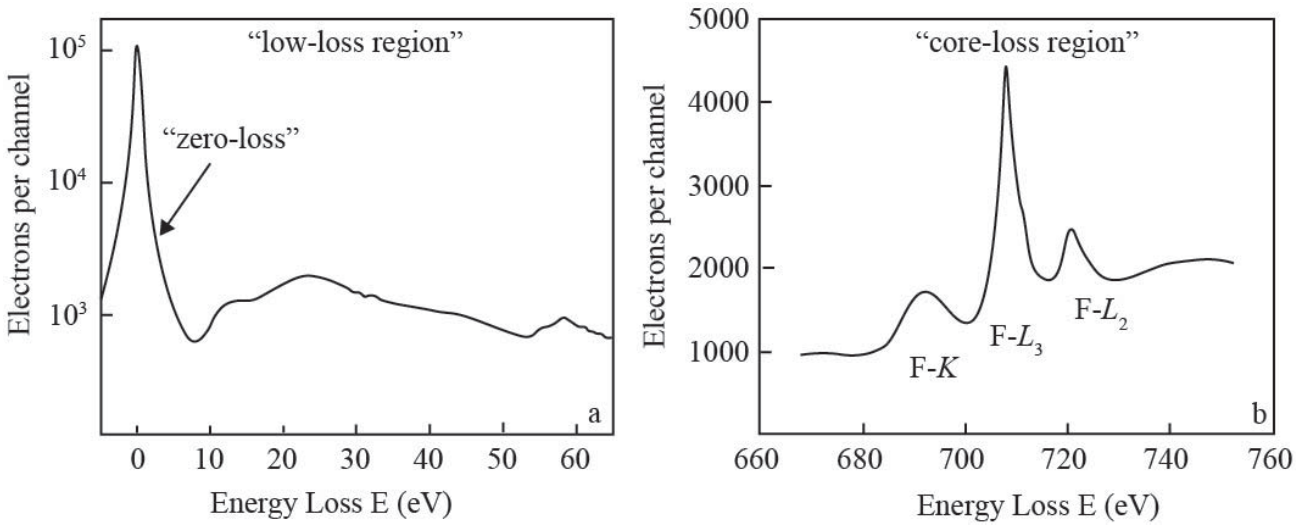

Figure 2.18: Example of an energy-loss spectrum of an iron fluoride film; **a)** low-loss region with a logarithmic intensity scale and **b)** part of the core-loss region, with linear vertical scale from Egerton (2009).

2.3 SYNCHROTRON-BASED SPECTROSCOPIES

In this section synchrotron-based spectroscopic techniques employed in this thesis are briefly overviewed. The advantage of using a synchrotron radiation source mainly resides on the high spatial resolution (essential for small volume samples), the high intensity of the beam over a broad energy range, the high degree of collimation, and the polarized character of the light source, which are not accessible with conventional X-ray tubes, and therefore allows probing structural and material properties in detail. The following paragraphs describe the fundamental principles and general spectroscopic background of SMS, XANES, IXS, and powder XRD.

2.3.1 Synchrotron Mössbauer Source Spectroscopy

Mössbauer source radiation can be generated from particle accelerators such as synchrotron facilities. The ^{57}Fe Synchrotron Mössbauer Source (SMS) has several advantages compared to conventional and point source Mössbauer spectroscopy (paragraph 2.2.3), including an optimized flux (a high signal/noise ratio in the spectra) due to the high brilliance of the synchrotron light, a shorter acquisition time to get a spectrum with sufficient statistics (minutes-hours instead of days), and a higher spatial resolution as a result of the smaller beam size (extreme focusing at $< 10 \times 10$ μm^2) which allows investigating heterogeneous samples in detail.

In this thesis, we conducted i) SMS experiments in DAC at different pressures and room temperature before and after laser heating (Chapter 3), ii) SMS measurements of synthetic run products recovered from multi anvil experiments and natural inclusions in sub-lithospheric diamonds at room conditions (Chapter 4). SMS data were collected at the ID18 Nuclear Resonance beamline (Rüffer & Chumakov, 1996) (Figure 2.19) at the European Synchrotron Radiation Facility (ESRF), in Grenoble (France).

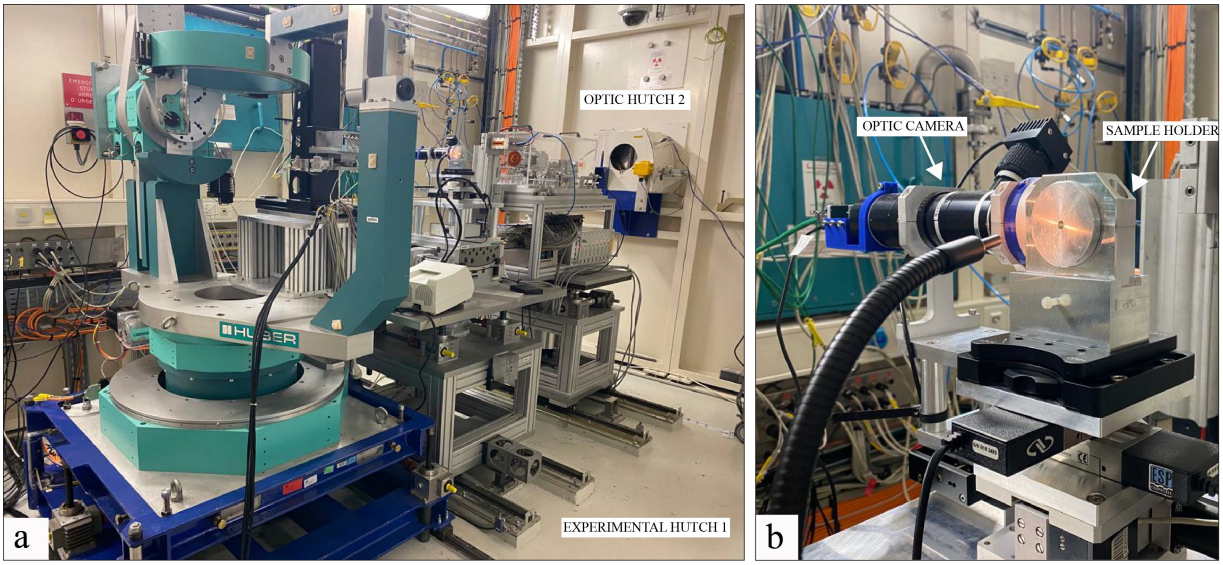

Figure 2.19: **a)** The experimental hutch of the Nuclear Resonance Beamline at ESRF after the most recent upgrade (September 2021); **b)** magnification of the newly installed optic camera station to facilitate the beam-sample alignment procedure.

The SMS technique operates using on iron borate $^{57}FeBO_3$ single crystal monochromator enriched with ^{57}Fe (Kotrbová et al., 1985) to produce resonant radiation with neV energy resolution at 14.4 keV.

The optical scheme for SMS high pressure experiments is shown in Figure 2.20 (Potapkin et al., 2012). The synchrotron beam passes through an undulator and then a high-heat load monochromator (HHLM) that prevent the formation of any temperature gradient on the iron-borate crystal. The uniqueness of the iron-borate crystal lies in allowing pure nuclear diffraction at specific Bragg reflections while electronic diffraction is instead denied. The $^{57}FeBO_3$ crystal is heated close to its Néel temperature of 348.75 K by a furnace and placed in an external magnetic field to reach a single-line nuclear resonance radiation within an energy bandwidth of ~20 neV by the collapse of the crystal hyperfine magnetic structure. To attain the resonance conditions and generate the Mössbauer effect by Doppler shift, the iron borate crystal is moved in the plane of the $^{57}FeBO_3$ surface by an oscillating drive. Additional details of the physics of the process are described in Smirnov et al. (2011). The SMS is followed by a pair of Kirkpatrick-Baez mirrors (KBM) which allow extreme focusing of the synchrotron beam on the sample and by an avalanche photo diode detector that records the transmitted radiation.

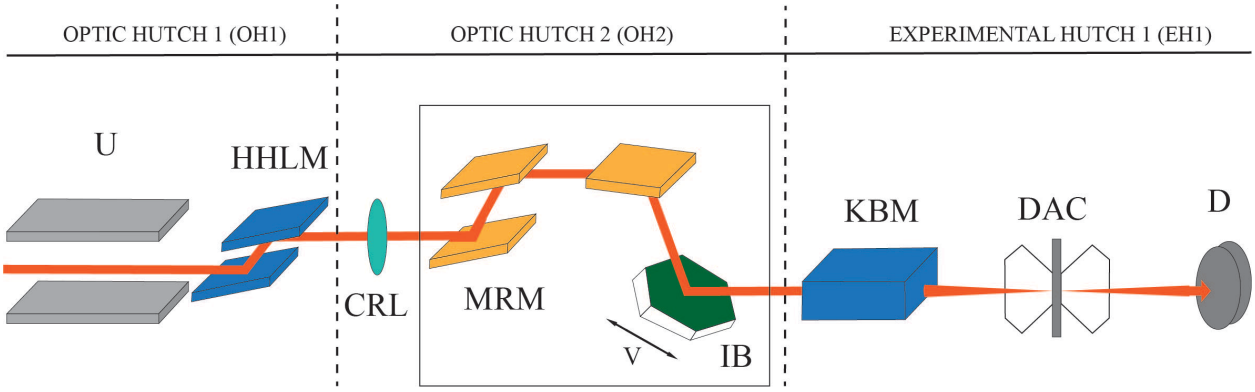

Figure 2.20: Optical scheme for a high-pressure experiment with the DAC using the Synchrotron Mössbauer Source at the ID18 beamline (ESRF) modified after Potapkin et al. (2012). U: undulator; HHLM: high-heat-load monochromator; CRL: compound refractive lens; MRM: medium-resolution monochromator; IB: iron borate ($^{57}FeBO_3$) crystal; KBM: Kirkpatrick-Baez mirrors; DAC: diamond anvil cell; D: avalanche photodiode detector.

During the SMS experiments discussed in this thesis the linewidth of the source was controlled before and after each spectrum acquisition using $K_2Mg^{57}Fe(CN)_6$, consisting of a single line Mössbauer spectrum. The velocity scale was calibrated using 25 μm thick α-Fe. The fitting of the data was performed using a full transmission integral pseudo-Voigt-squared source line-shape with a 1st order polynomial function (MossA software package, (Prescher et al., 2012).

2.3.2 Synchrotron X-ray diffraction

In this thesis, we performed powder X-ray diffraction experiments at ID15b (30 keV, $\lambda \sim 0.411$ Å, ~10 ×10 μm^2 beam, MAR555 flat-panel detector) and ID27 beamlines at the ESRF (Grenoble, France) and at the extreme conditions beamline P02.2 at DESY-PETRA III (42 keV, $\lambda \sim 0.29$ Å, ~2 × 2 μm^2 beam, PerkinElmer XRD 1621 flat-panel detector) (Hamburg, Germany) synchrotron facilities. The fine collimation and the high brilliance of the synchrotron light sources allowed precise focusing (<10 × 10 μm^2) of the beam, essential for phase equilibria studies in DAC (Chapter 3). Equations of state of different compounds, i.e., $(Mg_{0.75}Fe_{0.25})O$, $Fe_{0.4}Ir_{0.6}$, and $Fe_{0.67}Ni_{0.06}Si_{0.27}$ alloys, were collected at high pressure and room temperature conditions. A detailed description of individual measurements is given in the following chapters. Although the instrumentation geometry of each beamline has a specific configuration and operation routine, the collection procedure and the main structural components can be considered to be the same.

Figure 2.21 shows the ID15b experimental setup as an example for a typical X-ray diffraction beamline for high-pressure research. The ID15b beamline (Merlini & Hanfland, 2013) operates at 30 keV with a wavelength of approximately 0.411 Å. A set of horizontal and vertical slits define the shape of the primary beam which is further focused by a spherical mirror and a Si(111) Laue monochromator at ~10 × 10 μm^2 spot size. A pinhole reduces the tails of the beam before it passes through the sample. The sample holder is positioned on a translation stage equipped with a vertical rotational axis that allows acquisition of the data upon DAC rotation (ω-scan). A large area MAR-555 flat panel detector collects the diffracted reflections. The presence of an optic camera and a diode (counter) facilitates the beam-sample alignment procedure before data acquisition. A schematic drawing of the beamline is shown in Figure 2.21-bottom.

Before the data collection, it is important to measure a standard sample for creating a calibration file, where information like the X-ray wavelength, the x-y position of the primary beam, the pixel size of the detector, the sample to detector distance, corrections for the detector tilting, and the beam polarization, are stored. To this end, for each of our measurements, we acquired the powder diffraction of CeO_2 reference material.

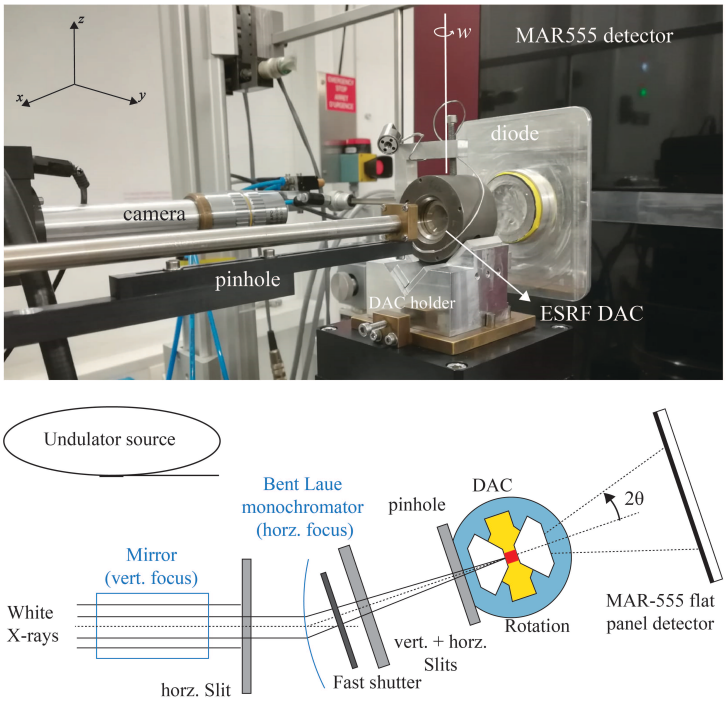

Figure 2.21: **Top**: High-pressure diffraction beamline (ID15b) at ESRF. **Bottom**: Schematic drawing of the experimental set up of ID15b beamline (modified after Merlini & Hanfland, 2013).

In the present thesis, we collected powder X-ray diffraction data either upon continuous rotation of the DAC from -20° to +20° ω (wide-scan mode) or without rotation on the still images with a few seconds beam exposure at different pressures. For the measurements in wide-scan mode, particularly suitable are the BX90 DACs equipped with Bohler-Almax diamond anvils which provide a 90° opening angle. To verify the homogeneity of the sample after laser heating (Chapter 3) we also performed grids of a few micrometers (both in still and wide scan mode) mapping with the beam the recrystallized multiphase material from the core to the rim.

Powder XRD data integration and phase identification were performed using Dioptas software (Prescher & Prakapenka, 2015). Integrated diffraction patterns were then processed either by Rietveld refinement or with the Le Bail method using Jana software package (Petrícek et al., 2014). The Rietveld algorithm minimizes the weighted sum of squared differences between the observed and calculated intensity values from a structural model (Rietveld, 1969). In contrast, the Le Bail method refines only the peak shapes and positions without taking into account the reflection intensities. The latter are treated as arbitrary unknowns since the structural factor and structural parameters are not considered. In summary, the main difference between the two approaches is the possibility to refine the atomic positions and obtain structural information with

the Rietveld method besides the improvement of the unit cell parameters and the peak shapes. In both cases the background was fit manually using the Chebyshev polynomial function. To estimate the reliability of the fit we evaluated the *R*-factors and the chi-squared (χ^2) parameters. The weighted profile *R*-factor (R_{wp} weighted residual of a structure factor) relates to the quantity that is minimized in the least-squared refinement. For a trustworthy dataset the refined structure should give a R_{wp} less than 0.05. Further details can be found in Massa (2004).

2.3.3 X-ray absorption near edge structure

X-ray absorption near edge structure (XANES) spectroscopy is a synchrotron-based technique that provides insights into the electronic, structural, and magnetic properties of the investigated material. The general theory consists of the ejection of a core-level electron (K, L, or M shell) of an atom (absorber) by an X-ray which promotes the absorption of the incident photon through the photoelectric effect (Figure 2.22-left). Therefore, the atom is left in an excited state with an empty electronic level defined as a "core hole". This phenomenon is likely to occur when the photon energy is equal or higher than the binding energy of the core level. The "escaped" photoelectron emits characteristic radiation and collides with the adjacent atoms, one of which becomes a "scattering center", leading to a cascade of scattering events and multiple interferences. This scattering sequence leads to the formation of characteristic XANES features, while the single oscillation event to EXAFS spectral structures, all together forming the modulated absorption spectrum (XAS) of an atom (Figure 2.22-right). A detailed description of the physics behind the technique can be found in Beran & Libowitzky (2004).

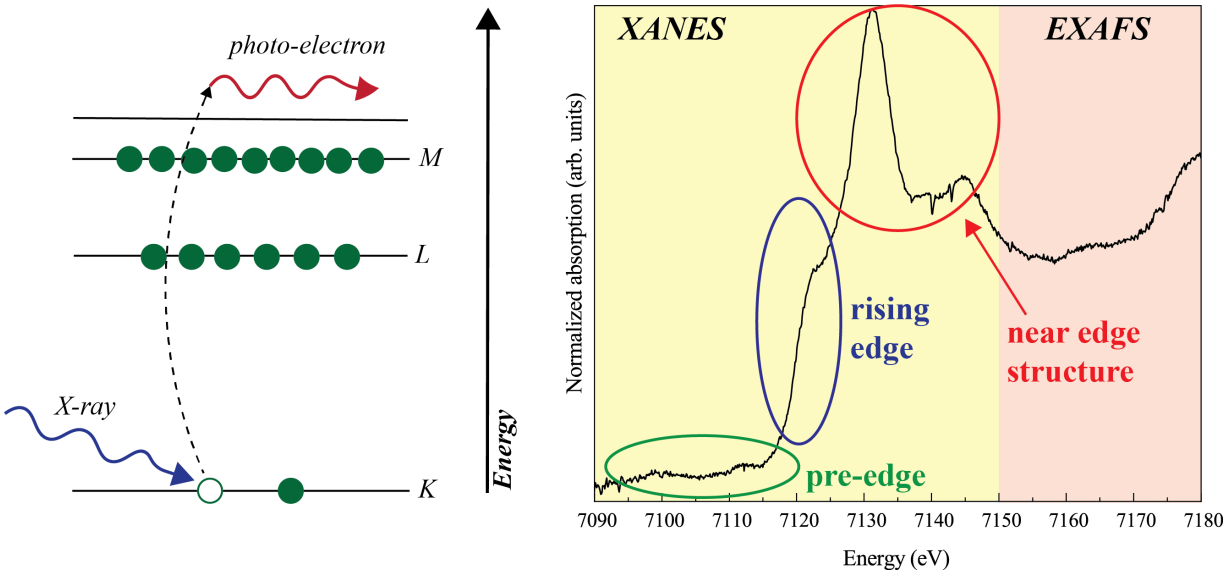

Figure 2.22: **Left**: Photoelectric absorption through the ejection of a core-level electron of an atom by an X-ray. **Right**: X-ray absorption spectrum of the K-edge of ferropericlase and Fe-Ir metal alloy phase assemblage at ~60 GPa. The energy regions are separated in two parts: The X-ray Absorption Near-Edge Structure (XANES) region (light yellow area) close to the absorption edge, and the Extended X-ray Absorption Fine Structure (EXAFS) in the range above the absorption edge (light red area).

In this thesis, we examined the XANES region of XAS spectra collected on polycrystalline samples (ferropericlase equilibrated with Fe-Ir alloy) to obtain chemical information about the Fe oxidation state and its coordination environment. Data acquisition was conducted at the Energy Dispersive X-ray Absorption Spectroscopy (ED-XAS) beamline (ID24) at the ESRF (Pascarelli et al., 2016).

The experimental set up of ID24 consists of different elliptically bent Si polychromators in Bragg and Laue geometries employed as a function of the energy range to optimize the horizontal beam focusing. Before passing through the polychromators, the collimated beam is pre-focused by Kirkpatrick-Baez mirrors. An additional vertical mirror is located behind the polychromator and used to refocus the beam on the sample at ~1 μm FWHM. Along with the optical scheme of the beamline, a position-sensitive detector is placed right after the sample to record the incident radiation. Each position on the detector is calibrated to a specific energy of the incident X-ray beam using known samples as reference materials (Figure 2.23). This technique allows collecting the whole absorption spectrum with a single exposure of the detector (generally on the order of milliseconds). A comprehensive description of XANES measurements performed in this thesis is given in the next chapter.

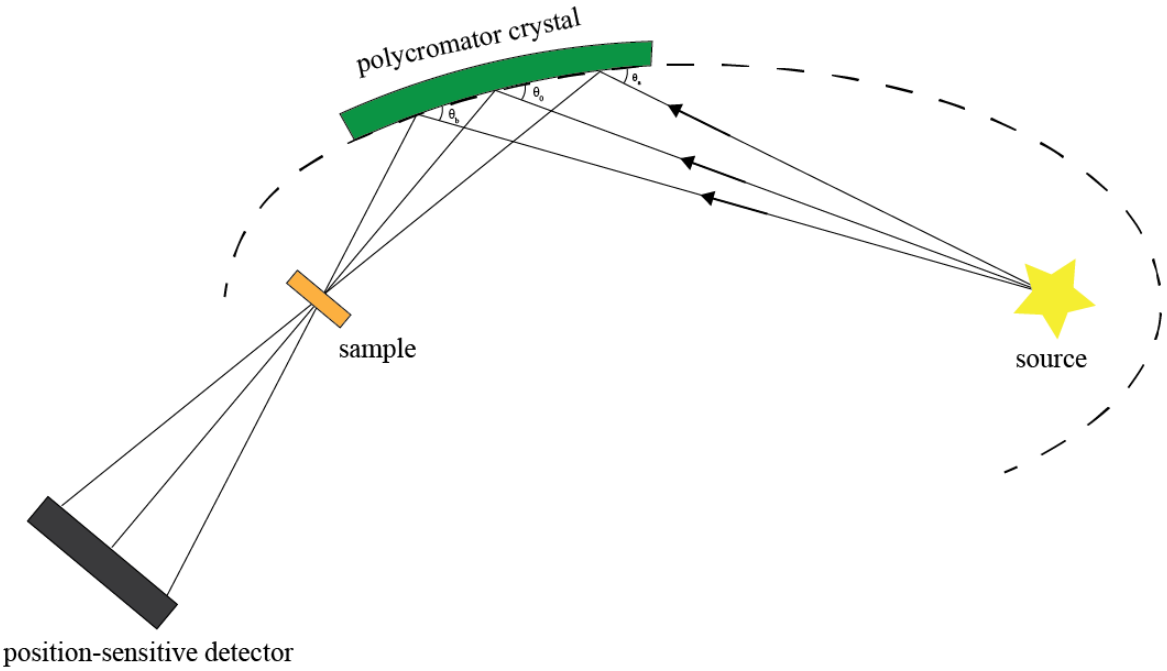

Figure 2.23: Principle of operation of XAS spectrometer at ID24 (modified after Pascarelli et al., 2016).

2.3.4 Inelastic X-ray scattering

Inelastic X-ray scattering (IXS) is a spectroscopic method that allows direct measurements of bulk sound wave velocities probing the phonon dynamics of crystalline materials and giving insights into their elasticity, vibrational thermodynamic properties, and phase transition mechanisms. This technique requires an intense synchrotron light source to achieve extremely high energy resolution on the order of ~1 meV (Burkel, 2000).

The physics principle behind IXS spectroscopy relates to the scattering theory, based on the interaction of X-rays with electrons. In a general scattering geometry, e.g., Figure 2.24, an incident beam with a wave vector k_i, energy E_i, and polarization e_i is scattered into the solid angle $d\Omega$ under the scattering angle of 2θ with a momentum transfer of $Q = k_f - k_i$ and energy bandwidth dE. The scattered intensity of the wave vector k_f (with energy E_f and polarization e_f) is described by the double-differential Thomson cross-section $\left(\frac{d^2\sigma}{d\Omega dE}\right)_{K_i e_i \rightarrow K_f e_f}$ and it is written as,

$$\left(\frac{d^2\sigma}{d\Omega dE}\right)_{K_i e_i \rightarrow K_f e_f} = \frac{k_f}{k_i} r_e^2 \left| e_f * e_i \right|^2 S(Q,\omega) \qquad (2.3)$$

where $r_e^2 \left| e_f * e_i \right|^2$ is the cross-section for a single electron (wherein r is the classical electron radius $r=e^2/mc^2=2.818 \times 10^{-13}$ cm) and $S(Q,\omega)$ is the dynamic structure factor or scattering function.

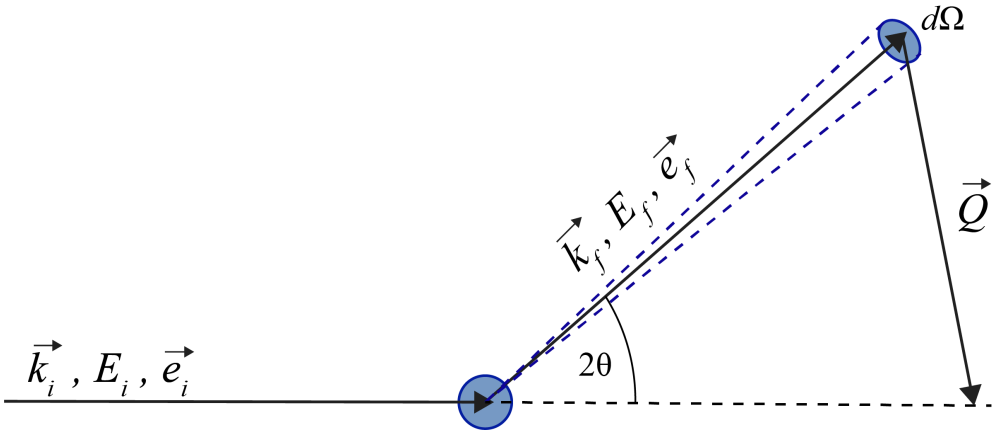

Figure 2.24: General scattering theory geometry (Burkel, 2000).

For a non-resonant inelastic scattering process ($E << E_i$), the energy (Equation 2.4) and momentum transfer (Equation 2.5) are given as,

$$E = h\omega = E_i - E_f \tag{2.4}$$

$$Q = k_i - k_f. \tag{2.5}$$

The magnitude of the momentum transfer depends only on the scattering angle 2θ and the scattering geometry of the system (Equation 2.6),

$$hQ = 2hk_i sin\theta \tag{2.6}$$

while there is no significant dependence on X-ray photon polarization.

The general formalism to describe the scattering function $S(Q,\omega)$ of particles with a position r_j and initial and final state Υ_i and Υ_f is expressed by,

$$S(Q,\omega) = \sum_{\Upsilon_i,\Upsilon_f} |\langle \Upsilon_f | \sum_j e^{iQr_j} | \Upsilon_i \rangle|^2 \, \delta(\hbar\omega + \mathrm{E}_{\Upsilon_f} - \mathrm{E}_{\Upsilon_i}) \tag{2.7}$$

in which e^{iQr_j} describes the scattering amplitude, the matrix includes the probability for excitations, and the δ parameter includes information about the frequency. According to Equation 2.7 the scattering amplitudes from different scattering centers interfere with one another. When an electron of an atom is confined in a crystal lattice the scattering process induced by an accelerated incident photon produces re-emission of a series of magnetic and electric radiation. Further insights on the theory of the scattering process and its applications to IXS spectroscopy are given in the literature (e.g., Burkel, 2000; Baron et al., 2000; Baron, 2020).

The instrumentation geometry of an IXS spectrometer is comparable to that of an X-ray diffractometer with an energy-scan option. The high flux of the synchrotron source allows achieving extremely high resolution (1 meV energy bandwidth) employing a set of crystal monochromators. The scattered beam from the sample passes through an analyzer with similar resolution. This spectrometer configuration usually operates at momentum transfer ranging from 0.5 to 100 nm^{-1} and energy transfer of ~ 300 meV with momentum resolution between 0.05 and 1 nm^{-1} and energy resolution between 0.6 and 6 meV as a function of the desired setup. A typical IXS measurement proceeds by moving the spectrometer 2θ arm (which holds the analyzer array) in order for the analyzer to intercept the scattered radiation at the momentum transfer of interest. The resulting spectrum (intensity vs energy transferred $\hbar\omega$) is proportional to the dynamic structure factor $S(Q,\omega)$.

In this thesis, we performed high-pressure IXS measurements at BLXU35 beamline (Ishikawa et al., 2013; Baron et al., 2000; 2020) at SPring-8 synchrotron facility to investigate the compressional sound wave velocities of B2 Fe-Ni-Si alloys. A schematic diagram of the IXS optic set up at SPring-8 is given in Figure 2.25. During our measurements, we selected a momentum transfer Q in the range of 4.24-7.62 nm^{-1} and a momentum resolution of 0.40 nm^{-1} full width at each experimental pressure. The BLXU35 beamline is equipped with twelve crystal analysers mounted on the spectrometer arm that rotates through the sample intercepting the inelastically scattered radiation. In this way the phonon dispersion curve for each acoustic mode was obtained and fit with a sinusoidal function to extract the velocity corresponding to the Brillouin zone center. A detailed description of IXS data collection and processing is provided in Chapter 5.

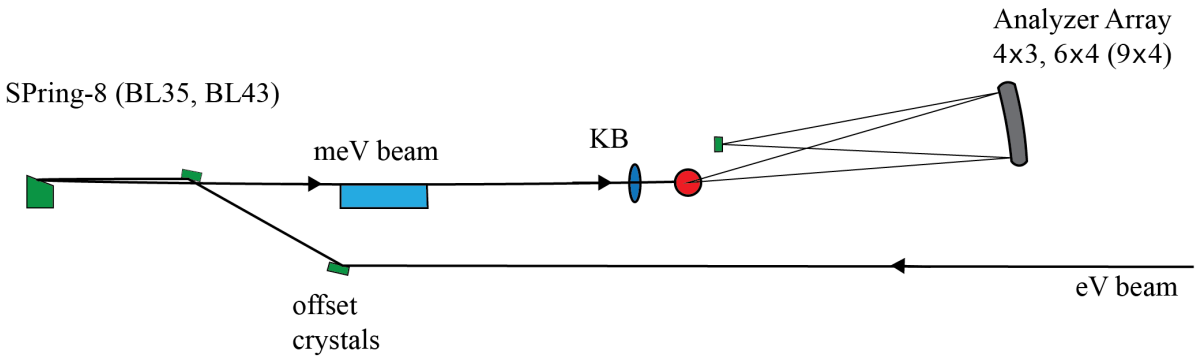

Figure 2.25: The IXS optic geometry at SPring-8 (modified after Baron, 2020).

2.4 DATA ANALYSIS

2.4.1 Equation of state

Equations of state (EOS) describe the change in volume of a solid material with pressure and temperature (e.g., Angel, 2000). EOS are usually formulated as a function of the isothermal bulk modulus, defined as $K = -V\delta P/\delta V$, and its pressure derivatives, i.e., $K' = -\delta K/\delta P$ and $K" = -\delta^2 K/\delta P^2$, evaluated at room conditions. The Birch-Murnaghan (BM) equation of state is commonly employed in geoscience for compressions higher than 10 % (Angel, 2000) and it is based on the assumption that the strain energy of a solid under compression can be expressed as a Taylor expansion of the Eulerian strain $f_E = \left[\left(\frac{V_0}{V}\right)^{\frac{2}{3}} - 1)\right]/2$ (Birch, 1947). The BM formalism expanded to the fourth order in the strain at a reference temperature (e.g., 298 K) is,

$$P(V) = 3K_0 f_E(1+2f_E)^{\frac{5}{2}}\left(1+\frac{3}{2}(K'-4)f_E+\frac{3}{2}\left(K_0K" + (K'-4)(K'-3)+\frac{35}{9}\right)f_E^2\right). \quad (2.8)$$

If the strain energy is truncated to the second order (BM2), the value of K' is implied to be equal to 4, whereas in a 3rd order truncation (BM3) K' is a free variable and only $K"$ has an implied value given by $K" = \left((3-K')(4-K')+\frac{35}{9}\right)$ (Anderson, 1995). The order of truncation is generally decided based on the quality of the data, and can be visualized plotting the normalized pressure $F_E = \frac{P}{3f_E(1+2f_E)^{\frac{5}{2}}}$ versus the Eulerian strain f_E (Angel, 2000). Analysis of the *F-f* plot provides a direct indication of the compression behavior of the investigated material. If the *P-V* data points lie on a horizontal line with constant *F*, then K'= 4 and data can be fit with a 2nd order truncation of the BM EOS (two free parameters V_0 and K_0). Conversely, in the case of data points following an inclined straight line with a slope equal to $\frac{3K_0(K'-4)}{2}$, they are better represented by a 3rd order BM fit (three free parameters V_0, K_0, and K_0'). In a few rare cases, when data points lie on a parabolic curve in the *F-f* plot and $f_E^2 \neq 0$, a fourth order BM fit (four free parameters V_0, K_0, K_0', $K_0"$) is considered more appropriate. For a proper evaluation of an *F-f* plot it is important to include the propagated uncertainties of f_E and F_E. Further insights can be found in Angel (2000). A discontinuity or divergence from the main trend line indicates a variation in the atomic electronic

properties (spin state) or a structural change of the investigated mineral or a change in the stress applied to the material (for example non hydrostatic stress).

In the present study, we fit pressure-lattice parameter data obtained for ferropericlase, Fe-Ir, and Fe-Ni-Si alloys using the EOSFit7-GUI software (Angel et al., 2014; Gonzalez-Platas et al., 2016). A Birch-Murnaghan EOS of 2nd or 3rd order was chosen depending on the *F-f* plots of the individual phases. Details are described in the following chapters. The fitting model of the program is based on the least-squares method, which minimizes the sum of the squares of the differences between the observed and calculated pressures at a given volume.

2.4.2 Determination of fo_2 during high-pressure experiments

Oxygen fugacity during laboratory experiments can be controlled using redox buffer equilibria, metal alloys as sliding redox sensors, or in the case of room pressure experiments using gaseous mixtures of H_2+CO_2 or CO+CO_2 (Nafziger et al., 1971; Huebner, 1971). The redox buffer approach consists of monitoring the fugacity of the system by means of mineral or metal oxide assemblages that impose the f_{O_2} at certain values. The redox sensor method, instead, employs Fe-noble metal binary alloys to detect the oxygen fugacity during the experiments (see section 1.3).
A summary of the different techniques commonly employed to probe the f_{O_2} during HP-HT laboratory experiments is given below:

i) sliding redox sensors (Fe-noble metal alloys) allow measuring the oxygen fugacity at either buffered or not buffered f_{O_2} conditions (Taylor et al., 1992; Borisov & Palme, 2000; Woodland & O'Neill, 1997);
ii) double capsule systems consisting of an external capsule containing the buffer equilibrium plus H_2O and an internal capsule including the sample plus H_2O that impose f_{H_2} at a certain fixed value (Eugster, 1957; Ulmer & Luth, 1991; Bromiley et al., 2004);
iii) metal capsules such as Fe or Re have been observed to affect the oxygen fugacity of the investigated system (McCammon & Ross, 2003);
iv) endmember redox equilibria (e.g., Re and ReO_2) can be added to the starting powder as oxygen buffer (Rubie, 1999).

For room pressure experiments f_{O_2} can be controlled using a gaseous mixture of H_2+CO_2 or CO+CO_2 (Nafziger et al., 1971; Huebner, 1971). At high-pressure instead two approaches are generally employed. One approach is to buffer the f_{O_2} of a system by using a solid assemblage redox equilibria. In this study we employed the redox sensor approach using the activity composition relations of Fe-Ir binary system at non-buffered (Chapter 3) and buffered f_{O_2} by the coexistence of diamond and carbonate (Chapter 4).

2.4.3 Determination of the Fe valence state in minerals: a comparison between SMS/MS, XANES and EELS methodologies

In the present study, we investigated the $Fe^{3+}/\Sigma Fe$ ratio of natural and experimental ferropericlase (Chapter 3 and 4) as a function of the oxygen fugacity using a combination of spectroscopic methods, i.e., point source Mössbauer spectroscopy, Synchrotron Mössbauer Source, electron energy-loss spectroscopy, and X-ray absorption near-edge structure spectroscopy. However, depending on the type and the purpose of the experiments, we used one method over another. Here, we briefly compare the employed techniques describing their differences, similarities, and applications.

The main difference between EELS and the other methodologies is its applicability only for *post-mortem* measurements since the instrumentation is combined with the TEM technology. The sample requires a high-vacuum environment during data collection, which prohibits the employment of any gaseous or liquid substances such as pressure media and excludes the possibility of measurements at high pressures and temperatures. Another disadvantage of EELS is the potential beam damage of the specimen by the high-energy (~200 keV) electron beam which can produce amorphization of the investigated material. Also, the sample preparation is quite demanding and involves the FIB to extract a sample thin foil of ~100 nm thickness. Nevertheless, a unique characteristic of the EELS technique is the possibility to perform spectroscopic analyses, transmission imaging, and electron diffraction analyses all in one instrument with a nanometer spatial resolution. The spectral information that one can retrieve from EELS is similar to that of XANES with quantification of $Fe^{3+}/\Sigma Fe$ based on the examination of Fe $L_{2,3}$ edges (Van Aken & Liebscher, 2002) and Fe *K*-edge fine structures, respectively. The energy resolution of XANES when combined with synchrotron radiation is ~0.1 eV while the spatial resolution can approach

~30 nm. Sample thickness does not affect the quality of the XANES measurement; therefore, the samples do not require a specific treatment prior to the analyses. Conversely, Mössbauer spectroscopy requires polished samples to the optimal thickness (based on the Fe content) to provide a good signal/noise ratio. Both XANES and Mössbauer spectroscopy are non-destructive measurements and allow *in situ* data collection at high pressure and temperatures when combined with LHDAC systems. Mössbauer measurements are optimized when samples are doped with ^{57}Fe while they are usually more challenging for natural samples with dilute levels of Fe (natural abundance 2.1 %) in terms of acquisition time and spectrum resolution. In contrast, XANES and EELS spectroscopies do not require the use of ^{57}Fe for good quality data. Sample dimensions represent a limitation for the applicability of conventional Mössbauer spectroscopy (diameter of ~1 cm) until the introduction of the point source MS and Synchrotron Mössbauer Source radiation. The extremely high brilliance of the SMS and the recent upgrades of the experimental setup at ID18 in terms of flux and beam size (sub micrometer scale) enhanced the spectra quality and overcame previous challenges of the technique.

Chapter 3

3 DETERMINATION OF THE OXYGEN FUGACITY IN DIAMOND ANVIL CELL EXPERIMENTS

3.1 INTRODUCTION

Oxygen fugacity strongly controls the redox state of the mantle, affects the speciation of multivalent elements, and exerts a fundamental role in mantle petrology as well as in the global cycle of the volatile elements (Frost & McCammon, 2008). Because of its significance in governing physicochemical processes occurring in Earth's interior, any experimental system designed to simulate natural conditions requires internal constraints of the f_{O_2}. Although for more than fifty years, large volume presses (e.g., multi anvil, piston-cylinder) experiments have been performed to investigate the effect of f_{O_2} on element partitioning, partial melting, mineral physical properties, as well as the link between f_{O_2} and the redox state of the mantle, we still have an incomplete picture of the complex redox processes occurring at the deepest portion of Earth's interior most likely due to experimental limitations. Indeed, the f_{O_2} was only poorly controlled or measured during diamond anvil cell experiments which represent a direct window to the extreme conditions of the Earth. In HP-HT experiments conducted using large volume presses, two main methods are usually employed to control the oxygen fugacity and are based on the use of i) calibrated solid assemblage to buffer the f_{O_2} at specific values (Eugster, 1957), and ii) Fe-noble metal alloys as sliding redox sensor (Taylor et al., 1992; Woodland & O'Neill, 1997; Borisov & Palme, 2000) to monitor the f_{O_2} at target P and T in the experiments. In the latter, the f_{O_2} imposed by an experimental system can be determined by the metal sensor through thermodynamic properties of either oxides or silicates containing transition metals that are commonly obtained by reduction reactions (Woodland & O'Neill, 1997). Theoretically, many noble metals might be used as a redox sensor as long as their activity-composition relations are well defined. Among different candidates (i.e. Ir, Pt, Pd) belonging to the platinum group elements (PGE) Ir is considered to be the most suitable redox sensor since only one phase *fcc*-Fe-Ir is stable over a large temperature range and its activity-composition relations are well known at 1bar (Schwerdtfeger and Zwell,

1968; Swartzendruber, 1984). Additional details can be found in section 1.3. Despite the existing thermodynamic model for the Fe-Ir redox sensor is relatively well constrained as a function of temperature and composition, the effect of pressure on the activity-composition relations was never investigated.

In this chapter, we present a new methodology based on the redox sensor technique to probe the oxygen fugacity during laser heating diamond anvil cell (LHDAC) experiments. We monitor the f_{O_2} during laser heating runs by combining Fe oxidation state and chemical analysis results through mass balance. We further implemented the Fe-Ir activity-composition relations including the pressure dependency on the interaction parameters, which allow to more accurately determine the oxygen fugacity at high-pressure and high-temperature conditions of laboratory experiments.

3.2 EXPERIMENTAL PROCEDURES

3.2.1 Starting materials

The starting materials consisted of polycrystalline and pre-synthesized ferropericlase plus iridium metal. Details of ferropericlase synthesis are described in Longo et al. (2011) and briefly summarized hereafter. Magnesium (Mg) and iron (Fe) metals were mixed in stoichiometric proportions to give a molar fraction of Fe of 25 mol %. To produce pure (Mg, Fe)O crystals, Longo et al. (2011) dissolved metals in nitric acid HNO_3, heated the mixture at 50 °C, and added ammonia hydroxide NH_4OH to the solution; excess of HNO_3 and NH_4OH was removed by drying the obtained gel at temperatures of ~1200-1500 °C. A pressed pellet of this mixture was equilibrated in a gas-mixing furnace under CO/CO_2 at 1300°C for 12 hours, at controlled oxygen fugacity ($\log f_{O_2}$ ranging from -11 to -7). The sample was then rapidly quenched in water to ensure no ferrite crystals formation (Longo et al., 2011). We confirmed the sample's homogeneity and oxidation state of Fe by conventional Mössbauer spectroscopy at BGI. Fit of the MS spectrum showed a $Fe^{3+}/\Sigma Fe$ content of ~12(2) % in ferropericlase and no appearance ferrite phases. Polycrystalline $(Mg_{0.75}Fe_{0.25})O$ was then ground with 5 mol % of reagent-grade iridium metal (99.999 % purity) for about 1 hour in an agate mortar under ethanol to achieve a homogeneous mixture. Our purpose was to observe the formation of a Fe-Ir alloy after increasing pressure and temperature with a specific Fe/(Fe+Ir) mole fraction and use its thermodynamic properties to measure the oxygen fugacity during experiments. The mixed powder was used both for diamond anvil cell and multi

anvil experiments, designed to compare the redox conditions achieved with both techniques. Table 3.1 shows an overview of all experimental conditions and spectroscopic analyses performed in this study, described in detail in the following paragraphs.

Table 3.1: Summary of experimental conditions and spectroscopic analyses of DAC and multi anvil experiments

Run	Device	P (GPa)	T (°C)	Methods	Analyses
SD001	LHDAC	36.0(5)	2150(150)	XRD, SMS	TEM-FIB
SD002	LHDAC	61.5(1)	2150(150)	XRD, SMS, XANES	
S7153	Multi Anvil	26(1)	1700(80)	SMS	EMPA

Note: LHDAC stands for laser-heating diamond anvil cell. Pressures indicated for LHDAC experiments refer to the highest pressures measured after laser heating.

3.2.2 Diamond anvil cell experiments

An irregularly-shaped compressed pellet of starting powder (~60 μm long in diagonal direction with thickness of ≤10 μm) was placed inside a drilled Re gasket hole (~100 μm diameter) pre-indented down to a thickness of ~30 μm. The sample chamber was loaded with Ne as quasi-hydrostatic pressure transmitting medium using the gas loading system installed at BGI (Kurnosov et al., 2008). We used piston-cylinder BX90 type DACs (Kantor et al., 2012) equipped with tungsten carbide seats and Boehler-Almax anvils design (Boehler & De Hantsetters, 2007). Diamonds with culet sizes of 250 μm (runs SD001 and SD002) were used for high-pressure and high-temperature experiments. High pressure was generated by manually tightening the screws of the DACs in steps of ~5 GPa up to 36.0(5) GPa (SD001) and 61.5(1) GPa (SD002). After reaching the target pressures, samples were double-side laser-heated at ~2000-2300 K using a portable double-side pulsed laser heating system. The laser setup was furnished with two IR ytterbium-doped fiber lasers (YLR-100-AC of IPG Photonics) that allow to heat the samples from both sides with a focal spot of ~10-15 μm and operate at 1070 nm with a maximum power of 100 W (further details can be found for example in Aprilis et al., 2017, and references therein). Temperatures were measured during heating on both sides of the samples using spectroradiometry, and related uncertainties of about ± 150 K arise from possible temperature gradients or heating instability (Kantor et al., 2018) .

3.2.3 Multi anvil experiments

The starting powder was placed inside a folded Re foil capsule, with dimensions of ~2 mm in length and ~1 mm in diameter. The sample S7153 was synthesized at 26(1) GPa and 1700(80) °C in a 1200-ton Kawai-type multi anvil press at BGI. Heating time was set for about 1 hour to ensure chemical homogeneity and equilibrium of the crystallized phases. Tungsten carbide WC anvils of 3 mm truncation edge length were used with 7 mm edge length Cr_2O_3-doped MgO octahedron (referred to as 7/3 assembly, see sketch in Figure 2.3 section 2.1.2). High temperature was reached employing a $LaCrO_3$ heater, and was monitored by a $W_{97\%}Re_{3\%}$–$W_{75\%}Re_{25\%}$ thermocouple (D-type) inserted horizontally through the wall of the furnace to be directly in contact with the Re capsule. The recovered sample was mounted in epoxy resin, sectioned to expose the capsule material and polished for analysis (paragraph 3.3.3). Then, the sample was double polished to the optimal thickness (200 μm) as function of the measured Fe content in ferropericlase and sample geometry for Synchrotron Mössbauer Spectroscopy measurements (section 3.2.5).

3.2.4 Synchrotron powder X-ray diffraction

Powder X-ray diffraction experiments were conducted at the High-Pressure Diffraction Beamline ID15B (Merlini & Hanfland, 2013) of the European Synchrotron Radiation Facility (ESRF). A summary description of the beamline operation system is given in section 2.3.2. X-rays (λ=0.411491 Å) were focused on areas of approximately 10×10 μm^2 FWHM vertically by a spherical mirror and horizontally by the Si (111) Laue monochromator installed on the optical table. A large area (430×350 mm) MAR555 flat panel detector was used for XRD data acquisition. Before the experiments, the detector-sample distance was calibrated using CeO_2 reference material. Compressibility of ferropericlase and Fe-Ir alloy was investigated during decompression on both quenched SD001 and SD002 run products. We acquired XRD wide-scan images during continuous rotation of DAC from -20° to +20° ω at each position of interest per pressure point (2 s of exposure time per degree of rotation). Additional XRD maps were acquired on SD002 experimental run at 61.5(1) GPa at the High-Pressure Beamline ID27 at ESRF (Perkin Elmer flat panel detector, λ=0.3738 Å) to explore possible inhomogeneity after heating. We calculate pressures from the positions of the X-ray diffraction lines of Ne (Fei et al., 2007).

The resulting diffraction data were analyzed using DIOPTAS software (Prescher & Prakapenka, 2015) for phase identification, pressure estimation, and integration of both preliminary still images and wide-scan images. Le Bail data processing and Rietveld refinements of integrated powder diffraction patterns were carried out with JANA2006 software (Petrícek et al., 2014) using manual background correction and pseudo-Voigt line shape.

3.2.5 Synchrotron Mössbauer Source

We performed energy-domain Mössbauer measurements at the Nuclear Resonance Beamline 1D18 (Rüffer & Chumakov, 1996; Potapkin et al., 2012) at ESRF to quantify the valence state of Fe. An overview of the Synchrotron Mössbauer Source (SMS) operation system at the ID18 beamline is given in section 2.3.1, while a thorough description can be found in Potapkin et al. (2012). The high brilliance X-ray beam emitted by SMS radiation was focused on 14 μm vertical and 13 μm horizontal dimensions using Kirkpatrick-Baez (KB) mirrors. The source linewidth was evaluated before and after the acquisition of each SMS spectrum using a $K_2Mg^{57}Fe(CN)_6$ single line absorber. The velocity scale of all SMS spectra was calibrated relative to a 25 μm thick α-Fe foil. We collected SMS spectra of diamond anvil cells samples (SD001 and SD002) before (on the starting ferropericlase) and after laser heating with acquisition time ranging from 1 to 2 hours. Two SMS spectra were also acquired on experimental run S7153 in different areas of the sample. All Mössbauer spectra were fitted using a full transmission integral with pseudo-Voigt line shape and 1st order polynomial baseline implemented in the MossA software package (Prescher et al., 2012).

3.2.6 X-ray absorption near-edge structure spectroscopy

Fe oxidation state in ferropericlase was also determined by X-ray absorption near edge structure (XANES) spectroscopy. XANES data acquisition was conducted at the energy-dispersive beamline ID24 of ESRF (described in section 2.3.3). The X-ray beam was focused horizontally at 4 μm FWHM employing an elliptically bent Si (311) crystal and vertically at 3 μm FWHM using a combination of Si mirrors in a KB configuration (Pascarelli et al., 2016). Pixel-energy calibration was performed using a reference α-Fe foil spectrum. XANES spectra were collected at the Fe *K*-edge at 7190 eV on the center position of sample SD002 after laser heating at 61.5(1) GPa.

We acquired XANES maps by scanning the DAC horizontally and vertically in steps of 5 μm in the focal plane of the X-ray beam (Figure 3.1). Fe *K*-edge XANES were recorded over 6 (h)

× 3 (v) step grid in order to cover an area of 450 μm^2. The resulting map contains 18 XANES spectra (one spectrum per pixel) (Aquilanti et al., 2009). We selected the best heated/reacted area of the sample (white dashed rectangle in Figure 3.1b) as best representation of equilibrium.

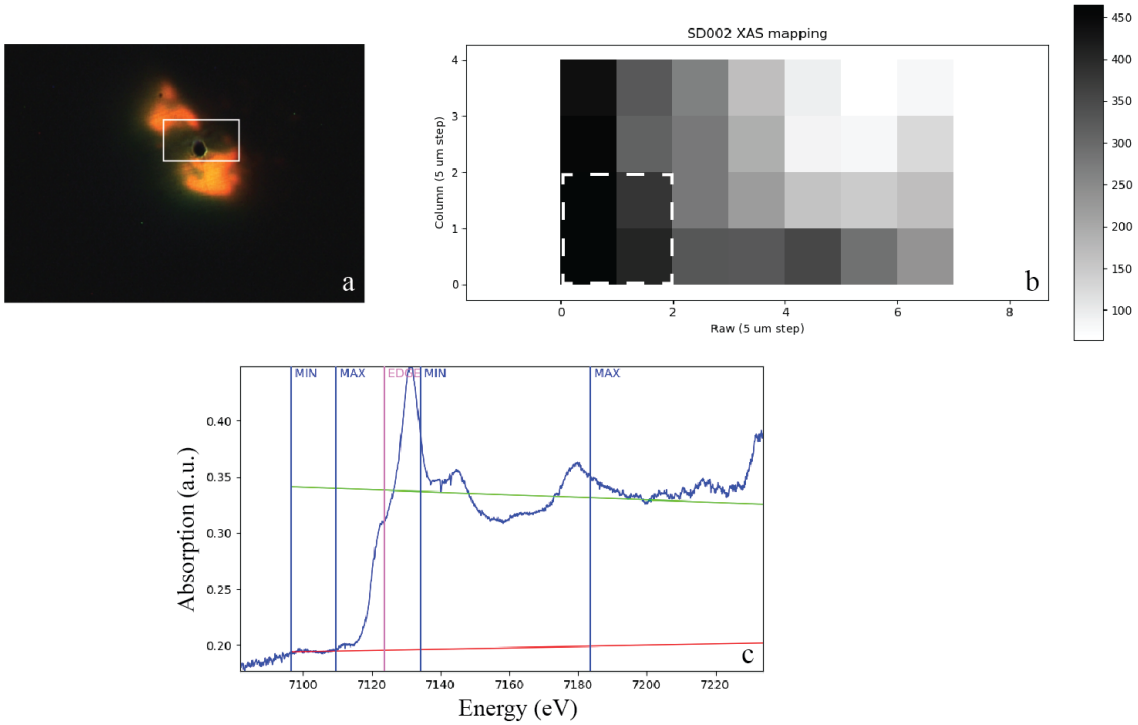

Figure 3.1: **a)** Microscope image of quenched SD002 sample at 61.5(1) GPa. Bright-orange areas correspond to the laser spot. The white rectangle indicates the selected area of XAS map; **b)** XAS map of SD002 sample. Dashed white rectangle encloses the selected pixels (spectra) corresponding to the best quality measurements; **c)** Example of a XANES spectrum normalization.

The data map was treated using the Region of Interest (ROI) Imaging Tool of the PyMCA software (Solé et al., 2007) which allows the normalization and the visualization of XANES spectra (one spectrum per pixel). Data processing was performed subtracting a linear pre-edge background and normalized the post-edge jump to unity (Figure 3.1c).

3.3 ANALYTICAL PROCEDURES

3.3.1 TEM lamella preparation

Characterization of the sample from DAC experiments was only possible using the Transmission Electron Microscope (section 2.2.6) due to the small size of crystallized phases after heating (few microns on average) and the brittleness of the recovered material. As shown below, we prepared a thin foil of SD001 sample using the focus ion beam instrument (FEI, Scios DualBeam) to enable TEM analyses on the best reacted area of the specimen. Firstly, the sample was carefully detached from the diamond anvil together with the Re gasket. Platinum rectangular layers were deposited by the Pt-GIS (Gas Injection System) needle at the sample/gasket boundary to ensure a solid connection between them before cutting (Figure 3.2a). Due to the brittleness of the specimen, we placed an additional Pt bridge across the sample surface (Figure 3.2b) to prevent the potential sample loss during the FIB-cut. A Pt layer of ~20 μm length and ~1-2 μm thickness was also located transversely to the Pt bridge on top of the selected area of interest (white rectangle, Figure 3.2c) where the foil was to be cut. The specimen was then tilted at ~52° and cut at the front and backside of the lamella by scanning ion beam (Figure 3.2d,e) employing an electric field of 30 kV and a current of 0.5 nA (Miyajima et al., 2010; Wirth, 2009). After completing the trenches, we tilted the stage at 7° and performed a parallel milling to detach the foil from the sides and lift it out using a tungsten needle driven by a micromanipulator. The foil was then attached to the copper grid (Figure 3.2f) by platinum. At the final step, the lamella was thinned down to 100 nm by tilting the stage at 57° and 47° to polish the front and back sides of the lamella respectively and reduce the effect of the irregular topography. Energy dispersive spectroscopy (EDS) analysis were performed turning the sample stage to zero degree after completing the cutting procedure. Measurements were acquired with a silicon drift detector (SDD) employing an acceleration voltage of 20 kV (Newbury & Ritchie, 2015). ZAF correction was applied.

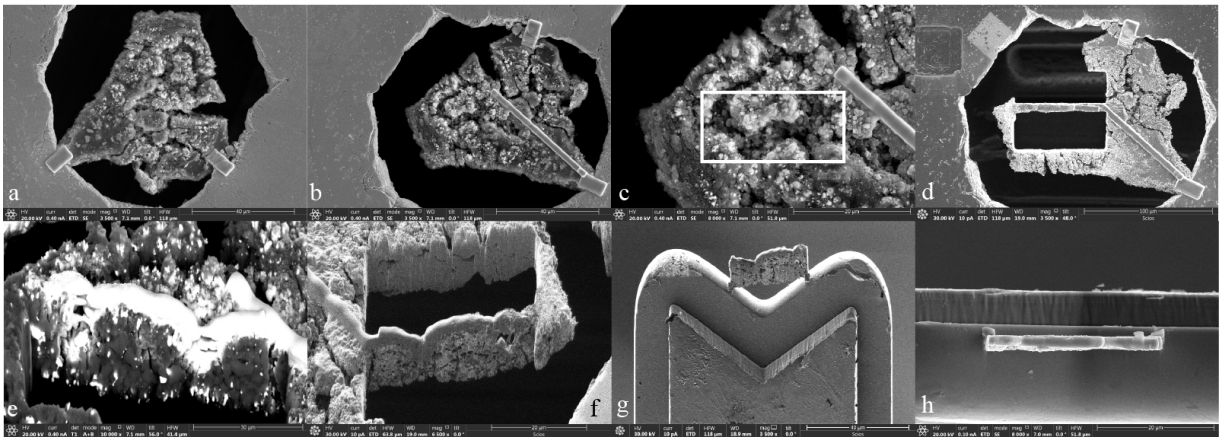

Figure 3.2: **a)** SD001 sample fixed to the gasket by Pt deposition; **b)** Pt layer for surface protection is deposited; **c)** the white rectangle shows the chosen region of the sample to be milled by focus ion beam; **d)** sample cut at the front and the back side of the Pt layer; **e)** BSE image of the lamella front side obtained after cutting; **f)** cross section of the lamella; **g)** SE image of the foil welded by Pt deposition to the TEM grid after being lifted out and ready for final polishing; **h)** ~100 nm thick lamella obtained after thinning.

3.3.2 Transmission Electron Microscope (TEM) analyses

Quantitative energy dispersive X-ray microanalyses, electron energy-loss spectroscopy (EELS) measurements and microstructure textural observations were conducted on the extracted film (sample SD001) using the high-resolution transmission electron microscopy FEI Titan G2 80-200 S/TEM equipped with an energy filter system, Gatan Quantum SE, operating at 200 kV. Analyses were performed at -170°C using a liquid nitrogen cooling holder to reduce the electron irradiation damage. We mapped the Fe valence state in ferropericlase grains collecting Fe $L_{2,3}$-edge electron energy-loss near-edge structure (ELNES) spectra in diffraction modes under the following operating conditions: a 2mm PEELS entrance aperture, an illumination angle of 2α=5.2 mrad, a collection angle 2β=14 mrad, an energy dispersion of 0.1 eV/channel, and 30 s of integration time per read-out. The incident beam current was about 6.1 nA and the fluorescence rate was 5.2×10^3 $eÅ^{-2}s^{-1}$. We examined a total of 10 ferropericlase grains to explore potential variation in the Fe valence state and to have good counting statistics. An EELS spectrum of the starting material was also acquired at the same operating conditions to compare the Fe^{3+} content in ferropericlase determined before and after LHDAC experiments. Data processing of the measured spectra includes the subtraction of the background intensity and corrections for both channel-to-channel gain variations and the dark current of the detector. We quantified the Fe $L_{2,3}$-edge ELNES determining the integral Fe $L_{2,3}$-edge white-line intensity ratio I(L_3)/I(L_2) as a function of the

ferric iron concentration using the EELSA[1] software package, following the procedure described by Van Aken et al. (1998, 2002). Two integrated windows of 2eV width were applied to the $L_{2,3}$ edges from 708.5 to 710.5 eV and from 719.7 to 721.7 eV centered around the maximum at L_3 edge for Fe^{3+} and at the L_2 edge for Fe^{2+}, respectively. Ferric/ferrous Fe ratio in ferropericlase was calculated using an empirical universal curve calibrated for natural samples and solid solutions (Van Aken et al., 1998, 2002).

3.3.3 Chemical analyses of the multi anvil run product

The recovered sample S7153 from the multi anvil experiment (section 3.2.3) was characterized using both the scanning electron microscope and the electron microprobe (section 2.2.1 and 2.2.2, respectively). Textural observation, preliminary phase identification and semi-quantitative chemical analyses of S7153 sample were conducted using the SEM (ZEISS Gemini 1530) equipped with an energy dispersive X-ray spectrometer (EDXS) operating at 15 kV. Accurate quantitative analyses of coexisting phases were obtained using the EMPA (JEOL J-XA 8200) microanalyzer furnished with five wavelength dispersive spectrometers. We selected an acceleration voltage of 20 kV and a beam current of 20 nA for alloy measurements (46 points), while for oxides analyses we set conditions of 15 kV and 15 nA (56 points). The ZAF and phi-rho-Z matrix corrections were applied to metals and oxides phases, respectively. Instrument calibration was done using in-house standards, i.e., Mg-enstatite, Fe-Fe metal, Ir-Ir metal.

[1] Program written by Clemens Prescher available at http://www.clemensprescher.com/programs/eelsa

3.4 RESULTS

3.4.1 XRD results and equations of state

Results of Synchrotron powder X-ray diffraction show the formation of a Fe-Ir alloy, with *fcc* structure, by the reaction of Ir metal and Fe from ferropericlase. Figure 3.3 illustrates the comparison between integrated diffraction patterns collected before (green) and after (red) laser heating at 11.0(5) GPa. Calculated intensity XRD profiles were obtained after performing Rietveld refinement. All quenched XRD patterns exhibit disappearance of Ir peaks indicating a complete reaction of Ir metal to form the Fe-Ir alloy as well as the homogeneity of the laser heating (magnified Figure 3.3b).

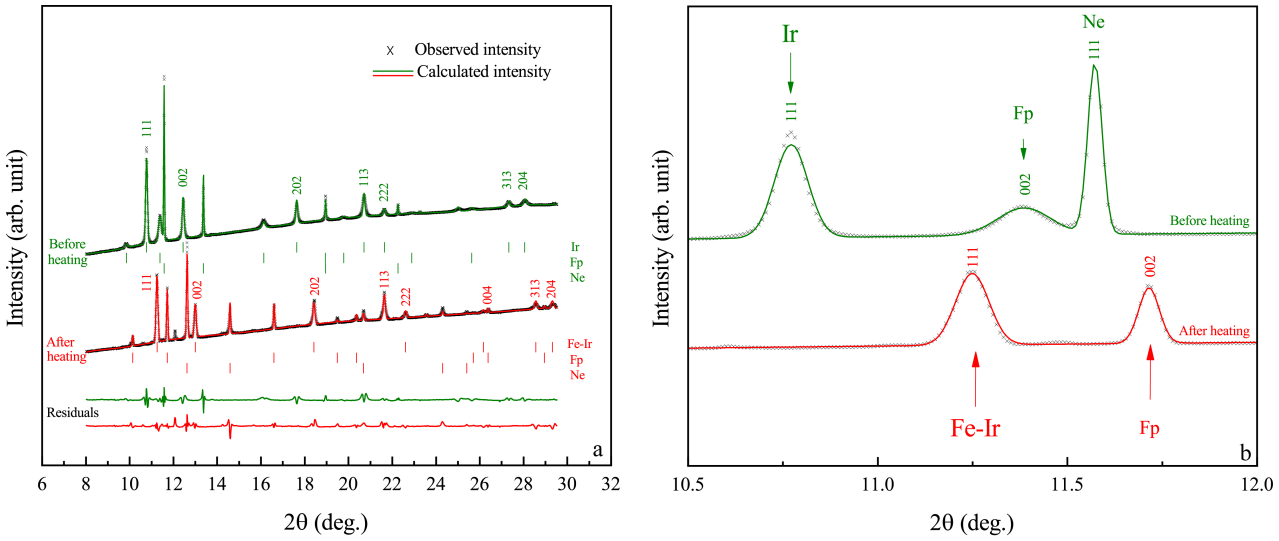

Figure 3.3: **a)** Comparison of XRD pattern collected on sample SD001 before (green) and after (red) laser heating at 11.0(5) GPa and 300 K. Identified phases before heating are ferropericlase, Ne (pressure transmitting medium) and Ir metal. After quenching a Fe-Ir alloy is formed by the reaction of Ir metal and Fe from ferropericlase; **b)** magnified image illustrates the vanishing of Ir peak after laser heating and appearance of the Fe-Ir diffraction peak. Rietveld refinement was performed using Jana software package (Petrícek et al., 2014).

Analysis of diffraction data at different pressures showed that all quenched diffraction patterns can be indexed with three phases, i.e., ferropericlase, Ne, and Fe-Ir alloy, in the *fcc* strucure and $Fm\bar{3}m$ space group. The newly crystallized Fe-Ir alloy maintains the *fcc* structure over the entire investigated pressure range (up to 61.5(1) GPa). An example of XRD pattern collected at the highest pressure after cooling is shown in Figure 3.4.

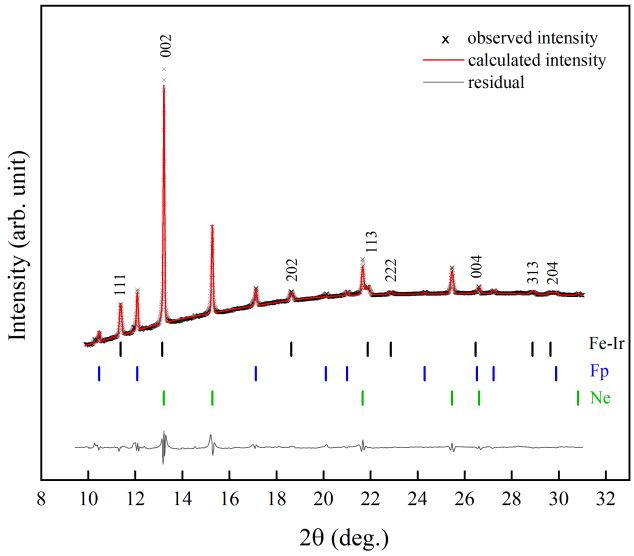

Figure 3.4: Integrated XRD pattern of quenched SD002 sample at 61.5(1) GPa. Three phases are identified: solid neon (green), ferropericlase (blue) and Fe-Ir metal alloy (black). Le Bail refinement was performed using the JANA2006 software (Petricek et al., 2014).

Pressure dependence of volume parameters for Fe-Ir alloy and ferropericlase (run SD002) were fit with a third-order Birch-Murnaghan EOS (see section 2.4.1) using the EosFit7-GUI software (Angel et al., 2014; Gonzalez-Platas et al., 2016) and are shown in Figure 3.5 and 3.6 with the corresponding F-*f* plots.

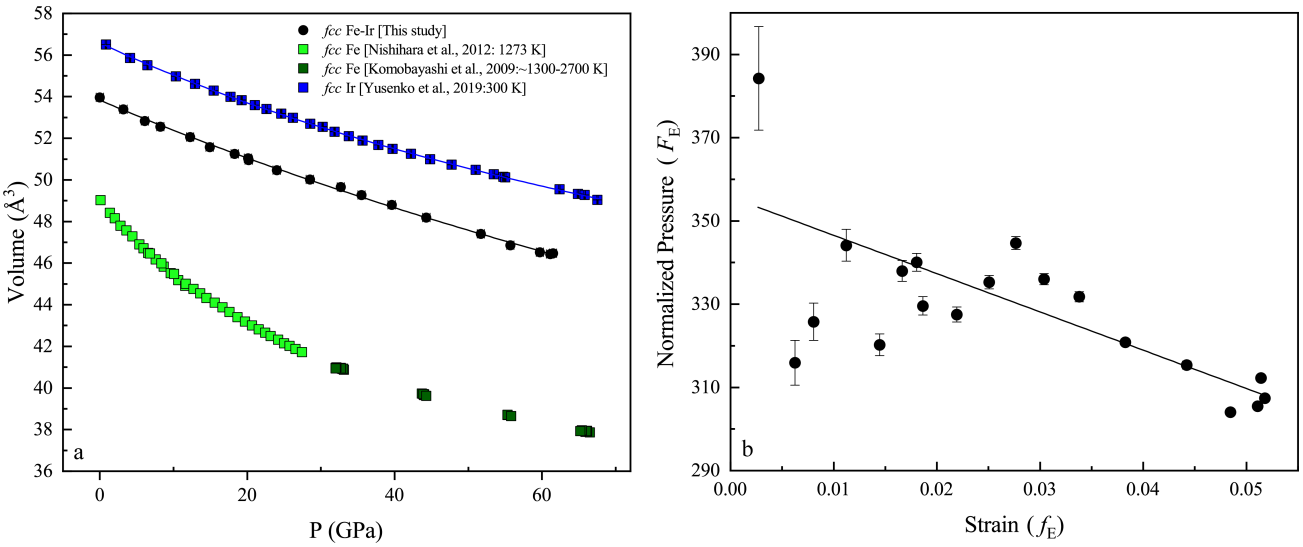

Figure 3.5: **a)** Isothermal EOS of *fcc* Fe-Ir alloy at 300 K collected for run SD002 in comparison with previous *P-V(-T)* equations of state for pure *fcc* Ir (Yusenko et al., 2019) and *fcc* Fe metals (Komobayashi et al., 2009; Nishihara et al., 2012). The solid black line represents the least squares fit to a third-order Birch-Murnaghan EOS of this study. Uncertainties on *P-V* data points are ~1 % (see Table 3.1) and plot inside the symbols. **b)** Normalized pressure as a function of the Eulerian strain. The solid line is a linear fit of the data based on the third-order Birch-Murnaghan EOS.

Figure 3.5a shows the *P-V* relationship for Fe-Ir determined in this study with those of the end member phases (Figure 3.5a), pure *fcc* Fe (Komobayashi et al., 2009; Nishihara et al., 2012) and *fcc* Ir (Yusenko et al., 2019) reported in selected previous works. Unit cell lattice parameters of *fcc* Fe are related to high-temperature measurements (i.e., 1273 K Nishihara et al., 2012, and ~1300-2700 K Komobayashi et al., 2009) since at room temperature and high pressures Fe is known to assume the *hcp* structural phase (see for example the phase diagram of metallic Fe reported from Tateno et al., 2010 and Anzellini et al., 2014). The calculated EOS curve for the Fe-Ir alloy shows no evidence of pressure-induced phase transitions over the investigated pressure range. The visible scatter among data points may be explained via crystallization of two alloy compositions with very close stoichiometry. Fits of the third-order Birch-Murnaghan equation of state to pressure-volume data yielded K_{T0} = 356 ± 11 GPa, K'_{T0} = 2.3 ± 0.3, and V_0 = 53.97 ± 0.06 Å^3. A comparison between EOS coefficients of the Fe-Ir alloy determined in this study and those of the end member phases (i.e., metallic *fcc* Fe and Ir) is given in Table 3.2.

Table 3.2: Equation of state (Birch-Murnaghan) parameters of the Fe-Ir alloy determined in this study and those of pure end member phases from the literature.

	Fe[a]-*fcc*	Fe[b]-*fcc*	Fe-Ir[c]-*fcc*	Ir[d]-*fcc*
V_0, Å^3	48.997 ± 0.040	47.00	53.97 ± 0.06	56.53 ± 0.01
V_0, cm^{3}mol^{-1}	7.376	7.076	8.126	8.512
K_{T0}, GPa	108.3 ± 2.4	133 ± 3	356 ± 11	341 ± 10
K'_{T0}	5.8 ± 0.2	5	2.3 ± 0.3	4.7 ± 0.3
T, K	1273	300	300	300

Note: [a]Nishiara et al. (2012); [b]Campbell et al. (2009); [c]This study; [d]Yusenko et al. (2019)

The compressibility of ferropericlase (25 mol % of Fe) is shown in Figure 3.6 in comparison with selected EOS of ferropericlase with different Fe content determined in previous studies (i.e., 25 mol % Fe-Mao et al., 2011; 35 mol % Fe-Chen et al., 2012; 48 mol % Fe-Solomatova et al., 2016). A visible reduction in volume appears in the pressure window (40-70 GPa, e.g., Badro et al., 2003; Lin et al., 2005) expected for the spin-pairing crossover (from high-spin HS to low-spin LS configuration) at room temperature, consistently with previous studies (e.g., Badro et al., 2003; Jacobsen et al., 2005; Lin et al., 2005;Mao et al., 2011; Chen et al., 2012; Solomatova et al., 2016). At the spin transition, Fe^{2+} ions in the octahedral site change electronic configuration, going from a high-spin state, in which electrons are split between the t_{2g} and the e_g

energy levels (two paired and four unpaired electrons), to a low-spin state, where six paired electrons are located in the t_{2g} energy level (Kantor et al., 2006).

Fit results of HS ferropericlase yielded EOS coefficients of $V_{0.}$ = 76.5 ± 0.1 Å^3, K_{T0} = 158 ± 5 GPa and K'_{T0} = 4.6 ± 0.3, in excellent agreement with EOS parameters reported by Mao et al. (2011) for a 3rd order BM fit of ferropericlase in HS state (i.e., $V_{0.}$ = 76.34 ± 0.1 Å^3; K_{T0} = 162 ± 1 GPa; K'_{T0} = 4(fixed)). A slight variation in *P-V* parameters from this study and previous works (Badro et al., 2003; Jacobsen et al., 2005; Lin et al., 2005; Mao et al., 2011b; Chen et al., 2012; Solomatova et al., 2016) most likely arises from differences in composition. The *P-V* points between 44.3(1) and 61.5(1) GPa of our dataset show anomalous compressibility behaviour and were excluded from the fit because they fall within the spin transition region. The complete list of lattice parameters obtained after Rietveld refinement for both ferropericlase and Fe-Ir alloy is given in Table 3.3.

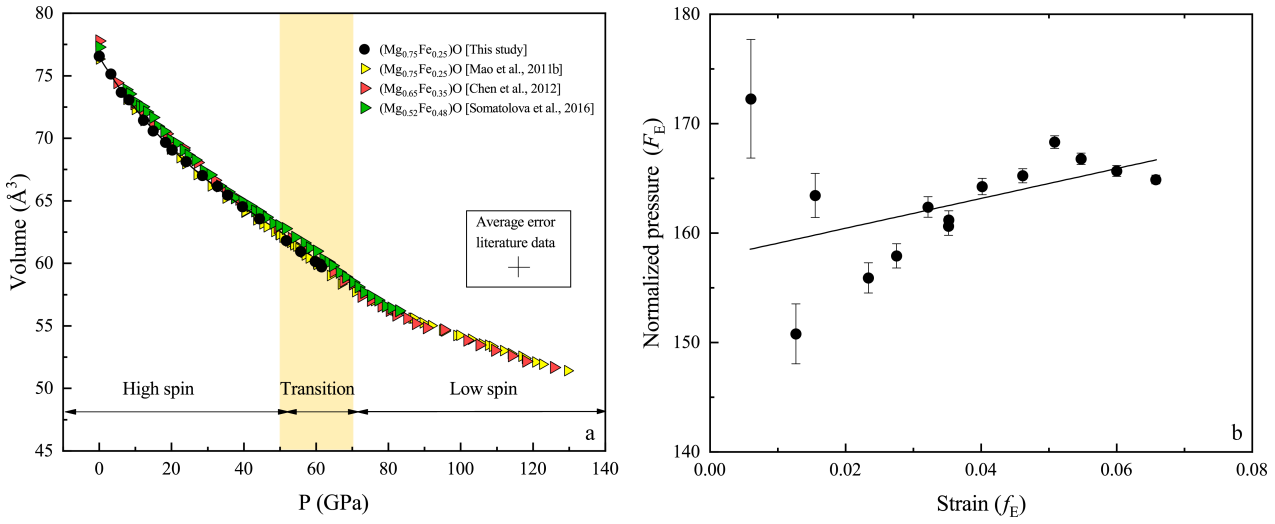

Figure 3.6: **a)** Compression curve of ferropericlase at 300 K (black solid circles, run SD002) compared with previous selected studies of ferropericlase with different Fe content. The solid black line represents the least squares fit to a third-order Birch-Murnaghan EOS. Uncertainties on *P-V* data points of this study plot inside the symbols while the average error bar of literature data is shown in the inset box. **b)** Normalized pressure as a function of the Eulerian strain of high-spin ferropericlase EOS determined in this study. The solid line is a linear fit of the data based on the third-order Birch-Murnaghan EOS.

Table 3.3: Lattice parameters of Fe-Ir alloy and ferropericlase determined after Rietveld refinement.

	Fe-Ir alloy		**Ferropericlase**	
P (GPa)	***a* (Å)**	***V* (Å^3)**	***a* (Å)**	***V* (Å^3)**
61.5(1)	3.596(3)	46.483(6)	3.909(2)	59.736(5)
61.1(1)	3.594(4)	46.435(8)	3.914(3)	59.939(7)
59.7(1)	3.597(4)	46.524(9)	3.918(3)	60.169(7)
55.7(1)	3.605(4)	46.858(10)	3.936(3)	60.954(7)
51.8(1)	3.619(5)	47.407(11)	3.954(3)	61.825(8)
44.3(1)	3.6391(19)	48.194(4)	3.991(2)	63.565(6)
39.6(1)	3.654(4)	48.803(1)	4.012(5)	64.545(13)
35.5(1)	3.666(4)	49.273(10)	4.030(4)	65.47(1)
32.7(1)	3.676(5)	49.658(11)	4.045(4)	66.165(11)
28.5(1)	3.685(4)	50.023(10)	4.062(4)	67.025(12)
18.3(1)	3.715(5)	51.254(11)	4.115(3)	69.681(10)
20.2(1)	3.707(5)	50.956(11)	4.103(4)	69.079(10)
24(1)	3.696(4)	50.474(10)	4.084(4)	68.138(11)
20.1(1)	3.710(4)	51.046(9)	4.103(4)	69.088(10)
12.25(1)	3.734(5)	52.069(12)	4.149(5)	71.442(14)
6.1(1)	3.753(5)	52.840(3)	4.193(8)	73.69(2)
14.9(1)	3.723(4)	51.581(9)	4.133(3)	70.602(9)
8.2(1)	3.746(3)	52.556(7)	4.181(5)	73.0843(14)
3.2(1)	3.766(1)	53.393(2)	4.211(8)	75.149(3)
0(1)	3.779(1)	53.974(3)	4.246(1)	76.571(4)

Note: Numbers in bracket are standard deviations.

3.4.2 Chemical analyses results

Results of chemical analyses and textural observations conducted on the recovered FIB lamella of sample SD001 show the formation of Fe-Ir alloys after increasing pressure and temperature by redox reaction (Figure 3.7). EDS chemical analyses collected on recovered FIB lamella (sample SD001) during the cutting procedure (paragraph 3.3.1) are consistent with EDS measurements performed with the TEM within experimental uncertainty. The average Fe content in Fe-Ir alloy and the wüstite content in ferropericlase were calculated at 0.42 ± 0.02 and 0.24 ± 0.04 respectively, and were used for the oxygen fugacity calculation (see paragraph 3.4.5).

Laser heating in DAC is known to potentially cause mobilization of carbon from the diamond anvils and its chemical interaction with Fe during continuous wave heating of the sample (Aprilis et al., 2019). Although spectroscopic measurements (section 3.4.3) did not show evidence of C-bearing Fe alloys, we cannot completely rule out the potential presence of carbon in the alloy, due to the lack of C-standardization for EDS, FIB, and TEM chemical analyses. Detail maps and point analysis results are listed in Table 3.4.

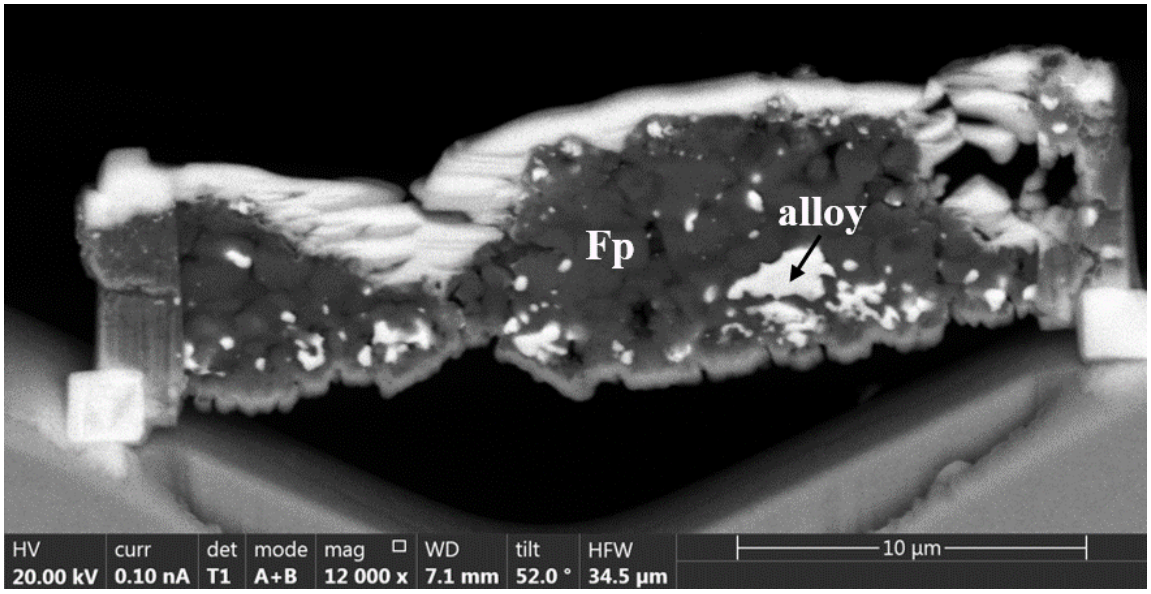

Figure 3.7: BSE image of SD001 sample: the bright phase is the Fe-Ir alloy and the grey phase is ferropericlase.

Table 3.4: Chemical analyses results collected during FIB cutting and with the TEM on recovered lamella (sample SD001).

EDS-FIB point analyses results		**EDS-TEM map results**	
SD001		**SD001**	
$X_{Fe}^{Fe\text{-}Ir}$	X_{FeO}^{Fp}	$X_{Fe}^{Fe\text{-}Ir}$	X_{FeO}^{Fp}
0.42(2)	0.20(1)	0.35(3)	0.24(3)
0.42(2)	0.22(1)	0.46(3)	0.28(3)
0.41(2)	0.21(1)	0.49(3)	0.22(3)
0.41(2)	0.24(1)	0.42(3)	0.28(3)
0.41(2)	0.20(1)	0.52(3)	0.28(3)
	0.19(1)	0.37(3)*	0.26(3)
	0.22(1)	0.42(3)*	0.29(3)
	0.20(1)		0.29(3)
	0.26(1)		0.21(3)
	0.18(1)		0.26(3)
	0.22(1)		0.30(3)
			0.25(2)*
			0.26(2)*
			0.26(2)*

Note: Numbers in brackets are instrumental errors.
*data acquired with point analyses

Furthermore, TEM elemental mapping of Fe, Mg, and Ir was performed on the recovered thin film from sample SD001 to explore the distribution of the chemical elements over the investigated sample surface (Figure 3.8). Elements selection was performed according to the chemical composition of the phases (Table 3.4). The presence of Si and Ca impurities was also detected likely as a result of starting material contamination during the grinding procedure.

Results of chemical analyses and textural observations conducted on the multi anvil experiment (run S7153) show the formation of Fe-Ir alloys by reaction of Fe from ferropericlase with metallic Ir. Figure 3.9 displays Fe-Ir alloys (bright) in the ferropericlase matrix (grey). The average molar fraction of Fe in the alloy was calculated at 14.0(1) % while the FeO content in ferropericlase at 29.0(1) %. Calculated values were used for f_{O_2} calculations.

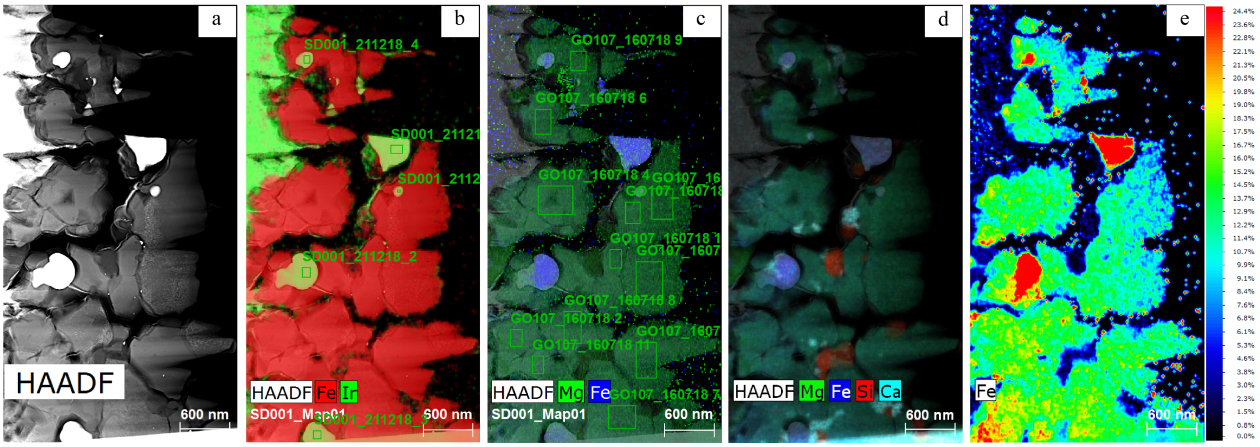

Figure 3.8: Quantitative TEM elemental mapping of Fe, Mg, Ir acquired with the HAADF detector. **a)** BSE image of a selected area of SD001 sample (~40 nm thick); elements selection was performed to highlight Fe-Ir alloys **(b)** and ferropericlase **(c)** grains**.** Green squares show the regions of individual spectrum measurements; **d)** elements distribution image showing contamination of Ca and Si; **e)** a quantitative color-coded map illustrates the Fe concentration in individual grains with highest intensity (red) corresponding to the alloy grains.

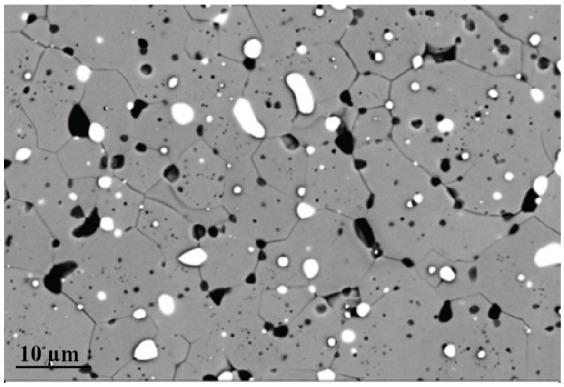

Figure 3.9: BSE image of the S7153 run product. The grey phase is ferropericlase and the bright phase is Fe-Ir alloy. Polishing imperfections are shown in black.

3.4.3 Fe oxidation state in ferropericlase determined by EELS, XANES and SMS spectroscopies

Fe oxidation state in ferropericlase was determined on the recovered DAC experiment SD001 by combining high-resolution Fe $L_{2,3}$-edge EELS, XANES, and SMS spectroscopic analyses. Quantitative EELS measurements were performed on the specimen foil SD001 re-thinned down to ~40 nm of thickness (original thickness of the FIB lamella ~100 nm) to improve the signal/noise ratio of the acquired spectra. Figure 3.10 shows a representative EELS spectrum collected on the TEM film (b) compared to that obtained for ferropericlase starting material (a). The latter shows characteristic white line features of Fe L_3-edge for both divalent and trivalent Fe with maximum intensities at approximately 708.0 eV and 709.5 eV, respectively. We calculated the $Fe^{3+}/\Sigma Fe$ ratio for starting ferropericlase powder at 6(5) % by averaging the results obtained for four EELS spectra, and following the procedure described in Van Aken et al. (1998, 2002). On the other hand, spectra collected on the SD001 sample exhibit a maximum at 707.8 eV followed by a broader and less intense peak at 710.8 eV, characteristic for the EELS on the Fe L_3-edge of divalent iron, indicating either the absence of Fe^{3+} in ferropericlase or that its value lies below the detection limit, i.e., ~5 % according to Van Aken et al., (1998, 2002) methodology.

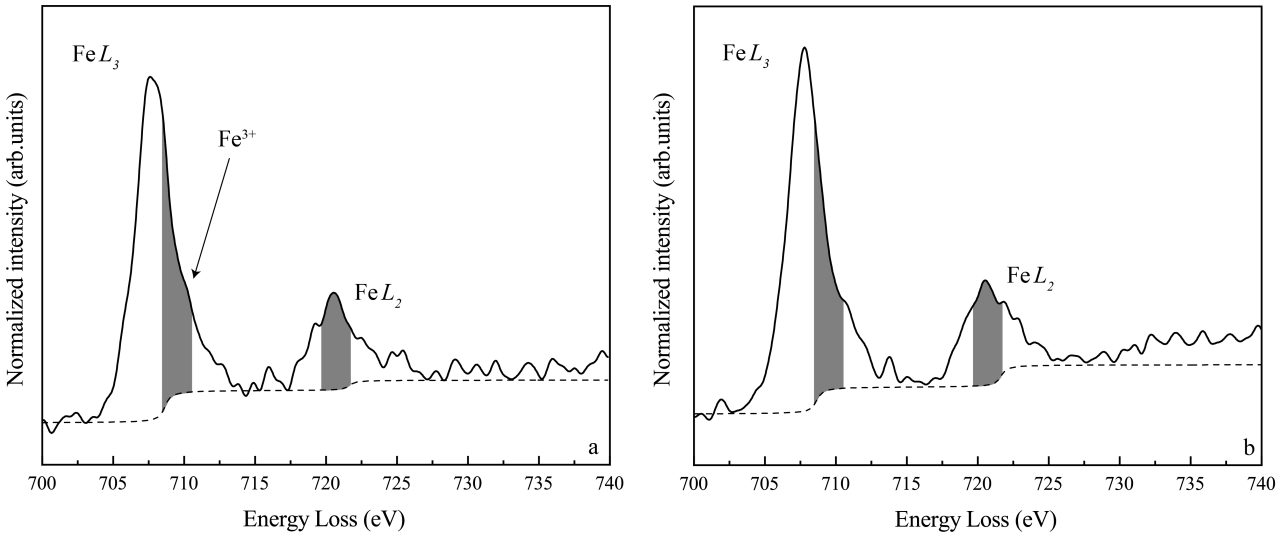

Figure 3.10: Fe $L_{3,2}$ EELS spectra normalized with respect to the integral intensity and corrected for the arctan background function of **a**) ferropericlase starting material and **b**) quenched experimental run SD001.

Results from *in situ* high-pressure XANES spectroscopy measurements collected at the Fe *K*-edge of the quenched sample SD002, provide a complementary qualitative estimation of the ferric/ferrous ratio in ferropericlase. Determination of the Fe oxidation state in ferropericlase was challenging because the intensity of the pre-edge peak, which is commonly used for quantifying the ferric iron content of candidate minerals (e.g., Waychunas et al., 1983; Berry et al., 2003), was significantly weak. For this reason, we followed a different approach adopted in previous XANES studies (e.g., Narygina et al., 2009) determining the ferric iron content in ferropericlase by the energy position of the inflection point of the main Fe *K*-absorption edge in the derivative (rising edge feature in the spectrum). Figure 3.11 shows a normalized XANES spectrum collected at 61.5(1) GPa at the Fe *K*-edge on the best heated region of the sample (black) in comparison with iron metal (red) and Fe oxides (FeO-orange, Fe_2O_3-blue, Fe_3O_4-green) standards related to approximately the same pressure conditions. Comparison of the energy position of the rising edge feature of the sample SD002 (i.e., 7122.7 eV) with respect to that of Fe and Fe oxides shows almost a complete overlap with the FeO component, suggesting that ferropericlase after laser heating is almost completely dominated by ferrous iron, in agreement with EELS results. Moreover, a close look at the absorption spectrum shown in Figure 3.11, highlights the occurrence of the spin cross over's characteristic features of the $^{VI}Fe^{2+}$ in ferropericlase, also observed by X-ray diffraction (see section 3.4.1). The black arrow in Figure 3.11 points out the pronounced peak at ~7144 eV which indicates the occurrence of the $^{VI}Fe^{2+}$ ferropericlase spin cross-over, previously reported in XANES spectra of ferropericlase collected at similar experimental conditions (Narygina et al., 2009).

Results from *in situ* Synchrotron Mössbauer Source spectroscopy for DAC and multi anvil experiments are shown in Table 3.5. We tested the sample's starting material at 11(1) and 36.0(5) GPa at ambient temperature to compare the ferric iron content in ferropericlase before and after laser heating. Figure 3.12a shows an example of SMS spectrum (SD001_84) fitted using a quadruple doublet for the Fe^{2+} and a singlet for the Fe^{3+} in ferropericlase (e.g., McCammon et al., 1998; Longo et al., 2011). The center shifts of the Fe^{2+} and Fe^{3+} absorption features range from 0.90(2) to 1.02(1) mm/s and from 0.07(2) to 0.1 mm/s, respectively, in agreement with previously determined hyperfine parameters for high-spin ferropericlase (e.g., Longo et al., 2011). $Fe^{3+}/\Sigma Fe$ was calculated at ~11(2) % based on the Mössbauer relative areas.

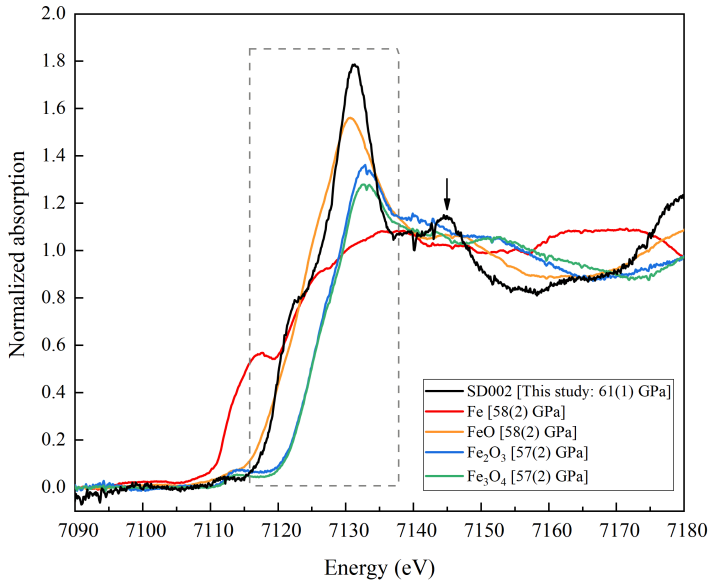

Figure 3.11: Normalized X-ray absorption spectrum of coexisting quenched ferropericlase and Fe-Ir alloy in Ne (black) taken from the center of the heated area (sample SD002). Standards of metal Fe (red), FeO (orange), Fe_2O_3 (blue), and Fe_3O_4 (green) collected at the same pressure within the uncertainty are plotted for comparison. Note that the dashed grey box highlights the XANES region of the spectrum, and the black arrow points out the feature representing the spin transition of the octahedrally coordinated Fe^{2+} in ferropericlase.

A different fitting model was employed to fit SMS spectra collected after laser heating, where along with ferropericlase, Fe metal in the Fe-Ir alloy was detected at approximately the same central shift position of the Fe^{3+} feature for ferropericlase phase. Therefore, we interpreted SMS spectra after laser heating applying fitting constraints based on EELS and XANES results, that detected almost no ferric iron in ferropericlase. A quadruple doublet was assigned to the divalent Fe in ferropericlase, with center shift ranging from 0.90(2) to 1.02(2) mm/s, while a singlet was selected for the metallic iron in the alloy considering the ferric iron component in ferropericlase as negligible (Figure 3.12b, c). Moreover, SMS spectra collected at 61.5(1) GPa show the appearance of a new spectral component (dashed singlet in Figure 3.12c) with a lower center shift compare to HS Fe^{2+} (e.g., 0.63(2)-0.67(7) mm/s) consistent with a low spin state of $^{VI}Fe^{2+}$, also detected by XANES spectroscopy results (Figure 3.11).

Figure 3.12d shows an example of SMS spectrum collected on sample S7153 recovered from a multi anvil run, performed employing the same starting composition of DAC experiments. We processed Mössbauer spectra using the same fitting criteria of that used for spectra acquired in DAC after laser heating, using a doublet for the HS Fe^{2+} in ferropericlase and a singlet for Fe^0 in the alloy. Noteworthy, is the higher background fluctuation of the spectrum in Figure 3.12d compared to that obtained for SMS spectra acquired on DAC samples related to the shorter

acquisition time. Furthermore, an asymmetric doublet was added to the fit of all SMS spectra to exclude the Fe contribution of the Be lenses placed in the optic setup of ID18 beamline from the $Fe^{3+}/\Sigma Fe$ calculation in ferropericlase (see section 2.3.1 for details).

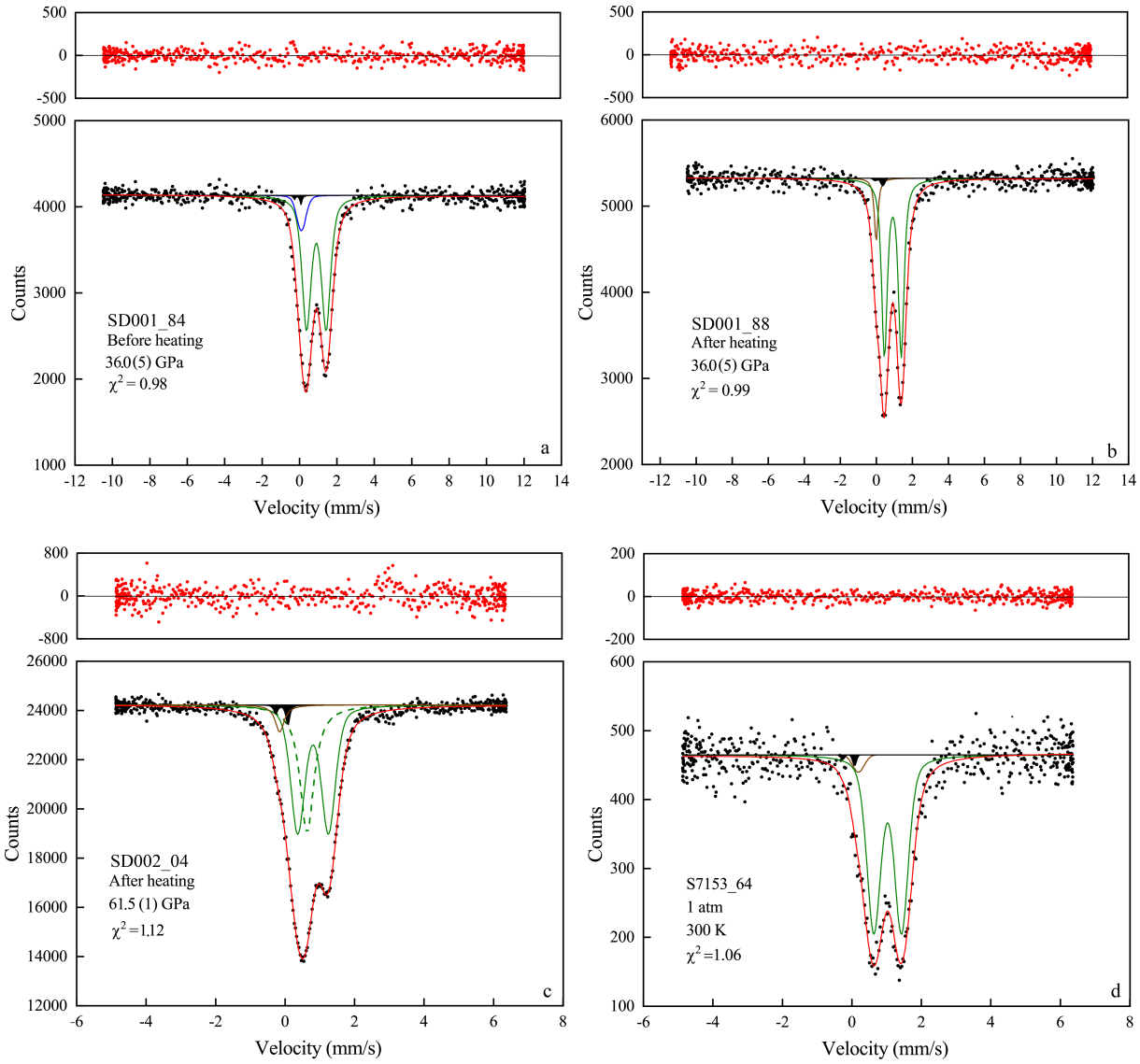

Figure 3.12: **a)** Room temperature Mössbauer spectrum of the starting material; **b)** The same material after laser heating in diamond anvil cell at 36.0(5) GPa, and, **c)** at 61.5(1) GPa (run SD002); **d)** SMS spectrum of the S7173 recovered run product from a multi anvil experiment collected at ambient conditions. In all spectra, solid circles (black) are experimental data, solid curves (red) represent the total fit performed with pseudo-Voigt functions, solid doublets (green) are high-spin Fe^{2+} absorption, and singlet features are either Fe^{3+} in ferropericlase (blue-Figure **a**) or Fe^{0} in Fe-Ir alloy (brown-Figure **b**, **c**, **d**). Spectra acquired at 61.5(1) GPa show the appearance of a new spectral component (dashed green singlet-Figure **c**) representing the low-spin Fe^{2+} absorption. An asymmetric doublet was added to the fit of all SMS spectra (solid black) to exclude the Fe contribution of the Be lenses placed in the optic setup of ID18 beamline from the $Fe^{3+}/\Sigma Fe$ calculation in ferropericlase. The residual is shown in red above each spectrum. The velocity scale is relative to α-Fe at ambient conditions.

Table 3.5: Hyperfine parameters derived from fitting to Synchrotron Mössbauer Source spectra of DAC (SD001 and SD002) and multi anvil experiments (S7153).

Run	P (GPa)	T(K)	IS (mm/s)	QS (mm/s)	W (mm/s)	Site	$Fe^{3+}/\Sigma Fe$ (%)	X^2
SD001_38	11(1)	300 (b.h.)	1.02(1)	0.98(1)	0.54(2)	Fe^{2+} Fp	12(1)	1.06
			0.07(2)	-	0.70(7)	Fe^{3+} Fp		
SD001_84	30(1)	300 (b.h.)	0.90(2)	1.04(3)	0.58(5)	Fe^{2+} Fp	11(2)	0.98
			0.1	-	***0.5***	Fe^{3+} Fp		
SD001_88	36.0(5)	300 (a.h.)	0.92(1)	0.93(2)	0.38(7)	Fe^{2+} Fp	-	0.99
			-0.01(4)	-	0.23(9)	Fe^{0} alloy		
SD001_89	36.0(5)	300 (a.h.)	0.92(2)	0.91(3)	0.47(6)	Fe^{2+} Fp	-	0.92
			-0.04(13)	-	0.5(3)	Fe^{0} alloy	-	
SD001_90	36.0(5)	300 (a.h.)	0.92(1)	0.92(2)	0.43(5)	Fe^{2+} Fp	-	0.98
			-0.03(5)	-	0.4(2)	Fe^{0} alloy	-	
SD001_110	1 atm	300 (a.h.)	1.03(3)	0.77(5)	0.4(2)	Fe^{2+} Fp	-	0.95
			0.1(2)	-	0.4(7)	Fe^{0} alloy	-	
SD001_111	1 atm	300 (a.h.)	1.04(2)	0.75(4)	0.43(6)	Fe^{2+} Fp	-	0.99
			0.1(1)	-	0.5(3)	Fe^{0} alloy		
SD001_112	1 atm	300 (a.h.)	1.03(2)	0.77(3)	0.3(1)	Fe^{2+} Fp	-	1.05
			0.09(7)	-	0.3(3)	Fe^{0} alloy		
SD002_04	61.5(1)	300 (a.h.)	0.81(2)	0.89(4)	0.49(5)	*Fe^{2+} Fp	-	1.12
			0.63(2)	-	0.5(1)	*Fe^{2+} Fp		
			-0.16(7)	-	0.3(5)	Fe^{0} alloy		
SD002_06	61.5(1)	300 (a.h.)	0.85(7)	0.83(6)	0.45(8)	*Fe^{2+} Fp	-	1.05
			0.67(6)	-	0.6(9)	*Fe^{2+} Fp		
			0.0	-	***0.3***	Fe^{0} alloy		
S7153_63	1 atm	300	1.03(2)	0.80(3)	0.47(4)	Fe^{2+} Fp	-	0.85
			0.06(8)	-	***0.4***	Fe^{0} alloy		
S7153_64	1 atm	300	1.03(3)	0.80(4)	0.48(7)	Fe^{2+} Fp	-	1.05
			0.2(3)	-	***0.4***	Fe^{0} alloy	-	

Note: Uncertainties of the last significant digit are shown in brackets. "b.h." and "a.h." stand for spectrum acquisition before and after laser heating, respectively. Numbers in bold italics were held fixed during the fitting.
*Fe^{2+} hyperfine parameters are related to the low spin state.

3.4.4 Mass balance calculation

Based on quantitative chemical analyses (section 3.4.2) and results on the iron valence state assessed with different methodologies (section 3.4.3) we tracked the redox reactions that occurred during the laser heating in diamond anvil cell using the mass balance approach. At high temperature, starting ferropericlase (Fe/ (Fe + Mg) = 0.25) reacted with Ir metal forming a Fe-Ir alloy containing 42(2) mol % of Fe, as determined by EDS measurements (section 3.4.2). According to *post mortem* chemical analyses and mass balance calculations, the initial Fe content in ferropericlase decreased to 22(2) mol % since it partitioned into the iridium structure forming a $Fe_{0.40}Ir_{0.60}$ alloy solid solution. The redox reaction that took place during the laser heating is shown below,

$$0.95Fe_{0.25}Mg_{0.75}O + 0.05Ir \rightarrow 0.92Fe_{0.22}Mg_{0.78}O + 0.08Fe_{0.4}Ir_{0.6} + 0.017O_2\,. \qquad (3.1)$$

SMS and EELS spectroscopies showed that the starting oxide contained between 6(5) to 12(2) % $Fe^{3+}/\Sigma Fe$, while, during laser heating most of the ferric iron in ferropericlase reduced to ferrous Fe (see section 3.4.3). According to this scenario, we can describe the reduction process (Equation 3.2) assuming that all Fe^{3+} in ferropericlase was reduced to Fe^{2+} as follows,

$$0.28Fe_2O_3 \rightarrow 0.057FeO + 0.014\,O_2. \qquad (3.2)$$

Moreover, considering that the diamond anvil cell is a closed system, the oxygen generated by equations 3.1 and 3.2 probably oxidized another phase, likely the Fe-Ir alloy (Equation 3.3):

$$0.62Fe + 0.31O_2 \rightarrow 0.062FeO \qquad (3.3)$$

This hypothesis is consistent with the Mossbauer relative areas of ferrous iron obtained before and after laser heating, as illustrated in Figure 3.12a and 3.12b.

3.4.5 Oxygen fugacity

Oxygen fugacity (f_{O_2}) in DAC and multi anvil experiments was calculated using the Fe-Ir redox sensor (Woodland & O'Neill, 1997; Borisov & Palme, 2000), starting from the equilibrium,

$$\underset{\text{alloy}}{2Fe} + \underset{}{O_2} = \underset{\text{Fp}}{2FeO} \tag{3.4}$$

using the expression,

$$\log(f_{O_2}) = \frac{-\Delta_r G°_{P,T}}{\ln(10)\,RT} + 2\log a_{FeO}^{Fp} - 2\log a_{Fe}^{alloy} \tag{3.5}$$

where, R is the gas constant and $\Delta_r G°_{P,T}$ is the standard Gibbs free energy of equilibrium (3.4) determined using the following expression (Cemič, 2005),

$$\Delta_r G°_{T,P} = \Delta_r H_T - T\Delta_r S_T + \int \Delta_r V_{298}\, dP\ (P - P_0). \tag{3.6}$$

$\Delta_r H_T$ and $\Delta_r S_T$ are enthalpy and entropy of the reaction, calculated as a function of temperature by equations (3.7) and (3.10), respectively. Temperature dependence is expressed by integrating the heat capacity C_p polynomials (3.9) and (3.11) at 2000 K. Thermodynamic parameters, including the C_p coefficients, standard enthalpies $\Delta_f H°_{298}$ and entropies S_{298} of formation for end member phases have been taken from Holland & Powell (1998, 2011) and are listed in Table 3.6.

Table 3.6: End member thermodynamic data used for calculating $\Delta_r G°_{T,P}$ of equilibrium 3.4.

	$\Delta_f H°_{298}$ †	S_{298} †	a†	b†	c†	d†	C_p	V_0^*	K_{T0}^*	α†
	Jmol^{-1}	JK^{-1}mol^{-1}	JK^{-1}	JK^{-2}	JK	JK$^{-0.5}$	JK^{-1}mol^{-1}	cm^{3}mol^{-1}	GPa	JK^{-1}
Fe	0	27.09	46.2	0.005159	723100	-556.2	23.66	7.076	133±3	0.0000356
FeO	-271970	60.6	44.4	0.00828	-1214200	185.2	43.94	12.2560	146.9±1.3	0.0000743
O2	0	205.2	48.3	0.000691	499200	-420.7	29.76	-		-

Note: †Values taken from Holland and Powell (1998; 2011); C_p is calculated from the heat capacity coefficients (i.e., a, b, c, and d) at 2000 K. * Values taken from Campbell et al. (2009).

$$\Delta_r H_T = -2\left(\Delta_f H°_{298} + \int C_p\, dT\right)_{Fe^{alloy}} - \left(\Delta_f H°_{298} + \int C_p\, dT\right)_{O_2} + 2\left(\Delta_f H°_{298} + \int C_p\, dT\right)_{FeO^{Fp}} \quad (3.7)$$

$$C_p = \mathrm{a} + \mathrm{b}T + \mathrm{c}T^{-2} + \mathrm{d}T^{-\frac{1}{2}} + \mathrm{e}T^2 \quad (3.8)$$

$$\int C_p\, \mathrm{d}T = \mathrm{a}(T - 298) + \frac{\mathrm{b}}{2}(T^2 - 298^2) - \frac{\mathrm{c}}{T^2}\left(\frac{1}{T} - \frac{1}{298}\right) + 2\mathrm{d}\left(T^{\frac{1}{2}} - 298^{\frac{1}{2}}\right) + \frac{\mathrm{e}}{3}(T^3 - 298^3) \quad (3.9)$$

$$\Delta_r S_T = -2\left(S_{298} + \int \frac{C_p}{T}\, dT\right)_{\mathrm{Fe}^{\mathrm{Fe-Ir}}} - \left(S_{298} + \int \frac{C_p}{T}\, dT\right)_{\mathrm{O_2}} + 2\left(S_{298} + \int \frac{C_p}{T}\, dT\right)_{\mathrm{FeO}^{\mathrm{Fp}}} \quad (3.10)$$

$$\int \frac{C_p}{T}\, dT = a\ln\left(\frac{T}{298}\right) + b(T - 298) - \frac{c}{2}(T^{-2} - 298^{-2}) - 2d\left(T^{-\frac{1}{2}} - 298^{-\frac{1}{2}}\right) + \frac{e}{2}(T^2 - 298^2) \quad (3.11)$$

$\Delta_r V_{298}$ represents the volume dependence of the reaction, and the integral $\int \Delta_r V_{298}\, dP$ reads,

$$\int \Delta_r V_{298}\, dP = \left[\Delta_r V_{298} + \Delta_r(\alpha V_{298})(T - 298) - \frac{\Delta_r(\beta V_{298})P}{2}\right](P - P_0) \quad (3.12)$$

$$\alpha = \alpha_0 + \alpha_1 T + \frac{\alpha_2}{T^2} + \frac{\alpha_3}{T}. \quad (3.13)$$

Therefore, the Gibbs free energy of the reaction (3.4) can be written as,

$$\Delta G^{\circ}_{P,T} = \Delta_r H_{298} + \int \Delta_r C_p \, dT \; - \; T\Delta_r S_{298} - T \int \frac{\Delta_r C_p}{T} \, dT \; +$$
$$+ \left[\Delta_r V_{298} + \Delta_r (\alpha V_{298}) (T - 298) - \frac{\Delta_r (\beta V_{298}) P}{2} \right] (P - P_0). \qquad (3.14)$$

The $a_{\mathrm{FeO}}^{\mathrm{Fp}}$ and $a_{\mathrm{Fe}}^{\mathrm{alloy}}$ in Equation (3.5) are activity-composition relations of the FeO and Fe component in ferropericlase (3.15) and Fe-Ir alloy (3.16), respectively, and are given as,

$$a_{FeO^{Fp}} = X_{FeO}^{Fp} \cdot \gamma_{FeO}^{Fp} \qquad (3.15)$$

$$a_{Fe}^{alloy} = X_{Fe}^{alloy} \cdot \gamma_{Fe}^{alloy} \qquad (3.16)$$

where γ_{FeO}^{Fp} and γ_{Fe}^{alloy} are the activity coefficients that describe the non-ideality of symmetric (3.17) and asymmetric (3.18) binary solid solutions, and are frequently determined using the Margules formalism (Thompson and Waldbaum, 1969):

$$RTln\gamma_{FeO}^{Fp} = (1 - X_{FeO})^2 \cdot W_{FeO-MgO}^{Fp} \qquad (3.17)$$

$$RT \; ln\gamma_{Fe}^{alloy} = (1 - X_{Fe})^2 \, [W_{Fe-Ir}^{H} \; + \; 2X_{Fe} \, (W_{Ir-Fe}^{H} \; - \; W_{Fe-Ir}^{V})]. \qquad (3.18)$$

$W_{FeO-MgO}^{Fp}$ (Equation 3.17) is the FeO-MgO interaction parameter for stoichiometric ferropericlase and is taken from the literature (Frost, 2003; O'Neill et al., 2003). W_{Fe-Ir}^{H} and W_{Ir-Fe}^{H} are the enthalpy-dependent asymmetric Margules parameters from Schwerdtfeger and Zwell (1968) that describe the interaction between Fe and Ir components in the metallic phase. W_{Fe-Ir}^{V} expresses the volume dependency of the interaction parameter and is given in Schwerdtfeger and Zwell (1968).

Oxygen fugacity of DAC and multi anvil experiments determined with the Fe-Ir sliding redox sensor are given in Table 3.7 together with the experimental conditions and employed thermodynamic parameters from the literature.

Table 3.7: Oxygen fugacities calculated with the Fe-Ir redox sensor model for DAC and multi anvil experiments are shown together with employed thermodynamic parameters from the literature.

Run	P (GPa)	T (K)	X_{Fe}^{alloy}	X_{FeO}^{Fp}	W_{Fe-Ir}^{H} (J/mol)	W_{Ir-Fe}^{H} (J/mol)	W_{Fe-Ir}^{V} (J/bar)	$W_{FeO-MgO}^{Fp}$ (J/bar)	logf_{O2}	logf_{O2} [IW]
SD001	36.0(5)	2000	0.42(2)	0.24(4)	-51814[a]	-62769[a]	0.0736[a]	11000[b]	-6.5(4)	0.9(4)
SD001	36.0(5)	2000	0.42(2)	0.24(4)	**-2819(143)**	**-13801(143)**	**0.15(6)**	**14960[b]**	**-2.8(4)**	**0.2(4)**
SD002	61.5(1)	2000	0.42(2)	0.24(4)	-51814[a]	-62769[a]	0.0736[a]	11000[b]	-6.5(4)	0.9(4)
SD002	61.5(1)	2000	0.42(2)	0.24(4)	**34247(659)**	**23265(659)**	**0.14(5)**	**17710[b]**	**-3.1(4)**	**-0.4(4)**
S7153	26(1)	2000	0.14(1)	0.29(1)	-51814[a]	-62769[a]	0.0736[a]	11000[b]	-4.4 (4)	3.0(4)
S7153	26(1)	2000	0.14(1)	0.29(1)	**-17974(66)**	**-28956(66)**	**0.15(6)**	**13860[b]**	**-2.0(4)**	**1.8(4)**

Note: Numbers in parenthesis are standard deviations on the last significant digit. Values in bold are parameters at high pressure (see section 3.5)
[a]Values at 1atm taken from Schwerdtfeger and Zwell (1968)
[b]Values taken from Frost et al. (2003) and O'Neill et al. (2003)

The f_{O_2} results determined for DAC experiments are 0.9(4) log units above to the iron wüstite (IW) buffer, reducing compare to that measured during multi anvil experiment, i.e., 3.0(4) log units normalized to IW, performed using the same starting composition. Uncertainties on the f_{O_2} were propagated on the activity-composition relation.

3.5 DISCUSSION

3.5.1 Calibration of the Fe-Ir oxybarometer at high pressure

The activity-compositional model employed to calculate the f_{O_2} of DAC and multi anvil experiments (section 3.4.5) is based on the Fe-Ir phase relations determined as a function of temperature and composition (Swartzendruber, 1984). However, to accurately determine the redox condition during high-pressure and high-temperature experiments it is also important to consider how the volume change with pressure affects the thermodynamic properties of the Fe-Ir alloy. Therefore, we implemented the existing activity model including the compressibility behaviour of the alloy obtained by X-ray diffraction, determining the excess molar volume of mixing $\Delta_m V^{ex}$ of Fe in Ir as a function of pressure, as follows,

$$\Delta_m V^{ex} = V_{Fe-Ir} - (X_{Fe}^{Pure} \cdot V_{Fe}^{Pure} + X_{Ir}^{Pure} \cdot V_{Ir}^{Pure}) \quad (3.19)$$

where V_{Fe-Ir} is the molar volume of the Fe-Ir alloy with 42(2) mol % of Fe (see section 3.4.2) and X_{Fe}^{Pure} / X_{Ir}^{Pure} and V_{Fe}^{Pure} /V_{Ir}^{Pure} are the molar fraction and molar volume of the pure endmembers of the solid solution. Our estimated molar volume (8.104(1) cm^3mol^{-1}) and $\Delta_m V^{ex}$ (0.20(2) J/bar) at room pressure (Figure 3.13) is in excellent agreement with existing data of Fe-Ir alloys reported for a wide compositional range (Schwerdtfeger and Zwell, 1968; Mohseni, Master Thesis 2014).

In order to determine $\Delta_m V^{ex}$ at high pressure, we compared the unit cell volume of our alloy composition with pure Fe and Ir equations of state from previous studies (Campbell et al., 2009; Yusenko et al., 2019) up to 100 GPa. Figure 3.14 shows the isothermal bulk modulus K_{T0} of $Fe_{0.42}Ir_{0.58}$ alloy in comparison with those determined for Fe (e.g., Campbell et al., 2009) and Ir (Yusenko et al., 2019) pure endmembers. The Fe-Ir compressibility-composition relation positively deviates from the K_{T0}-X_{Fe} ideal mixing of the pure components showing an additional evidence of a non-ideal binary solid solution.

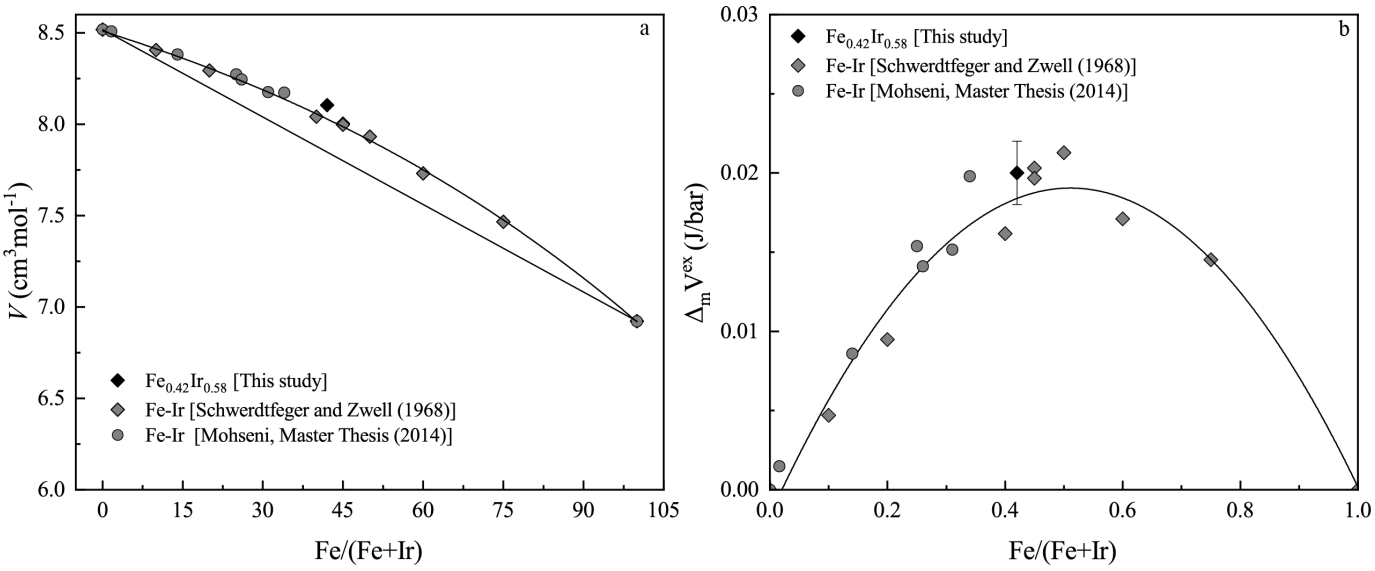

Figure 3.13: **a**) Molar volume and **b**) excess molar volume of mixing of Fe-Ir alloys at 1 bar. Solid black diamonds are $Fe_{0.42}Ir_{0.58}$ determined in this study, solid grey diamonds and circles are molar volume and $\Delta_m V^{ex}$ from Schwerdtfeger and Zwell (1968) and Mohseni (Master thesis, 2014), respectively.

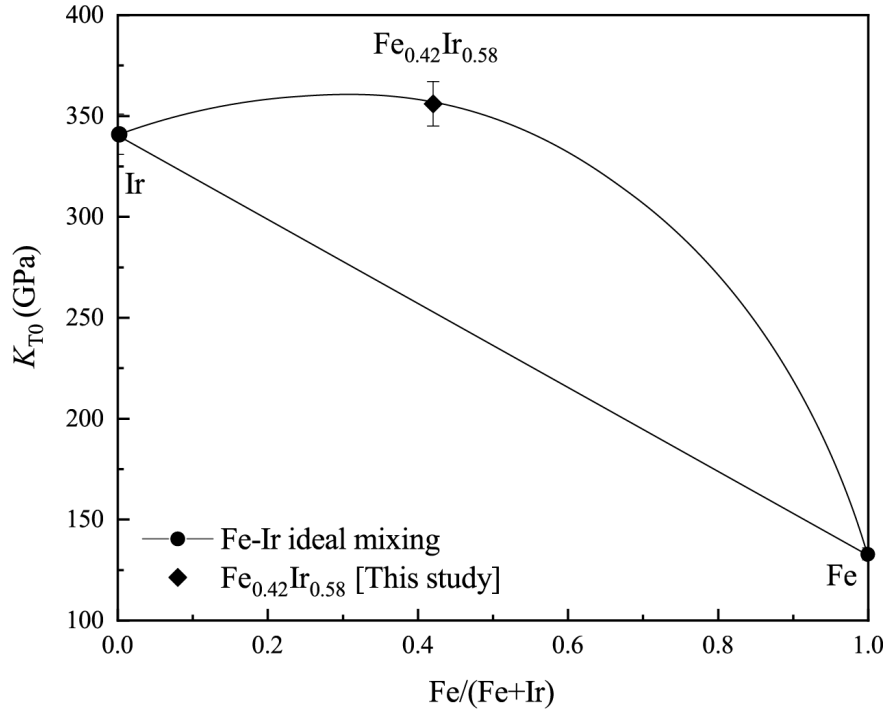

Figure 3.14: Compressibility-composition relation of $Fe_{0.42}Ir_{0.58}$ alloy (black diamond symbol) and pure metallic Fe (Campbell et al., 2009) and Ir (Yusenko et al., 2019) (black circles).

In order to include the pressure dependency in the Fe-Ir activity model, we modify Equation 3.18 calibrating the asymmetric Margules interaction parameters as a function of pressure, as shown below. Considering that the excess molar volume of mixing is proportional to the volume-dependent interaction parameter W_{Fe-Ir}^{V}, i.e.,

$$\Delta_m V^{ex} = X_{Fe}^{Fe-Ir} \cdot X_{Ir}^{Fe-Ir} \cdot W_{Fe-Ir}^{V} \tag{3.20}$$

we calculated W_{Fe-Ir}^{V} by means of Equation 3.21 up to 100 GPa, as follows:

$$W_{FeIr}^{V} = \frac{\Delta_m V^{ex}}{(X_{Fe}^{Fe-Ir} \cdot X_{Ir}^{Fe-Ir})} \tag{3.21}$$

in which $\Delta_m V^{ex}$ is the excess molar volume of mixing at a certain pressure. Figure 3.15 displays the obtained W_{Fe-Ir}^{V} up to 100 GPa.

To include the pressure effect on the W_{Fe-Ir}^{H} and W_{Ir-Fe}^{H} parameters, we fitted the HP W_{FeIr}^{V} parameters using a 4th order polynomial function (red line Figure 3.15),

$$(W_{FeIr}^{V})_{\text{fit}} = \text{ax}^4 + \text{bx}^3 - \text{cx}^2 + \text{dx} + \text{e}\,. \tag{3.22}$$

The integral of the polynomial (Equation 3.22) reads,

$$\int_{P_0}^{P} (W_{FeIr}^{V})_{\text{fit}}\ \text{dP} = \left(\frac{a}{5}P^5 - \frac{a}{5}P_0^5\right) + \left(\frac{b}{4}P^4 - \frac{b}{4}P_0^4\right) - \left(\frac{c}{3}P^3 - \frac{c}{3}P_0^3\right) + \left(\frac{d}{2}P^2 - \frac{d}{2}P_0^2\right) + \\ +(eP - eP_0). \tag{3.23}$$

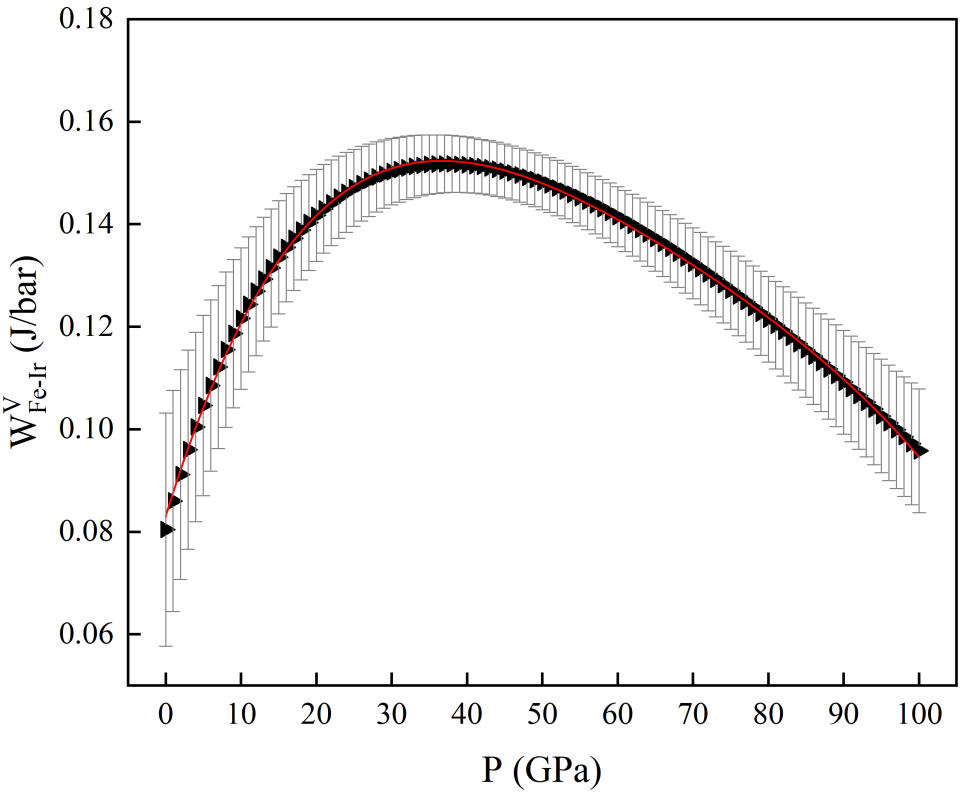

Figure 3.15: Volume-dependent Margules parameter as a function of pressure. The solid red line is the 4th order polynomial fit of the data.

The asymmetric interaction parameters were corrected for the pressure adding to the value the newly determined integral of W^V_{FeIr} as follows,

$$(W^H_{Fe-Ir})_P = (W^H_{Fe-Ir})_{1bar} + \int_{P_0}^{P} (W^V_{FeIr})_{\text{fit}}\ dP \tag{3.24}$$

$$(W^H_{Ir-Fe})_P = (W^H_{Ir-Fe})_{1bar} + \int_{P_0}^{P} (W^V_{FeIr})_{\text{fit}}\ dP\ . \tag{3.25}$$

Therefore, the non-ideal component (Equation 3.18) of the activity corrected for the pressure become

$$RT\ ln\gamma^{Fe-Ir}_{Fe} = (1 - X_{Fe})^2\ [(W^H_{Fe-Ir})_P\ +\ 2X_{Fe}\ ((W^H_{Ir-Fe})_P\ -\ (W^H_{Fe-Ir})_P)] \tag{3.26}$$

Figure 3.16 illustrates the comparison between oxygen fugacity results for multi anvil and diamond anvil cell experiments, determined with the existing redox sensor model (grey) and the newly calibrated oxybarometer at high pressure (black).

Redox buffer equilibria, i.e., Re-ReO_2, FMQ, and IW were taken from the literature and refer to 1 atm. A brief summary of the employed equations is given below. Oxygen fugacity for FMQ (Equation 1.16), IW (Equation 1.15), and Re-ReO_2 equilibria,

$$\mathrm{Re} + \mathrm{O_2} = \mathrm{ReO_2} \qquad \mathrm{Re} - \mathrm{ReO_2}\ (3.27)$$

were calculated from,

$$\log(f_{\mathrm{O_2}}) = \frac{\Delta G^{o}_{P,T(1.15;1.16;3.27)}}{\ln(10)RT} \qquad (3.28)$$

at room pressure and 2000 K.

Specifically, for equilibrium 1.16 the following analytical expression (FMQ: O'Neill, 1987) was employed,

$$\log\left(f_{\mathrm{O_2}}\right)_{1bar} = 82.75 + 0.00484 \times T - \frac{30681}{T} - 24.45 \times \log(10) \times T. \qquad \mathrm{FMQ}(3.29)$$

For Re-ReO_2 (equilibrium 3.27), the 1 bar expression of Pownceby & O'Neill (1994) was used to calculate $\Delta G^{o}_{T,1bar(3.27)}$, i.e.,

$$\Delta G^{o}_{T,1bar(3.27)} = -451020 + 297.595 \times T - 14.6585 \times T \times \ln T. \qquad (3.30)$$

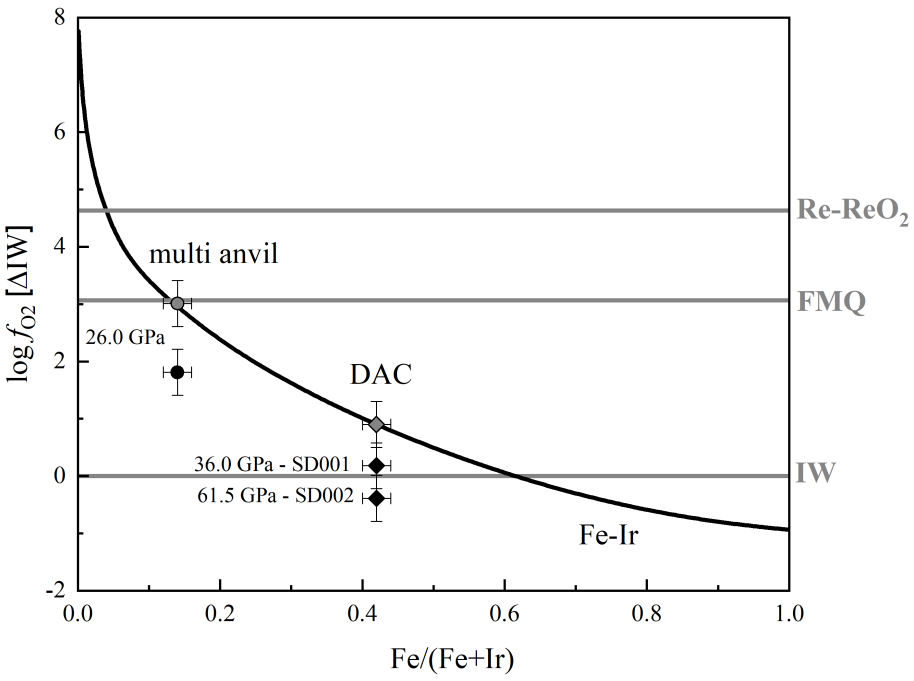

Figure 3.16: Oxygen fugacity determined with the existing redox sensor model (grey) compared to f_{O_2} results obtained with the newly calibrated model at high pressure (black) for multi anvil (circles) and DAC (diamonds) experiments. Grey lines are buffer equilibria calculated at 1 atm (Re-ReO$_2$:Pownceby & O'Neill, 1994; FMQ: O'Neill, 1987; IW: Huebner, 1971). The solid black line represents the logf_{O_2} normalized to IW as a function of the entire compositional range for the Fe-Ir solid solution at 1 atm (Mohseni Master thesis, 2014).

The f_{O_2} results are shown in Table 3.7 together with employed HP interaction parameters determined in this study. The complete list of thermodynamic variables is provided in the appendix (Table S1). Oxygen fugacities calculated at the specific experimental conditions with the updated activity model are lower than those estimated with the existing Fe-Ir sliding redox sensor, with f_{O_2} becoming more reducing with increasing pressure (see Table 3.7 and Figure 3.16). Moreover, comparison of the f_{O_2} obtained for DAC (i.e., 0.2 ± 0.4 log units normalized to IW, run number SD001) and multi anvil experiments (i.e., 1.8 ± 0.4 log units normalized to IW) performed at 36 GPa and 26 GPa, respectively, shows that the redox conditions are lower in DAC as already predicted by the existing model calibrated at 1 bar (section 3.4.5). A possible explanation relates to the capsule material (Re) of the multi anvil experiment that buffered the fugacity conditions at higher values.

3.6 CONCLUSION REMARKS

In this study we developed a novel approach to measure the redox conditions during diamond anvil cell experiments using the Fe-Ir sliding redox sensor. We found that the oxygen fugacity in DAC is lower than that determined for multi anvil experiments performed at comparable experimental conditions (i.e., 26 GPa and 36 GPa) and employing the same starting material. We further observed reducing conditions in DAC from EELS, XANES, and SMS spectroscopies, that showed negligible ferric iron in ferropericlase, and enabled to track the redox reactions that occurred during laser heating by mass balance. Moreover, we updated the existing redox sensor model including the pressure effect on the activity-composition relations of Fe-Ir solid solution. The inferred oxygen fugacities measured at the specific P-T conditions of the experiments are lower than estimates obtained with the existing model. The approach proposed in this study is a first step in considering the diamond anvil cell as a petrological tool to investigate the mantle redox state at the extreme conditions of Earth's interior and provides a new method to calculate the oxygen fugacity at high pressure.

Chapter 4

4 FERRIC IRON CONTENT OF NATURAL DIAMOND INCLUSIONS FROM RIO SORISO (JUINA, BRAZIL) AND SYNTHETIC FERROPERICLASE: IMPLICATIONS FOR REDOX MECHANISMS OF DIAMOND FORMATION

4.1 INTRODUCTION

Ferropericlase ($(Fe_xMg_{1-x})O$, $x \leq 0.5$) is one of the main mineral phases forming Earth's lower mantle according to the pyrolite compositional model (Ringwood, 1991; Kesson et al., 1998; Hirose, 2002; Irifune et al., 2010). Although it constitutes only ~20 volume % of the lower mantle assemblage, it is one of the most commonly found inclusions (> 50 % occurrence) in sub lithospheric diamonds (e.g., Kaminsky, 2012). Over the past decades, mineral inclusions have been extensively studied, giving new insights into diamond-forming processes simulated by laboratory and theoretical works (e.g., Shirey et al., 2013; Smith, et al., 2016; Nestola et al., 2016). In this context, the determination of the ferric iron content of natural ferropericlase inclusions provides important constraints in modelling the lower mantle redox state, being sensitive to the oxygen fugacity at high pressure. However, only few experimental studies exist that provide evidence of ferropericlase being redox-sensitive to the local oxygen redox state, i.e., its role in redox reactions resulting into diamond formation and oxidation is unclear. To date, the presence of ferropericlase in superdeep diamonds has been shown to present a diverse chemical composition expressed as Fe# (i.e., Fe/(Fe + Mg)) or Mg# (i.e., Mg/(Mg + Fe)) (Kaminsky, 2012 and references therein), with a composition much more Fe-rich (up to a Mg# of 0.36) with respect to what is observed in experimental data of synthetic ferropericlase (Mg# of ~0.73-0.88) (e.g., Wood, 2000; Lee et al., 2004). In addition, a preliminary oxybarometer for the lower mantle that involves ferropericlase promotes a lower mantle redox state as oxidized as that of the upper mantle (Wirth et al., 2014), in contrast with the consensus of a reduced lower mantle to f_{O_2} values where metallic Fe is present (Frost et al. 2004).

Although numerous advancements have been made combining both natural and experimental evidence, we still have an incomplete picture of the complex redox processes occurring at extreme conditions due to local variation of oxygen fugacities induced, for example, by the influx of (hydrated) carbonated subducting slabs. In this study, we examine the ferric iron content using Mössbauer spectroscopy of both natural diamond inclusions from the Rio Soriso (Juina area, Mato Grosso State, Brazil) and synthetic ferropericlase equilibrated at HP-HT with magnesite and diamond at lower mantle conditions. Our results provide unique information on the maximum ferric iron content that ferropericlase can incorporate at f_{O_2} conditions where both carbonate and diamond can coexist to shade light on processes such as redox-driven diamond formation and redox melting. Our experimental results are, then, integrated with measurements of $Fe^{3+}/\Sigma Fe$ on ferropericlase inclusions from Brazilian super deep diamonds to address the role of pressure, temperature and oxygen fugacity.

4.2 MATERIALS AND ANALYTICAL TECHNIQUES

4.2.1 Experimental multi anvil runs

Multi anvil experiments were performed at pressures of 25 and 40 GPa and temperature between 1500 and 1700 °C using a mixture of magnesite, graphite powder, pre-synthesized ferropericlase (X_{Fe} = 0.17), and reagent-grade iridium metal (3 wt. %, 99.999 % purity) added to act as a redox sensor (see section 1.3) all loaded into graphite capsules wrapped by Re foils. Details on the sample synthesis are reported by Stagno et al. (2011). The recovered run products were placed in epoxy resin sectioned and polished for chemical and spectroscopic measurements down to the nanoscale. Mössbauer spectroscopy measurements (section 4.2.3) were carried out on double-polished capsules according to the ideal thickness determined as a function of the Fe content. The analyses of recovered Fe-periclase show chemical variation with Fe# ranging from 0.149(4) and 0.349(2) within the investigated experimental P-T conditions (Stagno et al., 2011).

4.2.2 Natural ferropericlase inclusions

Natural inclusions of ferropericlase trapped in sub-lithospheric diamonds from the alluvial deposit of Rio Soriso (Mato Grosso State, Brazil) were supplied by Prof. Kaminsky and are shown in Figure 4.1. These inclusions appear opaque in color, with either subhedral morphology or as elongated laths. Their size varies from ~20 µm to ~500 µm within the same diamond. Optical analyses show also the presence of additional non-touching inclusions along with ferropericlase. Diamonds have been mounted in four different epoxy blocks and polished with a diamond plate to be analyzed. A summary of natural and experimental samples is given in Table 4.1. We focused on those inclusions exposed to the surface after polishing.

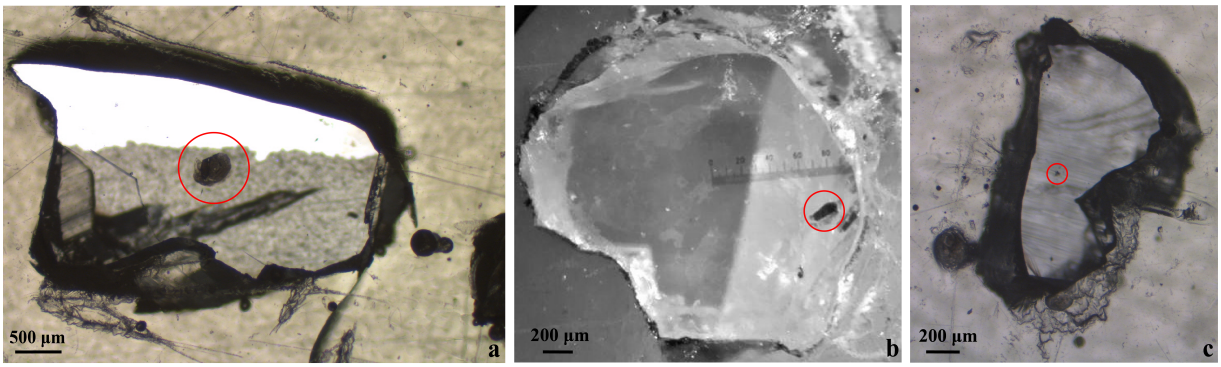

Figure 4.1: Super deep diamonds (**a**-2.7.2a, **b**-3.9.3b, **c**-3.5.2b) from the alluvial deposit of Rio Soriso (Mato Grosso State, Brazil). Natural ferropericlase inclusions are shown in the red circles.

4.2.3 Mössbauer Spectroscopy measurements on synthetic and natural ferropericlases

We determined the Fe oxidation state in synthetic ferropericlase and natural inclusions using Mössbauer spectroscopy. The experimental run products (Table 4.1) were analyzed at room temperature and pressure in transmission mode using a constant-acceleration Mössbauer spectrometer at Bayerisches Geoinstitut equipped with a 370 MBq ^{57}Co radioactive point source (500×500 µm^2) in a 12 µm Rh matrix, used as source of single-line γ-rays. The velocity scale was set from +5 to -5 mm/s and calibrated relative to α-Fe, with line widths of 0.36 mm/s obtained for outer lines of α-Fe at room temperature. Ta foil with a 500 µm hole was placed over the sample surface to select the area to be measured (see Figure S1 in the appendix). Gamma rays transmitted through the sample were recorded by a detector coupled with a multichannel analyzer. The signal

was then folded to obtain a flat background. Acquisition time of each spectrum ranged between 1 to 7 days.

Ferropericlase inclusions in natural diamonds were measured using the Synchrotron Mössbauer Source (SMS) at the Nuclear Resonance Beamline 1D18 (Rüffer & Chumakov, 1996; Potapkin et al., 2012) at ESRF. The high brilliance X-ray beam emitted by SMS radiation was focused on 8.3 μm vertical and 3.6 μm horizontal dimensions using Kirkpatrick-Baez (KB) mirrors. We evaluated the source linewidth before and after the acquisition of each SMS spectrum using a $K_2Mg^{57}Fe(CN)_6$ single line absorber. The velocity scale of all SMS spectra was calibrated relative to a 25 μm thick α-Fe foil. We collected a total of 11 SMS spectra in different ferropericlase inclusions with acquisition time ranging from 1 to 2 hours (details are shown in Table 4.1). We measured also SMS spectra of the Be lenses, located in the optic system of the beamline (see section 2.3.1), and of each epoxy mount to exclude their Fe content from the $Fe^{3+}/\Sigma Fe$ calculation in ferropericlase. All Mössbauer spectra (see Figure S2 in the appendix) were fitted using a full transmission integral with pseudo-Voigt line shape and 1st order polynomial implemented in the MossA software package (Prescher et al., 2012).

Table 4.1: List of synthesized samples and natural inclusions

Run numbers[a]	P (GPa)	T (°C)	Phases[b]	Spectrum number	Thickness[c] (μm)	Collection time[d]
H2981	25	1500	fp, mst, dia, Ni	a7538	128	1 day
H2982	25	1550	fp, mst, dia, Fe-Ir	a7536	186	7 days
H2887	25	1600	fp, mst, dia, Fe-Ir	b8219	123	5 day
S4807	25	1500	fp, mst, dia, Fe-Ir	b8221	193	5 day
M131	45	1700	fp, mst, dia, Ni	a7593	150	1 day
Natural inclusions						
3.5.2b - mount #1	-	-	fp	074	-	2.80 hours
3.9.3b - mount #1	-	-	fp	077 (core)	-	3.44 hours
3.9.3b - mount #1			fp	079 (rim)	-	1.37 hours
3.9.3b - mount #1			fp	081 (rim)	-	1.40 hours
2.7.2a - mount #1	-	-	fp	070 (rim)	-	1.30 hours
2.7.2a - mount #1			fp	072 (core)	-	1.46 hours
3.2.2b – mount #2	-	-	fp	057	-	2.62 hours
1.2.3b - mount #3	-	-	fp	115	-	35 minutes
1.2.3c - mount #3	-	-	fp	116	-	
Q1 - mount #4	-	-	fp	048	-	1.94 hours
E1 - mount #4	-	-	fp	118	-	30 minutes
E2 - mount #4	-	-	fp	044	-	

Note:
[a] From Stagno et al. (2011)
[b] fp: ferropericlase, mst: magnesite, dia: diamond
[c] Final thickness after double polishing performed according to Fe content in ferropericlase
[d] Collection time related to the acquisition of MS and SMS spectra for experimental run products and natural inclusions, respectively.

4.2.4 Textural observation and chemical analyses of synthetic and natural ferropericlase

Previous analyses of the polished run products by Stagno et al. (2011) were combined with new acquisition of high-resolution images and EDS chemical analyses using the scanning electron microscope (SEM, ZEISS LEO 1530). Spot analyses were acquired at 20-kV using MgO, SiO_2, Al_2O_3, FeO, Ni, Fe and Ir as instrument internal standards, and employing a working distance (WD) of 14 mm between the electron gun and the selected specimen, while high magnified images were taken using a WD of 11 mm to maximize the resolution. We performed data evaluation using the Aztec software (see section 2.2.1).

Preliminary quantitative chemical analyses of major and minor elements of natural ferropericlase inclusions were provided by Prof. Kaminsky and were performed at the Vernadsky Institute of Geochemistry and Analytical Chemistry, Russian Academy of Sciences using both SEM and EMPA.

4.2.5 Analyses of synthetic run products by Focus Ion Beam-assisted Transmission Electron Microscopy

The experimental run products were further investigated with the TEM to have a more detailed picture on the grain boundaries and to investigate the possible presence of accessory phases such as magnesioferrite, widely observed in natural inclusions in diamonds (e.g., Wirth et al., 2014; Anzolini et al., 2020). A thin foil was extracted from runs H2981, H2887, and M131 (Figure 4.2) using a dual-beam (Ga and field emission electron guns) FIB milling machine (FEI, Scios) equipped with a sample-lift-out manipulator system. Area selection for Ga milling was made after textural observations performed with the SEM.

For each sample, a platinum rectangular layer of ~20 μm length and ~ 1-2 μm thick was deposited using the Pt-GIS (Gas Injection System) for surface protection across the chosen area (see details in section 2.2.5). Then, we tilted the specimen by ~52° with respect to the horizontal stage, and cut it stepwise by means of regular cross-section patterns at the front and backside of the lamella by scanning ion beam. The Ga-beam conditions of the trench milling process were 30 kV and 5-30 nA. The surface of the cross sections was further polished and milled by a 3 nA Ga beam to leave a foil of about 1 μm thickness. After completing the trenches, we tilted the stage by 7° and performed a parallel milling to detach the foil from the sample host and lift it out using a tungsten needle driven by a micromanipulator (Easylift system). The lamella was then attached to

the Cu grid by Pt deposition. At the final step, we thinned down the lamella to 100 nm of thickness tilting the stage alternatively to 57° and 47° to clean the surface on both sides and reduce the effect of the irregular topography. We selected final thinning conditions at 30 kV and 0.1-1 nA, and of 5 kV and 48 pA during the "ion shower" to remove Ga^{+} contamination.

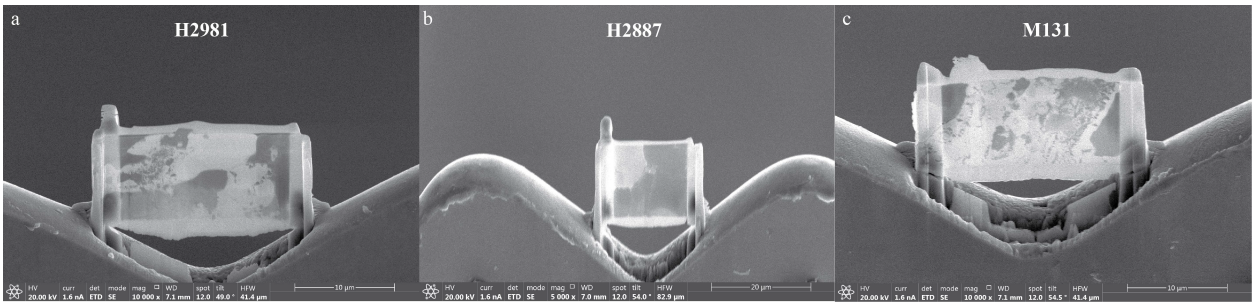

Figure 4.2: Recovered FIB thin films from (**a**) H2981, (**b**) H2887, and (**c**) M131 samples.

TEM characterization of H2981, H2887 and M131 recovered films was performed using a scanning FEI Titan G2 80-200 S/TEM operating at 200 kV and equipped with energy-dispersive X-ray spectrometers consisting of 4 Silicon drift Detectors (SDDs) (Bruker, QUANTAX EDS). We performed nanoscale imaging employing Bright Field (BF), Dark field (DF), and High-Angle Annular Dark-Field (HAADF) detectors using the TEM in scanning mode (STEM mode) to observe structural defects. All digital images were recorded with a Gatan Ultrascan charge coupled device camera, and processed using the Gatan Digital Micrograph software.

Energy dispersive X-ray chemical analyses and element maps were also performed. To obtain quantitative analyses of ferropericlase, we corrected the Z-number and absorption effects on the evaluations of EDX spectra (Van Cappellen, 1990; Van Cappellen and Doukhan, 1994). For an accurate quantification, a natural pyrope-almandine garnet (Pyc-garnet, Prp73Alm17Grs11 in Fujino et al., 1998; Miyajima et al., 1999; 2004) was employed as an EDS standard for major elements of Mg, Al, Si, Ca and Fe. Minor elements were quantified with theoretical K-factors (Z-number correction) in the EDS system. Selected Area Electron Diffraction (SAED) analyses were also performed on ferropericlase grains.

4.3 RESULTS

4.3.1 Textural and chemical analyses of the experimental run products

Textural analyses of the synthetic samples revealed an heterogenous grain size of both ferropericlase and magnesite with tiny bright grains of Fe-Ir alloy distributed throughout the capsule (Figure 4.3d). Notably, we observed the presence of newly formed micrometer-sized diamond grains different from the primary diamond grains formed by polymorphic transformation of the graphite in the starting mixture (Figure 4.3b-d). In addition, reaction rims ferropericlase occur around the magnesite grains.

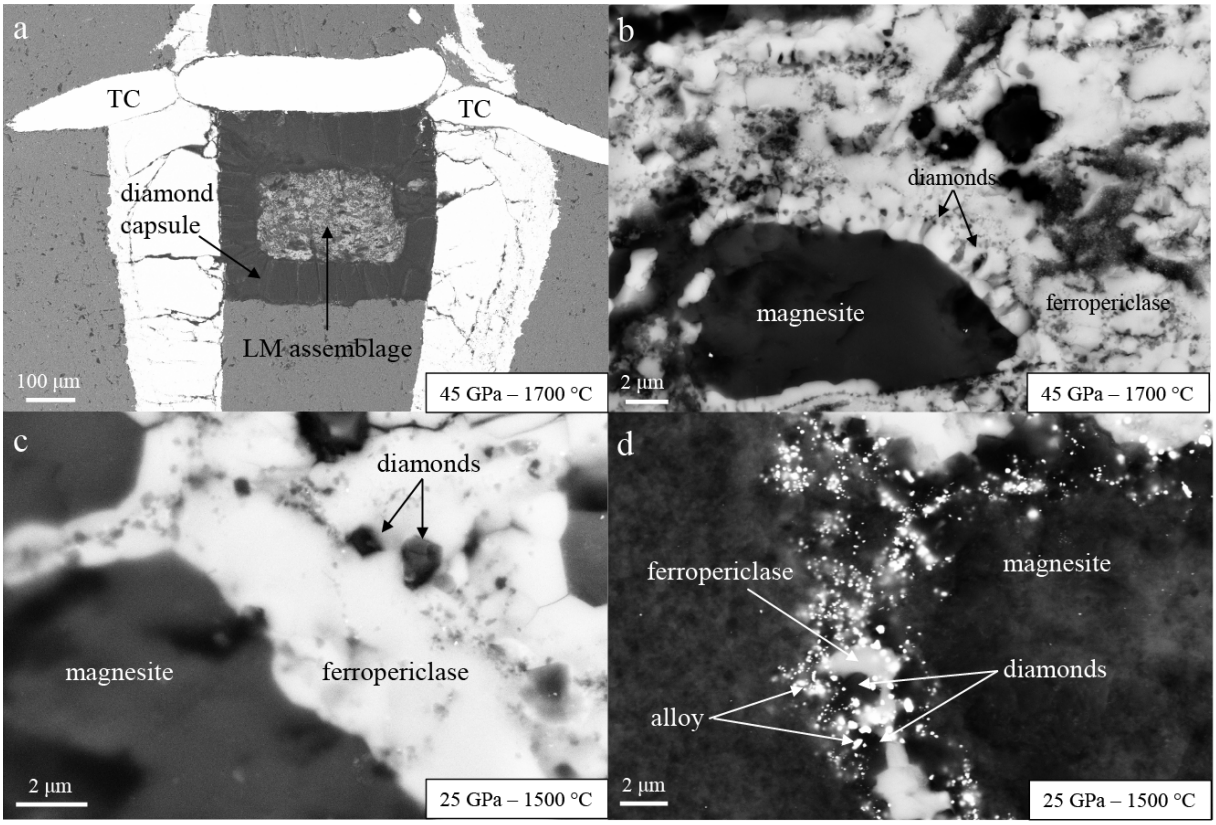

Figure 4.3: Back scattered electron images of experimental run products at different pressures. **a)** Cross section of a recovered multi anvil cell assembly. After the experiment graphite capsule turned into diamond; **b-d)** Highly magnified images showing the diamond formation process by redox freezing. Diamonds (black) are located at the redox front of ferropericlase (light grey) and magnesite (dark grey) grains. Bright grains are Fe-Ir alloys used to calculate the oxygen fugacity.

The results of the chemical analysis on synthetic ferropericlase recovered from HP-HT are taken from Stagno et al. (2011) and are shown in Table 4.2 along with the composition of natural ferropericlase inclusions. Some of these preliminary chemical analyses were individual measurements on a selected inclusion for which the uncertainty cannot be provided. In order to estimate a preliminary error on further calculations (e.g., Fe# and oxygen fugacity) we assigned a standard deviation of ~2% of the value (bold italic numbers on Table 4.2).

Importantly, the quenched synthetic ferropericlase was found to coexist with magnesite, diamond, and Fe-Ir alloys (i.e., the redox sensor), the composition of which can be found in Stagno et al. (2011). Chemical analysis results of the experimental run products determined by EDS (SEM) are consistent within uncertainty with the quantitative microprobe measurements reported by Stagno et al. (2011). Considering the better accuracy of EMPA with respect to EDS measurements we used previously determined compositions (Stagno et al., 2011) to calculate the oxygen fugacity. Calculated Fe# in synthetic and natural ferropericlase inclusions ranges between 0.16(1) to 0.37(1), and from 0.20(1) to 0.46(1), respectively.

Table 4.2: Chemical analyses results of synthetic and natural ferropericlase inclusions.

Sample	N° meas.	MgO wt. %	FeO wt. %	Fe_2O_3 † wt. %	NiO wt. %	SiO_2 wt. %	TiO_2 wt. %	Al_2O_3 wt. %	Cr_2O_3 wt. %	MnO wt. %	Na_2O wt. %	K2O wt. %	CaO wt. %	IrO_2 wt. %	Total wt. %	Fe#
S4807*	5	72.1(12)	27.2(6)	1.63	-			0.03(1)	-	-	-	-	-	0.3(2)	99.7(13)	0.18(1)
H2981*	13	54.2(11)	36.3(5)	3.63	11.2(2)	0.03(2)		-	-	-	-	-	-	-	101.8(11)	0.29(1)
H2887*	8	74.0(8)	28.5(8)	1.43	-	-	-	-	-	-	-	-	-	0.3(2)	102.92(16)	0.19(1)
H2982*	12	76.5(8)	23.9(7)	1.91	-	-	-	0.53(5)	-	-	-	-	-	0.2(2)	101.50(76)	0.16(1)
M131*_1	4	63.3(12)	34.2(19)	3.08	5.6(22)	0.10(5)	-	-	-	-	-	-	-	-	103.29(75)	0.25(1)
M131*_2	3	49.6(4)	47.5(1)	4.28	5.1(2)	0.05(1)	-	-	-	-	-	-	-	-	102.39(59)	0.37(1)
1.2.3b	1	40.1(***8***)	59.4(***12***)	0.06	0.23(***1***)	0.01(***1***)	-	0.05(***1***)	0.17(***1***)	0.43(***1***)	0.34(***1***)	0.03(***1***)	0.01(***1***)	-	100.7	0.45(***1***)
1.2.3c	2	39.09(4)	59.6(1)	0.60	0.21(**2**)	0.06(***1***)	0.03(***1***)	0.06(***1***)	0.14(***1***)	0.37(7)	0.18(8)	-	0.02(***1***)	-	99.63	0.46(***1***)
2.7.2a	1	66.2(***13***)	30.3(***6***)	0.30	1.22(***3***)	0.01(***1***)	-	0.09(***1***)	0.56(***1***)	0.43(***1***)	0.29(***1***)	-	0.01(***1***)	-	99.03	0.20(***1***)
3.9.3b	1	64.7(***13***)	32.7(***7***)	0.33	0.82(***2***)	0.04(***1***)	0.01(***2***)	0.03(***1***)	0.42(***1***)	0.29(***1***)	0.24(***1***)	-	0.01(***1***)	-	99.25	0.22(***1***)
E1	1	38.4(***8***)	59.2(***12***)	0.06	0.19(***1***)	0.17(***1***)	-	0.06(***1***)	0.15(***1***)	0.36(***1***)	0.09(***1***)	-	0.01(***1***)	-	98.70	0.46(***1***)
E2	3	42.7(5)	52.4(7)	1.05	0.74(2)	0.05(4)	-	0.06(1)	0.77(5)	0.74(2)	0.6(5)	0.01(1)	0.01(***1***)	-	97.82	0.41(***1***)

Note: Uncertainties are standard deviations on the last significant digit (e.g., 63.3(12) means 63.3 ± 1.2). Errors in bold italics were temporarily assigned to be ~2% of the value.

†Corrected value based on Mössbauer spectroscopy results (see section 4.3.2).

Fe# corresponds to Fe/(Fe+Mg)

*Values taken from Stagno et al. (2011)

Figure 4.4 shows the NiO content as a function of the Fe# of both natural (Figure 4.4a) and synthetic (Figure 4.4b) ferropericlases. With the exception of those runs where Ni was not added into the system, there is a negative correlation between NiO and Fe# as well as a heterogenous composition of both natural and synthetic ferropericlases. Ferropericlase inclusions in diamonds from Rio Soriso investigated in this study follow the general trend traced by previous data on

natural ferropericlase inclusions from diamond deposits worldwide (McCammon et al., 1997b; Harte et al., 1999; Stachel et al., 2000; Kaminsky et al., 2001; 2009). Similarly, our experimental data show a negative correlation between NiO and Fe# consistent with previous studies of both natural inclusions and synthetic ferropericlase (Kesson & Fitz Gerald, 1991; Kesson et al., 1998; Irifune et al., 2010).

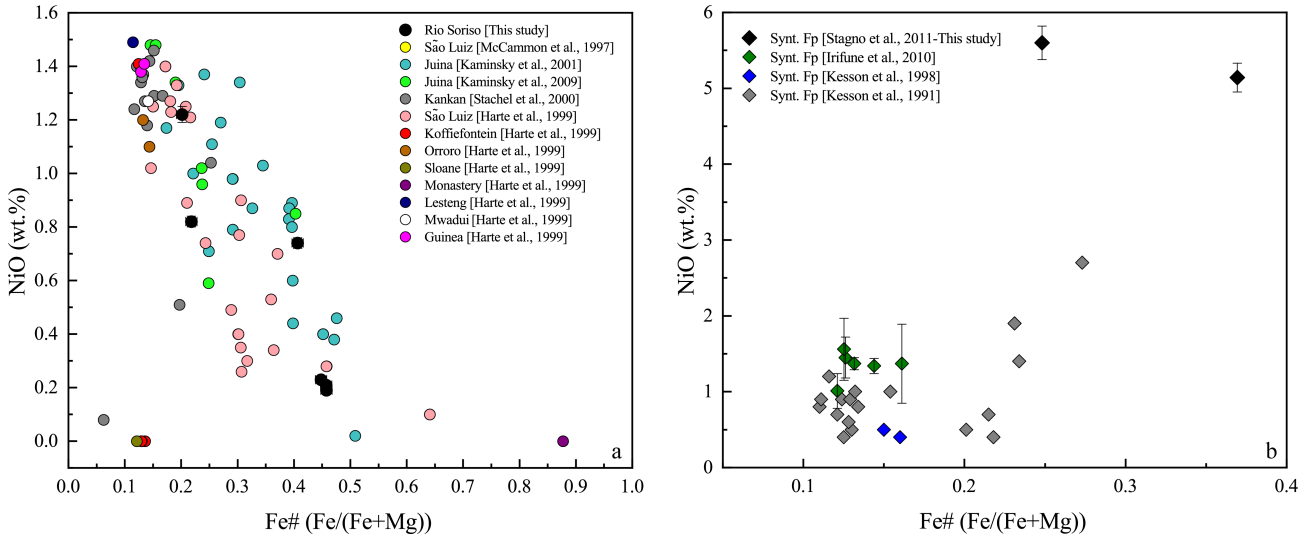

Figure 4.4: NiO versus Fe#(Fe/(Fe+Mg)) of (**a**) natural and (**b**) synthetic ferropericlases. Previous studies are plotted for comparison.

4.3.2 Determination of Fe oxidation state of natural and synthetic ferropericlase

Mössbauer spectra of experimental run products were collected on the bulk assemblages (beam size of ~ 500 × 500 μm) and show overlapping peaks from all iron-bearing phases. All spectra show a dominant quadrupole doublet as major absorption peak with a less intense feature at ~0.1 mm/s assigned to Fe^{2+} and Fe^{3+} in ferropericlase, respectively (Figure 4.5). Trivalent iron was fitted using either a singlet or a doublet with small quadruple splitting, i.e., 0-0.2 mm/s. In some spectra a quadrupole doublet with a large QS (~1.7 mm/s) was also detected and assigned to Fe^{2+} in magnesite (Figure 4.5d). No magnetic phases such as magnesioferrite were observed in any of the MS spectra. All data appear statistically well resolved using a fitting model employing pseudo-Voigt line shapes for all MS features. The $Fe^{3+}/\Sigma Fe$ ratio in synthetic ferropericlase was calculated

at 5(2)-10(4) % considering the relative absorption areas of divalent and trivalent iron. Uncertainties were determined based on the statistics of the fitting process.

Synchrotron Mössbauer source data were fit using the same approach of radioactive source Mössbauer spectra. We performed the fit including the full transmission integral pseudo-Voigt function implemented in MossA software (Prescher et al., 2012) to take into account the high absorption and the lack of non-resonant background. SMS spectra of natural ferropericlase inclusions were fitted to a quadruple doublet corresponding to Fe^{2+} and a singlet for Fe^{3+} in ferropericlase (Figure 4.5a). Typical features (sextet) of a magnetic component were also observed in some SMS spectra (Figure 4.5b) and assigned to Fe^{3+} in magnesioferrite which likely occurred as a result of ferric iron saturation within ferropericlase during decompression. A singlet with constrained parameters, i.e., CS= 0.2991 mm/s, FWHM= 0.8436 mm/s and Intensity= 0.0012 mm/s, was also included to the fit for the Fe contribution of Be lenses located in the optic setup of the beamline (see section 2.3.1) from the $Fe^{3+}/\Sigma Fe$ determination in ferropericlase. In this context, we also considered that natural diamonds were contained in resin blocks of ~1 mm thickness during data collection. For this reason, we acquired SMS spectra of each epoxy mount. Results show that the Fe absorption of each epoxy block is negligible (<1 %) and consequently no correction was applied to the fit.

The hyperfine parameters derived from synthetic and natural ferropericlase inclusions spectra are listed in Table S2. Obtained values for Fe^{2+} fall within the range observed for the octahedral site (Figure 4.6) while parameters observed for Fe^{3+} are consistent with values reported for the tetrahedral site of ferropericlase (e.g., Otsuka et al., 2010). In general, obtained hyperfine parameters for synthetic and natural ferropericlase inclusions in diamonds are in good agreement with previous estimates (e.g., McCammon et al., 1998; Otsuka et al., 2010;2013; Longo et al., 2011) within experimental error. All SMS and MS spectra are shown in the auxiliary materials with the corresponding sample images which also display the region of the specific spectrum acquisition (Figure S1 and S2). Estimated $Fe^{3+}/\Sigma Fe$ ratios in natural ferropericlase inclusions range between 0 to 10(1) % consistent, with our bulk estimation for synthetic ferropericlase and previous studies (e.g., McCammon et al., 1998; Otsuka et al., 2010;2013; Longo et al., 2011).

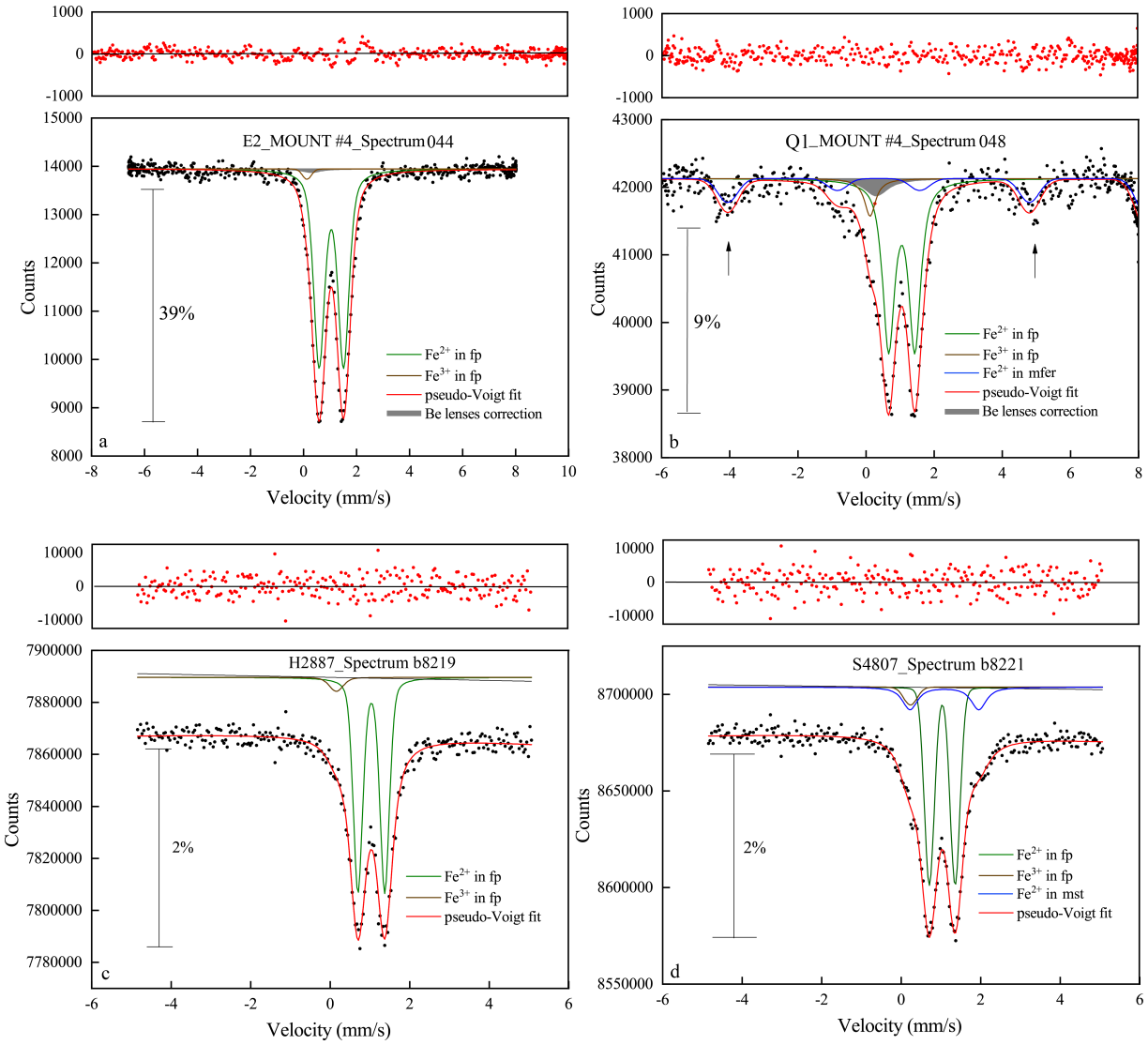

Figure 4.5: **a, b**) Room temperature SMS spectra of natural ferropericlase inclusions in diamonds. **c, d**) Mössbauer spectra of H2887 and S4807 run products dominated by a doublet (green) for Fe^{2+} and a singlet (brown) for Fe^{3+} in ferropericlase. Spectrum S4807 (c) shows also the contribution of another phase, most likely magnesite (blue doublet). In all spectra, solid circles (black) are experimental data, solid curves (red) represent the total fit performed with pseudo-Voigt functions. The velocity scale is relative to α-Fe at ambient conditions.

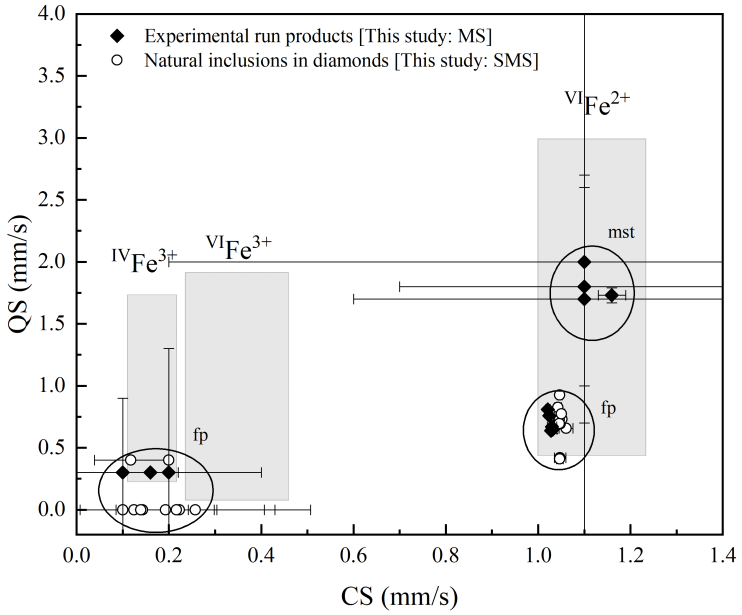

Figure 4.6: Hyperfine parameters for experimental run products (black diamonds) and natural ferropericlase inclusions in diamond (white circles). Shaded areas indicate previously observed values of Fe^{2+} and Fe^{3+} in different coordination environments for silicate and oxide minerals (Dyar et al., 2006).

4.3.3 Results from transmission electron microscope analyses

Textural observations of the recovered FIB films (H2981, H2887 and M131 runs) at the nanometric scale confirm the presence of newly formed diamond grains and the absence of amorphous phases. Examples of analyzed bright-field and HAADF transmission electron micrographs are display in Figure 4.7a-d. Structural defects were mainly observed in diamonds (eg., Figure 4.7c) and can possibly be related to the growing/crystallization process.

EDS map analyses conducted in various ferropericlase crystals show a homogeneous composition with a consistent Fe# for the investigated grains within the same sample, and agree within uncertainty with EDS and EMPA results (see paragraph 4.3.1). All EDS spectra exhibit characteristic peaks of Mg, O, Fe, and Ni of ferropericlase (Fe, Mg, Ni)O while Cu peaks are detected from the sample grid. M131 sample foil shows also a single bridgmanite grain likely due to contamination during the grinding of the starting material or loading of the capsule (Figure 4.8).

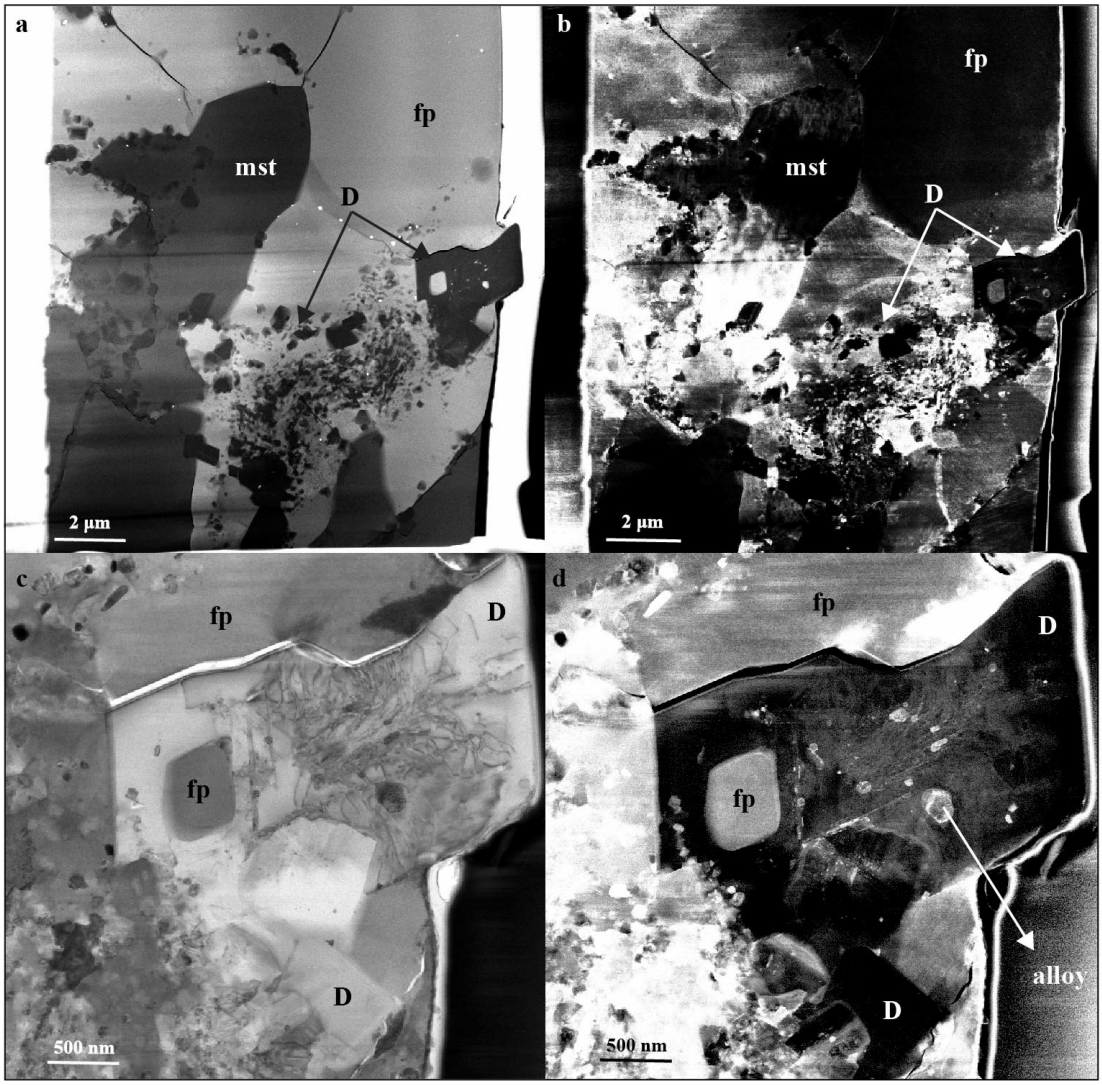

Figure 4.7: Transmission electron micrographs in HAADF **(a, c)** and bright-field (**b, d**) modes of M131 recovered film.

As mentioned, natural ferropericlases generally have shown the presence of magnesioferrite. We collected selection area electron diffraction data (SAED) in several ferropericlase grains in the vicinity of and distant from the magnesite reaction rims to investigate the possible occurrence of magnesioferrite nanocrystals exsolved from the ferropericlase matrix. Analyses of the single crystal electron diffraction patterns are consistent with those expected for ferropericlase at ambient conditions (e.g., Dubrovinsky et al., 2000), yielding lattice parameters of a = 4.263(1) Å. No magnesioferrite exsolutions (Figure 4.9) were observed in any of the investigated samples (i.e., H2981, H2887, and M131).

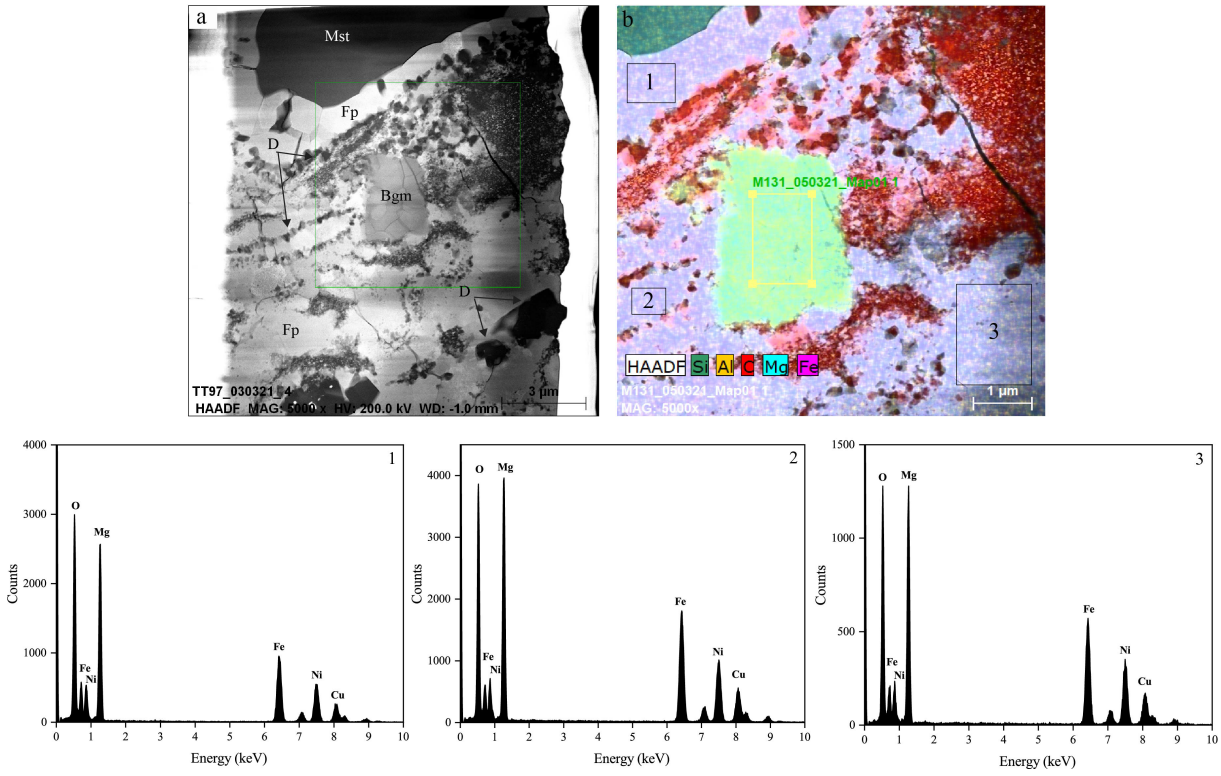

Figure 4.8: **a**) Bright field image of M131 retrieved FIB film; **b**) element distribution map of ferropericlase, magnesite, bridgmanite, and diamond. Black boxes drawn on ferropericlase phases indicated where EDX spectra shown below were collected.

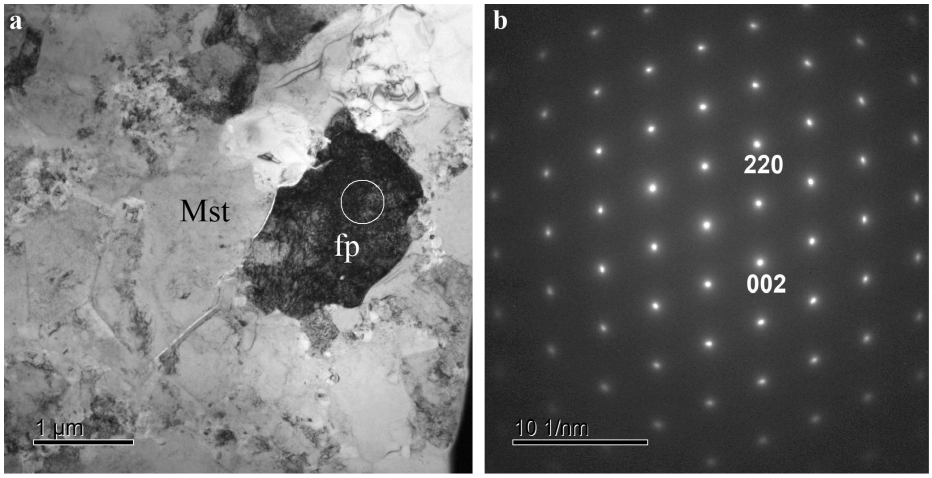

Figure 4.9: **a**) Bright-field TEM image of the M131 extracted film. The white circle highlights the investigated area in the selected ferropericlase grain (dark grey) for electron diffraction measurements (sample M131); **b**) the corresponding selected area electron diffraction pattern of ferropericlase, with no evidence of spinel type accessory phases.

4.4 DISCUSSIONS

4.4.1 Oxygen fugacity at which carbonate and diamond coexist in the lower mantle

In each synthetic run product, the f_{O_2} was buffered by the coexistence of elemental carbon (i.e., diamond) and magnesite by the simplified subsolidus mineral equilibrium,

$$MgCO_3 = MgO + C + O_2. \quad (4.1)$$

The addition of Ir to form Fe-Ir alloys (with Fe partitioned from ferropericlase) allows us to determine the f_{O_2} at a given P and T according to the equilibrium,

$$FeO_{Fp} = Fe_{alloy} + O_2. \quad (4.2)$$

We calculated the oxygen fugacity of each experiment using the newly established oxybarometer for the Fe-Ir system (details are shown in Chapter 3). From the equilibrium 3.4, we calculated the f_{O_2} (Equations 3.5 and 4.2) determining the activity-composition relations of wüstite in ferropericlase (Equation 3.15) and of Fe in the Fe-Ir alloy (Equation 3.16). The non-ideality component of the activity model was formulated as reported in Frost et al. (2003) and O'Neill et al. (2003) for ferropericlase (Equation 3.17) and as described in Chapter 3 (Equation 3.26) for the Fe-Ir alloy. The f_{O_2} results are listed in Table 4.3 and are plotted as a function of pressure and temperature in Figure 4.10 in comparison with previous studies. Obtained oxygen fugacities with the calibrated redox sensor at high pressure are lower than previous estimates (Stagno et al., 2011) obtained using the former activity model for the binary Fe-Ir system calibrated as a function of temperature and composition (Swartzendruber, 1984). Similarly, the temperature dependency on calculated oxygen fugacities (Figure 4.10b) shows lower f_{O_2} with respect to calculations of Stagno et al. (2011), with a larger deviation corresponding to the highest temperature. This implies a larger stability region of magnesite (dash-dot-dot black curve in Figure 4.10a) with respect to previous determination (dashed grey curve), with a difference becoming more significant with increasing pressure and temperature down to IW at about 45 GPa. It is therefore expected that at about 1500 km of depth magnesite can coexist with diamond and (C-bearing) Fe metal.

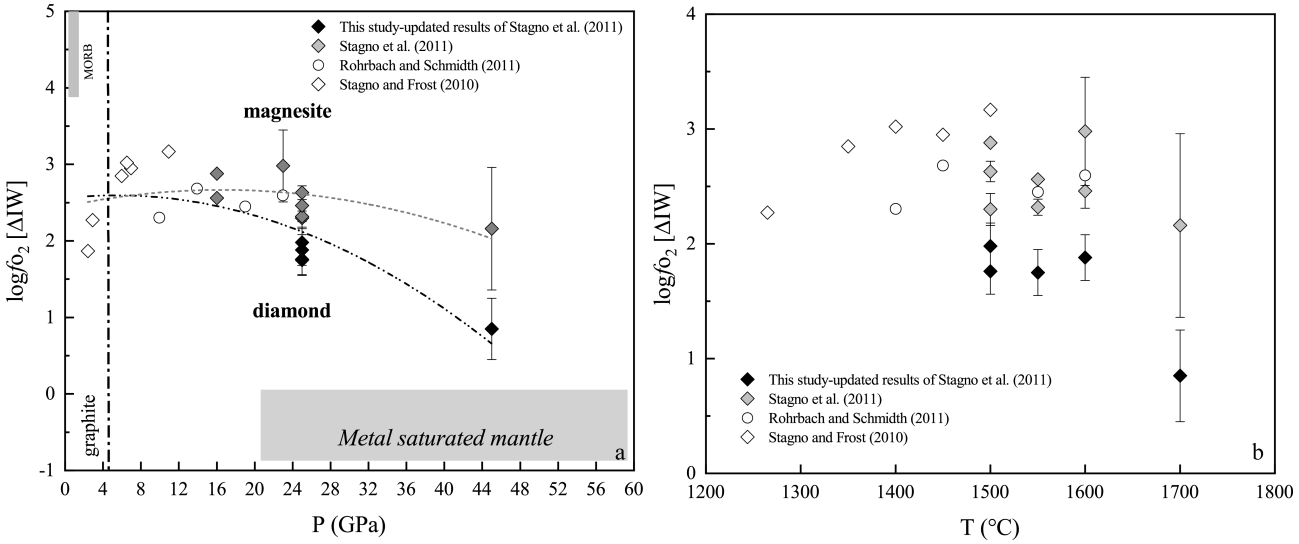

Figure 4.10: **a)** Oxygen fugacity normalized to IW as a function of pressure/depth at buffered redox conditions by the coexistence of diamond and magnesite. Dash-dot-dot black and dashed grey curves delineate the redox stability region of magnesite based on oxygen fugacity calculation performed with the Fe-Ir redox sensor model calibrated at high-pressure and at 1 atm, respectively. **b)** Oxygen fugacity normalized to the IW as a function of temperature at buffered redox conditions by the coexistence of diamond and magnesite.

Table 4.3: Thermodynamic parameters and oxygen fugacities results of experimental run products.

Run[+]	**P (GPa)**	**T (°C)**	$X_{Fe}^{alloy\dagger}$	$X_{FeO}^{fp\dagger}$	$W_{Fe\text{-}Ir}^{H*}$ (J/bar)	$W_{Ir\text{-}Fe}^{H*}$ (J/bar)	W^{V*} (J/bar)	log f_{O2}	logf_{O2} [IW]
H2982	25	1500	0.128(17)	***0.159(1)***	-19463	-30445	0.321	-3.6(2)	1.8(2)
H2946	25	1500	0.110(10)	0.175(4)	-19463	-30445	0.366	-3.4(2)	2.0(2)
H2887	25	1550	0.136(10)	**0.185(3)**	-19463	-30445	0.304	-3.2(2)	1.8(2)
S4807	25	1600	0.115(17)	**0.183(4)**	-19463	-30445	0.352	-2.8(2)	1.9(2)
M140	45	1700	0.07(2)	0.151(5)	10865	-117	0.563	-1.9(4)	0.9(4)

Note: Errors are standard deviations on the last digit.

[+]Details on sample synthesis are provided in Stagno et al. (2011)

[†]Molar fraction values are EMPA results taken from Stagno et al. (2011). Values in bold italics were corrected based on Mössbauer spectroscopy results (see section 4.3.2).

[*]Margules parameters were calculated using the calibrated oxybarometer at high pressure (see Chapter 4) and relate to the specific experimental conditions.

4.4.2 Oxygen fugacity of the lower mantle revealed by natural ferropericlase inclusions

Oxygen fugacity conditions of ferropericlase diamond inclusions from Rio Soriso were determined using Equation 4.3 formulated by Otsuka et al. (2013), which describes the solubility of Fe^{3+} in ferropericlase at the *P-T* conditions of the top of the lower mantle,

$$Fe^{3+} = C(X_{Fe}^{4} f o_2)^m \exp\ [-((1 - X_{Fe})E_{Mg}^{*} + X_{Fe}E_{Fe}^{*} + PV^{*})/RT] \quad (4.3)$$

where $C = 2.6(1) \times 10^{-3}$ and $m = 0.114(3)$ are constants and depend on the crystallographic site of Fe^{3+} (Otsuka et al., 2013). The value of the oxygen fugacity exponent *m* implies that Fe^{3+} mostly occupies the tetrahedral site (e.g., McCammon, et al., 2004a; Otsuka et al., 2010). The E_{Mg}^{*} = -35(3) kJ/mol and E_{Fe}^{*} = -98(2) kJ/mol parameters are enthalpies of the reaction for MgO and FeO components, respectively, V^{*} =2.09(3) cm^3/mol is the volume change in the reaction, R = 8.314 J/mol K is the universal gas constant, T is the temperature in K, and X_{Fe} is the molar fraction of Fe in ferropericlase corrected for the Fe_2O_3 component based on SMS results. Using this formalism, we calculated the redox conditions of ferropericlase inclusions formation assuming a pressure of 25 GPa and temperatures ranging from 1873-2373 K typical of the uppermost lower mantle. Specifically, we followed the same approach of Kaminsky et al. (2015) performing the calculations at three different temperatures., i.e., 1873 and 2373 K as representative of the lowest and the highest temperature of this pressure regime, and 1960 K which corresponds to the average mantle adiabat at the top of the lower mantle (Katsura et al., 2010). For the magnesioferrite-bearing ferropericlase inclusion of which we have chemical analysis information (inclusion n° 1.2.3.c), we tested the variation in f_{O_2} with temperature including the $Fe^{3+}/\Sigma Fe$ ratio of ferropericlase and the ferric iron contribution from magnesioferrite. We observed that at the adiabatic temperature the f_{O_2} strongly increases from -3.1 ± 0.5 to 5.7 ± 0.5 log units normalized to the iron-wüstite buffer. Oxygen fugacity results are listed in Table 4.4. We reported f_{O_2} values normalized to the IW buffer, using the thermodynamic relations described in Chapter 3. Uncertainties were propagated as a function of Fe oxidation state and chemical composition.

Table 4.4: Oxygen fugacity values of ferropericlase inclusions in super-deep diamonds from Rio Soriso, calculated assuming a pressure of 25 GPa and temperatures of 1873, 1960, and 2373 K.

Sample	X_{FeO}^{fp}	**$Fe^{3+}/\Sigma Fe$**	**$\log f_{O_2}$**	**$\log f_{O_2}$[IW]**	**$\log f_{O_2}$**	**$\log f_{O_2}$[IW]**	**$\log f_{O_2}$**	**$\log f_{O_2}$[IW]**
			1873 K	**1873 K**	**1960 K**	**1960 K**	**2373 K**	**2373 K**
1.2.3b	0.45	0.01	3.7E+00	-3.20(15)	1.44E+01	-3.00(15)	9.68E+01	-3.50(15)
1.2.3c	0.46	0.01	3.7E+00	-3.20(45)	1.28E+01	-3.10(45)	2.81E+01	-4.10(45)
1.2.3c	0.46	***0.11***	***6.0E+09***	***6.0(5)***	***8.04E+09***	***5.7(5)***	***2.40E+10***	***4.8(5)***
2.7.2a	0.20	0.01	3.8E+02	-1.0(10)	3.39E+02	-1.4(10)	2.05E+02	-3.0(10)
3.9.3b	0.22	0.1	3.9E+11	8.0(10)	3.57E+11	7.6(10)	2.57E+11	6.0(10)
E1	0.463	0.01	7.6E+00	-2.90(55)	4.58E+00	-3.50(55)	3.31E+01	-4.00(55)
E2	0.407	0.02	5.0E+03	0.0(7)	6.09E+03	-0.3(7)	1.22E+04	-1.4(7)

Note: Errors are standard deviations on the last digit. Values in bold italics represents the $Fe^{3+}/\Sigma Fe$ ratio and the calculated f_{O_2} including the ferric iron contribution of magnesioferrite.

Figure 4.11 shows the obtained f_{O_2} referred to the natural ferropericlase inclusions in diamonds from Rio Soriso compared with previous data on natural ferropericlase inclusions from Juina-Brazil (Kaminsky et al., 2015), São Luiz - Brazil and Kankan-Guinea (McCammon, et al., 2004a; Otsuka et al., 2013) and experimental results of this study on synthetic ferropericlase equilibrated with magnesite and diamond. This diagram illustrates a clear redox heterogeneity in the lower mantle from about -3.5 ± 0.5 to 7.6 ± 1.0 $\log f_{O_2}$ normalized to the IW buffer correlated with chemical heterogeneities expressed with the Fe#. A similar variation is observed in Figure 4.12a and 4.12b where the $Fe^{3+}/\Sigma Fe$ of both natural and synthetic ferropericlases is plotted versus the Fe# and $\log f_{O_2}$, respectively. Figure 4.12b particularly highlights the potential role of ferropericlase as a redox tracer displaying a positive correlation between oxygen fugacity and oxidation state.

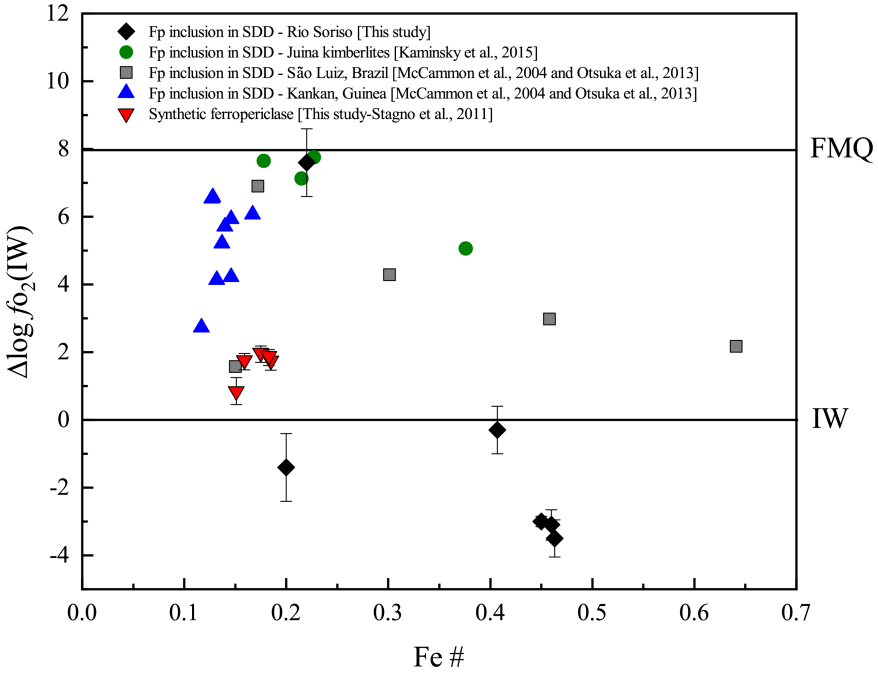

Figure 4.11: Oxygen fugacities normalized to the IW buffer in natural ferropericlase inclusions in SDD versus Fe# = Fe/(Fe+Mg). Black diamond symbols are f_{O_2} results of ferropericlase inclusions from Rio Soriso calculated assuming P = 25 GPa and T = 1960 K. Uncertainties on f_{O_2} were determined as a function of temperature (in the range of 1873-2373 K). Previous studies of natural ferropericlase inclusions from different areas (i.e., McCammon et al., 2004; Otsuka et al., 2013; Kaminsky et al., 2015) and our experimental results are plotted for comparison.

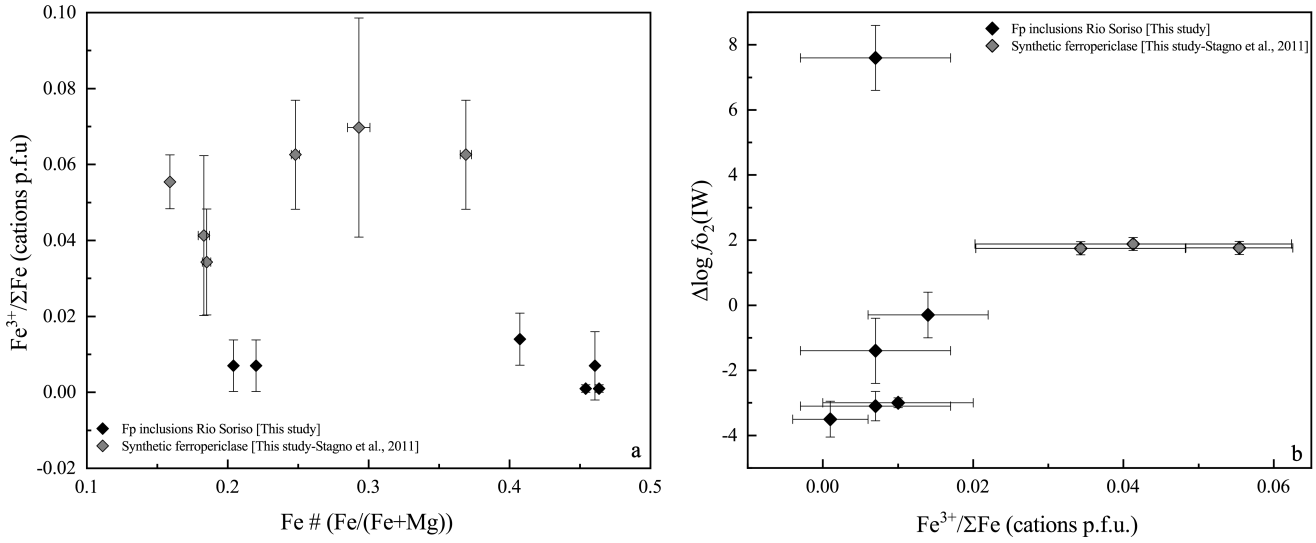

Figure 4.12: a) $Fe^{3+}/\Sigma Fe$ versus **(a)** Fe# and **(b)** oxygen fugacity normalized to the IW buffer in synthetic (grey) and natural (black) ferropericlase.

4.4.3 Mechanisms of super deep diamond formation: evidence of primordial lower mantle

There is evidence that the Earth's lower mantle is saturated with 1% Fe metal (Frost et al. 2004). However, both the presence of carbonate (melt and solid) included in sub-lithospheric diamonds and the rarity of Fe metal appear in contrast with this conclusion. Our experiments simulate the interaction of a Fe-saturated lower mantle with an influx of carbonate to increase the local f_{O_2} from IW up to conditions where carbonate and diamond can coexist, i.e. the lowest f_{O_2} at which carbonate can survive and the highest f_{O_2} at which diamonds are stable in the lower mantle. The chemical and redox heterogeneities displayed by both natural and synthetic ferropericlases seem to suggest multiple oxidation events through which the lower mantle reacts with CO_2-bearing fluids increasing therefore the local f_{O_2}. This can be expressed by the equilibrium,

$$\mathrm{Fe(Ni)} + \mathrm{MgCO_3} = \mathrm{(Mg,Fe,Ni)O} + \mathrm{C} + \mathrm{O_2} \quad (4.4)$$

This reaction points out the negligible amount of Fe of subducted carbonates as demonstrated by Stagno et al. (2011) and implies that any redox reaction is susceptible to changes in the Fe# of syngenetic ferropericlase inclusions. In fact, Auzende et al. (2008) show that primordial Fe# of ferropericlase is expected to be ~0.20 in equilibrium with Fe metal. However, the variability of ferropericlases included in diamonds can be through redox reactions like Equation 4.4. As more CO_2 interacts with the lower mantle, the local f_{O_2} increases and leads to consumption of Fe(Ni) metal. In other words, ferropericlases recording low f_{O_2} are likely to be protogenetic, while the more oxidized are syngenetic. A similar conclusion was reached by Anzolini et al. (2020) and Nimis et al. (2019) who show the association of Fe_xO_y phases (e.g., Fe_4O_5, Fe_5O_6, Fe_7O_9, and Fe_7O_{11}) as a result of oxidizing processes in the lower mantle at the expense of the Fe metal.

Importantly, our experiments provide evidence of these redox reactions with formation of secondary ferropericlase and diamonds. The diagram in Figure 4.13 shows the Fe-Mg exchange coefficient ($K_D^{\text{Mst-fp}}$) between synthetic magnesite and ferropericlase and the measured log f_{O_2}. It can be seen that $K_D^{\text{Mst-fp}}$ is systematically less than unity for all investigated experimental runs with a significant variation over the entire *P-T* range representative of the upper-middle lower mantle, indicative of preferential partitioning of Fe, relative to Mg, into ferropericlase. This implies, therefore, that most of the ferropericlase inclusions experienced interaction with CO_2-rich

fluids at conditions where carbonate and diamond can be stable. Once all Fe metal oxidized (about 8000 ppm of C as CO_2 are needed) and the carbonate is reduced to diamond, ferropericlases are exposed to epigenetic reactions that lead to the formation of magnesioferrite and/or Fe_xO_y phases. No magnesioferrite was observed in our experimental runs highlighting the fact that these exsolutions are likely to form upon decompression and cooling (Anzolini et al., 2020). Hence, we conclude that as an effect of the CO_2 ingassing into the deep Earth's interior via subduction, the current lower mantle is far from saturated in Fe metal. This hypothesis is supported by evidence recorded by natural inclusions in CLIPPIR (Cullinan-like, large, inclusion poor, pure, irregular, resorbed) diamonds (Smith et al., 2016; 2017) that exhibit geochemical signatures of subduction-related serpentinization processes (Smith et al., 2021).

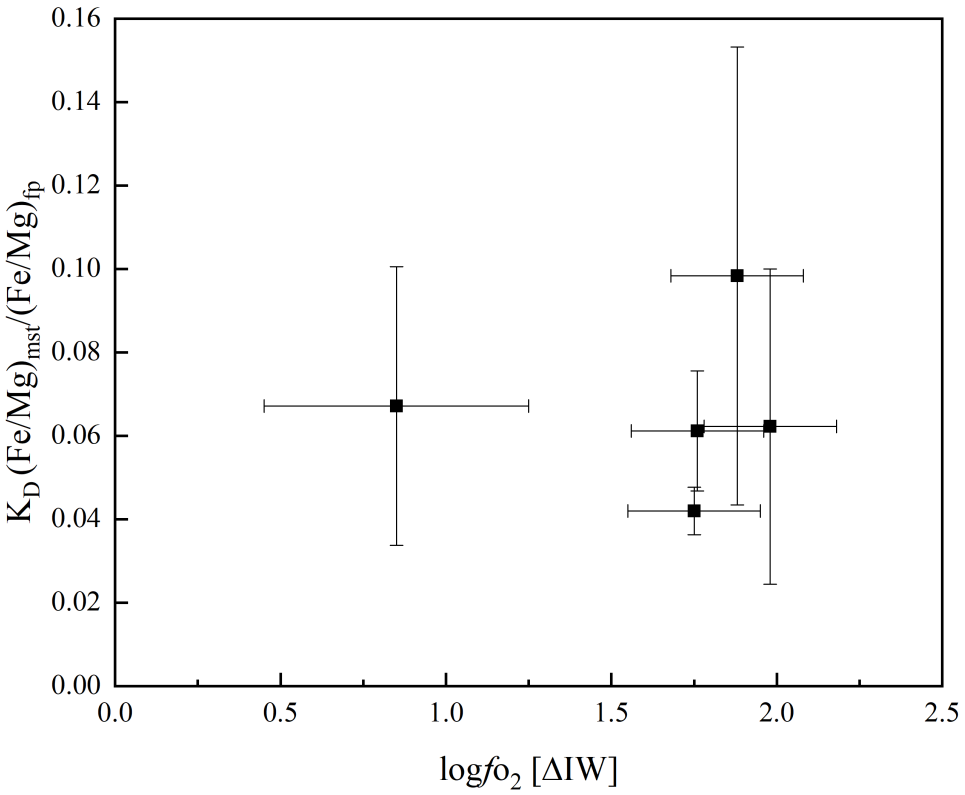

Figure 4.13: Fe-Mg exchange coefficients between coexisting magnesite (mst) and ferropericlase (fp) synthesized in Stagno et al. (2011) and further analyzed in this study.

4.5 CONCLUSIONS

In this study, we have investigated the redox state of natural ferropericlase inclusions in diamonds from Rio Soriso and synthetic ferropericlase equilibrated with magnesite at lower mantle conditions combining Mössbauer spectroscopy, chemical analyses, and transmission electron microscopy measurements. Our results show a ferric iron content in natural and synthetic ferropericlase ranging from 0 to ~10 % in good agreement with previous studies conducted on both natural and synthetic ferropericlase. Oxygen fugacities calculated with the newly calibrated Fe-Ir redox sensor for experimental run products are lower than previous estimates, varying from ~1 to 2 log units above the IW buffer, and show a general trend that decrease as both pressure and temperature increase. These new results indicate an expanded stability field of magnesite down to 1500 km depth coexisting with diamond and (C-bearing) Fe metal. The f_{O_2} recorded by natural ferropericlase inclusions ranges from -3.5 ± 0.5 to 7.6 ± 1.0 logf_{O_2} normalized to the IW buffer reflecting a lower mantle redox heterogeneity consistent with values reported in the literature. Similar variations were also observed in terms of Fe# (Fe/(Fe+Mg)) both for natural ferropericlase inclusions and synthetic samples. This chemical and redox heterogeneity potentially suggests multiple oxidation events through which the lower mantle reacts with CO_2-bearing fluids, increasing, therefore, the local oxygen fugacity at the expense of Fe(Ni) metal. In this scenario, ferropericlases recording low f_{O_2} are likely to be protogenetic, while the more oxidized are syngenetic. On the other hand, ferropericlases containing exsolved magnesioferrite and/or Fe_xO_y phases in the matrix are likely to be epigenetic and to occur once all Fe metal oxidized and the carbonate is reduced to diamond by redox freezing. This hypothesis is supported by the absence of ferric iron-rich phases in the investigated experimental ferropericlases emphasizing that these exsolutions are likely to form upon decompression and cooling.

Chapter 5

5 SOUND VELOCITY MEASUREMENTS OF B2-FE-NI-SI ALLOY UNDER HIGH PRESSURE BY INELASTIC X-RAY SCATTERING: IMPLICATIONS FOR THE COMPOSITION OF EARTH'S CORE

5.1 INTRODUCTION

Knowledge of elastic properties of Fe-Ni alloys at high pressure is crucial for understanding the structure, composition, and dynamics of Earth's core. In this context, particularly relevant is the comparison of density (ρ), compressional (V_P), and shear (V_S) wave velocities of Fe alloys with seismological observations, e.g., PREM (Dziewonski & Anderson, 1981). Since the pioneering work of Birch (1952), it is considered likely that light elements, are alloyed with iron in Earth's core to account for the density deficit between *hcp* Fe and geophysical observations. Among several suggested candidates such as C, O, H, and S (Birch, 1964; Mao et al., 1990), Si is favored based on its affinity for the metallic phase during Earth's differentiation (Lin et al., 2003; Antonangeli et al., 2010; Mao et al., 2012; Siebert et al., 2013; Fischer et al., 2015; Tateno et al., 2015) and its effect on the compressional sound wave velocity of Fe (Badro et al., 2007). However, despite extensive work was conducted in investigating the sound velocities and density of candidate alloys at high pressure and temperature, controversies remain about the effect of light elements on the elastic properties of Fe-Ni alloys and their abundance in Earth's core.

Fe is known to possess the *hcp* structure at Earth's inner core conditions (Mao et al., 2001; Tateno et al., 2010; Ohtani et al., 2013) although some studies provide experimental and computational evidence that the *bcc* phase may also be stable close to the Fe melting curve or as a consequence of Si dissolution into *hcp* Fe (e.g., Belonoshko et al., 2003; Dubrovinsky et al., 2007). Phase relations in the Fe-(Ni)Si system have been extensively studied for various compositions (e.g., Fischer et al., 2013) of which a detailed description is given in sections 1.4.1 and 1.4.2. Previous studies argued that variation of Si concentration from 9 to 16 wt. % in Fe-Ni alloys promotes the coexistence of B2 + *hcp* phases up to ~145 GPa and 2400 K (Fischer et al., 2013; Ikuta et al., 2021) and that the extrapolation of the *hcp* + B2 phase boundaries at 329 GPa and 6650

K promotes the stability of Si-depleted (Si < 2 wt. %) *hcp* and Si-enriched (Si > 10-15 wt. %) B2 phase mixture at Earth's inner core conditions (Fischer et al., 2012, 2013; Fischer & Campbell, 2015; Ikuta et al., 2021).

In this study, we tested the hypothesis of a *hcp*+B2 phase mixture for Earth's inner core performing inelastic X-ray scattering and X-ray diffraction measurements on the Si-rich B2 component with a composition of Fe-(7wt. %)Ni-(15wt. %)Si alloy. We argue about the effect of Si and Ni on elastic properties of pure Fe and propose a compositional model for the Earth's inner core assuming a linear mixing between Si-depleted *hcp* and Si-enriched B2 alloys.

5.2 MATERIALS AND METHODS

5.2.1 Sample synthesis

The starting material was made from powders of reagent-grade metallic Fe (99.9 % purity), Ni (99.7 % purity), and Si (99.9995 % purity). We mechanically ground the mixture of Fe (78 wt. %), Si (15 wt. %) and Ni (7 wt. %) for about 1 hour in an agate mortar under ethanol to achieve a homogeneous mixture.

Two different samples (runs H4973 and S7389) of Fe-Ni-Si alloy were synthesized using the 1000-ton and 1200-ton Kawai-type multi-anvil apparatus at Bayerisches Geoinstitut, University of Bayreuth (BGI). Multi-anvil experiments were carried out using tungsten-carbide cubes with truncation edge lengths of 11 mm. A Cr_2O_3-doped MgO octahedron with an edge length of 18 mm (18/11 configuration) was used as pressure medium. A triple-stepped graphite heater was used to reduce the thermal gradient inside the capsule (Rubie, 1999). Thermal insulation was provided by a ZrO_2 sleeve located outside the heater. A single crystal MgO capsule loaded with the starting mixture was placed inside the cylindrical heater. A thin polycrystalline MgO sleeve was placed between the capsule and heater. Sample temperature was monitored using a $W_{97\%}Re_{3\%}$–$W_{75\%}Re_{25\%}$ (D-type) thermocouple directly in contact with the top of the MgO capsule. Synthesis experiments were performed at sub-solidus conditions at 8.0(5) GPa and 1200(50) °C, where uncertainties are estimated according to Rubie (1999). After 1 hour, during which temperature was maintained within ± 10-20 °C, experiments were quenched rapidly by switching off the power and then decompressed to ambient pressure over 15 hours.

Recovered MgO capsules were mounted in epoxy and polished to expose the samples for phase identification and compositional analysis. Phase identification of H4973 and S7389 samples was made using the microfocus X-ray powder diffractometer (MF-XRD) Bruker D8 DISCOVER (Co-Kα wavelength of 1.78 Å) installed at BGI. Results showed only *fcc* Fe-Ni-Si (Figure S3). Sample homogeneity was confirmed using a scanning electron microscope (SEM, ZEISS LEO 1530) with an energy dispersive X-ray spectrometer. SiO_2, Fe and Ni were used as standards for chemical analyses. Alloy compositions were calculated to be $Fe_{0.665(2)}Ni_{0.060(1)}Si_{0.275(5)}$ and $Fe_{0.666(2)}Ni_{0.060(1)}Si_{0.274(1)}$ for H4973 and S7389, respectively. Examples of backscattered electron (BSE) images are given in Figures 5.1a and 5.1b, which show polycrystalline textures with grain sizes ranging from ~5 to 20 μm.

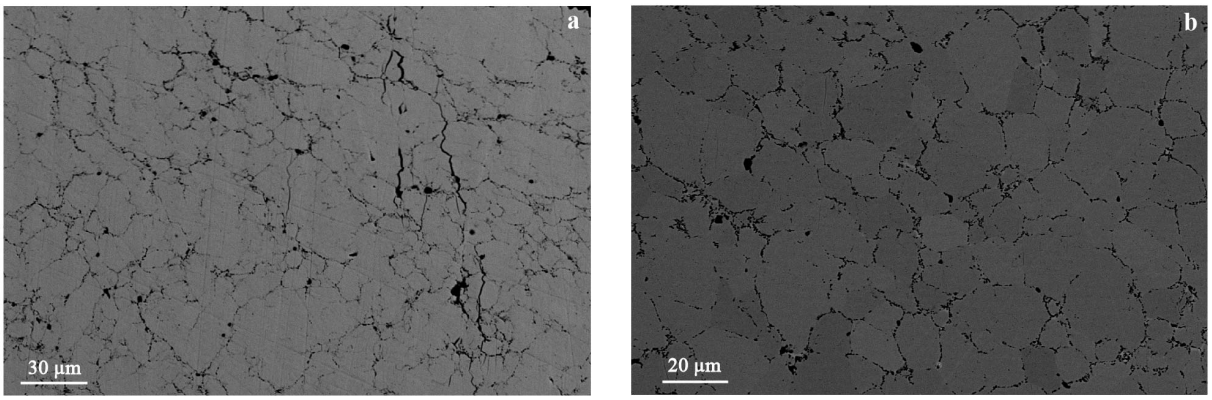

Figure 5.1: Backscattered electron images of the synthesized $Fe_{0.67}Ni_{0.06}Si_{0.27}$ alloy (run products a-H4973, b-S7389). Both run products consist of a single-phase alloy (grey). Polishing imperfections at grain boundaries are black. The average grain size of the crystallites ranges from 5 to ~20 μm.

5.2.2 Diamond anvil cell experiments

A fragment of the alloy was placed inside a drilled Re gasket hole that was pre-indented to a thickness of 25-30 μm. The sample chamber was loaded with Ne as quasi-hydrostatic pressure transmitting medium using the gas loading system installed at BGI (Kurnosov et al., 2008). We used a piston-cylinder type DAC with BX90 and BX90-mini configuration (Kantor et al., 2012) equipped with tungsten carbide seats and Boehler-Almax anvil design (Boehler & De Hantsetters, 2007). Diamonds with culet sizes of 250 μm (runs SD005 and SD009) and 120 μm (run SD008) were used for IXS and XRD experiments. The complete list of experimental runs is given in Table 5.1.

Table 5.1. Summary of high-pressure experiments. Ne was gas loaded as pressure medium in all DAC experiments.

Synthesis	DAC	Culet size (µm)	Beamline	Experiments	Pressure range (GPa)
H4973	SD005[a]	250	BL35 (SPring-8)	IXS+XRD	6.8(2) – 73(2)
S7389	SD008[b]	120	P02.02 (DESY)	XRD	10.38(5) - 84.2(7)
S7389	SD009[c]	250	BL35 (SPring-8)	IXS+XRD	45(1), 67(2), 98(3)

[a] data collection in pressure steps of ~10 GPa
[b] gold was loaded for pressure calibration
[c] data collection of three pressure points

5.2.3 IXS measurements at SPring-8

IXS data were collected at BL35XU (Baron et al., 2000) at the SPring-8 synchrotron facility, Japan (see section 2.3.4). A ~60 µm × 50 µm sample with ~5-10 µm thickness was chosen for a good signal/noise ratio. During IXS data collection (runs SD005 and SD009) the DAC was set on the Eulerian cradle of the IXS spectrometer in a helium gas atmosphere. The beam size was focused to about 14 µm vertically and 17 µm horizontally (full-width at half maximum, FWHM) using a Kirkpatrick-Baez mirror pair (Ishikawa et al., 2013). A Si (999) instrument configuration was used providing 2.8 meV FWHM resolution at 17.794 keV. The scattered X-rays were collected by 12 crystals arranged in a two-dimensional array. The momentum transfer $Q = 2\ k_0 \sin(2\theta/2)$, which is defined as a function of the wave vector of the incident photons k_0 and the scattering angle 2θ, was selected by rotating the spectrometer arm in the horizontal plane. IXS spectra were collected for ~8-10 hours over a Q range of 4.24 to 7.62 nm^{-1} and momentum resolution of 0.40 nm^{-1} full width at each experimental pressure. The sample was compressed offline to about 100 GPa at room temperature through steps of roughly 10 GPa according to Raman spectra measured at the center of the diamond culet (micro Raman spectroscopy system: 785 nm diode laser installed at BL10XU) (Akahama & Kawamura, 2006). Pressure was subsequently determined more accurately using the equation of state (EOS) of the sample determined by XRD.

The relationship between momentum transfer and energy of acoustic phonons was determined. The scattering produced by the longitudinal acoustic (LA) phonons was fit with a

Lorentzian function to obtain the LA mode energy at each momentum transfer, Q. We then derived the aggregate compressional sound velocity V_{P} from a sine fit to the phonon dispersion using

$$\mathrm{E} = 4.192 \times 10^{-4} V_{\mathrm{P}} \times Q_{\mathrm{MAX}} \times \sin\left(\frac{\pi}{2} \frac{Q}{Q_{\mathrm{MAX}}}\right), \tag{5.1}$$

where E is the energy in meV, Q is the momentum transfer (nm^{-1}), V_{P} is the compressional wave sound velocity (km/s), and Q_{MAX} is the momentum transfer where the phonon dispersion turns over, roughly the boundary of the Brillouin zone. Dispersion relationships have been determined by fitting each set of data (12 data points for each investigated pressure step) using Equation 5.1 in the main text. Firstly, V_{P} and Q_{MAX} were taken as free parameters. Then, the dispersion curves were fitted constraining Q_{MAX} values as follows:
by considering that Q_{MAX} varies as a function of the cell volume (V), i.e.,

$$Q_{\mathrm{MAX}} \propto \frac{1}{\sqrt[3]{V}}, \tag{5.2}$$

we fitted all of the experimentally determined Q_{MAX} values with the following nonlinear function:

$$Q_{MAX} = C + \frac{S}{\sqrt[3]{V}} \tag{5.3}$$

in which C and S are fitting parameters. The resulting curve is displayed in red in Figure 5.2. In order to constrain the Q_{MAX} parameters for fitting individual dispersion relationships, we determined Q_{MAX} values relevant to each investigated experimental volume. The error on constrained Q_{MAX} values was calculated considering the uncertainty in fitting parameters (C, S) and cell volume (V) according to the following error propagation equation:

$$\frac{\delta Q_{MAX}}{|Q_{MAX}|} = \sqrt{\left(\frac{\delta C}{C}\right)^2 + \frac{\left(\frac{3}{2}\left(\frac{\delta V}{V}\right)^2 + \left(\frac{\delta S}{S}\right)^2 - \frac{2\delta S \times \delta V^2}{S \times V}\right)}{\left(\frac{S}{\sqrt[3]{V}}\right)}}. \tag{5.4}$$

Compressional sound velocities (V_P) at each experimental volume (i.e., pressure) were obtained by fitting the dispersion curves (Equation 5.1) and fixing Q_{MAX} to the value calculated from Equation 5.3. Uncertainties on V_P were calculated by considering two contributions: i) the statistical error

on V_P calculated at fixed Q_{MAX} ($\delta V_P^{Q_{MAX}}$) using Origin software (OriginLab Corporation); ii) the error on Q_{MAX} calculated as the semi-difference between V_P calculated at Q_{MAX} + δQ_{MAX} ($V_P^{Q_{MAX}+\delta}$) and Q_{MAX} - δQ_{MAX} ($V_P^{Q_{MAX}-\delta}$). This is obtained through the following equation,

$$\delta V_P = \delta V_P^{Q_{MAX}} + \left(\frac{V_P^{Q_{MAX}+\delta} - V_P^{Q_{MAX}-\delta}}{2} \right). \quad (5.5)$$

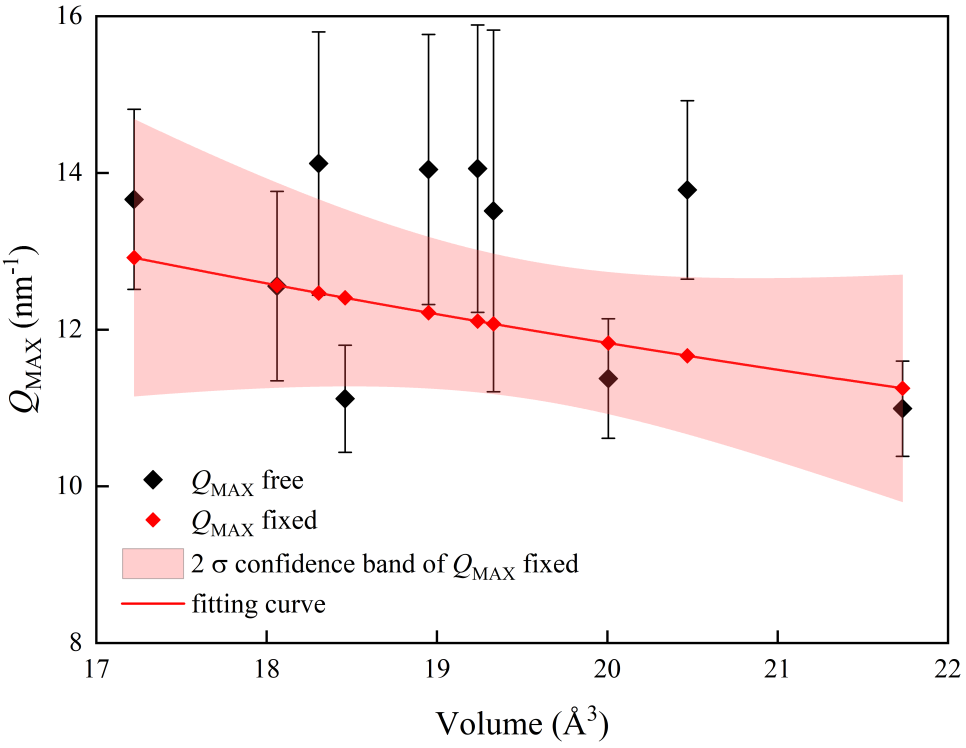

Figure 5.2. Experimentally determined Q_{MAX} values plotted as a function of the cell volume. The red curve represents the weighted fit of experimental data (χ^2 = 1.50).

5.2.4 Synchrotron powder XRD measurements

We determined the density of $Fe_{0.67}Ni_{0.06}Si_{0.27}$ alloy (runs SD005 and SD009) at the same pressures as IXS experiments by *in situ* XRD using a flat panel detector (C9732DK, Hamamatsu Photonics K.K.) calibrated using CeO_2 reference material. Diffraction still images were collected with acquisition times of 3 s at each pressure and then integrated using DIOPTAS software (Prescher & Prakapenka, 2015). The unit cell parameters, background and line-profile parameters of the sample were refined using JANA 2006 software (Petrícek et al., 2014).

The EOS of the same material (run SD008) was calculated from volume measurements up to 84.2(7) GPa using powder XRD. High-pressure XRD experiments were performed at P02.2 beamline, PETRA III, DESY in Hamburg, Germany (λ = 0.2915 Å) using a Perkin Elmer XRD1621 (2048 × 2048 pixels, 200 × 200 μm^2) flat panel detector and a beam size of 2(v) × 2(h) μm^2. In run SD008 we loaded a piece of Fe-Ni-Si alloy of ~20 μm × 15 μm^2 with ~5-10 μm thickness along with a piece of gold (pressure calibrant) in the sample chamber using Ne as pressure medium. The sample-detector distance was calibrated using CeO_2. Pressure was manually increased by tightening the DAC screws in steps of ~5 GPa and evaluated using an equation of state for Au (Fei et al., 2007). 2D diffraction images were acquired for 5 s each. XRD data reduction (DIOPTAS program) and processing (JANA 2006) were used to obtain the lattice parameters. The *P-V* data of the alloy, obtained after Le Bail refinement, were fitted using EosFit7-GUI software (Angel et al., 2014; Gonzalez-Platas et al., 2016).

5.3 RESULTS

5.3.1 XRD results and equation of state

Powder XRD measurements (runs SD005, SD008, SD009) reveal that $Fe_{0.67}Ni_{0.06}Si_{0.27}$ alloy is stable in the B2 structure (CsCl-type) throughout the entire investigated pressure range (6.8(2) – 98(3) GPa). An integrated diffraction pattern collected at 84.2(7) GPa and room temperature is shown in Figure 5.3.

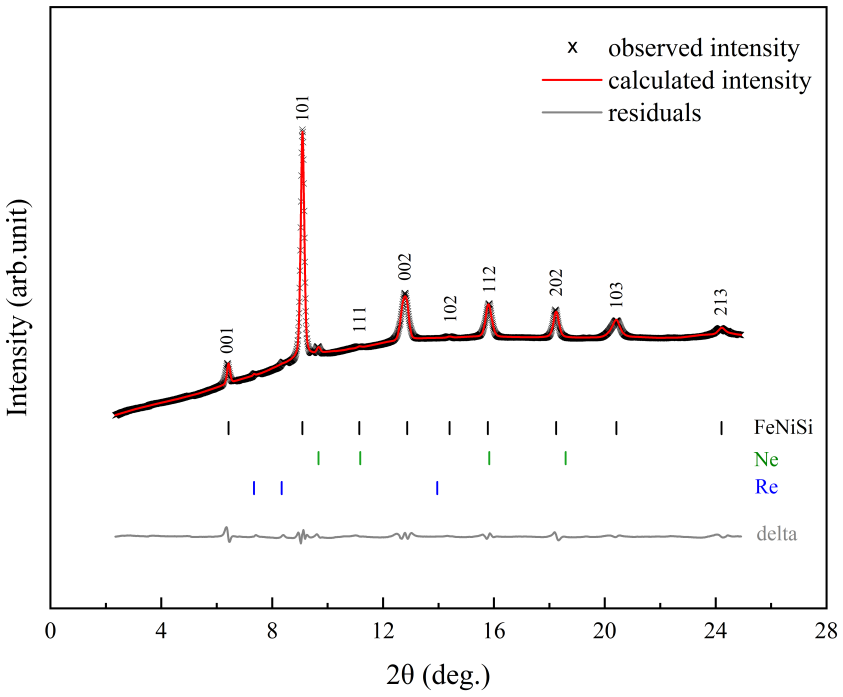

Figure 5.3: Integrated XRD pattern of B2-$Fe_{0.67}Ni_{0.06}Si_{0.27}$ alloy at 84.2(7) GPa. Ne (pressure medium) and Re (gasket) have been also identified. The contribution of Re peaks is likely detected by the tail of the beam which presents a Lorentzian line shape after focusing. However, a slight misalignment during data acquisition cannot be excluded. The powder profile was refined with the Le Bail method using JANA 2006 software (Petrícek et al., 2014).

The Le Bail method was used for data processing to refine lattice parameters, peak shapes, and the background. The Debye rings of the sample (runs SD005 and SD009) collected at the IXS beamline BL35XU (beam size 17 × 14 μm^2) show no evidence of inhomogeneous intensity distribution, consistent with the absence of notable preferred orientation (Figure 5.4a). On the other hand, 2D diffraction images collected at P02.2 DESY on run SD008 show spotted Debye rings at all pressures (Figure 5.4b). These likely arise from the reduced beam size (2 × 2 μm^2) compared to

powder crystallites (grain size estimated to be on the order of a few microns), and possibly poor grain sampling statistics of the polycrystalline sample.

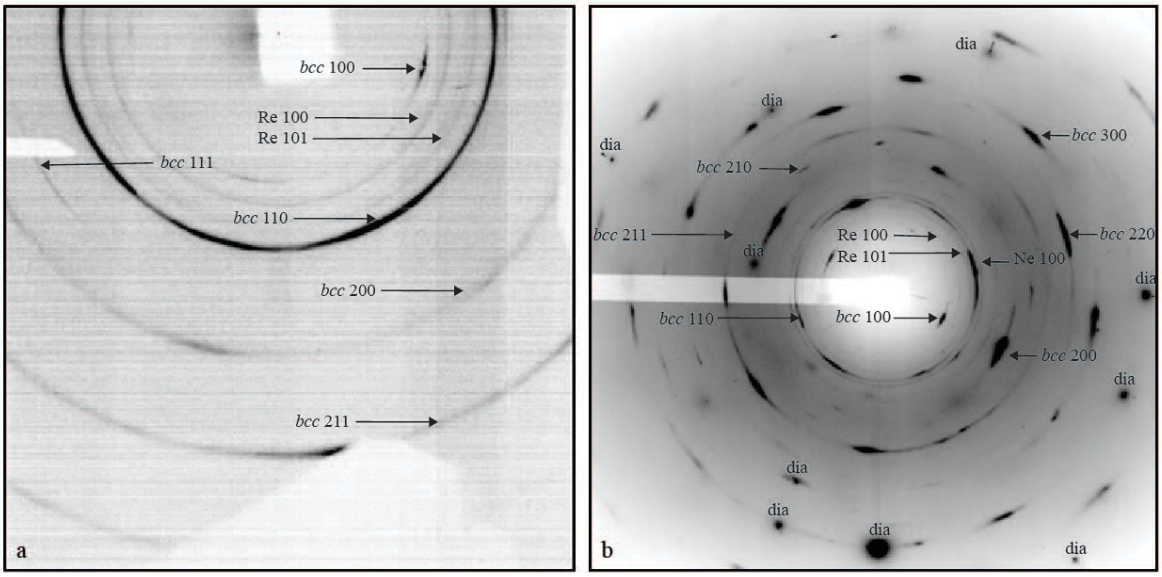

Figure 5.4: **a)** XRD pattern of B2-$Fe_{0.67}Ni_{0.06}Si_{0.27}$ alloy collected at 72.9(22) GPa and 300 K at BL35XU of SPring-8 (run SD005); **b)** XRD pattern collected at 84.2(7) GPa and 300 K at P02.2 DESY, PETRA III (run SD008). "*bcc*" indicates the $Fe_{0.67}Ni_{0.06}Si_{0.27}$ alloy; "dia" stands for diamond (from the DAC), and Debye rings from Re (gasket) and Ne (pressure medium) were also observed.

We therefore consider our IXS measurements to be unaffected by preferred orientation and any potential effects of preferred orientation on sound velocities to be negligible compared to the magnitude of estimated uncertainties in V_P (section 5.2.3).

The equation of state (EOS) collected in run SD008 is consistent with previous studies on Fe-Si and is shown in Figure 5.5a. Observed differences between EOS parameters of this study and previous work (Kamada et al., 2018; Edmund et al., 2019a, 2019b) are related to differences in composition and employed fitting models (third order Birch-Murnaghan (BM3) or Vinet). Volumes in the 10.4(1) – 84.2(7) GPa pressure range at 300 K were fitted to a second order Birch-Murnaghan (BM2) equation of state ($K'_{T0} = 4$) with the following coefficients: $V_0 = 22.37(8)$ Å^3, $K_{T0} = 222(6)$ GPa. To explore other possible models, we fitted data using a third order Birch Murnaghan and a Vinet equation of state. Comparison of the obtained statistical parameters showed that the addition of K'_{T0} did not improve the quality of the fit, which also appears more consistent with a BM2 EOS as seen in the *F-f* plot (Figure 5.5b).

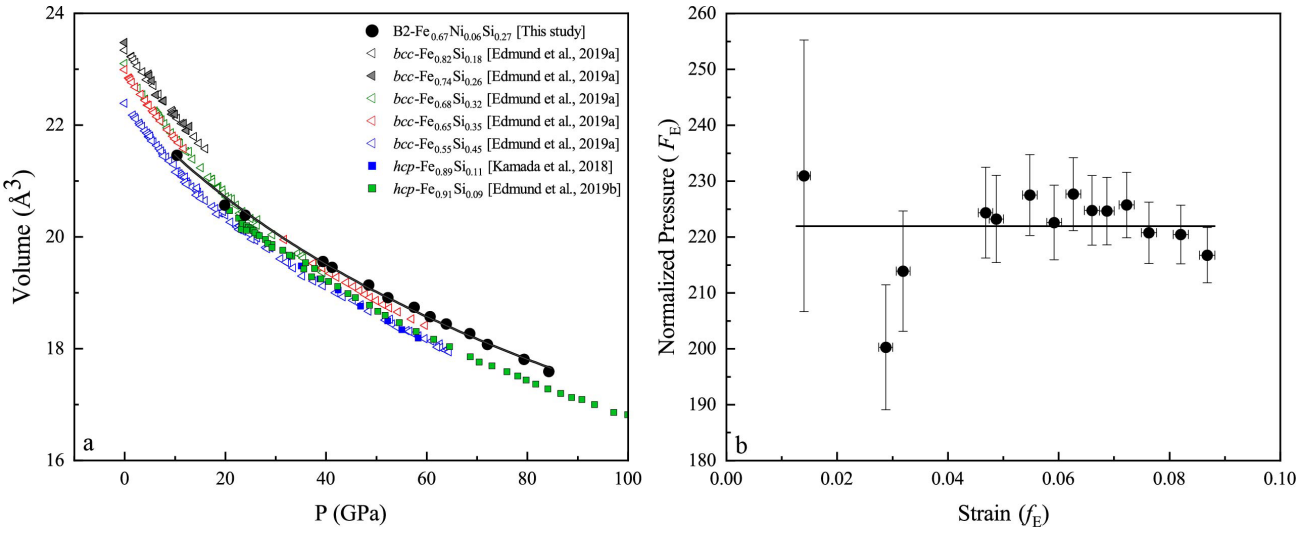

Figure 5.5: **a)** Isothermal EOS of B2-$Fe_{0.67}Ni_{0.06}Si_{0.27}$ alloy at 300 K collected in run SD008 (solid black circles). The solid line represents the least squares fit to a second-order Birch-Murnaghan EOS. Uncertainties on P-V data points are ~1 % (see Table S3) and plot inside the symbols. Equations of state of *bcc* and *hcp* Fe-Si alloys from previous studies are shown for comparison. **b)** Normalized pressure $F_E = P/\left[3f_E(1+2f_E)^{5/2}\right]$ as a function of the Eulerian strain $f_E = 1/2\left[(V_0/V)^{2/3} - 1\right]$. The solid line is a linear fit of the data based on a second-order Birch-Murnaghan EOS.

The complete list of refined lattice parameters is given in the supplementary material (Table S3) and was used to calculate the pressure and bulk modulus K_T from the measured volume for every pressure point of the IXS experiments as well as the shear wave velocities (V_S).

5.3.2 Sound velocity and Birch's law

IXS measurements (runs SD005 and SD009) were conducted at room temperature in the pressure range from 6.8(2) to 98(3) GPa. Figure 5.6a shows a fitted IXS spectrum collected at 98(3) GPa and momentum transfer 4.43 nm^{-1} on run SD009. The spectrum is characterized by an elastic peak, centered at zero energy, and inelastic features assigned to the longitudinal acoustic (LA) aggregate phonons of B2-$Fe_{0.67}Ni_{0.06}Si_{0.27}$ alloy and diamond and the transverse acoustic (TA) phonon of diamond. Experimental data and error bars are shown together with the best fit. Sample phonons are usually well resolved and visible for the investigated Q range (Figure S4). Energy positions of the phonons were determined by fitting data with Lorentzian functions, and did not change within uncertainty if a pseudo-Voigt lineshape was used instead (Figure S5).

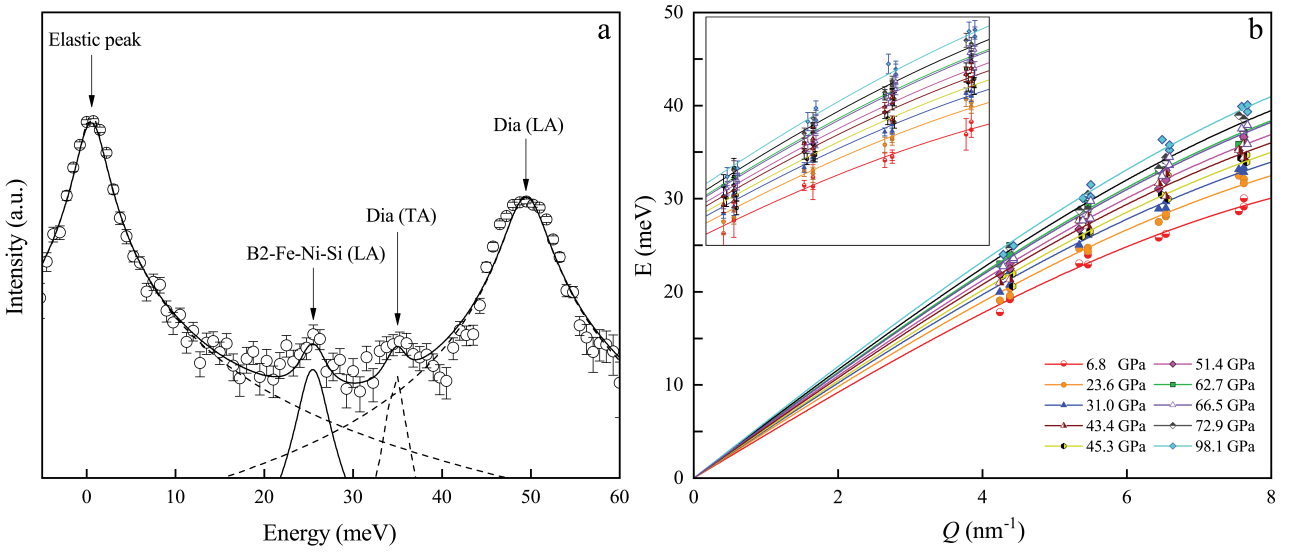

Figure 5.6: **a)** IXS spectrum of B2-$Fe_{0.67}Ni_{0.06}Si_{0.27}$ collected at 98(3) GPa and $Q = 4.43$ nm^{-1}. Lines show individual contributions from the sample (solid) and the elastic peak and diamond (TA and LA) (dashed). **b)** Longitudinal acoustic (LA) phonon dispersion of B2-$Fe_{0.67}Ni_{0.06}Si_{0.27}$ at different pressures and room temperature. Solid curves are sine fits obtained using equation 1. Inset: magnified with error bars.

The complete list of energy parameters and associated errors at different pressures and momentum transfers is given in Table S4. Results from each pressure were then fitted with a sinusoidal function to obtain the aggregate compressional sound velocity V_P (Equation 5.1). Dispersion curves of B2- $Fe_{0.67}Ni_{0.06}Si_{0.27}$ alloy for each pressure are shown in Figure 5.6b. The phonon energy of inelastic scattering increases with pressure; hence compressional sound velocity increases with pressure. The data obtained from fitting IXS spectra provide a good constraint on compressional sound velocity. The experimentally determined densities and velocities for B2-$Fe_{0.67}Ni_{0.06}Si_{0.27}$ alloy are summarized in Table 5.2.

The measured compressional velocities V_P are plotted as a function of density in Figure 5.7 and compared with previous results for pure Fe, Fe-Ni, Fe-Si and Fe-Ni-Si alloys with different crystal structures. The relation between V_P and density of B2-$Fe_{0.67}Ni_{0.06}Si_{0.27}$ alloy follows Birch's law,

$$V_P\ (\mathrm{km/s}) = 1.13(7) \times \rho\ (\mathrm{g/cm^3}) - 1.25(58)\,, \qquad (5.6)$$

indicating a linear relationship between density and sound velocity.

Table 5.2: Density ($\boldsymbol{\rho}$), momentum transfer where the phonon dispersion turns over ($\boldsymbol{Q_{MAX}}$), isothermal bulk modulus ($\boldsymbol{K_T}$), aggregate longitudinal ($\boldsymbol{V_P}$) and transverse ($\boldsymbol{V_S}$) velocities of B2-$Fe_{0.67}Ni_{0.06}Si_{0.27}$ obtained from IXS and XRD measurements at 300 K.

Run	P (GPa)	ρ (g/cm^3)	V_P (km/s)	Q_{MAX} (nm^{-1})	K_T (GPa)	V_S (km/s)
SD005	7(2)	7.4(2)	7.1(4)	11(2)	249(6)	3.5(5)
SD005	23.6(7)	7.9(2)	7.5(4)	12(2)	312(7)	3.6(6)
SD005	31.0(9)	8.0(2)	7.8(3)	12(2)	340(8)	3.8(5)
SD005	43(1)	8.3(2)	8.3(4)	12(2)	384(9)	4.0(6)
SD009	45(1)	8.4(2)	8.0(3)	12(2)	391(9)	3.6(5)
SD005	51(2)	8.5(2)	8.4(4)	12(2)	413(9)	4.1(5)
SD005	63(2)	8.7(2)	8.7(3)	12(2)	452(10)	4.2(5)
SD009	67(2)	8.8(2)	8.6(4)	13(2)	465(10)	4.0(6)
SD005	73(2)	8.9(2)	8.9(3)	12(2)	487(11)	4.3(5)
SD009	98(3)	9.3(2)	9.2(3)	13(2)	572(13)	4.1(5)

Note: Pressure was calculated using the EOS of the sample. Numbers in parentheses are errors on the last digit.

Our velocity measurements for B2-$Fe_{0.67}Ni_{0.06}Si_{0.27}$ are systematically higher than for pure *bcc* Fe (Liu et al., 2014; Shibazaki et al., 2016) and *hcp* Fe (Antonangeli et al., 2018; Ohtani et al., 2013; Morrison et al., 2019) as a consequence of the effect of Si which increases V_P for a given density (Figure 5.7a). On the other hand, comparison of elastic properties of pure Fe and Fe-Ni alloys (Lin et al., 2003; Kantor et al., 2007; Wakamatsu et al., 2018; Morrison et al., 2019) shows that Ni has the opposite effect to Si, reducing V_P at the same density with respect to pure Fe. We note that crystal structure has a minimal effect on the slope of Birch's law, as all data with the same composition can be fit to a common line (grey and red lines in Figure 5.7a, dark green line in Figure 5.7c). The difference observed between previous data of *hcp* Fe (Ohtani et al., 2013; Antonangeli et al., 2018) and *hcp* ^{57}Fe (Morrison et al., 2019) as well as between *hcp* Fe-Ni (Kantor et al., 2007; Wakamatsu et al., 2018) and *hcp* ^{57}Fe-Ni alloys (Lin et al., 2003; Morrison et al., 2019) is because ^{57}Fe is 1.8 % denser than non-enriched iron.

Figure 5.7b shows our V_P-density measurements compared with previous studies conducted on Fe-Si alloys using IXS (Badro et al., 2007; Antonangeli et al., 2018; Sakairi et al., 2018), NRIXS (Lin et al., 2003), and PA (Edmund et al., 2019a, 2019b) techniques. All data show that increasing Si content increases V_P for a given density. There is some variation in the slope $dV_P/d\rho$, which can be influenced by bonding (e.g., Edmund et al., 2019a), but can also be affected by experimental conditions (for example if a pressure medium was used or not) and different geometries used for different techniques (Edmund et al., 2019b). While differences in slope are relatively minor within

the pressure range of data collection, they become more significant when data are extrapolated to core conditions.

Our data for B2-$Fe_{0.67}Ni_{0.06}Si_{0.27}$ are consistent with previous measurements of *bcc* and *hcp* Fe-Ni-Si alloys (Figure 5.7c). As above, Si and Ni have opposing effects on V_P at the same density. Overall, the compressional sound velocity of B2-$Fe_{0.67}Ni_{0.06}Si_{0.27}$ is dominated mainly by the effect of Si incorporation with a smaller effect due to Ni.

We derived the aggregate shear wave velocity V_S by combining our measurements of V_P and ρ with the adiabatic bulk modulus (K_S) from the EOS using the relation,

$$V_S = \left[\frac{3}{4}\left(V_P^2 - \frac{K_S}{\rho}\right)\right]^{\frac{1}{2}}. \quad (5.7)$$

Considering that the difference between K_S and the isothermal bulk modulus (K_T) is negligible at room temperature ($K_S = K_T(1 + \alpha\gamma T) \sim K_T$), we used K_T obtained from our isothermal EOS to calculate V_S. Results are shown in Table 5.2 together with uncertainties that were propagated on V_P, ρ and K_T.

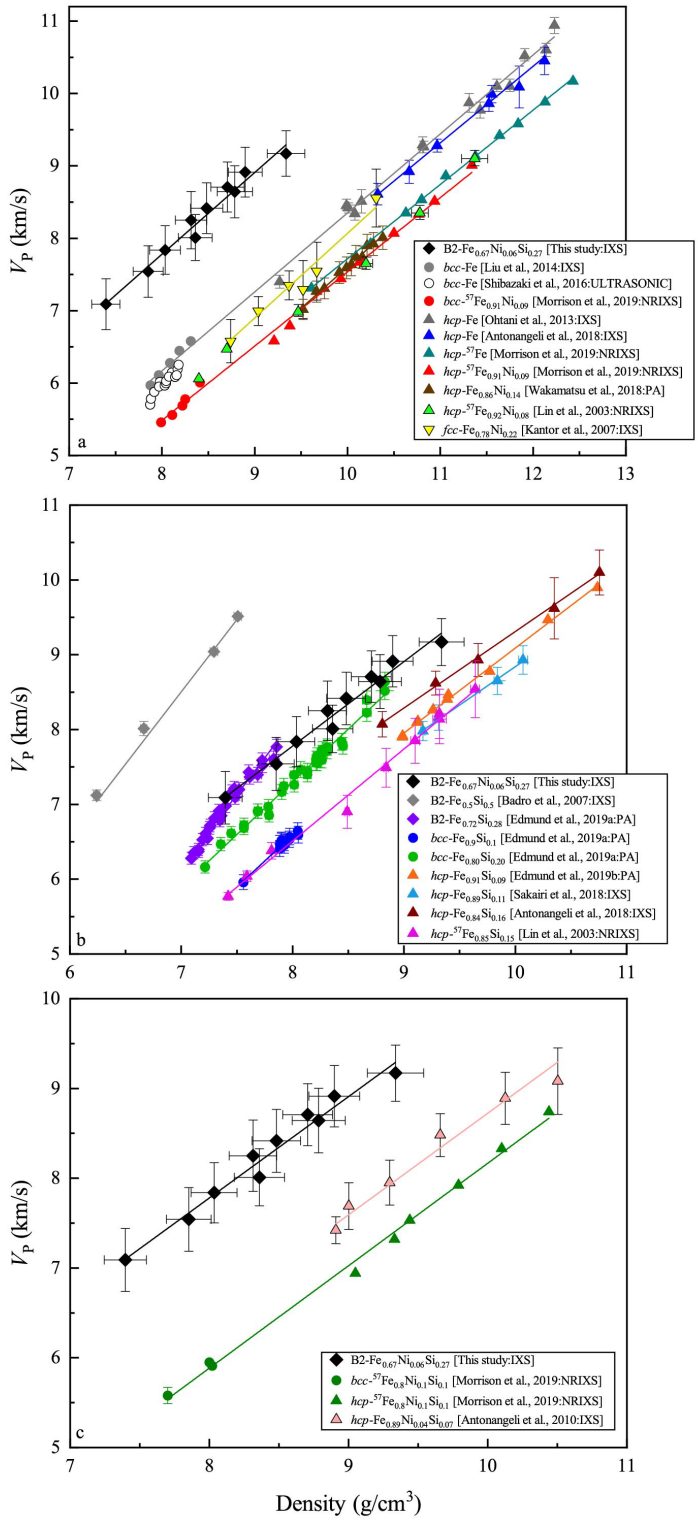

Figure 5.7: Birch's law of B2-$Fe_{0.67}Ni_{0.06}Si_{0.27}$ alloy compared with previous studies of pure Fe, Fe-Ni (**a**) Fe-Si (**b**) and Fe-Ni-Si alloys (**c**). Data reported by Lin et al. (2003) and Morrison et al. (2019) involve ^{57}Fe which is 1.8 % denser than non-enriched Fe. Solid black lines show the Birch's law fit to our data in each panel. Crystal structure has a minimal effect since data with the same composition and different structures can be fitted with a common Birch's law (grey and red lines in Figure 5.7a, dark green line in Figure 5.7c). We included systematic errors in the estimation of error bars on the velocities (see section 5.2.3).

5.4 DISCUSSION

In order to compare our room temperature measurements with seismological models, we extrapolated the V_P-ρ and V_S-ρ linear relationships obtained from Birch's law to conditions of the inner core boundary (ICB) according to PREM (330 GPa and 6370 K, Alfè et al., 2002). Extrapolation of V_P for B2-$Fe_{0.67}Ni_{0.06}Si_{0.27}$ alloy was performed using a parameterization of Birch's law described by Sakamaki et al. (2016),

$$V_P\,(\rho, T) = M\rho + B + A(T - T_0)(\rho - \rho^*)], \tag{5.8}$$

where M and B are Birch's law coefficients at room temperature, and A and ρ^* are fixed parameters that describe the temperature dependence. Values of A and ρ^* were taken from Sakairi et al. (2018) and include the temperature dependence for Fe-Si alloys. We formulated the equation using T_0 = 300 K, T = 6370 K, M = 1.13(7), B = – 1.25(58), A = 3.8 ± 1.8 × 10^{-5} and ρ^* = 15.4 ± 1.5 g/cm^3. We estimated a large uncertainty for A to take the difference in composition into account between our B2-Fe-Ni-15 wt.% Si alloy and the Fe-6 wt.% Si alloy of Sakairi et al. (2018). We estimated the uncertainty of ρ^* to be of the same magnitude to that for *hcp*-Fe (Sakamaki et al., 2016). Error propagation of V_P was performed following Sakamaki et al. (2016). Extrapolation of the density to 330 GPa and 6370 K was performed using the isothermal EOS determined for the sample (section 5.3.1) corrected for the thermal pressure (P_{th}). We applied the P_{th} correction using the Mie-Grüneisen Debye (MGD) model (e.g., Poirier, 2000). Thermoelastic parameters (i.e., Debye temperature θ, Grüneisen parameter γ and its logarithmic volume derivative $q\backslash\beta$) of *hcp* and *hcp* + B2-$Fe_{0.84}Si_{0.16}$ (Fischer et al., 2014), *hcp*-$Fe_{0.81}Ni_{0.09}Si_{0.1}$ (Morrison et al., 2018), *hcp*-$Fe_{0.91}Si_{0.09}$ (Edmund et al., 2019b), and *hcp*-$Fe_{0.86}Ni_{0.05}Si_{0.9}$ (Edmund et al., 2020) from previous studies were used in the calculation. Table 5.3 summarizes the thermodynamic parameters used to extrapolate density and sound velocities to ICB conditions.

We fit our room temperature P-V data with a second-order Birch-Murnaghan equation of state (EOS),

$$P_{300K}(V) = \frac{3}{2}\,K_{T0}\left(\left(\frac{V_0}{V}\right)^{\frac{7}{3}} - \left(\frac{V_0}{V}\right)^{\frac{5}{3}}\right), \tag{5.9}$$

where K_{T0} is the isothermal bulk modulus at ambient conditions.

The Mie-Grüneisen Debye temperature correction of the isothermal EOS in the quasi-harmonic approximation is presented below as formulated by Poirier (2000). The pressure at high temperature is expressed as the following,

$$P\,(V,T) = P_{300\mathrm{K}} + \Delta P_{\mathrm{th}}\,(V,T) \tag{5.10}$$

$$\Delta P_{\mathrm{th}} = P_{\mathrm{th}}\,(V,T) - P_{\mathrm{th}}(V,300\mathrm{K}). \tag{5.11}$$

Table 5.3: Thermodynamic parameters used for the high-temperature correction. Density (ρ), adiabatic bulk modulus (K_S), and wave velocities (V_P, V_S) of B2-$Fe_{0.67}Ni_{0.06}Si_{0.27}$ alloy extrapolated to ICB conditions (330 GPa and 6370 K) as a function of the thermoelastic parameters (i.e., zero pressure Debye temperature θ_0, Grüneisen parameter γ_0 and its logarithmic volume derivative $q\backslash\beta$) using the MGD model. Uncertainties are given as the error in the equivalent last digits of the value: 11.1 (1) means 11.1 ± 0.1 and 9.4 (11) means 9.4 ± 1.1.

γ_0	$q\backslash\beta$	θ_0 (K)	ρ (g/cm^3) *	K_S (GPa)*	V_P (km/s) *	V_S (km/s) *
1.66(9)[a]	0.67[a]	422[a]	11.1(1)	967(13)	9.4(11)	0.6(13)
2.13(8)[b]	0.67[b]	422[b]	10.8(1)	898(11)	9.0 (11)	1.5(13)
1.82(9)[c]	1.0[c]	417[c]	11.1(1)	980(12)	9.4(11)	0.9(13)
2.3(9)[d]	1.0[d]	417[d]	10.9(1)	917(12)	9.1(11)	1.2(13)
1.72(13)[e]	0.65(23)[e]	422[e]	11.0(1)	956(6)	9.3(11)	0.2(11)
2.0(1)[f]	1.0(2)[f]	417[f]	11.0(1)	956(9)	9.3 (11)	0.2(12)
2.22(8)[g]	1.0[g]	417[g]	10.9(1)	927(10)	9.1(11)	1.1(13)
1.14(14)[h]	1.0[h]	417 [h]	11.5(1)	1071(18)	10.0(11)	2.1(14)

Note: Thermoelastic parameters are taken from the literature (a-h).
[a]Edmund et al. (2020) - *hcp*-$Fe_{0.86}Ni_{0.05}Si_{0.9}$ (case #1)
[b]Edmund et al. (2020) - *hcp*-$Fe_{0.86}Ni_{0.05}Si_{0.9}$ (case #2)
[c]Edmund et al. (2020) - *hcp*-$Fe_{0.86}Ni_{0.05}Si_{0.9}$ (case #3)
[d]Edmund et al. (2020) - *hcp*-$Fe_{0.86}Ni_{0.05}Si_{0.9}$ (case #4)
[e]Edmund et al. (2019b) - *hcp*-$Fe_{0.91}Si_{0.09}$
[f]Morrison et al. (2018) - *hcp*-$Fe_{0.81}Ni_{0.09}Si_{0.1}$
[g]Fischer et al. (2014) - *hcp*-$Fe_{0.84}Si_{0.16}$
[h]Fischer et al. (2014) - *hcp*+B2 $Fe_{0.84}Si_{0.16}$
*P-T conditions: 330 GPa and 6370 K

The thermal pressure P_{th} is defined as:

$$P_{\mathrm{th}}\,(V,T) = 9\mathrm{n}RT\frac{\gamma}{V}\left(\frac{T}{\theta}\right)^{3}\int_{0}^{\frac{\theta}{T}}\frac{\mathrm{z}^{3}}{\mathrm{e}^{\mathrm{z}}-1}\,d\mathrm{z}, \tag{5.12}$$

where n is the number of atoms in the formula unit ($\mathrm{n} = 2$ for B2-$Fe_{0.67}Ni_{0.06}Si_{0.27}$ alloy), R is the gas constant, γ is the Grüneisen parameter (Equation 5.13) and θ is the Debye temperature (Equation 5.14).

$$\gamma_{(V)} = \gamma_0\left(\frac{V}{V_0}\right)^{q} \tag{5.13}$$

$$\theta_{(V)} = \theta_0\exp\left(\frac{\gamma_0-\gamma_V}{q}\right). \tag{5.14}$$

The electronic and anharmonic contribution to the thermal pressure (second and third terms of the following equation) was included as shown in Dewaele et al. (2006),

$$P_{\mathrm{th}}\,(V,T) = \frac{9R\gamma}{V}\left(\frac{\theta}{8}+T\left(\frac{T}{\theta}\right)^{3}\int_{0}^{\frac{\theta}{T}}\frac{\mathrm{z}^{3}\mathrm{dz}}{\mathrm{e}^{\mathrm{z}}-1}\right)+\frac{3R}{2V}ma_0x^{m}T^{2}+\frac{3R}{2V}ge_ox^{g}T^{2}\,. \tag{5.15}$$

Anharmonic and electronic parameters are fixed at a_0 = 3.7 × 10^{-5} K^{-1}, m = 1.87, e_o= 1.95 × 10^{-4} K^{-1}, g= 1.339 (Dewaele et al., 2006 and references therein).

Alternatively, Fei et al. (2016) and Edmund et al. (2019b, 2020), provided a different expression to include the electronic and anharmonic contribution to the thermal pressure:

$$P_{\mathrm{th}}\,(V,T) = \frac{9R\gamma}{V}\left(\frac{\theta}{8}+T\left(\frac{T}{\theta}\right)^{3}\int_{0}^{\frac{\theta}{T}}\frac{\mathrm{z}^{3}\mathrm{dz}}{\mathrm{e}^{\mathrm{z}}-1}\right)+\frac{\gamma_e}{V}\beta_0\left(\frac{V}{V_0}\right)^{k}T^{2} \tag{5.16}$$

where γ_e is the electronic Grüneisen parameter, β_0 is the electronic heat capacity, and k characterizes the volume dependence. The latter parameters were fixed at $\gamma_e = 2$, $\beta_0 = 3.2\times10^{-6}\,\mathrm{cm^3mol^{-1}JK^{-1}}$ and $k = 1.34$. Our calculations explored both methodologies

(Equations 5.15 and 5.16) and found that they show a consistent electronic and anharmonic contribution to the thermal pressure within experimental uncertainty.

The isothermal K_T and adiabatic K_S bulk moduli at high pressure and high temperature are given as,

$$K_T = K_0 \left(\frac{V_0}{V}\right)^{\frac{5}{3}} \left(1 + \frac{7}{2}\left(\left(\frac{V_0}{V}\right)^{\frac{2}{3}} - 1\right)\right) + (\gamma + 1 - q)\frac{\gamma \Delta U q}{V} - \frac{\gamma^2 \Delta (C_V T)}{V} \quad (5.17)$$

$$K_S = K_T(1 + \alpha\gamma T). \quad (5.18)$$

The thermal expansion α was calculated as the following:

$$\alpha = \frac{\gamma C_V}{K_T V}\ . \quad (5.19)$$

V_S determination at ICB was performed by applying Equation 5.7 in which V_P was calculated using Equation 5.8, and ρ and K_S were obtained using the MGD model. To compare extrapolated data of B2-$Fe_{0.67}Ni_{0.06}Si_{0.27}$ alloy with sound velocities and densities of *hcp* Fe-Ni alloys reported previously at the ICB (Lin et al., 2003; Martorell et al., 2013; Wakamatsu et al., 2018), we explored the pressure and temperature dependence of our V_P and V_S-ρ relations at inner core conditions. Variation of both target pressure and temperature in the ranges 330-360 GPa and 5500-6370 K showed that our extrapolated V_P, V_S, and density values are consistent within uncertainties.

Figure 5.8 shows extrapolated V_P and V_S-density relations of B2-$Fe_{0.67}Ni_{0.06}Si_{0.27}$ together with PREM (Dziewonski and Anderson, 1981) and *hcp* Fe-Ni (Lin et al., 2003; Martorell et al., 2013; Wakamatsu et al., 2018) at the ICB. Birch's law relations at 300 K determined in this study are also shown for comparison. As shown below, a mechanical mixture (Fischer et al., 2013; Fischer and Campbell, 2015) of B2-$Fe_{0.67}Ni_{0.07}Si_{0.27}$ and *hcp* Fe-Ni matches PREM values of V_P, V_S, and ρ at the ICB within experimental uncertainties.

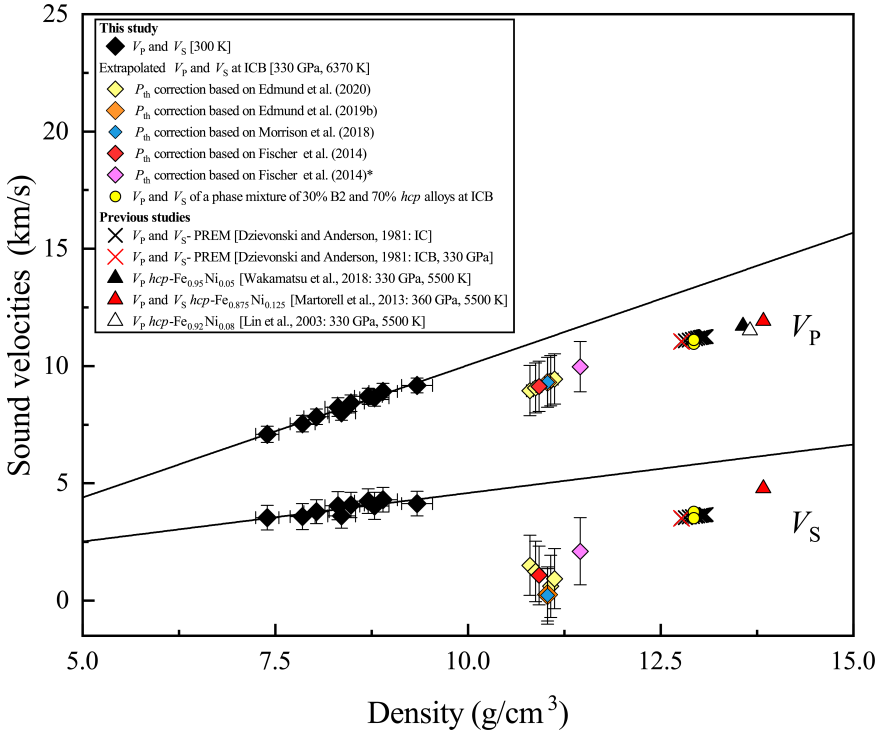

Figure 5.8: Density dependence of aggregate compressional (V_P) and shear (V_S) wave velocities of B2-$Fe_{0.67}Ni_{0.06}Si_{0.27}$ at ICB conditions. Colored diamonds are the present data extrapolated to 330 GPa and 6370 K using different thermoelastic parameters for the thermal pressure correction P_{th} based on *hcp*-$Fe_{0.84}Si_{0.16}$: Fischer et al. (2014) (red); *hcp*+B2-$Fe_{0.84}Si_{0.16}$: Fischer et al. (2014) (magenta); *hcp*-$Fe_{0.81}Ni_{0.09}Si_{0.1}$: Morrison et al. (2018) (blue); *hcp*-$Fe_{0.91}Si_{0.09}$: Edmund et al, (2019b) (orange); *hcp*-$Fe_{0.86}Ni_{0.05}Si_{0.9}$: Edmund et al. (2020) (yellow) (from case #1 to case #4, see Table S5). Black diamonds and associated solid lines are Birch's law of B2-$Fe_{0.67}Ni_{0.06}Si_{0.27}$ at 300 K. Triangles represent V_P and V_S-density relations from previous selected studies of *hcp* $Fe_{0.92}Ni_{0.08}$ (white: Lin et al., 2003 at 330 GPa and 5500 K), *hcp* $Fe_{0.875}Ni_{0.125}$ (red: Martorell et al., 2013 at 360 GPa and 5500 K), *hcp* $Fe_{0.95}Ni_{0.05}$ and *hcp* $Fe_{0.86}Ni_{0.14}$ (black: Wakamatsu et al., 2018 at 330 GPa 5500 K). Yellow circles are estimated V_P and V_S averages of the mechanical mixture 30 vol. % B2 + 70 vol. % *hcp* consistent with preliminary reference Earth model (PREM) values within uncertainty. Crosses: PREM inner core (black); PREM values at ICB (red).

To estimate core composition, we compared PREM sound velocity and density to values for a mixture of *hcp* and B2 phases (Fischer et al., 2013; Fischer and Campbell, 2015) using our B2-$Fe_{0.67}Ni_{0.06}Si_{0.27}$ data extrapolated to ICB conditions and previous *hcp* Fe-Ni data (Martorell et al., 2013) recalculated at PREM ICB conditions (i.e., 330 GPa and 6370 K). We used the linear mixing model presented by Badro et al. (2007) to determine the properties of an ideal mixture of *hcp* Fe-Ni and B2-$Fe_{0.67}Ni_{0.06}Si_{0.27}$. This arithmetic approach was also used by Wyllie et al. (1956) who calculated the average velocity of a two-phase mixture in porous media, and is also frequently used to determine the velocity of rocks (e.g., Christensen and Silisbury, 1975). This model provides a good starting point since the dominant influence on density and sound velocity is Si composition. The average density ρ and sound velocity V_P of PREM can be expressed as (Badro et al., 2007):

$$\rho = x\rho^{\mathrm{FeNiSi}} + (1-x)\rho^{\mathrm{FeNi}} \tag{5.20}$$

and,

$$V_{\mathrm{P}} = \frac{{V_{\mathrm{P}}}^{\mathrm{FeNiSi}}{V_{\mathrm{P}}}^{\mathrm{FeNi}}}{\left[(1-x){V_{\mathrm{P}}}^{\mathrm{FeNiSi}} + x{V_{\mathrm{P}}}^{\mathrm{FeNi}}\right]}, \tag{5.21}$$

where x is the volume fraction of B2-$Fe_{0.67}Ni_{0.06}Si_{0.27}$ alloy, ${V_{\mathrm{P}}}^{\mathrm{FeNiSi}}$ and ${V_{\mathrm{P}}}^{\mathrm{FeNi}}$ are extrapolated compressional velocities at ICB of B2-$Fe_{0.67}Ni_{0.06}Si_{0.27}$ and Fe-Ni alloys (Martorell et al., 2013), and ρ^{FeNiSi} and ρ^{FeNi} are corresponding densities at ICB of B2-$Fe_{0.67}Ni_{0.06}Si_{0.27}$ and Fe-Ni alloys from this study and Martorell et al. (2013). Solving equations 5.20 and 5.21 simultaneously gives a volume fraction x of 0.30(5), which corresponds to 4.1(6) wt. % Si. and 11.4(5) % Ni at ICB conditions. We consider the Si content to be well determined from this calculation due to the strong effect of Si on sound velocity, while Ni is less well constrained and depends on the Ni content of the Fe-Ni alloy endmember. We also determined Si and Ni content using *hcp* Fe-Ni data from Lin et al. (2003) and Wakamatsu et al. (2018) at ICB conditions (i.e., 330 GPa and 6370 K) and found that, although the Si content is the same within uncertainty, the Ni content in the inner core varies as a function of the composition of the *hcp* endmember. For example, using *hcp*-$Fe_{0.95}Ni_{0.05}$ data from Wakamatsu et al. (2018) and *hcp*-$Fe_{0.92}Ni_{0.08}$ data from Lin et al. (2003), the Ni content predicted in the inner core changes from ~5.7(5) to ~8.0(5) wt. %, respectively.

To test the validity of our determination, we calculated elastic properties of the same composite assemblage (30 vol. % B2 + 70 vol. % *hcp*) at the ICB using the Voigt-Reuss-Hill (VRH) average (e.g., Man & Huang, 2011), which is commonly used to estimate elastic properties of polycrystalline materials. We derived bulk and shear moduli from V_{P}, V_{S}, and density of the B2 and *hcp* phases. Using the VRH approach, we obtained the same average elastic properties within uncertainty as the linear mixing model by Badro et al. (2007).

The estimated Si content, ~3-5 wt. % agrees with values proposed by Sakairi et al. (2018) (3-6 wt. % Si), while it is slightly higher than the value proposed by Badro et al. (2007) (2.3 wt. % Si) and Antonangeli et al. (2010, 2018) (2 wt. % Si) and lower than the estimate of Mao et al. (2012) (8 wt. % Si). The difference to the latter study might arise from the different model that they used to extrapolate V_{P}-ρ to the ICB (power law). The inferred amount of Ni (5-12 wt. %) is consistent with geochemical estimates (e.g., 5.2 wt.%, McDonough, 2003; 5-15 wt. % Ni, Li &

Fei, 2014). The inferred Si and Ni contents satisfy the melting requirement at ICB conditions according to results of previous studies (e.g., Fischer et al., 2013; Zhang et al., 2018). In general, Si has a relatively mild effect on the melting temperature of iron compared to other light elements such as S and O.

5.5 CONCLUSIONS

Sound velocity and density measurements performed on B2-$Fe_{0.67}Ni_{0.06}Si_{0.27}$ under pressure yielded values of V_P that are significantly faster than pure Fe at the same density, mainly as a consequence of the effect of Si on the elastic properties of pure Fe. We tested the hypothesis that the inner core is composed of a mixture of Si-depleted *hcp* and Si-enriched B2 phases, and found that PREM V_P and ρ values are consistent with an inner core consisting of a mixture of ~30 vol % B2-$Fe_{0.67}Ni_{0.06}Si_{0.27}$ and ~70 vol % *hcp* Fe-Ni, which corresponds to 3-5 wt. % Si and 5-12 wt. % Ni. We emphasize that the inferred amount of Si and Ni may vary depending on the presence of other light elements in the inner core (e.g., Caracas, 2017) and/or anharmonic/pre-melting effects of core material (Martorell, et al., 2013; Antonangeli et al., 2018). Further uncertainties arise from the choice of thermoelastic parameters used for the temperature correction. The model could therefore be improved by performing sound velocity measurements on Fe-Ni-Si alloys at combined high pressure and high temperature.

Chapter 6

6 MAJOR CONCLUSIONS AND FUTURE OUTLOOKS

This chapter outlines the major findings of this study in relation to the research aims and summarizes the contribution thereof reviewing the limitations and proposing opportunities for future research.

One of the main objectives of this thesis was to introduce an oxybarometer for high pressure and high temperature experiments in DAC using the redox sensor methodology. Our results compared with complementary multi anvil experiments performed at similar experimental conditions and with the same starting composition, show lower oxygen fugacities and highlight the importance of measuring the f_{O_2} during LHDAC experiments. In fact, one of the possible reasons why previous LHDAC studies achieved contradictory results on the stability of carbonates at lower mantle conditions (e.g., Cerantola et al., 2017 and Dorfman et al., 2018) may be due to the lack of control of the oxygen fugacity during the experiments. Therefore, any experimental study designed to simulate the stability of high-pressure phases in the Earth's interior should be considering the f_{O_2} parameter in addition to pressure and temperature to correctly reproduce a more realistic system for Earth's mantle. The redox sensor approach based on the Fe-Ir system adopted in this study was further implemented including the volume dependency on the activity-composition relations up to 100 GPa. Our results provide a more accurate method to calculate the oxygen fugacity and show lower values compared to the f_{O_2} obtained using the former activity model with a difference increasing with increasing pressure. The calibration of the Fe-Ir redox sensor at high pressure was conducted comparing thermodynamic properties of our alloy composition (i.e., $Fe_{0.40}Ir_{0.60}$) with the end member phases and invites further studies on different alloy compositions, such as $Fe_{0.20}Ir_{0.80}$, $Fe_{0.60}Ir_{0.40}$, $Fe_{0.80}Ir_{0.20}$, to test the magnitude of the compositional effect on the oxygen fugacity calculation. Moreover, these results may be used to calculate the high-pressure high-temperature phase relations in the Fe-Ir binary system and improve the existing activity model at high pressure as a function of a wide range of temperature and composition. Along the same lines, a similar experimental strategy could be extended to the Fe-Pt and Fe-Pd systems, often employed as sliding redox sensors.

Testing the applicability of this newly calibrated oxybarometer and evaluating the oxygen fugacity variation in experimental systems designed to simulate the interaction between a carbonated subducting slab and a metal saturated lower mantle, was an additional focus of this study. Our results, determined for a simplified lower mantle assemblage in which magnesite, diamond, and ferropericlase coexist, show lower oxygen fugacities compared to previous estimates obtained for the same multi anvil run products (Stagno et al., 2011). This implies a wider stability region of magnesite coexisting with diamond and (C-bearing) Fe metal down to 1500 km depth. A primary aim of this study was to evaluate the $Fe^{3+}/\Sigma Fe$ ratio in ferropericlase to infer the maximum ferric iron content that the mineral can incorporate before the exsolution of spinel-type phases from the ferropericlase matrix upon ferric iron saturation. Our results show a $Fe^{3+}/\Sigma Fe$ ratio consistent with previous studies (i.e., 0-10 %) and confirm the suitability of using ferropericlase as a redox tracer for the lower mantle displaying a positive correlation between Fe oxidation state and oxygen fugacity. Moreover, experimental data were integrated with analyses of natural ferropericlase inclusions in diamonds from Rio Soriso (Brazil). Both natural and experimental results show compositional (Fe#) and redox heterogeneities that potentially suggest multiple oxidation events through which the lower mantle reacts with CO_2-bearing fluids perturbing, therefore, the local oxygen fugacity at the expense of Fe(Ni) metal. Our main findings support the scenario in which ferropericlase recording low f_{O_2} are protogenetic, the more oxidized are syngenetic, while the ones showing evidences of exsolved Fe_xO_y phases are likely to be epigenetic and occurred upon decompression and cooling. This hypothesis is corroborated by nanotextural observations and SAED analyses of our experimental run products that reveal no formation of ferrite phases in the investigated ferropericlase grains. Hence, considering the broad variation in Fe# and oxygen fugacity recorded by both synthetic and natural ferropericlases, we conclude that as effect of the CO_2 ingassing into the deep Earth's interior via subduction, the current lower mantle is far to be saturated in Fe metal. A valuable integration of these results would be to further analyze the natural inclusions in diamonds with the transmission electron microscopy to elucidate on the crystal chemistry of these spinel phases and compare results with observations of ferropericlase inclusions in the literature. Moreover, the addition of bridgmanite (the most abundant phase in the lower mantle) to the experimental system would provide an important starting point in understanding the degree of interaction and involvement of this mineral with respect to ferropericlase in redox-driven

diamond formation processes that, in turn, may explain the rarity of bridgmanite occurrence as a natural inclusion in super deep diamonds.

Another topic that was address in this thesis concerns the investigation of the effect of light elements on elastic properties of metal alloys relevant for the inner core. Specifically, we tested the hypothesis that the inner core is composed of a mixture of Si-depleted *hcp* and Si-enriched B2 phases, performing sound velocity and density measurements on polycrystalline B2-$Fe_{0.67}Ni_{0.06}Si_{0.27}$ alloy to provide new constraints on the role of Si as a light element in the inner core. Our room temperature results on density and compressional sound velocity show a consistent trend with previous studies conducted on Fe-Si, Fe-Ni-Si, and Fe-Ni alloys with different composition revealing a dominant effect of Si on compressional sound velocity that produces an increase in V_P for a given density and a mild effect of Ni that yields a slight decrease in V_P at the same density. In order to compare our results with geophysical observations, such as PREM, we extrapolated V_P, V_S, and density to the inner core boundary conditions using the Mie-Grüneisen Debye model. Assuming a mechanical mixture of our extrapolated Si-rich alloy and a Si-poor Fe-Ni phase from the literature determined at ICB conditions, our results can account for V_P, V_S, and density of PREM. Important to mention, is the observed variation in extrapolated $V_P - \rho$ and $V_S - \rho$ results for B2-$Fe_{0.67}Ni_{0.06}Si_{0.27}$ alloy that arise from the choice of thermoelastic parameters for Fe-Si and Fe-Ni alloys used in the model for the temperature correction, representing a limitation for the reproducibility of the exact conditions existing at the ICB. The model could therefore be improved by performing sound velocity measurements on B2-$Fe_{0.67}Ni_{0.06}Si_{0.27}$ alloys at combined high pressure and high temperature as well as determining the *P-V-T* equation of state of the investigated alloy composition to evaluate the magnitude of a potential compositional effect on thermoelastic coefficients such as the Grüneisen parameter. Moreover, based on the results of this study we infer an inner core composition of ~3-5 wt. % of Si and ~5-12 wt. % of Ni assuming a linear mixing model between the two end member phases (i.e., 30 vol % of Si-rich B2 and 70 vol % of Si-depleted *hcp* alloy), which is consistent with experimental and geochemical estimates. We emphasise that the inferred amount of Si and Ni may vary depending on the presence of other light elements in the inner core and suggest for further studies aiming at explore a combination of light elements candidate for the inner core.

Chapter 7

7 ACKNOWLEDGMENTS

I would like to acknowledge the International Research and Training Group (IRTG) "Deep Earth Volatile Cycles" supported by the Deutsche Forschungsgemeinschaft (DFG) and the Japanese Society for the Promotion of Science (JSPS), DFG GRK 2156/1 for providing the funding for the present study.

I would like to sincerely thank my supervisor Catherine McCammon for her invaluable advice, support, and assistance during the course of my PhD degree. Her experience and dedication to scientific research have inspired and encouraged me to pursue an academic career.

I am grateful to Dan Frost, Leonid Dubrovinsky, and Tiziana Boffa Ballaran for their insightful comments and suggestions throughout my studies and for inspiring me with their brilliant ideas. Many thanks to Nobuyoshi Miyajima for his assistance and teaching during TEM measurements.

I would like to acknowledge Raphael Njul and Alexander Rother for the excellent sample preparation, Stefan Übelhack for providing adapters for mini-size DAC, Detlef Krausse for assistance with the electron microprobe, and Ulrike Trenz for aid with the chemical laboratory. I am extremely grateful to Doro Wiesner for her kind assistance and guidance during long SEM and FIB sessions. I am thankful to Petra Buchert, Janina Potzel, and Anna Dinius for their priceless administrative help.

I am greatly thankful to Vincenzo Stagno for his continuous support and teaching ever since my Master's degree and for providing synthetic samples for this work. I acknowledge Felix Kaminsky for giving me the unique opportunity to study mineral inclusions in natural diamonds and for his valuable comments on this project.

My sincere thank also goes to Ohtani-sensei for his precious supervision and for welcoming me in his research team during my stay at the Tohoku University. Many thanks to Ikuta-san and

Sakamaki-san for sharing with me their knowledge on inelastic X-ray scattering. I acknowledge Nakamura-sensei, Okuyama-san, and Ozawa-san for helping me during my stay in Japan.

I would like to express my gratitude to all the members of the CarboPaT research unit for fruitful discussions on carbonates at extreme conditions.

I am thankful for the help and support I received during my experiments at synchrotron facilities from beamline scientists and local contacts. I would like to particularly acknowledge Alexander Chumakov, Rudolf Rüffer, Dimitrios Bessas, Valerio Cerantola, Anja Rosenthal, Alfred Baron, Hiroshi Uchiyama, Hiroshi Fukui, Michael Hanfland, Hanns-Peter Liermann, and Konstantin Glazyrin.

I am in debt to Florian Heidelbach for the translation of my thesis summary into German.

I am the most thankful to all my colleagues and friends, Sumith Abeykoon, Giacomo Criniti, Giulia Marras (from Rome), George Aprilis, Stella Chariton, Egor and Iuliia Koemets, Tim Fedotenko, Saiana Khandarkhaeva, Alex Kurnosov, Caterina Melai, Ingrid Blanchard, Lisa Eberhard, Laura Czekay, and Lélia Libon (from Potsdam). Thank you all for the times you helped and encouraged me, the sleepless beamtimes, and all the unforgettable moments we shared.

A special thanks to Adriano, mamma, Simona, zia Igina, nonna, my family, and all my friends from Rome for all the things they have done for me, their endless support and care. Finally, thank you dad for always giving me the strength to face difficult times.

8 APPENDIX

H2981

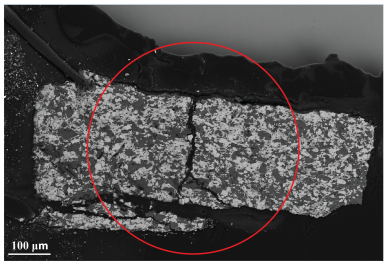

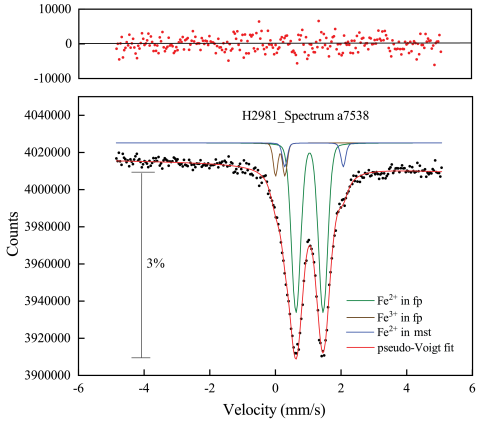

H2982

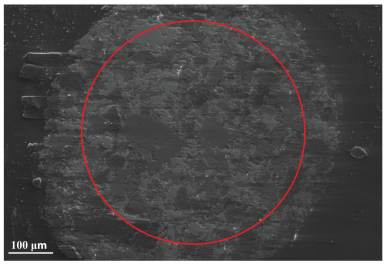

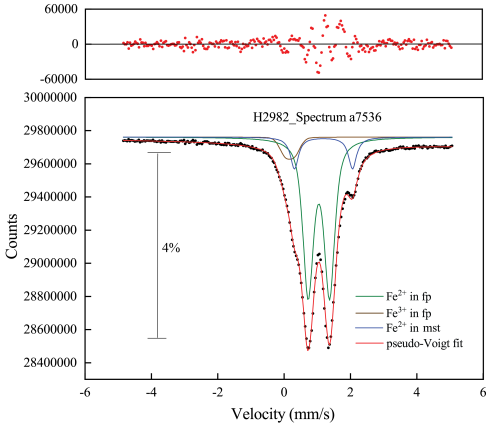

H2887

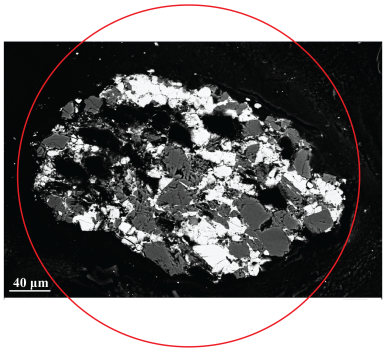

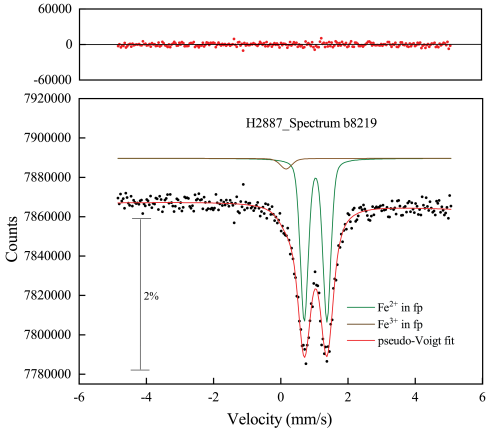

continued on next page

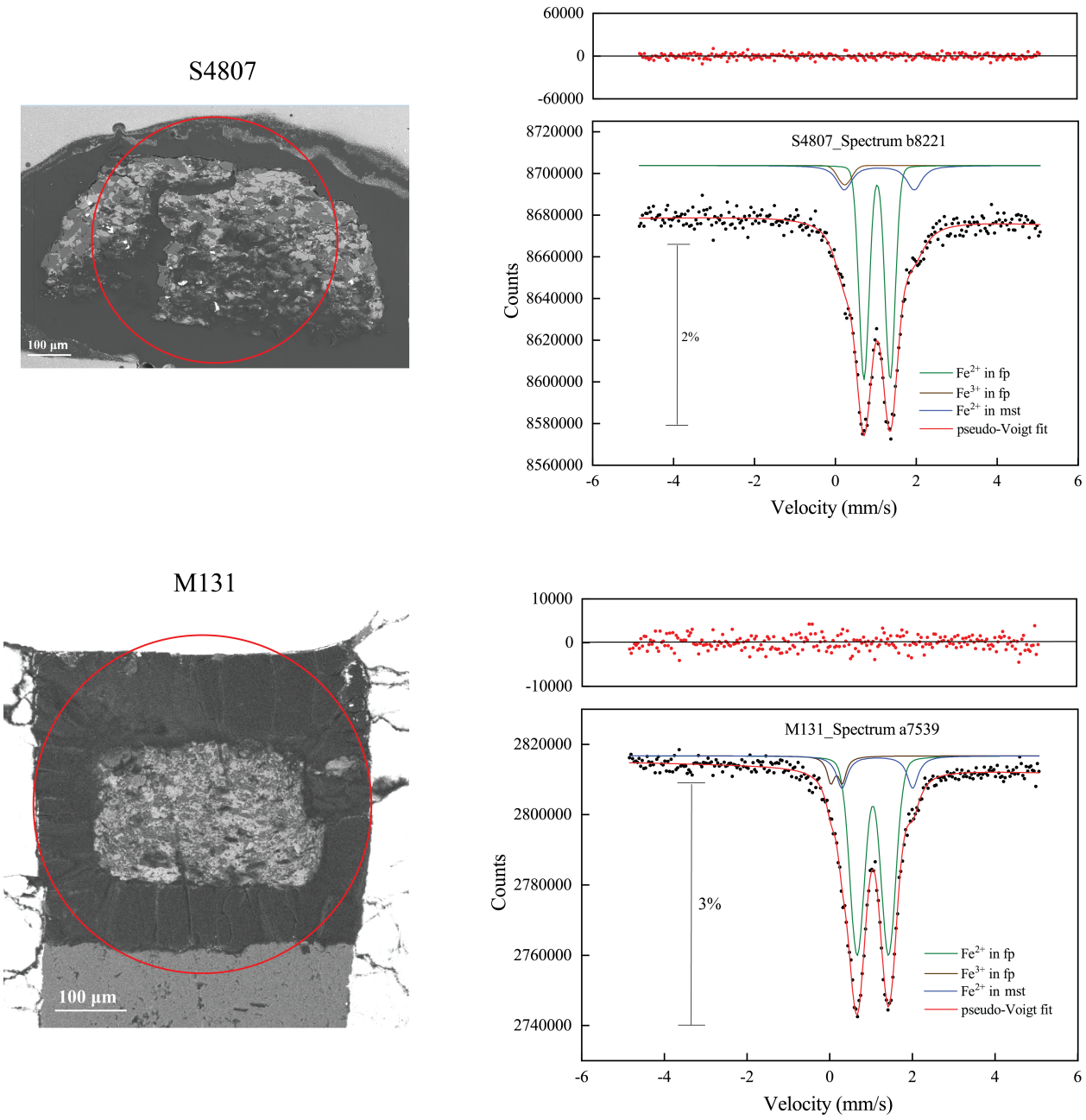

Figure S1: Investigated area of synthetic samples by Mössbauer spectyroscopy with corresponding fit results. Red circles represent the beam size (500 × 500 µm^2) of the ^{57}Co Mössbauer point source. Details of the data collection are shown in Table 4.1 of Chapter 4 and resulting hyperfine parameters are given in Table S2.

3.9.3b_MOUNT #1

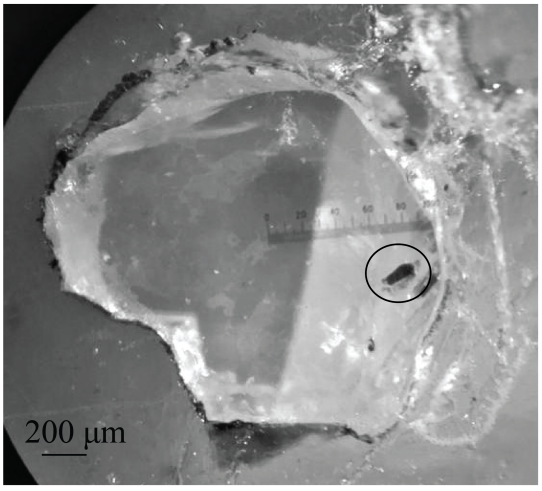

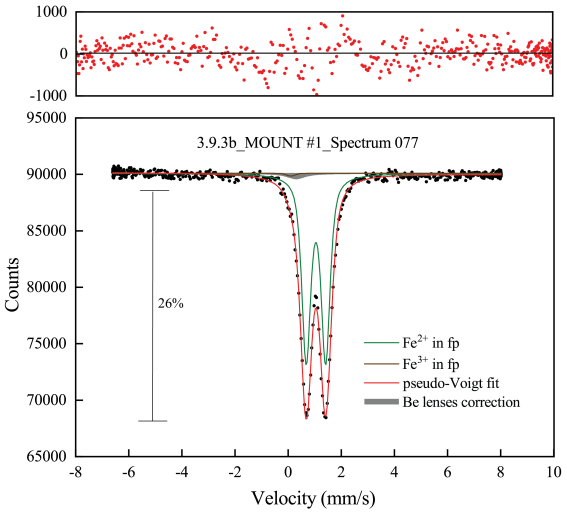

Pos_1_Spectrum 077
Pos_2_Spectrum 079
Pos_3_Spectrum 081

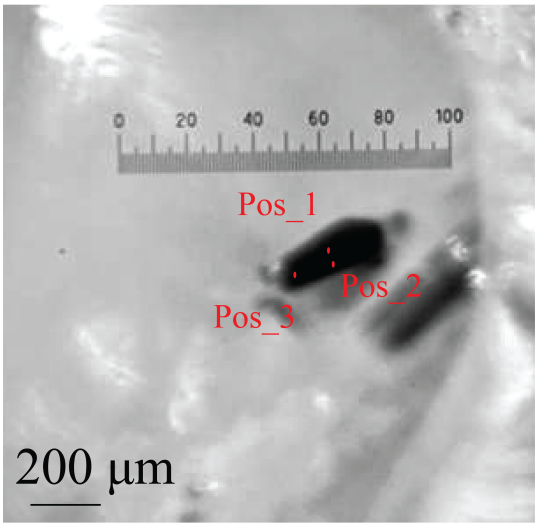

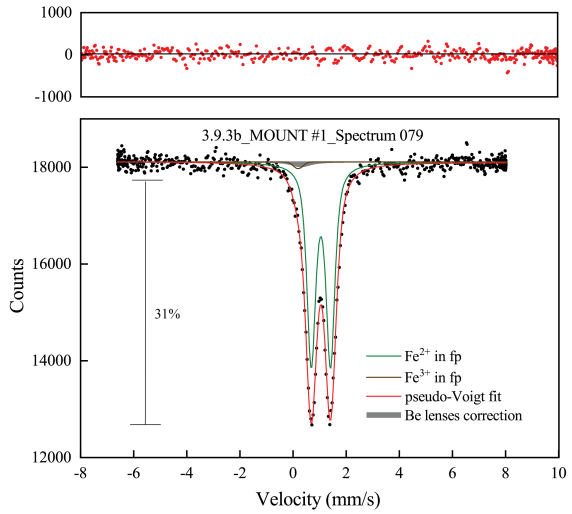

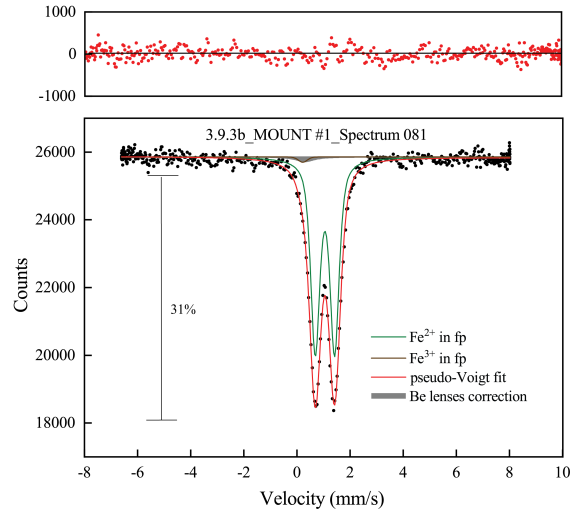

continued on next page

2.7.2a_MOUNT #1

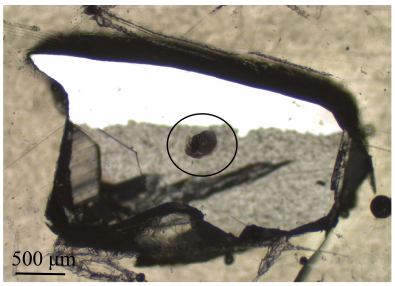

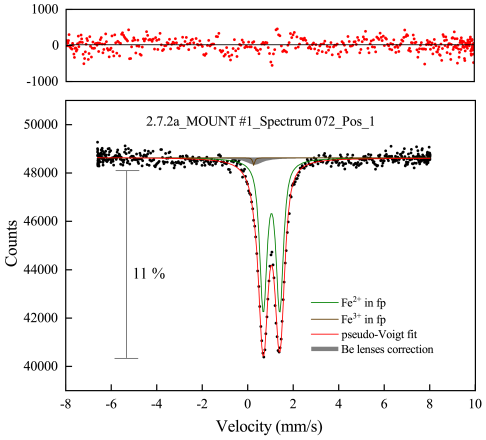

Pos_1_Spectrum_072
Pos_2_Spectrum_070

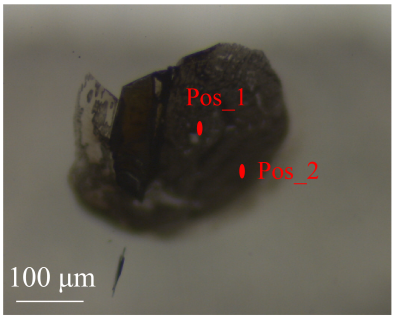

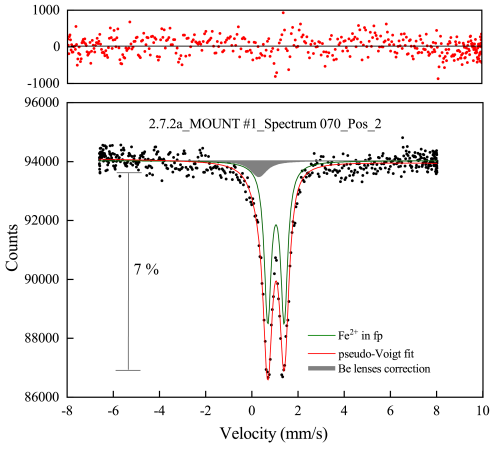

3.5.2b_MOUNT #1

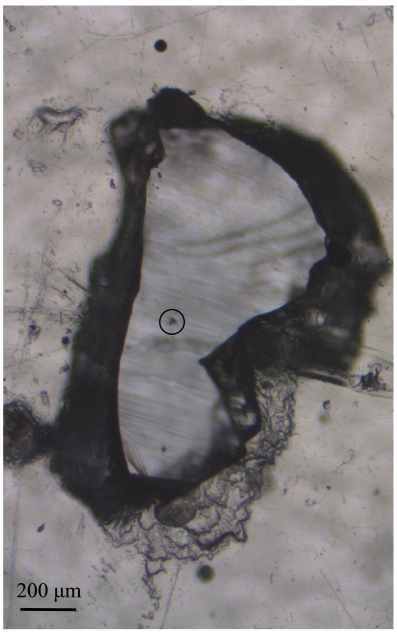

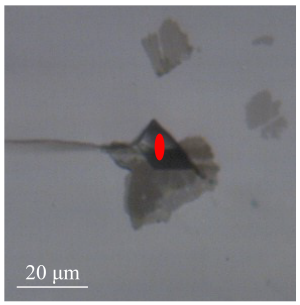

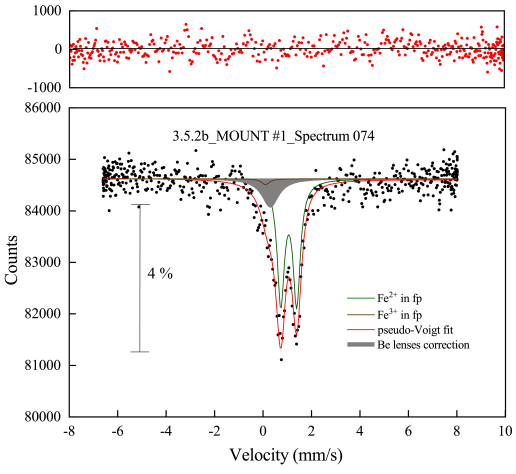

continued on next page

3.2.2b Mount #2

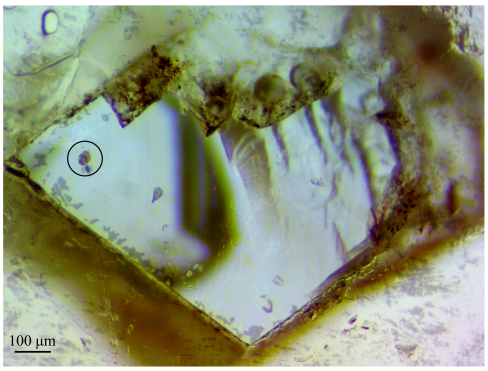

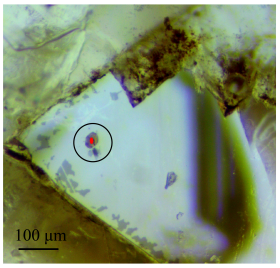

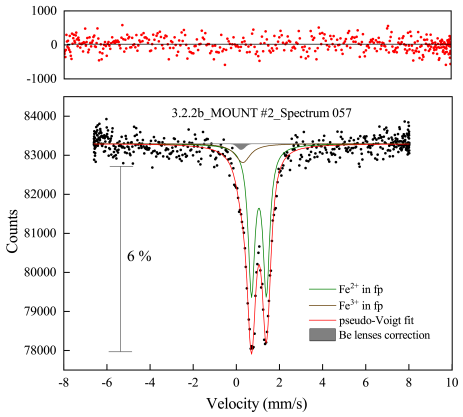

1.2.3b Mount #3

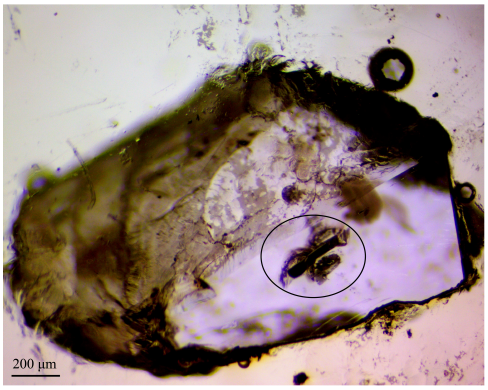

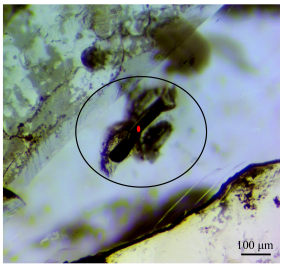

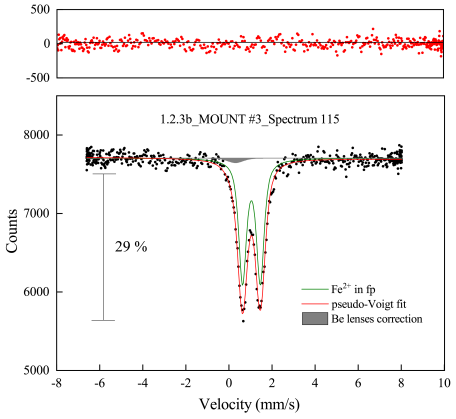

1.2.3c Mount #3

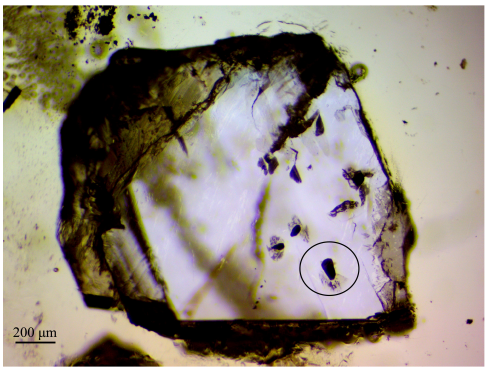

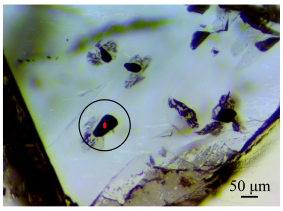

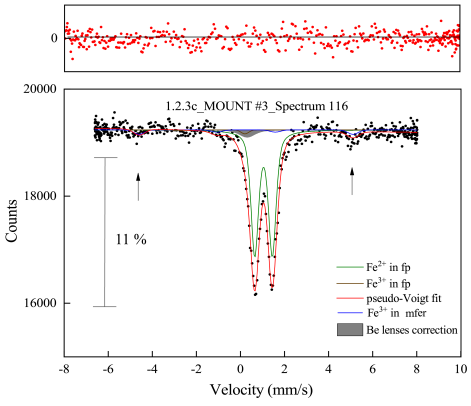

continued on next page

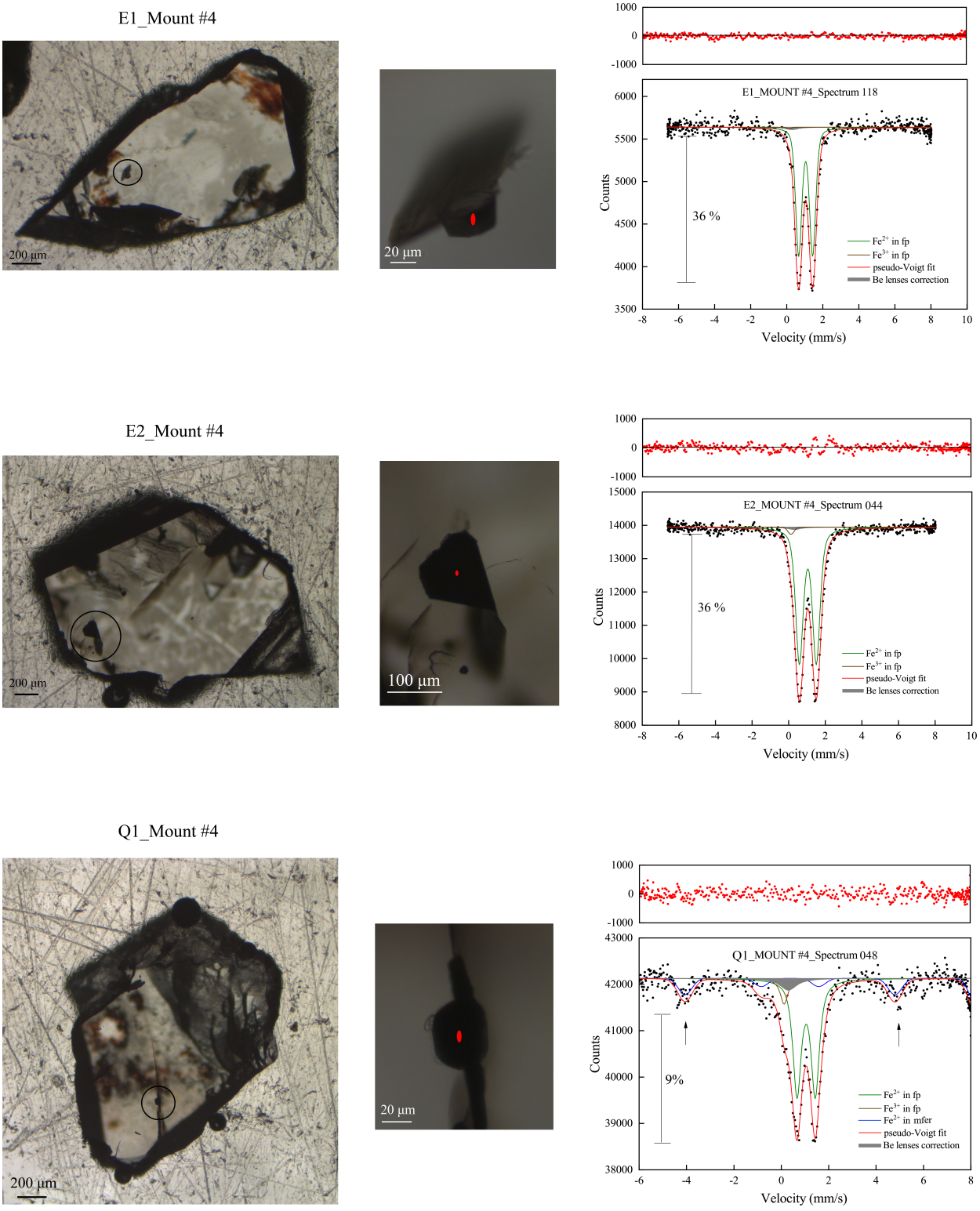

Figure S2: Investigated area of natural ferropericlase inclusions in diamonds by Synchrotron Mössbauer Source spectroscopy with the corresponding fit results. Black circles mark the investigated inclusions while the red-filled ellipses represent the beam size (8v × 3h µm) of the SMS source. Details of the data collection are shown in Table 4.1 of Chapter 4 and the resulting hyperfine parameters are given in Table S2.

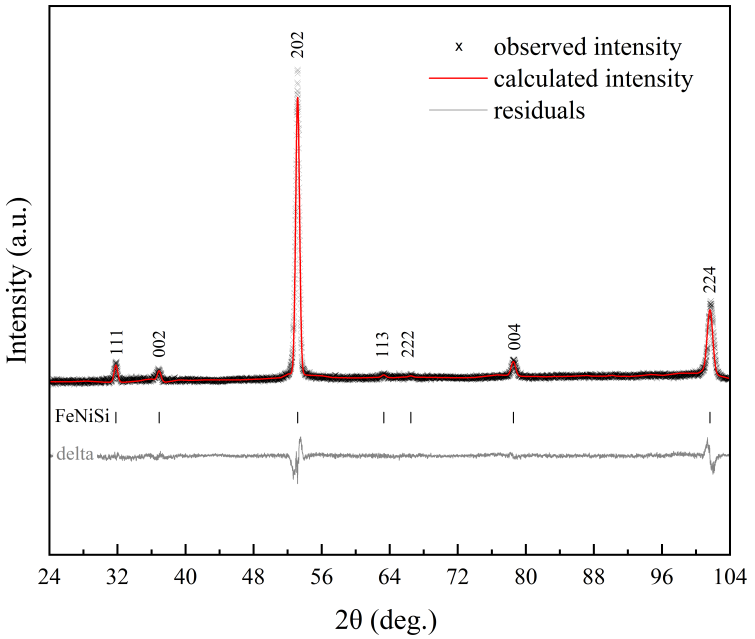

Figure S3: XRD pattern of the synthesized $Fe_{0.67}Ni_{0.06}Si_{0.27}$ alloy (run H4973) collected at ambient conditions. The identified phase corresponds to the *fcc* structure. The powder profile was refined with the Le Bail method using JANA 2006 software (Petrícek et al., 2014)

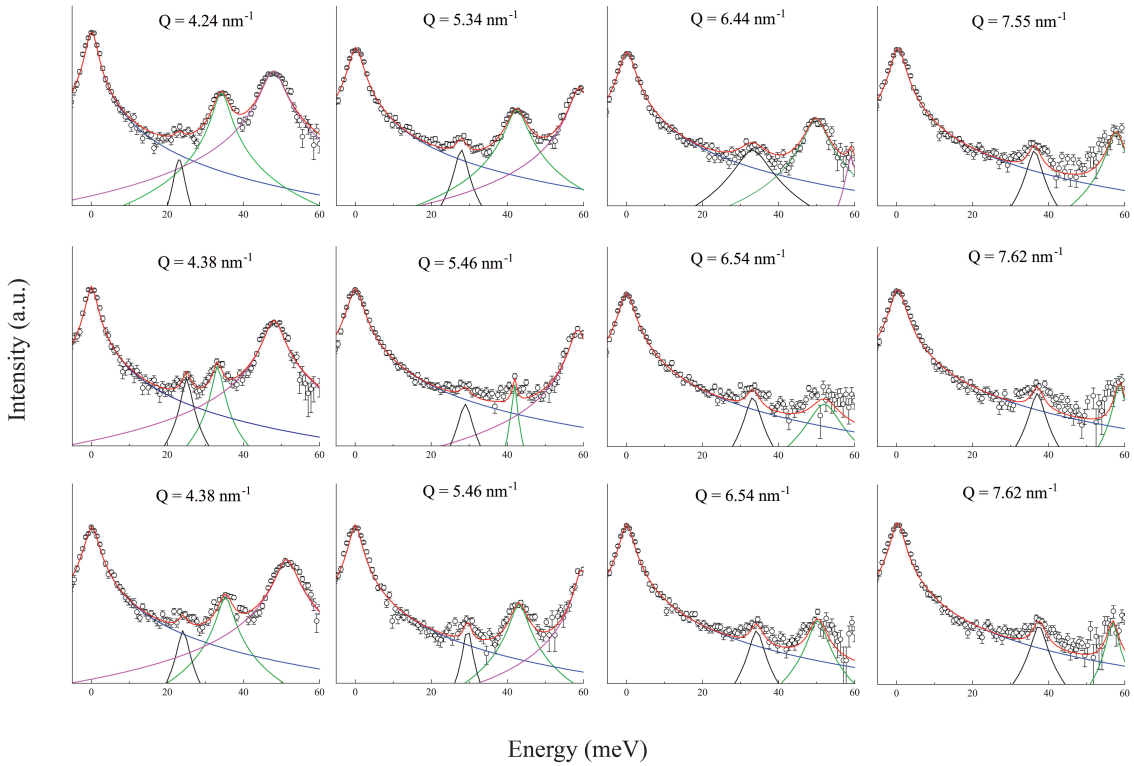

Figure S4: IXS spectra of B2-$Fe_{0.67}Ni_{0.06}Si_{0.27}$ alloy at 62.7(19) GPa and 300 K collected at different values of Q using 12 crystal analysers (Materials and Methods section 2.3). The peak at zero energy (blue) is from elastic scattering. The TA (green) and LA (pink) phonons of diamond are visible at low Q and higher energies compared to LA phonons of the sample (black).

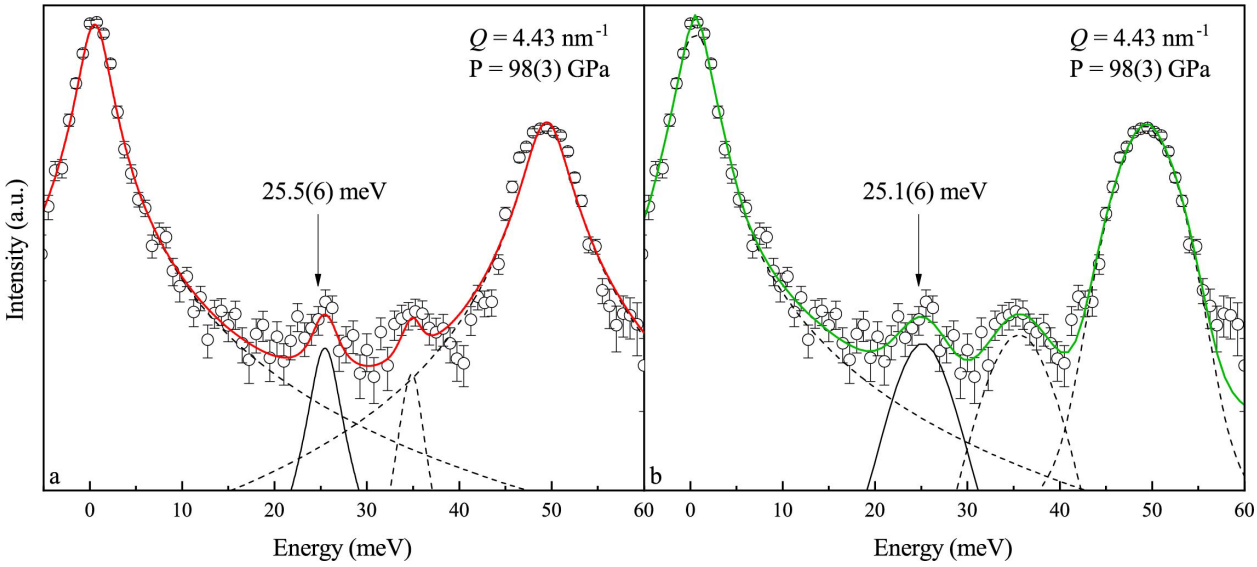

Figure S5: IXS spectra of B2-$Fe_{0.67}Ni_{0.06}Si_{0.27}$ collected at 31.0(9) GPa and Q = 4.38 nm^{-1}, fitted with Lorentzian (a) and pseudo-Voigt (b) line shapes. The comparison shows that both fitting models provide consistent values for the sample peak position (solid black line) within uncertainties. Lines show individual contributions from the sample (solid) and the elastic peak and diamond (TA and LA) (dashed).

Table S1: Thermodynamic parameters for the Fe-Ir redox sensor calculated at 2000 K as a function of pressure.

P GPa	V^{a} *fcc* Ir cm^3mol^{-1}	V^{b} *fcc* Fe cm^3mol^{-1}	*V fcc* alloy cm^3mol^{-1}	$\Delta_m V^{ex}$ J/bar	$\Delta_r G^{o}_{P,T}$ $Jmol^{-1}$	W^{V}_{alloy} J/bar	W^{H}_{Fe-Ir} J/bar	W^{H}_{Ir-Fe} J/bar
0	8.51130	7.076	8.10441	0.020	-284456	0.0804	-50951	-61934
1	8.48655	7.024	8.08173	0.021	-277366	0.0860	-50044	-61027
2	8.46219	6.974	8.05926	0.022	-270413	0.0912	-49095	-60077
3	8.43824	6.926	8.03699	0.023	-263596	0.0960	-48105	-59087
4	8.41466	6.880	8.01492	0.024	-256916	0.1005	-47076	-58059
5	8.39145	6.836	7.99303	0.025	-250372	0.1046	-46012	-56994
6	8.36859	6.793	7.97135	0.026	-243965	0.1085	-44912	-55894
7	8.34607	6.752	7.94984	0.027	-237695	0.1121	-43780	-54762
8	8.32389	6.713	7.92852	0.028	-231561	0.1155	-42615	-53598
9	8.30205	6.674	7.90738	0.029	-225564	0.1187	-41422	-52404
10	8.28052	6.637	7.88643	0.030	-219703	0.1216	-40200	-51182
11	8.25929	6.601	7.86564	0.030	-213980	0.1243	-38952	-49934
12	8.23835	6.566	7.84501	0.031	-208393	0.1269	-37679	-48661
13	8.21773	6.532	7.82457	0.031	-202942	0.1293	-36382	-47364
14	8.19737	6.499	7.80427	0.032	-197628	0.1315	-35064	-46046
15	8.17729	6.467	7.78414	0.033	-192451	0.1335	-33724	-44706
16	8.15748	6.436	7.76418	0.033	-187410	0.1354	-32365	-43347
17	8.13792	6.405	7.74437	0.033	-182506	0.1372	-30989	-41971
18	8.11863	6.375	7.72471	0.034	-177739	0.1388	-29595	-40577
19	8.09959	6.347	7.70519	0.034	-173108	0.1403	-28185	-39167
20	8.08079	6.318	7.68583	0.035	-168614	0.1417	-26761	-37744
21	8.06221	6.291	7.66661	0.035	-164257	0.1430	-25324	-36306
22	8.04387	6.264	7.64753	0.035	-160036	0.1442	-23875	-34857
23	8.02576	6.238	7.62861	0.035	-155952	0.1452	-22414	-33396
24	8.00787	6.212	7.60981	0.036	-152004	0.1462	-20943	-31925
25	7.99019	6.187	7.59115	0.036	-148193	0.1471	-19463	-30445
26	7.97272	6.162	7.57262	0.036	-144519	0.1479	-17975	-28957
27	7.95545	6.138	7.55422	0.036	-140981	0.1486	-16479	-27461

Continued on the next page

28	7.93840	6.115	7.53596	0.036	-137580	0.1492	-14977	-25959
29	7.92152	6.092	7.51782	0.036	-134316	0.1498	-13469	-24451
30	7.90485	6.069	7.49981	0.037	-131188	0.1502	-11957	-22939
31	7.88835	6.047	7.48191	0.037	-128197	0.1506	-10440	-21422
32	7.87205	6.025	7.46415	0.037	-125342	0.1510	-8919	-19901
33	7.85592	6.004	7.44650	0.037	-122625	0.1513	-7396	-18378
34	7.83997	5.983	7.42897	0.037	-120043	0.1515	-5872	-16854
35	7.82419	5.962	7.41155	0.037	-117599	0.1516	-4345	-15328
36	7.80858	5.942	7.39425	0.037	-115291	0.1517	-2819	-13801
37	7.79313	5.922	7.37706	0.037	-113119	0.1518	-1292	-12274
38	7.77785	5.903	7.35998	0.037	-111085	0.1517	235	-10748
39	7.76272	5.884	7.34302	0.037	-109187	0.1517	1760	-9222
40	7.74774	5.865	7.32614	0.037	-107425	0.1516	3284	-7698
41	7.73293	5.846	7.30938	0.037	-105801	0.1514	4806	-6176
42	7.71825	5.828	7.29273	0.037	-104312	0.1512	6326	-4657
43	7.70372	5.810	7.27619	0.037	-102961	0.1510	7843	-3140
44	7.68934	5.793	7.25973	0.037	-101746	0.1507	9355	-1627
45	7.67510	5.775	7.24338	0.037	-100668	0.1504	10865	-118
46	7.66101	5.758	7.22712	0.037	-99726	0.1500	12370	1389
47	7.64704	5.741	7.21097	0.036	-98921	0.1496	13871	2889
48	7.63320	5.725	7.19490	0.036	-98253	0.1491	15367	4385
49	7.61950	5.708	7.17895	0.036	-97721	0.1487	16858	5876
50	7.60592	5.692	7.16306	0.036	-97326	0.1482	18344	7362
51	7.59248	5.676	7.14729	0.036	-97068	0.1476	19823	8841
52	7.57914	5.661	7.13158	0.036	-96946	0.1470	21296	10314
53	7.56594	5.645	7.11599	0.036	-96961	0.1464	22764	11781
54	7.55285	5.630	7.10046	0.036	-97112	0.1458	24224	13242
55	7.53989	5.615	7.08503	0.035	-97400	0.1452	25678	14696
56	7.52703	5.600	7.06968	0.035	-97825	0.1445	27125	16143
57	7.51430	5.586	7.05443	0.035	-98386	0.1438	28565	17583
58	7.50168	5.571	7.03924	0.035	-99084	0.1430	29997	19015
59	7.48915	5.557	7.02414	0.035	-99919	0.1422	31422	20440
60	7.47675	5.543	7.00913	0.034	-100890	0.1415	32838	21857
61	7.46445	5.529	6.99418	0.034	-101998	0.1406	34247	23265
62	7.45224	5.515	6.97932	0.034	-103243	0.1398	35648	24666
63	7.44015	5.502	6.96453	0.034	-104624	0.1389	37041	26059

Continued on the next page

64	7.42815	5.489	6.94982	0.034	-106142	0.1381	38425	27443
65	7.41626	5.475	6.93519	0.033	-107796	0.1372	39800	28819
66	7.40446	5.462	6.92063	0.033	-109587	0.1362	41167	30186
67	7.39276	5.449	6.90615	0.033	-111515	0.1353	42525	31544
68	7.38115	5.437	6.89174	0.033	-113579	0.1343	43874	32893
69	7.36965	5.424	6.87739	0.032	-115780	0.1333	45214	34232
70	7.35822	5.412	6.86312	0.032	-118118	0.1323	46545	35563
71	7.34689	5.400	6.84891	0.032	-120592	0.1313	47867	36885
72	7.33565	5.387	6.83477	0.032	-123203	0.1303	49179	38197
73	7.32450	5.375	6.82071	0.031	-125950	0.1292	50481	39499
74	7.31343	5.363	6.80670	0.031	-128834	0.1282	51774	40792
75	7.30244	5.352	6.79277	0.031	-131855	0.1271	53057	42075
76	7.29156	5.340	6.77889	0.031	-135013	0.1260	54329	43348
77	7.28073	5.329	6.76508	0.030	-138307	0.1249	55592	44610
78	7.27000	5.317	6.75134	0.030	-141737	0.1238	56845	45863
79	7.25936	5.306	6.73765	0.030	-145305	0.1226	58087	47105
80	7.24877	5.295	6.72403	0.030	-149009	0.1215	59318	48336
81	7.23828	5.284	6.71047	0.029	-152849	0.1203	60539	49557
82	7.22786	5.273	6.69696	0.029	-156826	0.1191	61749	50767
83	7.21752	5.262	6.68353	0.029	-160940	0.1179	62948	51966
84	7.20727	5.252	6.67013	0.028	-165191	0.1167	64135	53154
85	7.19706	5.241	6.65681	0.028	-169578	0.1155	65311	54330
86	7.18694	5.231	6.64353	0.028	-174102	0.1142	66476	55494
87	7.17690	5.220	6.63033	0.028	-178762	0.1130	67628	56650
88	7.16692	5.210	6.61717	0.027	-183559	0.1117	68769	57787
89	7.15701	5.200	6.60406	0.027	-188493	0.1105	69897	58915
90	7.14718	5.190	6.59100	0.027	-193563	0.1092	71013	60031
91	7.13741	5.180	6.57800	0.026	-198770	0.1079	72115	61133
92	7.12770	5.170	6.56505	0.026	-204113	0.1066	73205	62223
93	7.11806	5.160	6.55216	0.026	-209594	0.1053	74281	63299
94	7.10850	5.150	6.53930	0.025	-215210	0.1039	75343	64361
95	7.09899	5.141	6.52651	0.025	-220964	0.1026	76392	65410
96	7.08955	5.131	6.51377	0.025	-226854	0.1013	77425	66443
97	7.08017	5.122	6.50107	0.024	-232881	0.0999	78444	67462
98	7.07085	5.113	6.48842	0.024	-239044	0.0985	79448	68466
99	7.06161	5.103	6.47582	0.024	-245344	0.0972	80436	69454
100	7.05241	5.094	6.46326	0.023	-251781	0.0958	81408	70426

Note:
[a]Yusenko et al. (2019)
[b]Campbell et al. (2009)

Table S2: Hyperfine parameters derived from the fitting of Mössbauer spectra of synthetic (MS) and natural (SMS) ferropericlase inclusion in diamonds.

Run/natural inclusion	Spectrum	IS* (mm/s)	QS (mm/s)	W (mm/s)	Area %	BHF (T)	Phase	Site	$Fe^{3+}/\Sigma Fe$ bulk	X^2
H2981	a7538	1.021(5)	0.81(1)	0.37(3)	82(4)	-	fp	Fe^{2+}	0.10(4)	1.05
		0.1(3)	0.3(6)	0.2(2)	9(2)	-	fp	Fe^{3+}		
		1.1(4)	1.8(8)	0.2(1)	9(4)	-	mst	Fe^{2+}		
H2982	a7536	1.028(3)	0.639(5)	0.29(2)	79(2)	-	fp	Fe^{2+}	0.08(1)	4.7
		0.16(6)	0.3(1)	0.3(1)	7(1)	-	fp	Fe^{3+}		
		1.16(3)	1.73(6)	0.17(4)	13(1)	-	mst	Fe^{2+}		
H2887	b8219	1.03(1)	0.67(1)	0.28(5)	95(5)	-	fp	Fe^{2+}	0.05(2)	1.1
		0.15(17)	-	0.41(77)	5(5)	-	fp	Fe^{3+}		
S4807	b8221	1.03(1)	0.65(3)	0.30(7)	77(18)	-	fp	Fe^{2+}	0.06(3)	1.3
		0.2(10)		***0.4***	5(6)	-	fp	Fe^{3+}		
		1.1(5)	1.7(10)	0.5(5)	18(19)	-	mst	Fe^{2+}		
M131	a7539	1.024(5)	0.76(2)	0.35(3)	81(5)	-	fp	Fe^{2+}	0.09(2)	0.85
		0.2(13)	0.3(25)	0.2(4)	8(2)	-	fp	Fe^{3+}		
		1.1(9)	2(2)	0.2(1)	11(5)	-	mst	Fe^{2+}		
3.5.2b - mount #1	074	1.06(2)	0.66(2)	0.36(9)	77	-	fp	Fe^{2+}	0.03(2)	0.53
		0.1	-	***0.4***	2	-	fp	Fe^{3+}		
3.9.3b - mount #1	077	1.04(1)	0.73(1)	0.40(1)	86	-	fp	Fe^{2+}	0.01(1)	0.88
		0.1	-	***0.4***	1	-	fp	Fe^{3+}		
3.9.3b - mount #1	079	1.05(1)	0.73(1)	0.39(2)	96	-	fp	Fe^{2+}	0.01(1)	0.69
		0.2(2)	-	0.4(8)	1	-	fp	Fe^{3+}		
3.9.3b - mount #1	081	1.05(1)	0.73(1)	0.41(2)	96	-	fp	Fe^{2+}	0.01(1)	0.74
		0.22(8)	-	0.2(4)	1	-	fp	Fe^{3+}		
2.7.2a - mount #1	070	1.04(1)	0.71(1)	0.36(5)	89	-	fp	Fe^{2+}	0.00	0.66
2.7.2a - mount #1	072	1.04(1)	0.72(1)	0.38(2)	94	-	fp	Fe^{2+}	0.01(1)	0.68
		0.26(2)	-	0.21(7)	1	-	fp	Fe^{3+}		
3.2.2b – mount #2	057	1.05(1)	0.69(2)	0.37(6)	86	-	fp	Fe^{2+}	0.01(1)	0.53
		0.2(3)	-	***0.4***	1.3	-	fp	Fe^{3+}		
1.2.3b - mount #3	115	1.04 (1)	0.82(1)	0.42(3)	97	-	fp	Fe^{2+}	0.00	0.53
1.2.3c - mount #3	116	1.05(1)	0.80(1)	0.41(3)	85	-	fp	Fe^{2+}	0.01(1)	0.52
		0.2	-	***0.4***	1	-	fp	Fe^{3+}		
		0.3(1)	***0***	0.5(4)	9	52	mfer	Fe^{3+}		
Q1 - mount #4	048	1.05(1)	0.77(3)	0.42(6)	58	-	fp	Fe^{2+}	0.10(1)	1.2
		0.12(8)	-	***0.4***	7	-	fp	Fe^{3+}		
		0.47(3)	0.19(7)	0.68(11)	29	47.4(3)	mfer	Fe^{3+}		
E1 - mount #4	118	1.05(1)	0.77(1)	0.41(2)	97	-	fp	Fe^{2+}	0.00	0.64
		0.1(10)	-	***0.4***	0	-	fp	Fe^{3+}		
E2 - mount #4	044	1.05(1)	0.92(1)	0.49(1)	96	-	fp	Fe^{2+}	0.02(1)	0.85
		0.1(1)	-	***0.4***	2	-	fp	Fe^{3+}		

Note: 2σ errors are shown in brackets. Numbers in bold italics were held fixed during the fitting.
*Relative to α-Fe.
Fe in Be lenses contribution is not included in this table.
Fp, mst, and mfer stand for ferropericlase, magnesite, and magnesioferrite respectively.

Table S3: Pressure dependence of volume parameters of B2-$Fe_{0.67}Ni_{0.06}Si_{0.27}$ alloy determined in DAC experiment SD008. Pressure was determined using the EOS of Au.

P (GPa)	*a* (Å)	V (Å^3)
10.4(1)	2.7791(5)	21.463(2)
19.9(1)	2.7399(8)	20.569(2)
23.9(1)	2.7318(8)	20.387(1)
39.4(6)	2.6944(6)	19.561(1)
41.2(1)	2.6896(5)	19.457(6)
48.5(1)	2.6750(6)	19.140(7)
52.3(4)	2.6644(6)	18.914(7)
57.5(6)	2.6562(6)	18.740(7)
60.7(3)	2.6483(6)	18.573(8)
63.9(2)	2.6420(7)	18.442(9)
68.6(3)	2.6338(8)	18.270(1)
72.1(2)	2.6245(9)	18.078(9)
79.3(6)	2.6116(9)	17.812(9)
84.2(7)	2.6000(6)	17.595(9)

Numbers in parentheses are errors on the last digit.

Table S4: Energy (meV) parameters of B2-$Fe_{0.67}Ni_{0.06}Si_{0.27}$ alloy at different pressure (GPa) and momentum transfer (*Q*) obtained after fitting all IXS spectra with Lorentzian functions.

		***P*=6.8[a]**	***P*=23.6[a]**	***P*=31.0[a]**	***P*=43.4[a]**	***P*=45.3[b]**	***P*=51.4[a]**	***P*=62.7[a]**	***P*=66.5[b]**	***P*=72.9[a]**	***P*=98.1[b]**
***Q*[a] (nm^{-1})**	***Q*[b] (nm^{-1})**	***E*[a] (meV)**	***E*[a] (meV)**	***E*[a] (meV)**	***E*[a] (meV)**	**E[b] (meV)**	***E*[a] (meV)**	***E*[a] (meV)**	***E*[b] (meV)**	***E*[a] (meV)**	***E*[b] (meV)**
4.24	4.28	17.8(13)	19.1(14)	20.0(5)	21.0(9)	21.7(10)	21.9(11)	23.0(12)	22.7(7)	-	24.0(10)
5.34	5.38	23.1(6)	24.7(6)	25.0(5)	27.6(6)	26.0(6)	26.7(8)	27.7(6)	27.7(9)	28.8(6)	30.0(10)
6.44	6.48	25.8(8)	27.5(8)	28.9(4)	31.6(5)	30.4(7)	31.1(7)	33.0(6)	32.5(7)	33.2(6)	36.4(11)
7.55	7.58	28.6(17)	32.5(8)	33.1(6)	35.2(8)	34.3(10)	35.2(8)	35.8(6)	37.5(8)	38.9(8)	39.9(10)
4.38	4.42	19.2(18)	19.6(8)	20.7(10)	21.3(6)	20.6(7)	23.1(13)	25.0(10)	23.4(9)	-	24.9(8)
5.46	5.49	22.9(14)	24.8(14)	26.2(4)	27.1(8)	26.4(4)	27.5(18)	28.9(9)	27.8(7)	28.9(9)	30.2(11)
6.54	6.57	26.2(4)	28.1(6)	29.0(3)	30.3(4)	30.0(6)	33.0(6)	33.1(4)	33.6(6)	34.4(6)	35.2(11)
7.62	7.66	29.2(9)	32.1(8)	32.8(6)	35.9(5)	33.9(9)	37.6(8)	36.6(7)	35.9(8)	38.6(7)	39.3(10)
4.38	4.42	19.5(7)	20.4(9)	22.2(3)	23.7(13)	22.0(6)	22.5(12)	24.0(9)	23.6(8)	24.7(10)	-
5.46	5.49	23.9(13)	24.4(7)	26.1(5)	28.2(12)	26.5(9)	27.6(12)	29.5(5)	29.8(10)	30.4(6)	31.5(8)
6.54	6.57	26.2(7)	28.3(6)	29.7(4)	32.7(7)	32.5(7)	32.0(7)	34.1(4)	34.5(7)	34.1(7)	35.8(9)
7.62	7.66	30.0(9)	31.7(7)	33.3(5)	34.4(6)	34.7(10)	36.6(8)	37.1(4)	37.9(5)	37.2(8)	40.1(10)

Note: numbers in parentheses are errors on the last digit
[a]run SD005
[b]run SD009

9 REFERENCES

Akahama, Y., & Kawamura, H. (2006). Pressure calibration of diamond anvil Raman gauge to 310 GPa. *Journal of Applied Physics*, *100*(4), 43516. https://doi.org/10.1063/1.2335683

Akaishi, M., Shaji Kumar, M. D., Kanda, H., Yamaoka, S. (2000). Formation process of diamond from supercritical H_2O-CO_2 fluid under high pressure and high temperature conditions. *Diamond and Related Materials*, *9*(12), 1945–1950. https://doi.org/10.1016/S0925-9635(00)00366-6

Akaishi, M., Kumar, M. D. S., Kanda, H., Yamaoka, S. (2001). Reactions between carbon and a reduced C-O-H fluid under diamond-stable HP-HT condition. *Diamond and Related Materials*, *10*, 2125–2130. https://doi.org/10.1016/S0925-9635(01)00490-3

Van Aken, P., Liebscher, B. Styrsa, V. (1998). Quantitative determination of iron oxidation states in minerals using Fe $L_{2,3}$-edge electron energy-loss near-edge structure spectroscopy. *Phys Chem Min,* 25, 323–327. https://doi.org/10.1007/s002690050122

Van Aken, P. A., & Liebscher, B. (2002). Quantification of ferrous/ferric ratios in minerals: New evaluation schemes of Fe L_{23} electron energy-loss near-edge spectra. *Physics and Chemistry of Minerals*, *29*(3), 188–200. https://doi.org/10.1007/s00269-001-0222-6

Alfè, D., Gillan, M. J., Price, G. D. (2002). Composition and temperature of the Earth's core constrained by combining ab initio calculations and seismic data. *Earth and Planetary Science Letters*, *195*(1–2), 91–98. https://doi.org/10.1016/S0012-821X(01)00568-4

Allègre, C. J., Poirier, J. P., Humler, E., Hofmann, A. W. (1995). The chemical composition of the Earth. *Earth and Planetary Science Letters*, *134*(3–4), 515–526. https://doi.org/10.1016/0012-821X(95)00123-T

Anderson, D. L., & Bass, J. D. (1984). Mineralogy and composition of the upper mantle. *Geophysical Research Letters*, *11*(7), 637–640. https://doi.org/10.1029/GL011i007p00637

Anderson, O. L. (1995). Equations of state of solids for geophysics and ceramic science. *Oxford University Press on Demand*,31.

Andrault, D., & Bolfan-casanova, N. (2001). High-pressure phase transformations in the $MgFe_2O_4$. *Physics and Chemistry of Minerals*, *28*, 211–217. https://doi.org/10.1007/s002690000149

Angel, R. J. (2000). Equations of State. *Reviews in Mineralogy and Geochemistry*, *4*(1), 35–59. https://doi.org/10.2138/rmg.2000.41.2

Angel, R. J., Gonzalez-Platas, J., Alvaro, M. (2014). EosFit7c and a Fortran module (library) for equation of state calculations. *Zeitschrift Für Kristallographie*, *229*(5), 405–419. https://doi.org/10.1515/zkri-2013-1711

Antonangeli, D., Siebert, J., Badro, J., Farber, D. L., Fiquet, G., Morard, G., Ryerson, F. J. (2010). Composition of the Earth's inner core from high-pressure sound velocity measurements in Fe-Ni-Si alloys. *Earth and Planetary Science Letters*, *295*(1–2), 292–296. https://doi.org/10.1016/j.epsl.2010.04.018

Antonangeli, D., Morard, G., Paolasini, L., Garbarino, G., Murphy, C. A., Edmund, E., Decremps, F., Fiquet, G., Bosak, A., Mezouar, M. and Fei, Y. (2018). Sound velocities and density measurements of solid hcp-Fe and hcp-Fe–Si (9 wt.%) alloy at high pressure: Constraints on the Si abundance in the Earth's inner core. *Earth and Planetary Science Letters*, *482*, 446–453. https://doi.org/10.1016/j.epsl.2017.11.043

Anzellini, S. (2014). Phase diagram of iron under extreme conditions measured with time resolved methods (Doctoral dissertation, Paris 6).

Anzolini, C., Marquardt, K., Stagno, V., Bindi, L., Frost, D. J., Pearson, D. G., Harris, J. W., Hemley, R. J.,Nestola, F. (2020). Evidence for complex iron oxides in the deep mantle from FeNi(Cu) inclusions in superdeep diamond. *Proceedings of the National Academy of Sciences of the United States of America*, *117*(35), 2108–21094. https://doi.org/10.1073/pnas.2004269117

Aprilis, G., Strohm, C., Kupenko, I., Linhardt, S., Laskin, A., Vasiukov, D. M., Cerantola, V., Koemets, E. G., McCammon, C. A., Kurnosov, A., Chumakov, A. I. (2017). Portable double-sided pulsed laser heating system for time-resolved geoscience and materials science applications. *Review of Scientific Instruments*, *88*(8). https://doi.org/10.1063/1.4998985

Aprilis, G., Kantor, I., Kupenko, I., Cerantola, V., Pakhomova, A., Collings, I. E., Torchio, R., Fedotenko, T., Chariton, S., Bykov, M., Bykova, E. (2019). Comparative study of the influence of pulsed and continuous wave laser heating on the mobilization of carbon and its chemical reaction with iron in a diamond anvil cell. *Journal of Applied Physics*, *125*(9). https://doi.org/10.1063/1.5067268

Aquilanti, G., Pascarelli, S., Mathon, O., Mũoz, M., Narygina, O., Dubrovinsky, L. (2009). Development of micro-XANES mapping in the diamond anvil cell. *Journal of Synchrotron Radiation*, *16*(3), 376–379. https://doi.org/10.1107/S0909049509007134

Arima, M., Kozai, Y., Akaishi, M. (2002). Diamond nucleation and growth by reduction of carbonate melts under high-pressure and high-temperature conditions. *Geology*, *30*(8), 691–694. https://doi.org/10.1130/0091-7613(2002)030<0691:DNAGBR>2.0.CO;2

Asahara, Y., Frost, D. J., Rubie, D. C. (2007). Partitioning of FeO between magnesiowüstite and liquid iron at high pressures and temperatures: Implications for the composition of the Earth's outer core. *Earth and Planetary Science Letters*, *257*(3–4), 435–449. https://doi.org/10.1016/j.epsl.2007.03.006

Asanuma, H., Ohtani, E., Sakai, T., Terasaki, H., Kamada, S., Hirao, N., Sata, N., Ohishi, Y. (2008). Phase relations of Fe-Si alloy up to core conditions: Implications for the Earth inner core. *Geophysical Research Letters*, *35*(12), 2–5. https://doi.org/10.1029/2008GL033863

Auzende, A. L., Badro, J., Ryerson, F. J., Weber, P. K., Fallon, S. J., Addad, A., Siebert, J., Fiquet, G. (2008). Element partitioning between magnesium silicate perovskite and ferropericlase: New insights into bulk lower-mantle geochemistry. *Earth and Planetary Science Letters*, *269*(1–2), 164–174. https://doi.org/10.1016/j.epsl.2008.02.001

Badro, J., Fiquet, G., Guyot, F., Rueff, J. P., Struzhkin, V. V., Vankó, G., Monaco, G. (2003). Iron partitioning in Earth's mantle: Toward a deep lower mantle discontinuity. *Science*, *300*(5620), 789–791. https://doi.org/10.1126/science.1081311

Badro, J., Fiquet, G., Guyot, F., Gregoryanz, E., Occelli, F., Antonangeli, D., d'Astuto, M. (2007). Effect of light elements on the sound velocities in solid iron: Implications for the composition of Earth's core. *Earth and Planetary Science Letters*, *254*(1–2), 233–238. https://doi.org/10.1016/j.epsl.2006.11.025

Balchan, A. S., & Cowan, G. R. (1966). Shock compression of two iron-silicon alloys to 2.7 megabars. *Journal of Geophysical Research*, *71*(14), 3577–3588. https://doi.org/10.1029/jz071i014p03577

Bancroft, G. M. (1973). *Mössbauer spectroscopy: an introduction for inorganic chemists and geochemists*. (John Wiley and Sons, Ed.).

Baron, A. Q. R., Tanaka, Y., Goto, S., Takeshita, K., Matsushita, T., Ishikawa, T. (2000). An X-ray scattering beamline for studying dynamics. *Journal of Physics and Chemistry of Solids*, *61*(3), 461–465. https://doi.org/10.1016/S0022-3697(99)00337-6

Baron, A. Q. R. (2020). Introduction to High-Resolution Inelastic X-Ray Scattering. https://doi.org/http://arxiv.org/abs/1504.01098

Bassett, W. A. (1979). The diamond cell and the nature of the Earth's mantle. *Annual Review of Earth and Planetary Sciences. Vol. 7*, 357–384. https://doi.org/10.1146/annurev.ea.07.050179.002041

Bassett, W. A. (2009). High Pressure Research : An Diamond anvil cell , 50th birthday. *High Pressure Research*, *29*(2), 163–186. https://doi.org/10.1080/08957950802597239

Bataleva, Y. V., Palyanov, Y. N., Sokol, A. G., Borzdov, Y. M., Palyanova, G. A. (2012). Conditions for the origin of oxidized carbonate-silicate melts: Implications for mantle metasomatism and diamond formation. *Lithos*, *128–131*, 113–125. https://doi.org/10.1016/j.lithos.2011.10.010

Bayarjargal, L., Fruhner, C. J., Schrodt, N. and Winkler, B. (2018). $CaCO_3$ phase diagram studied with Raman spectroscopy at pressures up to 50 GPa and high temperatures and DFT modeling. *Physics of the Earth and Planetary Interiors*, 281, 31-45. https://doi.org/10.1002/adom.201800497

Belonoshko, A. B., Ahuja, R., Johansson, B. (2003). Stability of the body-centred-cubic phase of iron in the Earth's inner core. *Nature*, *424*(6952), 1032–1034. https://doi.org/10.1038/nature01954

Beran, A., & Libowitzky, E. (2004). *Spectroscopic Methods in Mineralogy*. The Mineralogical Society of Great Britain and Ireland.

Berry, A. J., O'Neill, H. S. C., Jayasuriya, K. D., Campbell, S. J., Foran, G. J. (2003). XANES calibrations for the oxidation state of iron in a silicate glass. *American Mineralogist*, *88*(7), 967–977. https://doi.org/10.2138/am-2003-0704

Bézos, A., & Humler, E. (2005). The $Fe^{3+}/\Sigma Fe$ ratios of MORB glasses and their implications for mantle melting. *Geochimica et Cosmochimica Acta*, *69*(3), 711–725. https://doi.org/10.1016/j.gca.2004.07.026

Birch, F. (1947). Finite elastic strain of cubic crystals. *Physical Review*, *71*(11), 809–824. https://doi.org/10.1103/PhysRev.71.809

Birch, F. (1952). Elasticity and constitution of the Earth's interior. *Journal of Geophysical Research*, *57*(2), 227–286. https://doi.org/10.1029/jz057i002p00227

Birch, F. (1964). Density and Composition of Mantle and Core. *Journal of Geophysical Research*, *69*(20). https://doi.org/10.1029/JZ069i020p04377

Boehler, R., & De Hantsetters, K. (2007). New anvil designs in diamond-cells. *High Pressure Research*, *24*(3), 391–396. https://doi.org/10.1080/08957950412331323924

Borisov, A., & Nachtweyh, K. (1998). Ru solubility in silicate melts: experimental results in oxidizing region. *Lunar and Panetary Science XXIX*, Abstract No 1320.

Borisov, A., & Palme, H. (1995). The solubility of iridium in silicate melts: New data from experiments with $Ir_{10}Pt_{90}$ alloys. *Geochimica et Cosmochimica Acta*, *59*(3), 481–485. https://doi.org/0016-7037(94)00358-0

Borisov, A., & Palme, H. (1996). Experimental determination of the solubility of Au in silicate melts. *Mineralogy and Petrology*, *56*(3), 297–312. https://doi.org/10.1007/bf01162608

Borisov, A., & Palme, H. (1997). Experimental determination of the solubility of platinum in silicate melts. *Geochimica et Cosmochimica Acta*, *61*(20), 4349–4357. https://doi.org/10.1016/S0016-7037(97)00268-8

Borisov, A., & Palme, H. (2000). Solubilities of noble metals in Fe-containing silicate melts as derived from experiments in Fe-free systems. *American Mineralogist*, *85*(11–12), 1665–1673. https://doi.org/10.2138/am-2000-11-1209

Borisov, A., Palme, H., Spettel, B. (1994). Solubility of palladium in silicate melts: Implications for core formation in the Earth. *Geochimica et Cosmochimica Acta*, *58*(2), 705–716. https://doi.org/10.1016/0016-7037(94)90500-2

Bragg, L. (1914). The analysis of crystals by the X-ray spectrometer. *Proceedings of the Royal Society of London. Series A, Containing Papers of a Mathematical and Physical Character*, *89*(613), 468–489. https://doi.org/https://doi.org/10.1098/rspa.1914.0015

Brenker, F. E., Vollmerb, C., Vinczec, L., Vekemans, B., Szymanski, A., Janssens, K., Szaloki, I., Nasdala, L., Joswig, W., Kaminsky, F. (2007). Carbonates from the lower part of transition zone or even the lower mantle, *260*, 1–9. https://doi.org/10.1016/j.epsl.2007.02.038

Bromiley, G., Hilaret, N., McCammon, C. (2004). Solubility of hydrogen and ferric iron in rutile and TiO2 (II : Implications for phase assemblages during ultrahigh-pressure metamorphism and for the stability of silica polymorphs in the lower mantle. *Geophysical Research Letters*, *31*(4), 2–6. https://doi.org/10.1029/2004GL019430

Brown, J. M., & McQueen, R. G. (1986). Phase transitions, Grüneisen parameter, and elasticity for shocked iron between 77 GPa and 400 GPa. *Journal of Geophysical Research: Solid Earth*, *91*(B7), 7485–7494. https://doi.org/10.1029/jb091ib07p07485

Brown, M. J. (2001). The equation of State of iron to 450 GPa: Another high pressure solid phase? *Geophysical Research Letters*, *28*(22), 4339–4342. https://doi.org/10.1029/2001GL013759

Bulanova, G., Griffin, W. L., Ryan, C. G. (1998). Nucleation environment of diamonds from Yakutian kimberlites. *Cambridge.Org*. https://doi.org/10.1180/002646198547675

Bundy, F. P., Hall, H. T., Strong., H. M., Wentorf, R. H. (1955). Man-Made Diamonds. *Nature*, 51–55.

Burkel, E. (2000). Phonon spectroscopy by inelastic X-ray scattering. *Reports on Progress in Physics*, *63*(2), 171–232. https://doi.org/10.1088/0034-4885/63/2/203

Campbell, A. J. (2008). Measurement of temperature distributions across laser heated samples by multispectral imaging radiometry. *Review of Scientific Instruments*, *79*(1). https://doi.org/10.1063/1.2827513

Campbell, A. J., Danielson, L., Righter, K., Seagle, C. T., Wang, Y., Prakapenka, V. B. (2009). High pressure effects on the iron-iron oxide and nickel-nickel oxide oxygen fugacity buffers. *Earth and Planetary Science Letters*, *286*(3–4), 556–564. https://doi.org/10.1016/j.epsl.2009.07.022

Canil, D. (2002). Vanadium in peridotites, mantle redox and tectonic environments: Archean to present. *Earth and Planetary Science Letters*, *195*(1–2), 75–90. https://doi.org/10.1016/S0012-821X(01)00582-9

Canil, D., & O'Neill, H. S. C. (1996). Distribution of ferric iron in some upper mantle assemblages. *Journal of Petrology*, 37(3), 609-635. https://doi.org/10.1093/petrology/37.3.609.

Van Cappellen, E. (1990). The parameterless correction method in X-ray microanalysis, *1*, 1–22. https://doi.org/10.1051/mmm:01990001010100

Van Cappellen, E., & Doukhan, J. C. (1994). Quantitative transmission X-ray microanalysis of ionic compounds. *Ultramicroscopy*, *53*, 343–349. https://doi.org/10.1016/0304-3991(94)90047-7

Caracas, R., & Wentzcovitch, R. (2004). Equation of state and elasticity of FeSi. *Geophysical Research Letters*, 31(20). https://doi.org/10.1029/2004GL020601

Caracas, R. (2017). The influence of carbon on the seismic properties of solid iron. *Geophysical Research Letters*, *44*, 128–134. https://doi.org/10.1002/2016GL071109

Catalli, K., Shim, S. H., Prakapenka, V. B., Zhao, J., Sturhahn, W., Chow, P., Xiao, Y., Liu, H., Cynn, H. Evans, W. J. (2010). Spin state of ferric iron in $MgSiO_3$ perovskite and its effect on elastic properties. *Earth and Planetary Science Letters*, *289*(1–2), 68–75. https://doi.org/10.1016/j.epsl.2009.10.029

Cemič (2005). Thermodynamics in Mineral Sciences. An introduction. *Springer.*

Cerantola, V., Bykova, E., Kupenko, I., Merlini, M., Ismailova, L., McCammon, C., Bykov, M., Chumakov, A. I., Petitgirard, S., Kantor, I., Svitlyk, V. (2017). Stability of iron-bearing carbonates in the deep Earth's interior. *Nature Communications*, *8*. https://doi.org/10.1038/ncomms15960

Chatterjee, S. K. (2008). *Crystallography and the World of Symmetry*. Springer.

Chen, B., Jackson, J. M., Sturhahn, W., Zhang, D., Zhao, J., Wicks, J. K., & Murphy, C. A. (2012). Spin crossover equation of state and sound velocities of $(Mg_{0.65}Fe_{0.35})O$ ferropericlase to 140 GPa. *Journal of Geophysical Research: Solid Earth*, 117(B8). https://doi.org/10.1029/2012JB009162

Chijioke, A. D., Nellis, W. J., Soldatov, A., Silvera, I. F. (2005). The ruby pressure standard to 150 GPa. *Journal of Applied Physics*, *98*(11). https://doi.org/10.1063/1.2135877

Christie, D. M., Carmichael, I. S. E., Langmuir, C. H. (1986). Oxidation states of mid-ocean ridge basalt glasses. *Earth and Planetary Science Letters*, *79*(3–4), 397–411. https://doi.org/10.1016/0012-821X(86)90195-0

Christensen, N. I., Carlson, R. L., Salisbury, M. H., Fountain, D. M. (1975). 27. Elastic wave velocities in volcanic and plutonic rocks recovered on DSDP LEG 31.

Dasgupta, R., & Hirschmann, M. M. (2010). The deep carbon cycle and melting in Earth's interior. *Earth and Planetary Science Letters*, *298*(1–2), 1–13. https://doi.org/10.1016/j.epsl.2010.06.039

Delano, J. W. (2001). Redox history of the Earth's interior since ~3900 Ma: Implications for prebiotic molecules. *Origins of Life and Evolution of the Biosphere*, *31*(4–5), 311–341. https://doi.org/10.1023/A:1011895600380

Dewaele, A., Loubeyre, P., Occelli, F., Mezouar, M., Dorogokupets, P. I., Torrent, M. (2006). Quasihydrostatic equation of state of Iron above 2 Mbar. *Physical Review Letters*, *97*(21), 29–32. https://doi.org/10.1103/PhysRevLett.97.215504

Dobson, D. P., Vočadlo, L., Wood, I. G. (2002). A new high-pressure phase of FeSi. *American Mineralogist*, *87*(5–6), 784–787. https://doi.org/10.2138/am-2002-5-623

Dobson, D. P., Crichton, W. A., Bouvier, P., Vočadlo, L., Wood, I. G. (2003). The equation of state of CsCl-structured FeSi to 40 GPa: Implications for silicon in the Earth's core. *Geophysical Research Letters*, *30*(1), 14-1-14–4. https://doi.org/10.1029/2002gl016228

Dorfman, S. M., Badro, J., Nabiei, F., Prakapenka, V. B., Cantoni, M., Gillet, P. (2018). Carbonate stability in the reduced lower mantle. *Earth and Planetary Science Letters*, *489*, 84–91. https://doi.org/10.1016/j.epsl.2018.02.035

Dubrovinskaia, N., Dubrovinsky, L., Solopova, N. A., Abakumov, A., Turner, S., Hanfland, M., Bykova, E., Bykov, M., Prescher, C., Prakapenka, V. B., Petitgirard, S. (2016). Terapascal static pressure generation with ultrahigh yield strength nanodiamond. *Science Advances*, *2*(7). https://doi.org/10.1126/sciadv.1600341

Dubrovinsky, L. S., Dubrovinskaia, N. A., Saxena, S. K., Annersten, H., Halenius, E., Harryson, H., Tutti, F., Rekhi, S., Bihan, T. L. (2000). Stability of ferropericlase in the lower mantle. *Science*, *289*(5478), 430–432. https://doi.org/10.1126/science.289.5478.430

Dubrovinsky, L., Dubrovinskaia, N., Narygina, O., Kantor, I., Kuznetzov, A., Prakapenka, V.B., Vitos, L., Johansson, B., Mikhaylushkin, A. S., Simak, S .I., Abrikosov, I. A. (2007). Body-centered cubic iron-nickel alloy in Earth's core. *Science*, 316(5833), 1880-1883. https://doi.org/10.1126/science.1142105

Dyar, M. D., Agresti, D. G., Schaefer, M. W., Grant, C. A., Sklute, E. C. (2006). Mössbauer spectroscopy of Earth and planetary materials. *Annual Review of Earth and Planetary Sciences*, *34*, 83–125. https://doi.org/10.1146/annurev.earth.34.031405.125049

Dziewonski, A. M., & Anderson, D. L. (1981). Preliminary reference Earth model. *Phys. Earth Planet. Inter*, *25*, 297–356. https://doi.org/10.1016/0031-9201(81)90046-7

Edmund, E., Antonangeli, D., Decremps, F., Morard, G., Ayrinhac, S., Gauthier, M., Boulard, E., Mezouar, M., Hanfland, M., Guignot, N. (2019a). Structure and elasticity of cubic Fe-Si alloys at high pressures. *Physical Review B*, *100*(13), 134105. https://doi.org/10.1103/PhysRevB.100.134105

Edmund, E., Antonangeli, D., Decremps, F., Miozzi, F., Morard, G., Boulard, E., Clark, A. N., Ayrinhac, S., Gauthier, M., Morand, M, Mezouar, M. (2019b). Velocity-Density Systematics of Fe-5wt%Si: Constraints on Si Content in the Earth's Inner Core. *Journal of Geophysical Research: Solid Earth*, *124*(4), 3436–3447. https://doi.org/10.1029/2018JB016904

Edmund, E., Miozzi, F., Morard, G., Boulard, E., Clark, A., Decremps, F., Garbarino, G., Svitlyk, V., Mezouar, M., Antonangeli, D. (2020). Axial compressibility and thermal equation of state of hcp Fe–5wt%Ni–5wt%Si. *Minerals*, *10*(2), 1–12. https://doi.org/10.3390/min10020098

Egerton, R. F. (2009). Electron energy-loss spectroscopy in the TEM. *Reports on Progress in Physics*, *72*(1). https://doi.org/10.1088/0034-4885/72/1/016502

Elliot, R. P. (1965). *Constitution of binary alloys*.

Eugster, H. P. (1957). Heterogeneous reactions involving oxidation and reduction at high pressures and temperatures. *The Journal of Chemical Physics*, *26*(6), 1761–1762. https://doi.org/10.1063/1.1743626

Fedorov, I. I., Chepurov, A. A., Dereppe, J. M. (2002). Redox conditions of metal-carbon melts and natural diamond genesis. *Geochemical Journal*, *36*(3), 247–253. https://doi.org/10.2343/geochemj.36.247

Fei, Y., Ricolleau, A., Frank, M., Mibe, K., Shen, G., Prakapenka, V. (2007). High-Pressure Geoscience Special Feature: Toward an internally consistent pressure scale. *Proceedings of the National Academy of Sciences*, *104*(22), 9182–9186. https://doi.org/10.1073/pnas.0609013104

Fei, Y., Murphy, C., Shibazaki, Y., Shahar, A., Huang, H. (2016). Thermal equation of state of hcp-iron: Constraint on the density deficit of Earth's solid inner core. *Geophysical Research Letters*, *43*(13), 6837–6843. https://doi.org/10.1002/2016GL069456

Fischer, R. A., & Campbell, A. J. (2015). The axial ratio of hcp Fe and Fe-Ni-Si alloys to the conditions of Earth's inner core. *American Mineralogist*, *100*(11–12), 2718–2724. https://doi.org/10.2138/am-2015-5191

Fischer, R. A., Campbell, A. J., Caracas, R., Reaman, D. M., Dera, P., Prakapenka, V. B. (2012). Equation of state and phase diagram of Fe-16Si alloy as a candidate component of Earth's core. *Earth and Planetary Science Letters*, *357–358*, 268–276. https://doi.org/10.1016/j.epsl.2012.09.022

Fischer, R. A., Campbell, A. J., Reaman, D. M., Miller, N. A., Heinz, D. L., Dera, P., Prakapenka, V. B. (2013). Phase relations in the Fe-FeSi system at high pressures and temperatures. *Earth and Planetary Science Letters*, *373*, 54–64. https://doi.org/10.1016/j.epsl.2013.04.035

Fischer, R.A., Campbell, A.J., Caracas, R., Reaman, D.M., Heinz, D.L., Dera, P., Prakapenka, V. B. (2014). Journal of Geophysical Research : Solid Earth. *AGU: Journal of Geophysical Research, Solid Earth*, *119*, 3678–3699. https://doi.org/10.1002/2013JB010898.

Fischer, R. A., Nakajima, Y., Campbell, A. J., Frost, D. J., Harries, D., Langenhorst, F., Miyajima, N., Pollok, K., Rubie, D. C. (2015). High pressure metal-silicate partitioning of Ni, Co, V, Cr, Si, and O. *Geochimica et Cosmochimica Acta*, *167*, 177–194. https://doi.org/10.1016/j.gca.2015.06.026

Frost, B. R. (1991). Introduction To Oxygen Fugacity and its petrologic importance, *2*, 1–9. https://doi.org/10.1515/9781501508684-004

Frost, D. J., Mann, U., Asahara, Y., Rubie, D. C. (2008). The redox state of the mantle during and just after core formation. *Philosophical Transactions of the Royal Society A: Mathematical, Physical and Engineering Sciences*, *366*(1883), 4315–4337. https://doi.org/10.1098/rsta.2008.0147

Frost, D. J. (2003). Fe^{2+} - Mg partitioning between garnet, magnesiowüstite, and $(Mg,Fe)_2SiO_4$ phases of the transition zone. *American Mineralogist*, *88*(2–3), 387–397. https://doi.org/10.2138/am-2003-2-315

Frost, D. J., & Langenhorst, F. (2002). The effect of Al_2O_3 on Fe-Mg partitioning between magnesiowustite and magnesium silicate perovskite. *Earth and Planetary Science Letters*, *199*. https://doi.org/10.1016/S0012-821X(02)00558-7

Frost, D. J., & McCammon, C. A. (2008). The Redox State of Earth's mantle. *Annual Review of Earth and Planetary Sciences*, *36*, 389–420. https://doi.org/10.1146/annurev.earth.36.031207.124322

Frost, D. J., Liebske, C., Langenhorst, F., McCammon, C. A., Trønnes, R. G., Rubie, D. C. (2004). Experimental evidence for the existence of iron-rich metal in the Earth's lower mantle. *Nature*, *428*(6981), 409–412. https://doi.org/10.1038/nature02413

Frost, D. J. (2008). The Upper Mantle and Transition Zone. *Elements*, 171–176. https://doi.org/10.2113/GSELEMENTS.4.3.171

Fujino, K., Miyajima, N., Yagi, T., Kondo, T., Funamori, N. (1998). Analytical electron microscopy of the Garnet-Perovskite transformation in a laser-heated diamond anvil cell. *Geophysical Monograph Series*, *101*, 409–417. https://doi.org/10.1029/GM101p0409

Gibb, T. C. (2013). Principles of Mössbauer Spectroscopy. *Springer*.

Gonzalez-Platas, J., Alvaro, M., Nestola, F., Angel, R. (2016). EosFit7-GUI: A new graphical user interface for equation of state calculations, analyses and teaching. *Journal of Applied Crystallography*, *49*(4), 1377–1382. https://doi.org/10.1107/S1600576716008050

Green, D. H., Eggins, S. M., Yaxley, G. (1993). The other carbon cycle. *Nature*, *365*, 210–211. https://doi.org/10.1038/365210a0

Gudmundsson, G., & Holloway, J. R. (1993). Activity-composition relationships in the system Fe-Pt at 1300 and 1400°C and at 1 atm and 20 kbar. *American Mineralogist*, *78*(1–2), 178–186.

Gudmundsson, G., & Wood, B. J. (1995). Experimental tests of garnet peridotite oxygen barometry. *Contributions to Mineralogy and Petrology*, *119*(1), 56–67. https://doi.org/10.1007/BF00310717

Gütlich, P., Link, R., Trautwein, A. X. (1978). *Mössbauer Spectroscopy and Transition Metal Chemistry–Inorganic Chemistry*.

Haggerty, S. E. (1995). Upper mantle mineralogy stephen. *J. Geodynamics*, *3707*(4), 331–364. https://doi.org/10.1016/0264-3707(95)00016-3

Haggerty, S. E. (1999). A diamond trilogy: Superplumes, supercontinents, and supernovae. *Science*, *285*(5429), 851–860. https://doi.org/10.1126/science.285.5429.851

Hammouda, T., & Keshav, S. (2015). Melting in the mantle in the presence of carbon: Review of experimentsand discussion on the origin of carbonatites. *Chemical Geology*, *418*, 171–188. https://doi.org/ 10.1016/j.chemgeo.2015.05.018

Hansen, M., & Anderko, K. (1958). Constitution of Binary Alloys. *Journal of the Electrochemical Society*, 105(12), 260.

Harte, B., Fitzsimons, I., Harris, J., Otter, M. (1999). Carbon isotope ratios and nitrogen abundances in relation to cathodoluminescence characteristics for some diamonds from the Kaapvaal Province, S. Africa. Mineralogical Magazine, 63(6), 829-856. https://doi.org/10.1180/002646199548961

Heald, E. F. (1967). Thermodynamics of iron-platinum alloys. *Trans. Met. Soc. AIME*, *239*, 1337-1340.

Heaney, P. J., Vicenzi, E. P., Giannuzzi, L. A., Livi, K. J. T. (2001). Focused ion beam milling: A method of site-specific sample extraction for microanalysis of Earth and planetary materials. *American Mineralogist*, *86*(9), 1094–1099. https://doi.org/10.2138/am-2001-8-917

Van Der Hilst, R. D., & Kárason, H. (1999). Compositional heterogeneity in the bottom 1000 kilometers of Earth's mantle: Toward a hybrid convection model. *Science*, *283*(5409), 1885–1888. https://doi.org/10.1126/science.283.5409.1885

Hirao, N., Ohtani, E., Kondo, T., Kikegawa, T. (2004). Equation of state of iron–silicon alloys to megabar pressure. Physics and chemistry of minerals, 31(6), 329-336. https://doi.org/10.1007/s00269-004-0387-x

Hirose, K., Takafuji, N., Sata, N., Ohishi, Y. (2005). Phase transition and density of subducted MORB crust inthe lower mantle. *Earth and Planetary Science Letters*, *237*, 239–251. https://doi.org/doi:10.1016/j.epsl.2005.06.035

Hirose, K. (2002). Phase transitions in pyrolitic mantle around 670-km depth: Implications for upwelling of plumes from the lower mantle. *Journal of Geophysical Research: Solid Earth*, *107*(B4), ECV 3-1-ECV 3-13. https://doi.org/10.1029/2001jb000597

Hofer, F., Schmidt, F. P., Grogger, W., Kothleitner, G. (2016). Fundamentals of electron energy-loss spectroscopy. *IOP Conference Series: Materials Science and Engineering*, *109*(1). https://doi.org/10.1088/1757-899X/109/1/012007

Holland, T. J. B., & Powell, R. (1998). An internally consistent thermodynamic data set for phases of petrological interest. *Journal of Metamorphic Geology*, *16*(3), 309–343. https://doi.org/10.1111/j.1525-1314.1998.00140.x

Holland, T. J. B., & Powell, R. (2011). An improved and extended internally consistent thermodynamic dataset for phases of petrological interest, involving a new equation of state for solids. *Journal of Metamorphic Geology*, *29*(3), 333–383. https://doi.org/10.1111/j.1525-1314.2010.00923.x

Hong, S. M., Akaishi, M., Yamaoka, S. (1999). Nucleation of diamond in the system of carbon and water under very high pressure and temperature. *Journal of Crystal Growth*, *200*(1–2), 326–328. https://doi.org/10.1016/S0022-0248(98)01288-3

Horiuchi, H., Ito, E., Weidner, D. J. (1987). Perovskite-type $MgSiO_3$: Single-crystal X-ray diffraction study. *American Mineralogist*, *72*, 357–360.

Huebner, J. S. (1971). Research techniques for high pressure and high temperature. *Research Techniques for High Pressure and High Temperature*, *Springer,* 123–177.

Hultgren, R., Desai, P., Hawkins, D., Gleiser, M. (1973). Selected values of the thermodynamic properties of binary alloys.

Ikuta, D., Ohtani, E., Hirao, N. (2021). Two-phase mixture of Fe-Ni-Si alloys in the Earth's inner core. *Communications Earth and Environment*, *148*, 148–162. https://doi.org/10.1038/s43247-021-00298-1

Irifune, T, & Ringwood, A. E. (1993). Phase transformations in subducted oceanic crust and buoyancy relationships at depths of 600–800 km in the mantle. *Earth and Planetary Science Letters*, *117(1–2)*, 101–110. https://doi.org/10.1016/0012-821X(93)90120-X

Irifune, T. (1994). Absence of an aluminous phase in the upper part of the Earth' s lower mantle. *Nature*, *370*, 131–133. https://doi.org/10.1038/370131a0

Irifune, T., Shinmei, T., McCammon, C. A., Miyajima, N., Rubie, D. C., Frost, D. J. (2010). Iron partitioning and density changes of pyrolite in Earth's lower mantle. *Science*, *327*(5962), 193–195. https://doi.org/10.1126/science.1181443

Ishikawa, D., Uchiyama, H., Tsutsui, S., Fukui, H., Baron, A. Q. R. (2013). Compound focusing for hard-X-ray inelastic scattering. *Advances in X-Ray/EUV Optics and Components VIII*, *8848*, 88480F. https://doi.org/10.1117/12.2023795

Jacobsen S.D., Reichmann H. J., Spetzler H. A., Mackwell S. J., Smyth J. R., Angel R.J. , McCammon C. A. (2002). Structure and elasticity of single-crystal (Mg,Fe)O and a new method of generating shear waves for gigahertz ultrasonic interferometry. *Journal of Geophysical Research: Solid Earth*. 107(B2):2037. doi:10.1029/2001JB000490

Jambon, A. (2018). Earth degassing and large-scale geochemical cycling of volatile elements. https://doi.org/https://doi.org/10.1515/9781501509674-019

Jayaraman, A. (1983). Diamond anvil cell and high-pressure physical investigations. *Reviews of Modern Physics*, *55*(1), 65–108. https://doi.org/10.1103/RevModPhys.55.65

Kamada, S., Suzuki, N., Maeda, F., Hirao, N., Hamada, M., Ohtani, E., Masuda, R., Mitsui, T., Ohishi, Y. and Nakano, S. (2018). Electronic properties and compressional behavior of Fe–Si alloys at high pressure. *American Mineralogist: Journal of Earth and Planetary Materials*, 103(12), pp.1959-1965. https://doi.org/10.2138/am-2018-6425

Kaminsky, F. V., Zakharchenko, O. D., Davies, R., Griffin, W. L., Khachatryan-Blinova, G. K., Shiryaev, A. A. (2001). Superdeep diamonds from the Juina area, Mato Grosso State, Brazil. *Contributions to Mineralogy and Petrology*, *140*(6), 734–753. https://doi.org/10.1007/s004100000221

Kaminsky, F. V. (2012). Mineralogy of the lower mantle: A review of 'super-deep' mineral inclusions in diamond. *Earth-Science Reviews*, *110*(1–4), 127–147. https://doi.org/10.1016/j.earscirev.2011.10.005

Kaminsky, F. V., Khachatryan, G. K., Andreazza, P., Araujo, D., Griffin, W. L. (2009). Super-deep diamonds from kimberlites in the Juina area, Mato Grosso State, Brazil. *Lithos*, *112*, 833–842. https://doi.org/10.1016/j.lithos.2009.03.036

Kaminsky, F. V., Wirth, R., Schreiber, A. (2015a). A microinclusion of lower-mantle rock and other minerals and nitrogen lower-mantle inclusions in a diamond. *Canadian Mineralogist*, *53*(1), 83–104. https://doi.org/10.3749/canmin.1400070

Kaminsky, F. V., Ryabchikov, I. D., Wirth, R. (2015b). A primary natrocarbonatitic association in the Deep Earth. *Mineralogy and Petrology*, *110*(2–3), 387–398. https://doi.org/10.1007/s00710-015-0368-4

Kaminsky, F. V., Ryabchikov, I. D., McCammon, C. A., Longo, M., Abakumov, A. M., Turner, S., Heidari, H. (2015c). Oxidation potential in the Earth's lower mantle as recorded by ferropericlase inclusions in diamond. *Earth and Planetary Science Letters*, *417*(2015), 49–56. https://doi.org/10.1016/j.epsl.2015.02.029

Kaneshima, S., & Helffrich, G. (1999). Dipping low-velocity layer in the mid-lower mantle: Evidence for geochemical heterogeneity. *Science*, *283*(5409), 1888–1891. https://doi.org/10.1126/science.283.5409.1888

Kantor, A. P., Kantor, I. Y., Kurnosov, A. V., Kuznetsov, A. Y., Dubrovinskaia, N. A., Krisch, M., Bossak, A. A., Dmitriev, V. P., Urusov, V.S., Dubrovinsky, L. S. (2007). Sound wave velocities of fcc Fe-Ni alloy at high pressure and temperature by mean of inelastic X-ray scattering. *Physics of the Earth and Planetary Interiors*, *164*(1–2), 83–89. https://doi.org/10.1016/j.pepi.2007.06.006

Kantor, I., Prakapenka, V., Kantor, A., Dera, P., Kurnosov, A., Sinogeikin, S., Dubrovinskaia, N. A., Dubrovinsky, L. S. (2012). BX90: A new diamond anvil cell design for X-ray diffraction and optical measurements. *Review of Scientific Instruments*, *83*(12), 125102. https://doi.org/10.1063/1.4768541

Kantor, I., Marini, C., Mathon, O., Pascarelli, S. (2018). A laser heating facility for energy-dispersive X-ray absorption spectroscopy. *Review of Scientific Instruments*, *89*(1). https://doi.org/10.1063/1.5010345

Kantor, I., Dubrovinsky, L., McCammon, C., Kantor, A., Pascarelli, S., Aquilanti, G., Crichton, W., Mattesini, M., Ahuja, R., Almeida, J., Urusov, V. (2006). Pressure-induced phase transition in $Mg_{0.8}Fe_{0.2}O$ ferropericlase. *Physics and Chemistry of Minerals*, *33*(1), 35–44. https://doi.org/10.1007/s00269-005-0052-z

Katsura, T., Yoneda, A., Yamazaki, D., Yoshino, T., Ito, E. (2010). Adiabatic temperature profile in the mantle. *Physics of the Earth and Planetary Interiors*, 183(1-2), 212-218. https://doi.org/doi:10.1016/j.pepi.2010.07.001

Kawai, N., & Endo, S. (1970). The generation of ultrahigh hydrostatic pressures by a split sphere apparatus. *Review of Scientific Instruments*, *41*(8), 1178–1181. https://doi.org/10.1063/1.1684753

Kawakatsu, H., & Niu, F. (1994). Seismic evidence for a 920-km discontinuity in the mantle. *Nature*, *371*, 301–305. https://doi.org/10.1038/371301a0

Van Keken, P. E., Hauri, E. H., Ballentine, C. J. (2002). Mantle mixing: The generation, preservation and destruction of chemical heterogeneity. *Annual Review of Earth and Planetary Sciences*, *30*, 493–525. https://doi.org/10.1146/annurev.earth.30.091201.141236

Kellogg, L. H., Hager, B. H., Van Der Hilst, R. D. (1999). Compositional stratification in the deep mantle. *Science*, *283*(5409), 1881–1884. https://doi.org/10.1126/science.283.5409.1881

Kennett, B. L. N., & Engdahl, E. R. (1991). Traveltimes for global earthquake location and phase identification. *Geophysical Journal International,* *105*, 429–465. https://doi.org/10.1111/j.1365-246X.1991.tb06724.x

Kennett, B. L. N., Engdahl, E. R., Buland, R. (1995). Constraints on seismic velocities in the Earth from traveltimes. *Geophysical Journal International*, *122*(1), 108–124. https://doi.org/10.1111/j.1365-246X.1995.tb03540.x

Keppler, H., & Frost, D. J. (2005). Introduction to minerals under extreme conditions. *Mineral Behaviour at Extreme Conditions*, *7*, 1–30. https://doi.org/10.1180/emu-notes.7.1

Kessel, R., Beckett, J., Stolper, E. M. (2001). Thermodynamic properties of the Pt-Fe system. *American Mineralogist*, *86*, 1003–1014. https://doi.org/10.2138/am-2001-8-907

Kesson, E.S., Fitz Gerald J.D., Shelley M. J. (1998). Mineralogy and dynamics of a pyrolite lower mantle. *Nature*, *393*, 252–255. https://doi.org/https://doi.org/10.1038/30466

Kesson, S. E., & Fitz Gerald, J. D. (1991). Partitioning of MgO, FeO, NiO, MnO and Cr_2O_3 between magnesian silicate perovskite and magnesiowüstite: implications for the origin of inclusions in diamond and the composition of the lower mantle. *Earth and Planetary Science Letters*, *111*(2–4), 229–240. https://doi.org/10.1016/0012-821X(92)90181-T

Komobayashi, T., Fei, Y., Meng, Y., Prakapenka, V. (2009). In-situ X-ray diffraction measurements of the gamma-epsilon transition boundary of iron in an internally-heated diamond anvil cell. *Earth and Planetary Science Letters*, *282*, 252–257. https://doi.org/https://doi.org/10.1016/j.epsl.2009.03.025

Komobayashi, T., Fei, Y. (2010). Internally consistent thermodynamic database for iron to the Earth's core conditions. *Journal of Geophysical Research*, *115*(B03202). https://doi.org/doi:10.1029/2009JB006442

Kotrbová, M., Kadeckova, S., Novak, J., Badler, J., Smirnov, G. V., Shvydko, Y. V. (1985). Growth and perfection of flux grown $FeBO_3$ and $^{57}FeBO_3$ crystals. *Journal of Crystal Growth*, *71*, 607–614. https://doi.org/https://doi.org/10.1016/0022-0248(85)90368-9

Kumar, M. D. S., Akaishi, M., Yamaoka, S. (2000). Formation of diamond from supercritical H_2O-CO_2 fluid at high pressure and high temperature. *Journal of Crystal Growth*, *213*(1), 203–206. https://doi.org/10.1016/S0022-0248(00)00352-3

Kumar, P. S., Pavithra, K. G., Naushad, M. (2019). Characterization techniques for nanomaterials. *Nanomaterials for Solar Cell Applications*, 97–124. https://doi.org/10.1016/B978-0-12-813337-8.00004-7

Kupenko, I., Strohm, C., McCammon, C. A., Cerantola, V., Glazyrin, K., Petitgirard, S., Vasiukov, D., Aprilis, G., Chumakov, A.I., Rüffer, R., Dubrovinsky, L. (2015). Time differentiated nuclear resonance spectroscopy coupled with pulsed laser heating in diamond anvil cells. *Review of Scientific Instruments*, *86*(11). https://doi.org/10.1063/1.4935304

Kurnosov, A., Kantor, I., Boffa-Ballaran, T., Lindhardt, S., Dubrovinsky, L., Kuznetsov, A., Zehnder, B. H. (2008). A novel gas-loading system for mechanically closing of various types of diamond anvil cells. *Review of Scientific Instruments*, *79*(4), 045110. https://doi.org/10.1063/1.2902506

Kuwayama, Y., Sawai, T., Hirose, K., Sata, N., Ohishi, Y. (2009). Phase relations of iron–silicon alloys at high pressure and high temperature. *Physics and Chemistry of Minerals*, 36(9), 511-518. https://doi.org/10.1007/s00269-009-0296-0

Lauterbach, S., McCammon, C. A., Van Aken, P., Langenhorst, F., Seifert, F. (2000). Mössbauer and ELNES spectroscopy of $(Mg,Fe)(Si,Al)O_3$ perovskite: A highly oxidised component of the lower mantle. *Contributions to Mineralogy and Petrology*, *138*(1), 17–26. https://doi.org/10.1007/PL00007658

Lee, K. K. M., O'Neill, B., Panero, W. R., Shim, S. H., Benedetti, L. R., Jeanloz, R. (2004). Equations of state of the high-pressure phases of a natural peridotite and implications for the Earth's lower mantle. *Earth and Planetary Science Letters*, *223*(3–4), 381–393. https://doi.org/10.1016/j.epsl.2004.04.033

Li, J., & Agee, C. B. (1996). Geochemistry of mantle-core differentiation at high pressure. *Nature*, *381*(6584), 686–689. https://doi.org/10.1038/381686a0

Li, J., & Fei, Y. (2013). *Experimental Constraints on Core Composition*. *Treatise on Geochemistry: Second Edition*, 3. https://doi.org/10.1016/B978-0-08-095975-7.00214-X

Li, J., Chen, B., Mookherjee, M., Morard, G. (2019). Carbon versus Other Light Elements in Earth's Core. *Deep Carbon*, 40–65. https://doi.org/10.1017/9781108677950.003

Li, Z. X. A., & Lee, C. T. A. (2004). The constancy of upper mantle f_{O2} through time inferred from V/Sc ratios in basalts. *Earth and Planetary Science Letters*, *228*(3–4), 483–493. https://doi.org/10.1016/j.epsl.2004.10.006

Lin, J. F., Struzhkin, V. V., Jacobsen, S. D., Hu, M. Y., Chow, P., Kung, J., Liu, H., Mao, H. K., Hemley, R. J. (2005). Spin transition of iron in magnesiowüstite in the Earth's lower mantle. *Nature*, *436*, 377–380. https://doi.org/10.1038/nature03825

Lin, J., Heinz, D. L., Campbell, A. J., Devine, J. M., Shen, G. (2002). Iron-Silicon Alloy in Earth ' s Core ? *Science*, *295*, 313–316. https://doi.org/10.1126/science.1066932

Lin, J. F., Scott, H. P., Fischer, R. A., Chang, Y. Y., Kantor, I., Prakapenka, V. B. (2009). Phase relations of Fe-Si alloy in Earth's core. *Geophysical Research Letters*, 36(6). https://doi.org/10.1029/2008GL036990

Lin, J. F., Struzhkin, V. V., Sturhahn, W., Huang, E., Zhao, J., Hu, M. Y., Alp, E. E., Mao, H. K., Boctor, N., Hemley, R. J. (2003). Sound velocities of iron- nickel and iron- silicon alloys at high pressures. *Geophysical Research Letters*, *30*(21), 1–4. https://doi.org/10.1029/2003GL018405

Litvin, Y. A., & Zharikov, V. A. (1999). Primary fluid-carbonatitic inclusions in diamond simulating by the system K_2O-Na_2O-CaO-MgO-FeO-CO_2 as a diamond-producting medium in experiment at 7-9 GPa. *Doklady akademii nauk.*, *367*(113095), 397–401.

Liu, J., Lin, J. F., Alatas, A., Bi, W. (2014). Sound velocities of bcc-Fe and $Fe_{0.85}Si_{0.15}$ alloy at high pressure and temperature. *Physics of the Earth and Planetary Interiors*, *233*, 24–32. https://doi.org/10.1016/j.pepi.2014.05.008

Liu, L. (2002). An alternative interpretation of lower mantle mineral associations in diamonds. *Contributions to Mineralogy and Petrology*, *144*(1), 16–21. https://doi.org/10.1007/s00410-002-0389-y

Liu, Z., Ishii, T., Katsura, T. (2017). Rapid decrease of $MgAlO_{2.5}$ component in bridgmanite with pressure. *Geochemical Perspectives Letters*, *5*, 12–18. https://doi.org/10.7185/geochemlet.1739

Longo, M., McCammon, C. A., Jacobsen, S. D. (2011). Microanalysis of the iron oxidation state in (Mg,Fe)O and application to the study of microscale processes. *Contributions to Mineralogy and Petrology*, *162*(6), 1249–1257. https://doi.org/10.1007/s00410-011-0649-9

Lord, O. T., Walter, M. J., Dobson, D. P., Armstrong, L., Clark, S. M., & Kleppe, A. (2010). The FeSi phase diagram to 150 GPa. *Journal of Geophysical Research: Solid Earth*, 115(B6). https://doi.org/10.1029/2009JB006528

Luth, R. W. (1993). Diamonds, eclogites, and the oxidation state of the Earth's mantle. *Science*, 261(5117), 66–68. https://doi.org/10.1126/science.261.5117.66

Ma, Y., Somayazulu, M., Shen, G., Mao, H. K., Shu, J., Hemley, R. J. (2004). In situ X-ray diffraction studies of iron to Earth-core conditions. *Physics of the Earth and Planetary Interiors*, 143, 455-467. https://doi.org/10.1016/j.pepi.2003.06.005

Man, C. S. , Huang, M. (2011). A Simple Explicit Formula for the Voigt-Reuss-Hill Average of Elastic Polycrystals with Arbitrary Crystal and Texture Symmetries. *Journal of Elasticity*, 105, 29–48. https://doi.org/10.1007/s10659-011-9312-y

Mao, H. K., Xu, J., Bell, P. M. (1986). Calibration of the ruby pressure gauge to 800 kbar under quasi-hydrostatic conditions. *Journal of Geophysical Research*, *91*(B5), 4673. https://doi.org/10.1029/jb091ib05p04673

Mao, H. K., Wu, Y. Chen, L. C. Shu, J. F., Jephcoat, A. P. (1990). Static Compression of Iron to 300 GPa and $Fe_{0.8}Ni_{0.2}$ Alloy to 260 GPa: Implications for Composition of the Core. *Journal of Geophysical Research*, *95*(B13), 21737–21742. https://doi.org/10.1029/JB095iB13p21737

Mao, H. K., Kao, C., Hemley, R. J. (2001). Inelastic X-ray scattering at ultrahigh pressures. *Journal of Physics Condensed Matter*, *13*(34), 7847–7858. https://doi.org/10.1088/0953-8984/13/34/323

Mao, Z., Armentrout, M., Rainey, E., Manning, C. E., Dera, P., Prakapenka, V. B., Kavner, A. (2011a). Dolomite III: A new candidate lower mantle carbonate. *Geophysical Research Letters*, *38*(22), 2–5. https://doi.org/10.1029/2011GL049519

Mao, Z., Lin, J. F., Liu, J., Prakapenka, V. B. (2011b). Thermal equation of state of lower-mantle ferropericlase across the spin crossover. *Geophysical Research Letters*, *38*(23), 2–5. https://doi.org/10.1029/2011GL049915

Mao, Z., Lin, J. F., Liu, J., Alatas, A., Gao, L., Zhao, J., Mao, H. K. (2012). Sound velocities of Fe and Fe-Si alloy in the Earth's core. *Proceedings of the National Academy of Sciences of the United States of America*, *109*(26), 10239–10244. https://doi.org/10.1073/pnas.1207086109

Martorell, B., Vocadlo, L., Brodholt, J., Wood I.G. (2013). Strong premelting effect in the elastic properties of hcp-Fe under inner-core conditions. *Science*, *342*(6157). https://doi.org/10.1126/science.1243651

Massa, W. (2004). Crystal Structure Determination. *Crystal Structure Determination*. https://doi.org/10.1007/978-3-662-06431-3

McCammon, C. A., Peyronneau, J., Poirier, J. (1998). Low ferric iron content of (Mg,Fe)O at high pressures and temperatures. *Geophysical Research Letters*, *25*(10), 1589–1592. https://doi.org/10.1029/98GL01178

McCammon, C. A. (1997a). Perovskite as a possible sink for ferric iron in the lower mantle. *Nature*, *387*(6634), 694–696. https://doi.org/10.1038/42685

McCammon, C. A, Hutchison, M., Harris, J. (1997b). Ferric iron content of mineral inclusions in diamonds from São Luiz: A view into the lower mantle. *Science*, *278*(5337), 434–436. https://doi.org/10.1126/science.278.5337.434

McCammon, C. A. (2005c). Mantle Oxidation State and Oxygen Fugacity: Constraints on Mantle Chemistry, Structure, and Dynamics. https://doi.org/10.1029/160GM14

McCammon, C. A., & Ross, N. L. (2003). Crystal chemistry of ferric iron in (Mg,Fe) (Si,Al)O_3 majorite with implications for the transition zone. *Physics and Chemistry of Minerals*, *30*(4), 206–216. https://doi.org/10.1007/s00269-003-0309-3

McCammon, C. A., Chaskar, V., Richards, G. G. (1991). A technique for spatially resolved Mössbauer spectroscopy applied to quenched metallurgical slags. *Measurement Science and Technology*, *657*(2).

McCammon, C. A., Stachel, T., Harris, J. W. (2004). Iron oxidation state in lower mantle mineral assemblages. I. Empirical relations derived from high-pressure experiments. *Earth and Planetary Science Letters*, *222*(2), 423–434. https://doi.org/10.1016/j.epsl.2004.03.019

McCammon, C.A., & Beran, A. (2004). Mössbauer spectroscopy: applications. Spectroscopic methods in mineralogy 6 (2004): 369-398.

McCammon, C. A. (2000). Insights into Phase Transformations from Mössbauer Spectroscopy. *Reviews in Mineralogy and Geochemistry*, *39*(1), 241–264. https://doi.org/https://doi.org/10.2138/rmg.2000.39.09

McCammon, C. A. (2001a). Geophysics: Deep diamond mysteries. *Science*, *293*(5531), 813–814. https://doi.org/10.1126/science.1063295

McCammon, C. A. (2005a). Mantle oxidation state and oxygen fugacity: Constraints on mantle chemistry, structure, and dynamics. *Geophysical Monograph Series*, *160*, 219–240. https://doi.org/10.1029/160GM14

McCammon, C. A. (2005b). The paradox of mantle redox. *Science*, *308*(5723), 807–808. https://doi.org/10.1126/science.1110532

Mcdonough, W. F. (2003). Compositional Model for the Earth's Core. https://doi.org/10.1016/B0-08-043751-6/02015-6

McDonough, W. F., & Sun, S. (1995). The composition of the Earth. *Chemical Geology*, *120*(3–4), 223–253. https://doi.org/10.1016/0009-2541(94)00140-4

Merlini, M., & Hanfland, M. (2013). Single-crystal diffraction at megabar conditions by synchrotron radiation. *High Pressure Research*, *33*(3), 511–522. https://doi.org/10.1080/08957959.2013.831088

Miletich, R., Allan, D. R., Kuhs, W. F. (2000). High-Pressure Single-Crystal Techniques. *Reviews in Mineralogy and Geochemistry*, *41*(1), 445–519. https://doi.org/10.2138/rmg.2000.41.14

Miyajima, N., Holzapfel, C., Asahara, Y., Dubrovinsky, L., Frost, D. J., Rubie, D. C., Drechsler, M., Niwa, K., Ichihara, M. Yagi, T. (2010). Combining FIB milling and conventional Argon ion milling techniques to prepare high-quality site-specific TEM samples for quantitative EELS analysis of oxygen in molten iron. *Journal of Microscopy*, *238*(3), 200–209. https://doi.org/10.1111/j.1365-2818.2009.03341.x

Miyajima, N., Fujino, K., Funamori, N., Kondo, T., Yagi, T. (1999). Garnet-perovskite transformation under conditions of the Earth's lower mantle: An analytical transmission electron microscopy study. *Physics of the Earth and Planetary Interiors*, *116*(1–4), 117–131. https://doi.org/10.1016/S0031-9201(99)00127-2

Miyajima, N., Langenhorst, F., Frost, D. J., Yagi, T. (2004). Electron channelling spectroscopy of iron in majoritic garnet and silicate perovskite using a transmission electron microscope. *Physics of the Earth and Planetary Interiors*, *143*(1–2), 601–609. https://doi.org/10.1016/j.pepi.2003.07.023

Mohseni H. (2014). Effective Metal-Alloy Redox Sensors and the Oxygen Fugacity of Diamond Formation. *Master thesis, BGI, University of Bayreuth.*

Morrison, R. A., Jackson, J. M., Sturhahn, W., Zhang, D., Greenberg, E. (2018). Equations of State and Anisotropy of Fe-Ni-Si Alloys. *Journal of Geophysical Research: Solid Earth*, *123*(6), 4647–4675. https://doi.org/10.1029/2017JB015343

Morrison, R. A., Jackson, J. M., Sturhahn, W., Zhao, J., Toellner, T. S. (2019). High pressure thermoelasticity and sound velocities of Fe-Ni-Si alloys. *Physics of the Earth and Planetary Interiors*, *294*, 106268. https://doi.org/10.1016/j.pepi.2019.05.011

Mössbauer, R. L. (1958). Kernresonanzfluoreszenz von Gammastrahlung in Ir_{191}. *Zeitschrift Ffir Physik*, *151*, 124–143.

Murakami, M., Hirose, K., Kawamura, K., Sata, N., Ohishi, Y. (2004). Post-Perovskite Phase Transition in $MgSiO_3$. *Science*, *304*. https://doi.org/10.1126/science.1095932

Nafziger, R. H., Ulmer, G. C., Woermann, E. (1971). Gaseous Buffering for the Control of Oxygen Fugacity at One Atmosphere. *Research Techniques for High Pressure and High Temperature*, *Springer-V*, 9–41. https://doi.org/10.1016/0016-7037(72)90090-7

Narygina, O., Mattesini, M., Kantor, I., Pascarelli, S., Wu, X., Aquilanti, G., McCammon, C. A., Dubrovinsky, L (2009). High-pressure experimental and computational XANES studies of $(Mg,Fe)(Si,Al)O_3$ perovskite and (Mg,Fe)O ferropericlase as in the Earth's lower mantle. *Physical Review B - Condensed Matter and Materials Physics*, *79*(17), 1–10. https://doi.org/10.1103/PhysRevB.79.174115

Navrotsky, A. (1999). A lesson from ceramics. *Science*, *284*(5421), 1788-1789. https://doi.org/10.1126/science.284.5421.1788

Navrotsky, A., Schoenitz, M., Kojitani, H., Xu, H., Zhang, J., Weidner, D. J., Jeanloz, R. (2003). Aluminum in magnesium silicate perovskite: Formation, structure, and energetics of magnesium-rich defect solid solutions. *J. Geophys. Res*, *108*(B7), 2330. https://doi.org/10.1029/2002JB002055

Nestola, F., Cerantola, V., Milani, S., Anzolini, C., McCammon, C. A., Novella, D., Kupenko, I., Chumakov, A., Rueffer, R., Harris, J.W. (2016). Synchrotron Mössbauer Source technique for in situ measurement of iron-bearing inclusions in natural diamonds. *Lithos*, *265*, 328–333. https://doi.org/10.1016/J.LITHOS.2016.06.016

Nestola, F., Korolev, N., Kopylova, M., Rotiroti, N., Pearson, D. G., Pamato, M. G., Alvaro, M., Peruzzo, L., Gurney, J. J., Moore, A. E., Davidson, J. (2018). $CaSiO_3$ perovskite in diamond indicates the recycling of oceanic crust into the lower mantle. *Nature*, *555*(7695), 237–241. https://doi.org/10.1038/nature25972

Newbury, D. E., & Ritchie, N. W. (2015). Performing elemental microanalysis with high accuracy and high precision by scanning electron microscopy/silicon drift detector energy-dispersive X-ray spectrometry (SEM/SDD-EDS). *Journal of materials science*, 50(2), 493-518. https://doi.org/10.1007/s10853-014-8685-2

Nimis, P., Nestola, F., Schiazza, M., Reali, R., Agrosì, G., Mele, D., Tempesta, G., Howell, D., Hutchison, M. T., Spiess, R. (2019). Fe-rich ferropericlase and magnesiowüstite inclusions reflecting diamond formation rather than ambient mantle. *Geology*, *47*(1), 27–30. https://doi.org/10.1130/G45235.1

Nishihara, Y., Nakajima, Y., Akashi, A., Tsujino, N., Takahashi, E., Funakoshi, K. I., Higo, Y. (2012). Isothermal compression of face-centered cubic iron. *American Mineralogist*, *97*(8–9), 1417–1420. https://doi.org/10.2138/am.2012.3958

O'Neill, H. S. C., & Wall, V. J. (1987). The olivine - orthopyroxene - spinel oxygen geobarometer, the nickel precipitation curve, and the oxygen fugacity of the Earth's upper mantle. *Journal of Petrology*, *28*(6), 1169–1191. https://doi.org/10.1093/petrology/28.6.1169

O'Neill, H. S. C. (1987). Quartz-fayalite-iron and quartz-fayalite-magnetite equilibria and the free energy of formation of fayalite (Fe_2SiO_4) and magnetite (Fe_3O_4). *American Mineralogist*, *72*(1–2), 67–75.

O'Neill, H. S. C., Pownceby, M. I., McCammon, C. A. (2003). The magnesiowüstite: Iron equilibrium and its implications for the activity-composition relations of $(Mg,Fe)_2SiO_4$ olivine solid solutions. *Contributions to Mineralogy and Petrology*, *146*(3), 308–325. https://doi.org/10.1007/s00410-003-0496-4

Ohtani, E., Shibazaki, Y., Sakai, T., Mibe, K., Fukui, H., Kamada, S., Sakamaki, T., Seto, Y., Tsutsui, S., Baron, A. Q. R. (2013). Sound velocity of hexagonal close-packed iron up to core pressures. *Geophysical Research Letters*, *40*(19), 5089–5094. https://doi.org/10.1002/grl.50992

Okamoto, H. (2000). Phase diagram for binary alloys. *Materials Park (OH).*

Ono, S., Ito, E., Tomoo, K. (2001). Mineralogy of subducted basaltic crust (MORB) from 25 to 37 GPa, and chemical heterogeneity of the lower mantle. *Earth and Planetary Science Letters*, *190*(1–2), 57–63. https://doi.org/https://doi.org/10.1016/S0012-821X(01)00375-2

Otsuka, K., McCammon, C. A., Karato, S. I. (2010). Tetrahedral occupancy of ferric iron in (Mg,Fe)O: Implications for point defects in the Earth's lower mantle. *Physics of the Earth and Planetary Interiors*, *180*(3–4), 179–188. https://doi.org/10.1016/j.pepi.2009.10.005

Otsuka, K., Longo, M., McCammon, C. A., Karato, S. (2013). Ferric iron content of ferropericlase as a function of composition, oxygen fugacity, temperature and pressure: Implications for redox conditions during diamond formation in the lower mantle. *Earth and Planetary Science Letters*, *365*, 7–16. https://doi.org/10.1016/j.epsl.2012.11.030

Overwijk, M. H. F. (1993). Novel scheme for the preparation of transmission electron microscopy specimens with a focused ion beam. *Journal of Vacuum Science & Technology B: Microelectronics and Nanometer Structures*, *11*(6), 2021. https://doi.org/10.1116/1.586537

Palot, M., Jacobsen, S. D., Townsend, J. P., Nestola, F., Marquardt, K., Miyajima, N., Harris, J. W., Stachel, T., McCammon, C. A., Pearson, D. G. (2016). Evidence for H_2O-bearing fluids in the lower mantle from diamond inclusion. *Lithos*, *265*, 237–243. https://doi.org/10.1016/j.lithos.2016.06.023

Pal'yanov, Y. N., Sokol, A. G., Khokhryakov, A. F., Pal'yanova, G. A., Borzdov, Y. M., Sobolev, N. V. (2000). Diamond and graphite crystallization in COH fluid at PT parameters of the natural diamond formation. 375, 1395-1398.

Pal'yanov, Y. N., Sokol, A. G., Borzdov, Y. M., Khokhryakov, A. F., Sobolev, N. V. (2002). Diamond formation through carbonate-silicate interaction. *American Mineralogist*, *87*, 1009–1013.

Pal'yanov, Y. N., Bataleva, Y. V., Sokol, A. G., Borzdov, Y. M., Kupriyanov, I. N., Reutsky, V. N., Sobolev, N. V. (2013). Mantle-slab interaction and redox mechanism of diamond formation. *Proceedings of the National Academy of Sciences of the United States of America*, *110*(51), 20408–20413. https://doi.org/10.1073/pnas.1313340110

Pal'yanov, Yury N., Sokol, A. G., Tomilenko, A. A., Sobolev, N. V. (2005). Conditions of diamond formation through carbonate-silicate interaction. *European Journal of Mineralogy*, *17*(2), 207–214. https://doi.org/10.1127/0935-1221/2005/0017-0207

Pascarelli, S., Mathon, O., Mairs, T., Kantor, I., Agostini, G., Strohm, C., Pasternak, S., Perrin, F., Berruyer, G., Chappelet, P. and Clavel, C. (2016). The Time-resolved and Extreme-conditions XAS (TEXAS) facility at the European Synchrotron Radiation Facility: The energy-dispersive X-ray absorption spectroscopy beamline ID24. *Journal of Synchrotron Radiation*, *23*, 353–368. https://doi.org/10.1107/S160057751501783X

Pearson, D. G., Brenker, F. E., Nestola, F., McNeill, J., Nasdala, L., Hutchison, M. T., Matveev, S., Mather, K., Silversmit, G., Schmitz, S., Vekemans, B. (2014). Hydrous mantle transition zone indicated by ringwoodite included within diamond. *Nature*, *507*(7491), 221–224. https://doi.org/10.1038/nature13080

Petrícek, V., Dušek, M., Palatinus, L. (2014). Crystallographic computing system JANA2006: General features. *Zeitschrift Fur Kristallographie*. R. Oldenbourg Verlag GmbH. https://doi.org/10.1515/zkri-2014-1737

Poirier, J.-P. (2000). Introduction to the Physics of the Earth's Interior. *Cambridge University Press*. https://doi.org/10.1017/CBO9781139164467

Potapkin, V., Chumakov, A. I., Smirnov, G. V., Celse, J. P., Rüffer, R., McCammon, C., Dubrovinsky, L. (2012). The ^{57}Fe Synchrotron Mössbauer Source at the ESRF. *Journal of Synchrotron Radiation*, *19*(4), 559–569. https://doi.org/10.1107/S0909049512015579

Pownceby, M. I., & O'Neill, H. S. C. (1994). Thermodynamic data from redox reactions at high temperatures. IV. Calibration of the Re-ReO_2 oxygen buffer from EMF and NiO+Ni-Pd redox sensor measurements. *Contributions to Mineralogy and Petrology*, *118*(2), 130–137. https://doi.org/10.1007/BF01052864

Prescher, C., & Prakapenka, V. B. (2015). *DIOPTAS* : a program for reduction of two-dimensional X-ray diffraction data and data exploration. *High Pressure Research*, *35*(3), 223–230. https://doi.org/10.1080/08957959.2015.1059835

Prescher, C., McCammon, C. A., Dubrovinsky, L. (2012). MossA: A program for analyzing energy-domain Mössbauer spectra from conventional and synchrotron sources. *Journal of Applied Crystallography*, *45*(2), 329–331. https://doi.org/10.1107/S0021889812004979

Reed, S. J. B. (2005). Electron Microprobe Analysis and Scanning Electron Microscopy in Geology. *Electron Microprobe Analysis and Scanning Electron Microscopy in Geology*, *9780521848756*, 1–197. https://doi.org/10.1017/CBO9780511610561

Richmond, N. C., & Brodholt, J. P. (1998). Calculated role of aluminum in the incorporation of ferric iron into magnesium silicate perovskite. *American Mineralogist*, *83*(9–10), 947–951. https://doi.org/10.2138/am-1998-9-1003

Ricolleau, A., Perrillat, J., Fiquet, G., Daniel, I., Matas, J., Addad, A., Menguy, N., Cardon, H., Mezouar, M., Guignot, N. (2010). Phase relations and equation of state of a natural MORB: Implications for the density profile of subducted oceanic crustin the Earth's lower mantle. *Journal of Geophysical Research: Solid Earth*, *115*(B8). https://doi.org/https://doi.org/10.1029/2009JB006709

Rietveld. (1969). Equations of state of solids for geophysics and ceramic science. Journal of Applied Crystallography, 31. *International Union of Crystallography.* https://doi.org/10.1107/s0021889869006558

Righter, K., Drake, M. J. & Yaxley, G. (1997) Prediction of siderophile element metal/silicate partition coefficients to 20 GPa and 28008C: the effects of pressure, temperature, oxygen fugacity, and silicate and metallic melt compositions. *Phys. Earth Planet. Inter.* 100, 115–134. https://doi.org/10.1016/S0031-9201(96)03235-9

Ringwood, A. E. (1959). On the chemical evolution and densities of the planets. *Geochimica et Cosmochimica Acta*, *15*(4), 257–283. https://doi.org/10.1016/0016-7037(59)90062-6

Ringwood, A. E., (1991). Phase transformations and their bearing on the constitution and dynamics of the mantle. *Geochimica et Cosmochimica Acta*, 55(8), 2083-2110. https://doi.org/10.1016/0016-7037(91)90090-R

Rohrbach, A., & Schmidt, M. W. (2011). Redox freezing and melting in the Earths deep mantle resulting from carbon-iron redox coupling. *Nature*, *472*(7342), 209–214. https://doi.org/10.1038/nature09899

Rosenthal, A., Yaxley, G. M., Green, D. H., Hermann, J., Kovacs, I., Spandler, C. (2014). Continuous eclogite melting and variable refertilisation in upwelling heterogeneous mantle. *Science Reports*, *4*(6099), 1–6. https://doi.org/10.1038/srep06099

Rubie, D. C. (1999). Characterizing the sample environment in multianvil high-pressure experiments. *Phase Transitions*, *68*(3), 431–451. https://doi.org/10.1080/01411599908224526

Rubie, D. C., Melosh, H. J., Reid, J. E., Liebske, C., Righter, K. (2003). Mechanisms of metal-silicate equilibration in the terrestrial magma ocean. *Earth and Planetary Science Letters*, *205*(3–4), 239–255. https://doi.org/10.1016/S0012-821X(02)01044-0

Rubie, D. C., Frost, D. J., Mann, U., Asahara, Y., Nimmo, F., Tsuno, K., Kegler, P., Holzheid, A., Palme, H. (2011). Heterogeneous accretion, composition and core-mantle differentiation of the Earth. *Earth and Planetary Science Letters*, *301*(1–2), 31–42. https://doi.org/10.1016/j.epsl.2010.11.030

Rüffer, R., & Chumakov, A. I. (1996). Nuclear Resonance Beamline at ESRF. *Hyperfine Interactions*, *97–98*(1), 589–604. https://doi.org/10.1007/bf02150199

Sakai, T., Ohtani, E., Terasaki, H., Sawada, N., Kobayashi, Y., Miyahara, M., Nishijima, M., Hirao, N., Ohishi, Y., Kikegawa, T. (2009). Fe-Mg partitioning between perovskite and ferropericlase in the lower mantle. *American Mineralogist*, *94*(7), 921–925. https://doi.org/10.2138/am.2009.3123

Sakai, T., Ohtani, E., Hirao, N., Ohishi, Y. (2011). Stability field of the hcp-structure for Fe, Fe-Ni, and Fe-Ni-Si alloys up to 3 Mbar. *Geophysical Research Letters*, 38(9). https://doi.org/10.1029/2011GL047178

Sakairi, T., Sakamaki, T., Ohtani, E., Fukui, H., Kamada, S., Tsutsui, S., Uchiyama, H., Baron, A. Q. R., (2018). Sound velocity measurements of hcp Fe-Si alloy at high pressure and high temperature by inelastic X-ray scattering. *American Mineralogist*, *103*(1), 85–90. https://doi.org/10.2138/am-2018-6072

Sakamaki, T., Ohtani, E., Fukui, H., Kamada, S., Takahashi, S., Sakairi, T., Takahata, A., Sakai, T., Tsutsui, S., Ishikawa, D., Shiraishi, R. (2016). Geophysics: Constraints on Earth's inner core composition inferred from measurements of the sound velocity of hcp-iron in extreme conditions. *Science Advances*, *2*(2). https://doi.org/10.1126/sciadv.1500802

Sato, K., Akaishi, M., Yamaoka, S. (1999). Spontaneous nucleation of diamond in the system $MgCO_3$-$CaCO_3$-C at 7.7 GPa. *Diamond and Related Materials*, *8*(10), 1900–1905. https://doi.org/10.1016/S0925-9635(99)00157-0

Schwerdtfeger, K., & Zwell, L. (1968). Activities in solid iridium-iron and rhodium-iron alloys at 1200 °C. *Trans Met Soc Aime*, 242(4)

Shibazaki, Y., Ohtani, E., Fukui, H., Sakai, T., Kamada, S., Ishikawa, D., Tsutsui, S., Baron, A. Q. R., Nishitani, N., Hirao, N., Takemura, K. (2012). Sound velocity measurements in dhcp-FeH up to 70 GPa with inelastic X-ray scattering: Implications for the composition of the Earth's core. *Earth and Planetary Science Letters*, *313–314*(1), 79–85. https://doi.org/10.1016/j.epsl.2011.11.002

Shibazaki, Y., Nishida, K., Higo, Y., Igarashi, M., Tahara, M., Sakamaki, T., Terasaki, H., Shimoyama, Y., Kuwabara, S., Takubo, Y., Ohtani, E. (2016). Compressional and shear wave velocities for polycrystalline bcc-Fe up to 6.3 GPa and 800 K. *American Mineralogist*, *101*(5), 1150–1160. https://doi.org/10.2138/am-2016-5545

Shirey, S. B., Cartigny, P., Frost, D. J., Keshav, S., Nestola, F., Nimis, P., Pearson, D.G., Sobolev, N.V., Walter, M.J. (2013). Diamonds and the geology of mantle carbon. *Reviews in Mineralogy and Geochemistry*, *75*, 355–421. https://doi.org/10.2138/rmg.2013.75.12

Siebert, J., Badro, J., Antonangeli, D., Ryerson, F. J. (2013). Terrestrial Accretion Under Oxidizing Conditions. *Science*, *339 (6124)*, 1194–1198. https://doi.org/10.1126/science.1227923

Smirnov, G. V., Chumakov, A. I., Potapkin, V. B., Rüffer, R., Popov, S. L. (2011). Multispace quantum interference in a ^{57}Fe synchrotron Mössbauer source. *Physical Review A - Atomic, Molecular, and Optical Physics*, *84*(5), 1–12. https://doi.org/10.1103/PhysRevA.84.053851

Smith, E. M., Shirey, S. B., Nestola, F., Bullock, E. S., Wang, J., Richardson, S. H., Wang, W. (2016). Large gem diamonds from metallic liquid in Earth's deep mantle. *Science*, *354*(6318), 1403–1405. https://doi.org/10.1126/science.aal1303

Smith, E. M., Shirey, S. B., Wang, W. (2017). The very deep origin of the world's biggest diamonds. *Gems and Gemology*, *53*(4), 388–403. https://doi.org/10.5741/GEMS.53.4.388

Smith, E. M., Ni, P., Shirey, S. B., Richardson, S. H., Wang, W., Shahar, A. (2021). Heavy iron in large gem diamonds traces deep subduction of serpentinized ocean floor. *Science Advances*, *7*(14). https://doi.org/10.1126/sciadv.abe9773

Sokol, A.G., Pal'yanov, Y. N., Pal'yanova, G. A., Khokhryakov, A. F., Borzdov, Y. M. (2001). Diamond and graphite crystallization from C-O-H fluidsunder high pressure and high temperature conditions. *Diamond and Related Materials*, 2131–2136.

Sokol, Alexander G., Palyanova, G. A., Palyanov, Y. N., Tomilenko, A. A., Melenevsky, V. N. (2009). Fluid regime and diamond formation in the reduced mantle: Experimental constraints. *Geochimica et Cosmochimica Acta*, *73*(19), 5820–5834. https://doi.org/10.1016/j.gca.2009.06.010

Solomatova, N.V., Jackson, J.M., Sturhahn, W., Wicks, J.K., Zhao, J., Toellner, T.S., Kalkan, B. and Steinhardt, W.M. (2016). Equation of state and spin crossover of (Mg, Fe) O at high pressure, with implications for explaining topographic relief at the core-mantle boundary. American Mineralogist, 101(5), 1084-1093. https://doi.org/10.2138/am-2016-5510

Solé, V. A., Papillon, E., Cotte, M., Walter, P., Susini, J. (2007). A multiplatform code for the analysis of energy-dispersive X-ray fluorescence spectra. *Spectrochimica Acta - Part B Atomic Spectroscopy*, *62*(1), 63–68. https://doi.org/10.1016/j.sab.2006.12.002

Stachel, T., Brey, G. P., Harris, J. W. (2005). Inclusions in Sublithospheric Diamonds: Glimpses of Deep Earth. *Elements*, *1*(2), 73–78. https://doi.org/10.2113/gselements.1.2.73

Stachel, T., Harris, W., Brey, G. P. (2000). Kankan diamonds (Guinea) II : lower mantle inclusion parageneses, 16–27. https://doi.org/10.1007/s004100000174

Stagno, V., Tange, Y., Miyajima, N., McCammon, C. A., Irifune, T., Frost, D. J. (2011). The stability of magnesite in the transition zone and the lower mantle as function of oxygen fugacity. *Geophysical Research Letters*, *38*(19), 1–5. https://doi.org/10.1029/2011GL049560

Stagno, V. (2019). Carbon, carbides, carbonates and carbonatitic melts in the Earth's interior. *Journal of the Geological Society*, *176*(2), 375–387. https://doi.org/10.1144/jgs2018-095

Stagno, V., & Fei, Y. (2020). The redox boundaries of Earth's interior. *Elements*, *16*(3), 167–172. https://doi.org/10.2138/GSELEMENTS.16.3.167

Stagno, V., & Frost, D. J. (2010). Carbon speciation in the asthenosphere: Experimental measurements of the redox conditions at which carbonate-bearing melts coexist with graphite or diamond in peridotite assemblages. *Earth and Planetary Science Letters*, *300*(1–2), 72–84. https://doi.org/10.1016/j.epsl.2010.09.038

Stagno, V., Ojwang, D. O., McCammon, C. A., Frost, D. J. (2013). The oxidation state of the mantle and the extraction of carbon from Earth's interior. *Nature*, *493*(7430), 84–88. https://doi.org/10.1038/nature11679

Strong, H., & Hanneman, R. E. (1967). Crystallization of diamond and graphite. *The Journal of Chemical Physics*, 46(9), 3668-3676. https://doi.org/10.1063/1.1841272

Sumiya, H., Toda, N., Satoh, S. (2000). High-quality large diamond crystals. *New diamond and frontier carbon technology*, 10(5), 233-251.

Sun, L., Wu, Q., Wang, W. (2001). Bulk diamond formation from graphite in the presence of COH fluid under high pressure. *High Pressure Research*, 21(3-4), 159-173. https://doi.org/10.1080/08957950108201021

Sutton, M. A., Li, N., Joy, D. C., Reynolds, A. P., Li, X. (2007). Scanning electron microscopy for quantitative small and large deformation measurements Part I: SEM imaging at magnifications from 200 to 10,000. *Experimental Mechanics*, *47*(6), 775–787. https://doi.org/10.1007/s11340-007-9042-z

Swartzendruber, L. J. (1984). The Fe-Ir (Iron-Iridium) system. *Bulletin of Alloy Phase Diagrams*, *5*(2), 134. https://doi.org/10.1007/BF02868944

Takafuji, N., & Hirose, K. (2005). Solubilities of O and Si in liquid iron in equilibrium with $(Mg,Fe)SiO_3$ perovskite and the light elements in the core. *Geophysical Research Letters*, *32*. https://doi.org/10.1029/2005GL022773

Takahashi, T., & Basset, W. (1964). High-Pressure Polymorph of Iron. *Science*, *145*(3631), 483–486. https://doi.org/10.1126/science.145.3631.483

Tange, Y., Takahashi, E., Nishihara, Y., Funakoshi, K. I., Sata, N. (2009). Phase relations in the system MgO-FeO-SiO_2 to 50 GPa and 2000°C: An application of experimental techniques using multianvil apparatus with sintered diamond anvils. *Journal of Geophysical Research: Solid Earth*, *114*(2), 1–12. https://doi.org/10.1029/2008JB005891

Tateno, S., Hirose, K., Ohishi, Y., Tatsumi, Y. (2010). The structure of iron in Earth's inner core. *Science*, *330*(6002), 359–361. https://doi.org/10.1126/science.1194662

Tateno, S., Kuwayama, Y., Hirose, K., Ohishi, Y. (2015). The structure of Fe-Si alloy in Earth's inner core. *Earth and Planetary Science Letters*, *418*, 11–19. https://doi.org/10.1016/j.epsl.2015.02.008

Taylor, J. R., Wall, V. J., & Pownceby, M. I. (1992). The calibration and application of accurate redox sensors. *American Mineralogist*, *77*(3–4), 284–295.

Taylor, W. R., & Green, D. H. (1988). Measurement of reduced peridotite-C-O-H solidus and implications for redox melting of the mantle. *Letters to Nature*, *332*. https://doi.org/10.1038/332349a0

Terasaki, H., Kamada, S., Sakai, T., Ohtani, E., Hirao, N., Ohishi, Y. (2011). Liquidus and solidus temperatures of a Fe–O–S alloy up to the pressures of the outer core: Implication for the thermal structure of the Earth's core. *Earth and Planetary Science Letters*, *304*(3–4), 559–564. https://doi.org/10.1016/J.EPSL.2011.02.041

Thomson, A. R., Walter, M. J., Kohn, S. C., Brooker, R. A. (2016). Slab melting as a barrier to deep carbon subduction. *Nature*, *529*. https://doi.org/10.1038/nature16174

Tilley, R. J. D. (2006). Crystals and Crystal Structures. *Wiley & Sons.*

Tomiska, J. (1989). Massenspektrometrische Ermittlung der thermodynamischen Mischungsgrößen in der kfz-Phase und Berechnung des Schmelzdiagramms Eisen-Palladium / Mass Spectrometric Determination of the Thermodynamic Mixing Properties in the fcc phase and Calculation of the of the Phase Diagramm Iron-Palladium. *International Journal of Materials Research*, *80*(12), 888–893. https://doi.org/10.1515/IJMR-1989-801207

Uenver-Thiele, L., Woodland, A. B., Ballaran, T. B., Miyajima, N., Frost, D. J. (2017). Phase relations of $MgFe_2O_4$ at conditions of the deep upper mantle and transition zone. *American Mineralogist*, *102*(3), 632–642. https://doi.org/10.2138/am-2017-5871

Ulmer, P., & Luth, R. W. (1991). The graphite-COH fluid equilibrium in P, T, f_{O2} space An experimental determination to 30 kbar and 1600 C. *Contributions to Mineralogy and Petrology*, *106*(3), 265–272. https://doi.org/10.1007/bf00324556

Vočadlo, L., Price, G. D., Wood, I. G. (1999). Crystal structure, compressibility and possible phase transitions in ε-FeSi studied by first-principles pseudopotential calculations. *Acta Crystallographica Section B: Structural Science*, *55*(4), 484–493. https://doi.org/10.1107/S0108768199001214

Vočadlo, L., Alfè, D., Gillan, M. J., Wood, I. G., Brodholt, J. P., Price, G. D. (2003). Possible thermal and chemical stabilization of body-centered-cubic iron in the Earth's core. *Nature*, *424*(6948), 536–539. https://doi.org/10.1038/nature01829

Wade, J., & Wood, B. J. (2005). Core formation and the oxidation state of the Earth. *Earth and Planetary Science Letters*, *236*(1–2), 78–95. https://doi.org/10.1016/j.epsl.2005.05.017

Wakamatsu, T., Ohta, K., Yagi, T., Hirose, K., Ohishi, Y. (2018). Measurements of sound velocity in iron–nickel alloys by femtosecond laser pulses in a diamond anvil cell. *Physics and Chemistry of Minerals*, *45*(6), 589–595. https://doi.org/10.1007/s00269-018-0944-3

Walter, M. J., Bulanova, G. P., Armstrong, L. S., Keshav, S., Blundy, J. D., Gudfinnsson, G., Lord, O. T., Lennie, A. R., Clark, S. M., Smith, C. B., Gobbo, L. (2008). Primary carbonatite melt from deeply subducted oceanic crust. *Nature*, *454*(7204), 622–625. https://doi.org/10.1038/nature07132

Walter, M. J., Kohn, S. C., Araujo, D., Bulanova, G. P., Smith, C. B., Gaillou, E., Wang, J., Steele, A., Shirey, S. B. (2011). Deep mantle cycling of oceanic crust: Evidence from diamonds and their mineral inclusions. *Science*, *334*(6052), 54–57. https://doi.org/10.1126/science.1209300

Wasson, J. T., & Chou, C. (1974). Fractionation of moderately volatile elements in ordinary chondrites. *Meteoritics and Planetary Science*, *9*(1), 69–84. https://doi.org/10.1111/j.1945-5100.1974.tb00063.x

Waychunas, G. A., Apted, M. J. Brown, G. E. (1983). X-ray K-edge absorption spectra of Fe minerals and model compounds: Near-edge structure. *Physics and Chemistry of Minerals*, 10, 1–9. https://doi.org/10.1007/BF01204319

Weir, C. E., Lippincott, E. R., Van Valkenburg, A., Bunting, E. N. (1959). Infrared studies in the 1- to 15-micron region to 30,000 atmospheres. *Journal of Research of the National Bureau of Standards. Section A. Physics and Chemistry*, 63,1. https://doi.org/10.6028/jres.063A.003

Williams, D. B., & Carter, C. B. (1996). The Transmission Electron Microscope. *Transmission Electron Microscopy*. Springer, Boston, MA. https://doi.org/10.1007/978-1-4757-2519-3_1

Wicks, J. K. and Duffy, T.S., (2016). Crystal structures of minerals in the lower mantle. *Deep Earth Phys Chem Lower Mantle Core*, 217, 69.

Wirth, R., Dobrzhinetskaya, L., Harte, B., Schreiber, A., Green, H. W. (2014). High-Fe (Mg, Fe)O inclusion in diamond apparently from the lowermost mantle. *Earth and Planetary Science Letters*, *404*, 365–375. https://doi.org/10.1016/j.epsl.2014.08.010

Wirth, Richard. (2004). Focused Ion Beam (FIB): A novel technology for advanced application of micro- and nanoanalysis in geosciences and applied mineralogy. *European Journal of Mineralogy*, *16*(6), 863–876. https://doi.org/10.1127/0935-1221/2004/0016-0863

Wood, B. J. (2000). Phase transformations and partitioning relations in peridotite under lower mantle conditions. *Earth and Planetary Science Letters*, *174*(3–4), 341–354. https://doi.org/10.1016/S0012-821X(99)00273-3

Woodland, A. B., & O'Neill, H. S. C. (1997). Thermodynamic data for Fe-bearing phases obtained using noble metal alloys as redox sensors. *Geochimica et Cosmochimica Acta*, *61*(20), 4359–4366. https://doi.org/10.1016/S0016-7037(97)00247-0

Woodland, A. B., Kornprobst, J., Tabit, A. (2006). Ferric iron in orogenic lherzolite massifs and controls of oxygen fugacity in the upper mantle. *Lithos*, *89*(1–2), 222–241. https://doi.org/10.1016/j.lithos.2005.12.014

Wyllie, M. R. J., Gregory, A. R., Gardner, L. W. (1956). Elastic wave velocities in heterogeneous and porous media. *Geophysics*, 21(1), 41-70. https://doi.org/10.1190/1.1438217

Yamaoka, S., Kumar, M. D. S., Kanda, H., Akaishi, M. (2002). Formation of diamond from $CaCO_3$ in a reduced C–O–H fluid at HP–HT. *Diamond and Related Materials*, 1496–1504. https://doi.org/10.1016/S0925-9635(02)00053-5

Yusenko, K. V., Khandarkhaeva, S., Fedotenko, T., Pakhomova, A., Gromilov, S. A., Dubrovinsky, L. S., Dubrovinskaia, N. A. (2019). Equations of state of rhodium, iridium and their alloys up to 70 GPa. *Journal of Alloys and Compounds*, 65. https://doi.org/10.1016/j.jallcom.2019.02.206

Zhang, J., & Guyot, F. (1999a). Experimental study of the bcc-fcc phase transformations in the Fe-rich system Fe-Si at high pressures. *Physics and Chemistry of Minerals*, *26*(6), 419–424. https://doi.org/10.1007/s002690050203

Zhang, J., & Guyot, F. (1999b). Thermal equation of state of iron and $Fe_{0.91}Si_{0.09}$. *Physics and Chemistry of Minerals*, *26*(3), 206–211. https://doi.org/10.1007/s002690050178

Zhu, F., Li, J., Liu, J., Lai, X., Chen, B., Meng, Y. (2019). Kinetic Control on the Depth Distribution of Superdeep Diamonds. *Geophysical Research Letters*, *46*(4), 1984–1992. https://doi.org/10.1029/2018GL080740

(Eidesstattliche) Versicherungen und Erklärungen

(§ 9 Satz 2 Nr. 3 PromO BayNAT)

Hiermit versichere ich eidesstattlich, dass ich die Arbeit selbstständig verfasst und keine anderen als die von mir angegebenen Quellen und Hilfsmittel benutzt habe (vgl. Art. 64 Abs. 1 Satz 6 BayHSchG).

(§ 9 Satz 2 Nr. 3 PromO BayNAT)

Hiermit erkläre ich, dass ich die Dissertation nicht bereits zur Erlangung eines akademischen Grades eingereicht habe und dass ich nicht bereits diese oder eine gleichartige Doktorprüfung endgültig nicht bestanden habe.

(§ 9 Satz 2 Nr. 4 PromO BayNAT)

Hiermit erkläre ich, dass ich Hilfe von gewerblichen Promotionsberatern bzw. -vermittlern oder ähnlichen Dienstleistern weder bisher in Anspruch genommen habe noch künftig in Anspruch nehmen werde.

(§ 9 Satz 2 Nr. 7 PromO BayNAT)

Hiermit erkläre ich mein Einverständnis, dass die elektronische Fassung meiner Dissertation unter Wahrung meiner Urheberrechte und des Datenschutzes einer gesonderten Überprüfung unterzogen werden kann.

(§ 9 Satz 2 Nr. 8 PromO BayNAT)

Hiermit erkläre ich mein Einverständnis, dass bei Verdacht wissenschaftlichen Fehlverhaltens Ermittlungen durch universitätsinterne Organe der wissenschaftlichen Selbstkontrolle stattfinden können.

Bayreuth, 13/10/2022…….
Ort, Datum, Unterschrift